université
PARIS-SACLAY

# Lagrangian numerical methods for multi-material radiation hydrodynamics

*Méthodes numériques lagrangiennes pour l'hydrodynamique radiative multi-matériaux*

**Thèse de doctorat de l'université Paris-Saclay**

École doctorale n°74 mathématiques Hadamard (EDMH)
Spécialité de doctorat: Mathématiques appliquées
Graduate School : voir annexe. Référent : voir annexe

Thèse préparée dans la (ou les) unité(s) de recherche **Nom(s)** (voir annexe), sous la direction de **Prénom NOM**, titre du directeur ou de la directrice de thèse, la co-direction de **Prénom NOM**, titre du co-directeur ou de la co-directrice de thèse, le co-encadrement de **Prénom NOM**, titre, du co-encadrant ou de la co-encadrante ou la co-supervision de **Prénom NOM**, titre, du tuteur ou de la tutrice (en cas de partenariat industriel)

**Thèse soutenue à Paris-Saclay, le JJ mois AAAA, par**

# Bastien MANACH-PÉRENNOU

### Composition du jury
Membres du jury avec voix délibérative

| | |
|---|---|
| **Prénom NOM** | Président ou Présidente |
| Titre, Affiliation | |
| **Prénom NOM** | Rapporteur & Examinateur / trice |
| Titre, Affiliation | |
| **Prénom NOM** | Rapporteur & Examinateur / trice |
| Titre, Affiliation | |
| **Prénom NOM** | Examinateur ou Examinatrice |
| Titre, Affiliation | |
| **Prénom NOM** | Examinateur ou Examinatrice |
| Titre, Affiliation | |

**Titre:** Méthodes numériques lagrangiennes pour l'hydrodynamique radiative multi-matériaux

**Mots clés:** Numérique, Hydrodynamique lagrangienne, Radiatif, Multi-matériaux, Thermodynamique, Produits non-conservatifs

**Résumé:** Ce travail a pour objectif d'améliorer la compréhension et le développement des méthodes numériques lagrangiennes utilisées pour l'hydrodynamique radiative multi-matériaux. Dans ce contexte, la robustesse, la précision et les coûts de calcul des schémas numériques pour la résolution de ce modèle constituent un enjeu majeur.

Différents aspects des écoulements multi-matériaux et de leur discrétisation sont étudiés. Ceux-ci incluent notamment la comparaison des équations iso-pression et iso-déformation; la discrétisation multi-matériaux du transport radiatif; les couplages raides des systèmes à trois températures et leur implicitation; les aspects multi-vitesse au sein d'une stratégie de « Multi-Lagrange + Projection »; le traitement numérique des produits non-conservatifs. Dans ces différentes études qui s'étalent sur trois chapitres différents, les chocs multi-matériaux et multi-températures sont un intérêt majeur. Leur spécification et leur approximation robuste se fait grâce à un contrôle de la dissipation numérique entre les différents matériaux. Un quatrième et dernier chapitre traite cette même problématique sous un angle plus académique. Les produits non-conservatifs sont définis à l'aide de la notion de chemin et ce formalisme nécessite une stratégie numérique cohérente.

**Title:** Lagrangian numerical methods for multi-material radiation hydrodynamics

**Keywords:** Numerical, Lagrangian hydrodynamics, Radiation, Multi-material, Thermodynamics, Non-conservative products

**Abstract:** This work aims at improving the understanding and development of Lagrangian numerical methods for multi-material radiation hydrodynamics. In this context, robustness, accuracy and computational cost of numerical schemes are a major challenge.

Several aspects of multi-material flows and their discretization are studied. They include, among others, comparison between the equal-pressure and equal-strain assumptions; discrete multi-material radiation transport; stiff couplings inside three-temperature systems and their implicit time integration; multi-velocity aspects in the context of a "Multi-Lagrange + Remapping" strategy; numerical treatment of non-conservative products. These topics are treated in three separate chapters but multi-temperature multi-material shocks remain a major theme throughout. Their specification and robust approximation is guaranteed by a proper control of the numerical dissipation between the different materials. A fourth and last chapter is devoted to this very same issue while adopting a more academic-oriented approach. Shocks are there defined with the so-called path theory and their approximation requires adequate numerical strategies.

# Contents

# Introduction

## Contents

The present work is made of four distinct chapters. Each chapter is designed to be standalone and includes its own state of the art. Depending on the specific underlying physical assumptions made in each chapter, the number of equations can vary and additional terms can be considered. Although different, these systems of equations all stem from a unique modeling effort and most numerical challenges are similar. Consequently, this chapter aims at introducing in a unified manner the different equations and ensuing numerical issues encountered separately in each chapter. Overall, the connection between chapters 1, 2 and 3 is more apparent than with chapter 4 which adopts a more academic approach. This last chapter leans on a completely different formalism for deriving solutions and their numerical approximation. The global consistency of the manuscript is here addressed and duly motivated. In a first part, some generalities of hydrodynamics and thermodynamics are first discussed before delving into the multi-material aspects. In a second part, numerical strategies are discussed. Special attention is paid to shock capturing and dissipation.

## 1  Fluid models

### 1.1  Single-material hydrodynamics

To describe flows, different approaches are possible depending on the regime and required level of accuracy. In the limit of small Knudsen number, the mean free path is small compared to the system characteristic lengths; the continuum hypothesis can be made so that the flow evolution can be expressed with partial differential equations. Here is given a brief summary of the Euler equations which are formally obtained from the Navier-Stokes equations in the inviscid limit. Their elementary mathematical properties, the Lagrangian system of coordinates, the basics of

thermodynamics and shocks are discussed. A more detailed presentation of the following results can be found in [41, 102].

**Euler equations**

The Euler equations are an essential building block of any fluid description. The material state is entirely characterized by its density $\rho$, velocity $\mathbf{u}$ and specific total energy $E$. The pressure is denoted $p$.

$$\frac{\partial}{\partial t}\rho + \nabla \cdot (\rho\mathbf{u}) = 0, \tag{1a}$$

$$\frac{\partial}{\partial t}(\rho\mathbf{u}) + \nabla \cdot (\rho\mathbf{u} \otimes \mathbf{u}) + \nabla p = 0, \tag{1b}$$

$$\frac{\partial}{\partial t}(\rho E) + \nabla \cdot (\rho E\mathbf{u}) + \nabla \cdot (p\mathbf{u}) = 0. \tag{1c}$$

The equations describe, in order, the conservation of mass, momentum and total energy. Because all quantities are conserved, the Euler equations are an example of a system of conservation laws. In one dimension (see the aforementioned references for definition in arbitrary dimension), such equations are of the form

$$\frac{\partial}{\partial t}U + \frac{\partial}{\partial x}F(U) = 0 \tag{2}$$

where $U$ is the state vector and $F$ is the flux function. For the Euler equations $U = (\rho, \rho u, \rho E)$ and $F$ consists of a two separate fluxes: an advection flux associated with the transport of the variables and an acoustic flux associated with the pressure forces and their work. Defining $A(U)$ as the Jacobian of the flux $F(U)$, equation (2) can also be written

$$\frac{\partial}{\partial t}U + A(U)\frac{\partial}{\partial x}U = 0. \tag{3}$$

The properties of the matrix $A(U)$ are tied with the equation's response to a linear perturbation. In particular, if it is diagonalizable with real eigenvalues, the system is called hyperbolic and the initial-value problem is well-posed. The Euler equations can be shown to be hyperbolic under some conditions on the expression of $p$.

In the present work, fluid equations will be written in Lagrangian coordinates. By definition, the Lagrangian coordinate is constant along the flow of a given fluid parcel. This effectively factorizes transport fluxes into the time derivatives. Such factorization is critical for the numerical strategies detailed in the different chapters. The Lagrangian derivative of an arbitrary quantity $\phi$ is

$$\frac{\mathrm{d}}{\mathrm{d}t}\phi = \frac{\partial}{\partial t}\phi + \mathbf{u} \cdot \nabla\phi. \tag{4}$$

The Euler equations (1) can then be recast into the updated Lagrangian formalism [72]

$$\rho \frac{\mathrm{d}}{\mathrm{d}t}\left(\frac{1}{\rho}\right) - \nabla \cdot \mathbf{u} = 0, \tag{5a}$$

$$\rho \frac{\mathrm{d}}{\mathrm{d}t}\mathbf{u} + \nabla p = 0, \tag{5b}$$

$$\rho \frac{\mathrm{d}}{\mathrm{d}t}E + \nabla \cdot (p\mathbf{u}) = 0. \tag{5c}$$

Finally, the total energy $E$ is made of two contribution: kinetic energy and internal energy. The evolution of the specific kinetic energy $\frac{1}{2}\|\mathbf{u}\|^2$ is obtained from the momentum equation. The total energy conservation law can then be replaced with the internal energy $e = E - \frac{1}{2}\|\mathbf{u}\|^2$ evolution, which reads

$$\frac{\mathrm{d}}{\mathrm{d}t}e + p\frac{\mathrm{d}}{\mathrm{d}t}\left(\frac{1}{\rho}\right) = 0. \tag{6}$$

The internal energy formulation is crucial for taking into account thermodynamics and becomes all the more necessary for multi-material and multi-temperature applications.

**Thermodynamics**

In (1), a constitutive equation still needs to be written for the pressure. Under the assumption of local thermodynamic equilibrium, pressure is specified by thermodynamics. Thermodynamics is the cornerstone of hydrodynamics. It closes the equations, defines admissible solutions and has substantial consequences on the structure of these solutions. The two first laws of thermodynamics state that the internal energy is given as a function $e(v, s)$ of the volume $v = 1/\rho$ and the entropy $s$; pressure and temperatures are then defined as the partial derivatives of the energy, leading to the so-called Gibbs equation

$$\mathrm{d}e = -p\mathrm{d}v + T\mathrm{d}s. \tag{7}$$

The variation of internal energy is expressed as the sum of the work of pressure forces $-p\mathrm{d}v$ and the heat deposit $T\mathrm{d}s$. The second law states that, for an isolated system, entropy can only increase over time

$$\mathrm{d}s \geq 0. \tag{8}$$

Because of total energy conservation, the internal energy variation must correspond to exchanges with other energy potentials (e.g. kinetic energy). The work of pressure forces is unsigned and can go in one way or the other; in other words, it is reversible. By contrast, the heat deposit corresponds to an irreversible process as entropy cannot decrease. To illustrate the role of both, let's consider a piston on which a force is applied, thus increasing its internal pressure. If the piston is instantaneously freed from this force, the pressure imbalance between the inside and the outside will initiate an expansion. This expansion creates a pressure work leading to a conversion of internal energy into kinetic energy. Pressure then drops inside the material and, upon reaching pressure equilibrium with the outside, the total force acting on the box is zero. However, because of inertia, the piston continues to expand until the new resulting pressure imbalance induces a compression. If the only energy exchange is that of pressure work,

then the piston experiences a periodic oscillation between expansion and compression phases. In practice, such a perpetual motion does not exist because of dissipation. The term $T\mathrm{d}s$ progressively converts kinetic energy into heat in an irreversible manner. Oscillations are then damped or may not even start at all if dissipation is sufficient. This example is completely analogous to that of a swinging pendulum under gravitational acceleration. As the pendulum goes up, kinetic energy is converted into gravitational potential energy; as it goes down, the reverse process occurs. This essentially means that the work of gravity is reversible, as any force resulting from a potential. The periodic movement would then go on forever were it not for the air resistance which induces an irreversible transfer of kinetic energy into heat.

If pressure and temperatures consist in first order derivative of the energy (7), second and third order derivatives also play an important role in the behavior of the flow [78]. Here are mentioned two which are especially relevant for fluid applications. First, the speed of sound $c$ is defined as

$$c^2 = \left.\frac{\partial p}{\partial \rho}\right|_s \geq 0. \tag{9}$$

It is directly related to the eigenvalues of the matrix $A(U)$ (3) associated with the Euler equations which are $u - c$, $u$ and $u + c$. It then corresponds to a characteristic speed of propagation in the system. In particular, if $c \to +\infty$, compression waves are instantaneous, pressure progressively becomes decoupled from density and incompressible flows are eventually recovered. Strictly speaking, incompressible hydrodynamics are not in the scope of thermodynamics but rather in its closure. Another major thermodynamic coefficient is the fundamental derivative, defined as

$$\mathcal{G} = \frac{1}{c}\left.\frac{\partial \rho c}{\partial \rho}\right|_s. \tag{10}$$

It measures the convexity of isentropic curves in the $p - 1/\rho$ plane. Its sign is usually positive but can vary for some applications, a feature which has deep implications on the structure of shocks.

**Shocks**

The Euler equations describe isentropic behavior as seen when comparing (6) with (7). However, pressure discrepancy can generate compression which tends to steepen solutions. Without any opposing effect, gradients can become arbitrarily high in finite time and generate singularities. Physically, such singularities cannot exist; additional dissipative phenomena such as viscosity or heat exchange must be considered as in the Navier-Stokes equations [93]. The steepening induced by pressure forces compete with the smearing created by dissipation. When a balance is found between the two, a profile eventually settles down and propagates through the medium with a certain speed $\sigma$. Such a phenomenon is called a shock and its profile can spread over as little as a few nanometers. Dissipation is then substantial in the vicinity of the shock but reasonably negligible away from it. Integrating the solution from its left state $U_L$ to its right state $U_R$ yields the following jump condition

$$\sigma\left(U_R - U_L\right) = F(U_R) - F(U_L). \tag{11}$$

It is worth noticing that (11) does not include any contribution from the dissipation. The upstream and downstream states do not depend on these details although the exact shock profile does. Because of the necessary dissipation, shocks are irreversible processes; the entropy is always larger downstream than it is upstream so as to comply with the second principle of thermodynamics. The thermodynamics of the shock is contained in the so-called Rankine-Hugoniot relationship which is a direct consequence of (11)

$$e_R - e_L = \frac{p_R + p_L}{2} \left( \frac{1}{\rho_L} - \frac{1}{\rho_R} \right). \tag{12}$$

From a mathematical point of view, it is possible to define shocks without the explicit use of dissipation. Although (6) describes an isentropic evolution, algebraic manipulations used to derive it only make sense if the solution is smooth. Hyperbolic conservation laws usually develop discontinuities in finite time. In this case, solutions of (2) cannot be understood in the classical sense; a weak formulation is necessary. Discontinuity are then allowed and satisfy equation (11). For an arbitrary hyperbolic conservation law, a given shock is always associated to one of the eigenvalues $\lambda(U)$ of the matrix $A(U)$. For small amplitudes, its propagation speed $\sigma$ can reasonably be approximated by

$$\sigma \approx \frac{\lambda(U_L) + \lambda(U_R)}{2}. \tag{13}$$

For the Euler equation, it confirms the relationship between the propagation of shocks and the speed of sound $c$. The weak formulation alone is not enough to uniquely specify solutions. An entropy criterion must be added and shows that although not explicitly used, the evanescent effect of dissipation cannot be forgotten without failing to guarantee physically meaningful solutions. Because the full shock profile is replaced with a strict discontinuity, the entropy production is confined to an infinitely small region and takes the form of a Dirac distribution.

On a more general note, shocks consist in only one of the elementary wave patterns of general hyperbolic systems (and the only one associated with dissipation). The nature and properties of elementary waves depend on their associated eigenvalue and eigenvector fields. For the Euler equations, it boils down to the sign of the fundamental derivative $\mathcal{G}$. In particular, if its sign changes, elementary waves display complex composite behaviors [78].

## 1.2 Multi-temperature and multi-material aspects

### Averaging procedure

Multi-material flows are locally described with the Euler equations, possibly supplemented with dissipation. Thermodynamics vary discontinuously inside the medium depending on the material. Such a description requires a perfect knowledge of the position of interfaces throughout the entire evolution of the system. It is generally impossible, especially for dispersed phases where small structures are numerous and have characteristic lengths substantially smaller than the observation scale. The so-called averaging procedure is then a convenient tool for both modeling multi-material flows and numerically approximating them. Details on this wide-spread method can be found in [52, 31, 113, 49]. The main steps are here summarized.

- Single-fluid equations are multiplied with a function $b^k \in [0, 1]$. The function $b^k$ is a generic

way of quantifying the presence of material $k$. It can be taken as a local mass fraction or a geometrical indicator function. It can also depend on an additional variable $\omega$ living in a probability space $\Omega$ if the description is stochastic.

- An ensemble averaging $\overline{\cdot}$ is applied on the resulting equations. It consists in a moving average with an arbitrary kernel (or density function). Once again, the averaging is generic and can be performed with respect to space, time, probability realizations or any combination of the three.

- Material averaged quantities are defined as

$$\alpha^k \rho^k \phi^k = \overline{b^k \rho \phi} \tag{14}$$

for $\phi \in \{1/\rho, 1, \mathbf{u}, e\}$. In particular, the quantity $\alpha^k = \overline{b^k}$ corresponds to a presence probability, a time frequency or a volume fraction depending on the type of averaging. The historic terminology volume fraction is commonly used, regardless of the underlying measure.

- The resulting equations describe the evolution of averaged quantities. Part of the equations are expressed with the very same averaged variables but they also includes correlation terms for which no *a priori* closure can be given. These correlations depend on both the system and the nature of the averaging. They essentially encapsulate small-scale phenomena.

A phenomelogical description of correlation terms can be found in [49, app. B]. Because of their presence, finding a universal multi-material model is a wager lost in advance. Still, it remains possible to extract the greatest common denominator of all multi-material models [108, app. A] for which pressure discrepancy between materials is neglected and all dissipation is omitted. The resulting isentropic equations, written in a Lagrangian factorized form, are

$$\alpha^k \rho^k \frac{\mathrm{d}^k}{\mathrm{d}t} \left( \frac{1}{\alpha^k \rho^k} \right) - \nabla \cdot \mathbf{u}^k = 0, \tag{15a}$$

$$\alpha^k \rho^k \frac{\mathrm{d}^k}{\mathrm{d}t} \mathbf{u}^k + \alpha^k \nabla p = 0, \tag{15b}$$

$$\alpha^k \rho^k \left[ \frac{\mathrm{d}^k}{\mathrm{d}t} e^k + p^k \frac{\mathrm{d}^k}{\mathrm{d}t} \left( \frac{1}{\rho^k} \right) \right] = 0, \tag{15c}$$

$$p^k = p. \tag{15d}$$

The equations are devoid of any term that is not related to the work of pressure forces. As a result, they describe purely reversible (i.e. isentropic) processes and can also be derived from a least action principle [37, 108]. Pressure equality between the different materials is found to be a consequence of this variational approach. For applications where surface tension is needed, the additional potential it generates can be added to the system Lagrangian; pressure equality is then lost.

To get a better insight into the meaning of the averaging procedure and model (15), let's consider three materials in two dimensions. The first two consists in two identical dense materials

10

with an almost zero compressibility (e.g. water). They form two distinct diffused circular regions where their volume fraction $\alpha^k, k \in \{1, 2\}$ is maximal at the center and fades out around. They will be referred to as clouds. The last material is the ambient medium. It is assumed less dense and highly compressible so that its dynamics can be reasonably assumed not to affect the two other materials (e.g air). The situation can be visualized on the first picture of figure 1. Let's now assumed that the two clouds are given an initial velocity toward one another so that they eventually cross midway. Because materials are not coupled beyond pressure forces in (15), there is no reason for the two different clouds to interact with each other. It may sound surprising as, depending on the context, some form of interaction would be expected. An essential point of the averaging method is that it inherently hides in the correlation terms part of the underlying physics; information is then lost as soon as these terms are removed. As given in (15), nothing is said about the nature of the averaging, nor are specified the correlation terms. This situation can arise from infinitely many averaging procedures, and lead to radically different behaviors. As an illustration, two of them are here discussed.

First, the averaging procedure may have be done spatially with respect to the $z-$axis, and the two clouds may actually come from particles living in two distinct parallel planes as in figure 1. In this case, their volume fraction actually corresponds to a lineic fraction with respect to the $z-$axis. The two particles only interact through the acoustic waves their movement generates in the medium. The effect of the medium on the denser particles has already been deemed negligible, this approximation being all the more relevant if the two parallel planes are far from each other. Eventually, in the averaged model, the two clouds are expected to cross without seeing each other. Alternatively, the averaging procedure could have been performed with respect to a statistical mean. This choice is relevant if the clouds are formed by a large number of small droplets as in figure 1. A deterministic description of each droplet is out of reach and must be left out in favor of a stochastic approach where probability densities are used to describe the statistical distribution of their number, size, shape and position. In this case, the individual realizations of the stochastic process are not relevant and only its expected (i.e. averaged) value is of interest. The equations describing the average behavior are precisely the ones given by the averaging procedure where the measure is that of the aforementioned distribution. The volume fraction now corresponds to a probability of presence. The two clouds of droplets, which should physically interact with each other, only do so through the correlation terms which can be described macroscopically with an equivalent drag force.

The two previous examples show both the universality and the limited nature of the "averaging+closure" procedure. It covers a wide array of conceptually different approaches as all measures share the same algebraic properties so that the resulting averaged models are all *formally* equivalent. Still, the devil is in the details: differences are embedded in the correlation terms but remain crucial, especially in the vicinity of shocks.

### Multi-temperature hydrodynamics

For the applications in which the CEA is interested, extreme conditions, not unlike that occurring at the core of a star, can produce plasma. In completely ionized plasmas, ions and electrons can separately be assumed to be at local thermodynamic equilibrium. Although collisions between
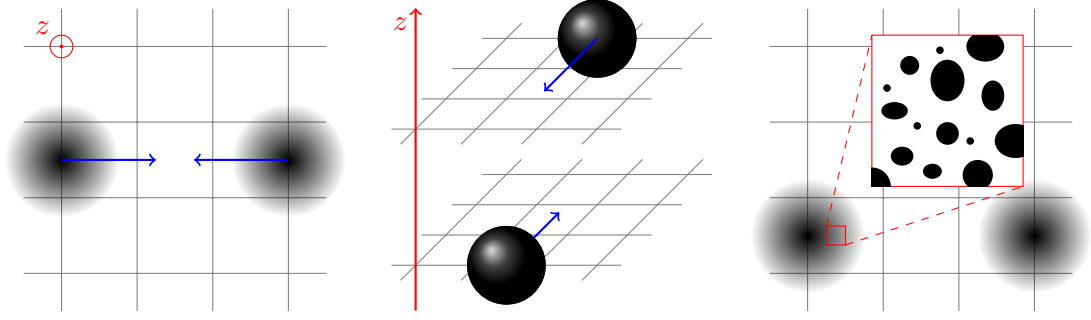
Figure 1: Illustration of the averaging procedure on a 3-material system. The middle and right images are real system whose averaging both yields the averaged system depicted on the left. Middle: two particles leaving in parallel planes undergo a spatial averaging along the $z-$axis; Right: two clouds of small droplets are smothered into a diffused region after taking the expected value of the position, size and form of the droplets.

the two drive them toward a common temperature, the characteristic times associated to that process can be smaller than the observation scale. In this case, each species of each material $k$ must be described with its own potential $e_e^k$ and $e_i^k$. Besides, if the medium is subject to strong radiation effects, a volumetric radiation energy $e_r^k$ is needed for a full description of the system. The previously derived universal model can then be supplemented with a three-temperature description of each material

$$\alpha^k \rho^k \frac{\mathrm{d}^k}{\mathrm{d}t}\left(\frac{1}{\alpha^k \rho^k}\right) - \nabla \cdot \mathbf{u}^k = 0, \tag{16a}$$

$$\alpha^k \rho^k \frac{\mathrm{d}^k}{\mathrm{d}t}\mathbf{u}^k + \alpha^k \nabla p = 0, \tag{16b}$$

$$\alpha^k \rho^k \left[\frac{\mathrm{d}^k}{\mathrm{d}t}e_i^k + p_i^k \frac{\mathrm{d}^k}{\mathrm{d}t}\left(\frac{1}{\rho^k}\right)\right] = 0, \tag{16c}$$

$$\alpha^k \rho^k \left[\frac{\mathrm{d}^k}{\mathrm{d}t}e_e^k + p_e^k \frac{\mathrm{d}^k}{\mathrm{d}t}\left(\frac{1}{\rho^k}\right)\right] = 0, \tag{16d}$$

$$\alpha^k \rho^k \left[\frac{\mathrm{d}^k}{\mathrm{d}t}\left(\frac{e_r^k}{\rho^k}\right) + p_r^k \frac{\mathrm{d}^k}{\mathrm{d}t}\left(\frac{1}{\rho^k}\right)\right] = 0, \tag{16e}$$

$$p_i^k + p_e^k + p_r^k = p. \tag{16f}$$

Once again, such model neglects all dissipation and can be obtained from the least action principle.

**Additional physics and model reduction**

Although equations (16) consist in a universal starting point for multi-temperature multi-material hydrodynamics, it must be supplemented with additional terms to describe real-world applications. As explained earlier, the possible combinations are infinite and system-dependant. For the applications of interest to the CEA, some terms cannot be neglected and are now discussed.

- Couples of materials with different velocities usually experience some form of drag. Be-

cause of total momentum conservation, the two forces must be opposite to one another; a possibility is given by the following expression

$$\alpha^1 \rho^1 \frac{\mathrm{d}^1}{\mathrm{d}t} \mathbf{u}^1 = \rho\nu(\mathbf{u}^2 - \mathbf{u}^1),$$ (17a)

$$\alpha^2 \rho^2 \frac{\mathrm{d}^2}{\mathrm{d}t} \mathbf{u}^2 = \rho\nu(\mathbf{u}^1 - \mathbf{u}^2),$$ (17b)

where $\rho$ is the mixture density and $\nu$ is homogeneous to a frequency. The greater it is, the more coupled the velocities are. In particular, the limit $\nu \to +\infty$ enforces velocity equality.

- For the applications of interest, ions, electrons and photons can have different temperatures but they remain tightly coupled. Temperature relaxation must be taken into account and reads [22, 26]

$$\alpha^k \rho^k \frac{\mathrm{d}^k}{\mathrm{d}t} e_i^k = c\kappa^k (T_e^k - T_i^k),$$ (18a)

$$\alpha^k \rho^k \frac{\mathrm{d}^k}{\mathrm{d}t} e_e^k = c\kappa^k (T_i^k - T_e^k) + c\sigma_P^k \left( a\left(T_r^k\right)^4 - a\left(T_e^k\right)^4 \right),$$ (18b)

$$\alpha^k \rho^k \frac{\mathrm{d}^k}{\mathrm{d}t} \left( \frac{e_r^k}{\rho^k} \right) = c\sigma_P^k \left( a\left(T_e^k\right)^4 - a\left(T_r^k\right)^4 \right).$$ (18c)

The relaxation coefficient $\kappa^k$ depends on both the ionic and electronic temperatures; the Planck opacity $\sigma_P^k$ depends on the electronic and radiation temperatures. Ionic and electronic temperature relaxation can also be considered between different materials but it usually occurs on larger time scales [55] and are here neglected.

- Radiation transport is an important feature of flows in the presence of strong radiation fields. It describes the propagation of photons and the energy they carry. For a single material, under the Rosseland diffusion approximation [22], it reads

$$\alpha^k \rho^k \frac{\mathrm{d}^k}{\mathrm{d}t} \left( \frac{e_r^k}{\rho^k} \right) = \nabla \cdot \left( \frac{c}{3\sigma_R^k} \nabla e_r^k \right)$$ (19)

The diffusion coefficient is proportional to the speed of light $c$ and inversely proportional to the Rosseland opacity $\sigma_R^k$ which is given as a function of the electronic temperature $T_e^k$. Equation (19) only takes into account diffusion inside each material separately; the expression of inter-material exchanges induced by the radiation transport will be discussed in chapter 2. Strictly speaking, there also exist ionic and electronic heat exchanges. For the applications of interest, they are not as stiff as their radiation counterpart and will not be considered in the present work.

The different couplings are represented in figure 2. In the limit of infinite stiffness, relaxation terms simplify models by rendering some equations redundant. Infinite drag between every couple of materials results in a single-velocity model. Infinite collision frequencies yield two-temperature or one-temperature models. With both, it reduces to a single-velocity one-temperature multi-material model. These models are studied respectively in chapters 2, 3 and

1. In general, complex systems can display different drag regimes depending on the couples of materials and likewise for collisions. It produces a whole hierarchy of mixed models where a single velocity is shared in between clusters of materials and where each materials is described with its own number of temperatures.

Additionaly, and perhaps more subtly, stability issues must be addressed. Contrary to the Euler equations, model (16) is not hyperbolic but rather displays a mixed hyperbolic-elliptic behavior. Ellipticity predicts instability at all wavelengths and prevents initial-value problems from being well-posed. Consequently, equations (16) must be supplemented with physical terms stabilizing short-wavelength phenomena. Such terms include surface tension or viscosity [89] among others. They must nonetheless leave unchanged the flow behavior at large wavelengths; if not, the resulting damping of hydrodynamic instabilities (e.g. Kevin-Helmotz instabilities) would jeopardize the physical relevance of the solution [108, app. A and refs therein]. The issue of ellipticity only concerns the multi-velocity aspects of model (16) and single-velocity equations are hyperbolic, independently of the number of materials or temperatures.

## Thermodynamics of multi-temperature and multi-material hydrodynamics

For multi-temperature and multi-material applications, each component (i.e. ions, electrons and photons) of each material possesses its own equation of state and hence its own energy, entropy, pressure and temperature. The previous discussion on thermodynamics remains valid but the multiplicity of energy potentials adds new complexities. In particular, individual Gibbs relationship can be written for each individual potentials

$$\mathrm{d}e_i^k = -p_i^k \mathrm{d}\left(\frac{1}{\rho^k}\right) + T_i^k \mathrm{d}s_i^k, \tag{20a}$$

$$\mathrm{d}e_e^k = -p_e^k \mathrm{d}\left(\frac{1}{\rho^k}\right) + T_e^k \mathrm{d}s_e^k, \tag{20b}$$

$$\mathrm{d}\left(\frac{e_i^k}{\rho^k}\right) = -p_r^k \mathrm{d}\left(\frac{1}{\rho^k}\right) + T_i^k \mathrm{d}s_e^k. \tag{20c}$$

Once again, the work of pressure forces produces a reversible exchange between the kinetic energy of all materials and the internal energy of each component of each material. The exchange between kinetic and internal energies is distributed between the different materials so as to comply with the prescribed volume evolution. Model (16) only accounts for the work of pressure forces so that it only describes reversible isentropic processes.

If dissipative forces are added, they also generate an exchange (albeit irreversible) between kinetic and internal energies. The total heat deposit (i.e. the loss of total kinetic energy) and its distribution between materials answers to the second principle of thermodynamics, namely the total entropy of the system cannot decrease. Beyond this requirement, no other constraint exists on the total heat deposit distribution; it may be shared arbitrarily between materials. This distribution is essentially system-dependent and encapsulates part of the missing information contained in the correlation terms of the averaged model. As an illustration of this concept, consider two materials whose velocities are coupled through a drag force (a similar computation can also be performed with viscosity). Pressure forces are omitted for simplicity and only one

temperature per material is considered. The loss of total kinetic energy induced by equations (17) is then

$$\alpha^1 \rho^1 \frac{d^1}{dt} \|\mathbf{u}^1\|^2 + \alpha^2 \rho^2 \frac{d^2}{dt} \|\mathbf{u}^2\|^2 = -\rho\nu\|\mathbf{u}^2 - \mathbf{u}^1\|^2 \leq 0. \tag{21}$$

The total heat deposit $\rho\nu\|\mathbf{u}^2 - \mathbf{u}^1\|^2 \geq 0$ indeed corresponds to dissipation. For total energy conservation, it is distributed between materials internal energies

$$\alpha^1 \rho^1 T^1 \frac{d^1}{dt} s^1 = \lambda^1 \rho\nu\|\mathbf{u}^2 - \mathbf{u}^1\|^2, \tag{22a}$$

$$\alpha^2 \rho^2 T^2 \frac{d^2}{dt} s^2 = \lambda^2 \rho\nu\|\mathbf{u}^2 - \mathbf{u}^1\|^2. \tag{22b}$$

where $\lambda^1$ and $\lambda^2$ sum up to one. In particular, if $\lambda^1 = 1 - \lambda^2 = 0$, material 2 bears all the dissipation while material 1 undergoes an isentropic evolution. More generally, the coefficients must be chosen so as to satisfy the following inequality

$$\alpha^1 \rho^1 \frac{d^1}{dt} s^1 + \alpha^2 \rho^2 \frac{d^2}{dt} s^2 = \left(\frac{\lambda^1}{T^1} + \frac{\lambda^2}{T^2}\right) \rho\nu\|\mathbf{u}^2 - \mathbf{u}^1\|^2 \geq 0. \tag{23}$$

It is worth noticing that $\lambda^1 \geq 0$ and $\lambda^2 \geq 0$ is a sufficient but not necessary condition. Only the total entropy of the system must increase and one material's entropy is allowed to decrease as long as it is compensated by the other material. This is typically what happens with exchanges between different internal energies. For instance, collisions between ions and electrons induce an energy transfer of the form

$$\alpha^k \rho^k \frac{d^k}{dt} e_i^k = c\kappa^k (T_e^k - T_i^k), \tag{24a}$$

$$\alpha^k \rho^k \frac{d^k}{dt} e_e^k = c\kappa^k (T_i^k - T_e^k). \tag{24b}$$

The colder species entropy increases while the hotter one decreases, but the evolution of the sum is always positive

$$\alpha^k \rho^k \frac{d^k}{dt} s_i^k + \alpha^k \rho^k \frac{d^k}{dt} s_e^k = c\kappa^k \frac{(T_e^k - T_i^k)^2}{T_e^k T_i^k} \geq 0. \tag{25}$$

Likewise, radiation transport can result in a local entropy diminution as hot regions radiate heat around them. However, once integrated over the whole domain $\Omega$ (assumed isolated), the entropy always increases.

$$\int_\Omega \alpha^k \rho^k \frac{d^k}{dt} s_r^k d\mathbf{x} = \int_\Omega \frac{4cT_r}{3\sigma_R} \|\nabla T_r^k\|^2 d\mathbf{x} \geq 0. \tag{26}$$

Just as in the single-material case, the mixture speed of sound can be derived from the eigenvalues of the matrix $A(U)$ (3) associated with the model of interest. For the multi-velocity equations, finding an analytical expression is possible when velocities are all equal and it yields

$$c_0^2 = \sum_k \beta^k (c^k)^2, \tag{27}$$

15
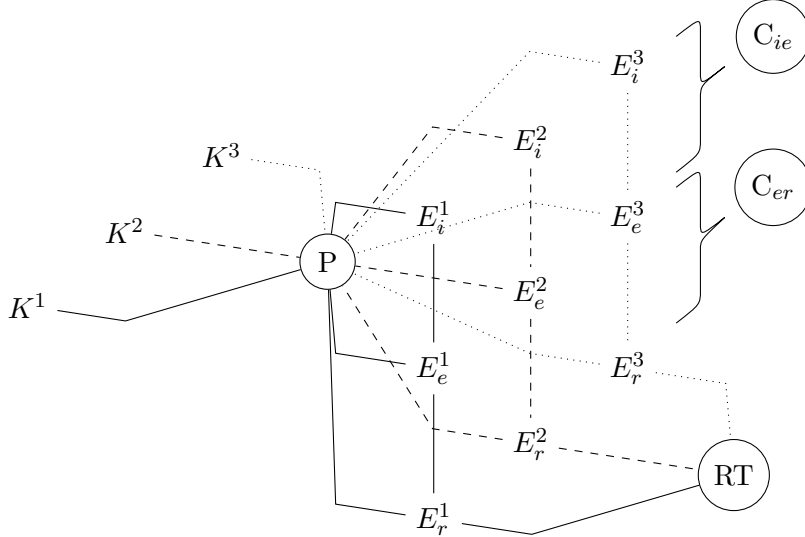
Figure 2: Schematic representation of the considered energy exchanges in a three-material system. $K^k$, $E_i^k$, $E_e^k$ and $E_r^k$ are respectively the kinetic, ionic, electronic and radiation energy of material $k$ integrated over the whole domain. P, C$_{ie}$, C$_{er}$ and RT are used to denote exchanges induced respectively by pressure, collisions between ions and electrons, collisions between electrons and photons and radiation transport. The different energies need not be homogeneously distributed over the whole domain; although not represented, spatial exchanges (i.e. fluxes) also exist.

where

$$\beta^k = \frac{\alpha^k/(\rho^k(c^k)^2)}{\sum_l \alpha^l/(\rho^l(c^l)^2)}. \tag{28}$$

Alternatively, with a single-velocity model (i.e. with an infinite drag force), it reads

$$c_\infty^2 = \sum_k \frac{\rho^k}{\rho}\beta^k(c^k)^2. \tag{29}$$

Equation (27) consists in a convex combinations of material speed of sounds while (29) does not. The latter can result in mixture speed of sound considerably lower than the one of its components (e.g. for mixtures of air and water). Generally speaking, the so-called subcharacteristic condition relates dissipation to slower speeds of sound [76]. The mixture fundamental derivative can also be obtained in a similar fashion [49] but it is here omitted for the sake of brevity.

## Multi-material shocks and non-conservative products

For single-fluid one-temperature equations, the second principle of thermodynamics excludes all non-physical behaviors and only one possible solution remains. It essentially means that all dissipative processes generate the same overall behavior and the differences are confined to narrow regions of the flow (namely in the profiles of shock). For multi-temperature or multi-material applications (and *a fortiori* for both), shocks are small-scale dependent and their global structure cannot be known without the details of what is happening along their width. As an illustration, the propagation of sound waves inside a thick smog is not as fast as in a light drizzle.

16

Both systems are essentially equivalent in terms of the water volume fraction, but not in the size and distribution of water droplets. The correlation terms differ greatly; the drag force is more pronounced inside the fog which results in a lower mixture speed of sound.

General jump relationships on material mass, total momentum and total energy can still be written and read as in the single-material case. For a three-temperature $N$-material multi-velocity system, the $5N$ evolution equations only produces a system of $N + 2$ partial jump conditions. The remaining $4N - 2$ equations then depend on small-scale phenomena and fall into two categories.

- $N - 1$ are related to the $N$ small-scale forces $F^k$ acting on each material. They can include various terms such as surface tension, viscosity or drag. Because of total momentum conservation, their sum must correspond to a flux whose contribution to the jump relationships is zero. Thus the $N - 1$ degrees of freedom.

- The remaining $3N - 1$ are related to the different thermodynamic potentials. Dissipation generates a total heat deposit $Q$ which needs to be shared between the different materials and their respective temperatures. As in (22), the following equation can be written without any loss of generality

$$\alpha^k \rho^k T_\theta^k \frac{\mathrm{d}}{\mathrm{d}t} s_\theta^k = \lambda_\theta^k Q, \tag{30}$$

where $\theta \in \{i, e, r\}$ and coefficients $\lambda_\theta^k$ are such that

$$\sum_k \sum_{\theta \in \{i,e,r\}} \lambda_\theta^k = 1. \tag{31}$$

Again, only having positive $\lambda_\theta^k$ is enough to ensure consistency with the second principle of thermodynamics but heat exchanges can widen the range of admissible coefficients.

Mathematically, the non-uniqueness of entropic solutions comes from the failure to write (16) as a system of conservation laws (2). No canonical weak formulation can be written. In [77], this limitation is overcome for hyperbolic systems of the form (3), thanks to the use of the so-called path theory. Paths $\phi(U_L, U_R, \xi)$ are functions used to define generalized jump relationships

$$\sigma(U_R - U_L) = \int_0^1 A(\phi(\xi, U_L, U_R)) \frac{\partial}{\partial \xi} \phi(\xi, U_L, U_R) \mathrm{d}\xi. \tag{32}$$

This definition is an extension of the jump relationships for conservation laws as (32) reduces to (11) when $A(U)$ is the jacobian of a flux function $F(U)$. Although this formalism offers a rigorous and convenient way to define shocks as a strict discontinuity, the path still needs to be specified. Identifying the one corresponding to a given regularization is not trivial and some choices may even result in unphysical solutions. The link between paths and their underlying physics is explored for a simple two-temperature system in chapter 4.

## On the Baer-Nunziato model

A widespread one-temperature model for two-phase flows is given by the so-called Baer-Nunziato (BN) equations [5]. Originally developed for the description of deflagration to detonation transition (DDT) in granular reactive flows, it was latter applied to general multi-material systems in [95] after which it gained considerable popularity. Over time, several modifications were performed on the original equations [55]; here is written the version found in [95] for which phase change and heat transfer are neglected.

$$\alpha^k \rho^k \frac{\mathrm{d}^k}{\mathrm{d}t}\left(\frac{1}{\alpha^k \rho^k}\right) - \nabla \cdot \mathbf{u}^k = 0, \tag{33a}$$

$$\alpha^k \rho^k \frac{\mathrm{d}^k}{\mathrm{d}t}\mathbf{u}^k + \alpha^k \nabla p^k = (p_I - p^k)\nabla \alpha^k, \tag{33b}$$

$$\alpha^k \rho^k \left[\frac{\mathrm{d}^k}{\mathrm{d}t}e^k + p^k \frac{\mathrm{d}^k}{\mathrm{d}t}\left(\frac{1}{\rho^k}\right)\right] = (p_I - p^k)(\mathbf{u}_I - \mathbf{u}^k)\cdot \nabla \alpha^k + \lambda(\mathbf{u}_I - \mathbf{u}^k)\cdot(\mathbf{u}^l - \mathbf{u}^k)$$
$$+ \mu(p_I - p^k)(p^l - p^k), \tag{33c}$$

$$\frac{\partial}{\partial t}\alpha^k + \mathbf{u}_I \cdot \nabla \alpha^k = \mu(p^k - p^l), \tag{33d}$$

with $l = 2$ if $k = 1$ and $l = 1$ if $k = 2$. Compared to equations (15), the BN model includes perturbations stemming from the use of interface pressure $p_I$ and velocity $\mathbf{u}_I$ which both require a dedicated closure. Throught coefficient $\lambda \geq 0$, it also accounts for a drag force which is essentially equivalent to (17). Finally, pressure equilibrium (15d) is replaced with an evolution equation on the volume fraction (33d). This equation corresponds to the transport of the interface supplemented with a compaction term. Compaction takes the form of a relaxation process, controlled by coefficient $\mu \geq 0$ and which drives volume evolution toward pressure equilibrium. Two asymptotic behavior can be identified and are discussed in details in chapter 1 for a single-velocity model.

- If $\mu \to +\infty$, then equality of pressures is formally recovered. Volume evolution is completely driven by thermodynamics. It is physically relevant [55] but couples all materials through pressure forces in a convoluted and possibly stiff way [49].

- Alternatively, if $\mu = 0$, the volume evolution becomes purely geometrical and disconnected from thermodynamics. Although questionable for highly contrasted mixtures [49] (e.g. air and water), it alleviates stiffness and substantially eases the numerical treatment.

The evolution of the mixture entropy is given by

$$\alpha^1 \rho^1 \frac{\mathrm{d}^1}{\mathrm{d}t}s^1 + \alpha^2 \rho^2 \frac{\mathrm{d}^2}{\mathrm{d}t}s^2 = \nabla \alpha^1 \cdot \left[\frac{p_I - p^k}{T^1}(\mathbf{u}_I - \mathbf{u}^1) - \frac{p_I - p^2}{T^2}(\mathbf{u}_I - \mathbf{u}^2)\right]$$
$$+ \frac{\lambda}{T^1 T^2}(\mathbf{u}^1 - \mathbf{u}^2)\cdot(T^2\mathbf{u}^1 - (T^2 - T^1)\mathbf{u}_I - T^1\mathbf{u}^2)$$
$$+ \frac{\mu}{T^1 T^2}(p^1 - p^2)(T^2 p^1 - (T^2 - T^1)p_I - T^1 p^2). \tag{34}$$

In general, for arbitrary interface pressure and velocity, the model needs not comply with the second principle of thermodynamics. The closure $p_I = p^1$ and $\mathbf{u}_I = \mathbf{u}^2$ is then often considered

as it yields

$$\alpha^1 \rho^1 \frac{\mathrm{d}^1}{\mathrm{d}t} s^1 + \alpha^2 \rho^2 \frac{\mathrm{d}^2}{\mathrm{d}t} s^2 = \frac{\lambda}{T^1} \|\mathbf{u}^1 - \mathbf{u}^2\|^2 + \frac{\mu}{T^2}(p^1 - p^2)^2 \geq 0. \tag{35}$$

It removes the contribution of interface terms while ensuring that relaxation processes imply an increase of total entropy. Material 1 bears all the dissipation induced by drag while compaction only applies dissipation on material 2.

In the literature, the BN model is sometimes introduced as a necessary starting point for modeling all multi-material flows. From this town-down perspective, 6-equation and 5-equation models can be derived by reduction (i.e in the limit of infinite drag or compaction) and consists in simplified versions of the ground truth that is assumed to be the BN model. Its hyperbolicity seems to be one of the main reasons for its appeal in the community [95]. However, concerns have been raised over its use outside the scope of its original purpose (namely modeling granular flows) [67]. Non-destruction of entropy is only assured under arbitrary closures on the interface variables. Such closures are relevant for some applications but are not compatible with the otherwise necessary degrees of freedom on shocks for general mixtures. Beyond its constrained distribution, dissipation is ubiquitous which makes it impossible to capture isentropic behavior for general values of $\lambda$ and $\mu$, even in expansion. As mentioned in [55], a more reasonable stance is then to consider the BN model as a perturbation of equations (15) in a bottom-up fashion, where drag, compaction and interface terms are specific closures of the correlation terms.

# 2    Numerical approximation of multi-material flows

Numerical approaches to the approximation of multi-material flows are numerous. They include finite difference, finite element or finite volume dicretizations; staggered or cell-centered settings; and a variety of both widespread and niche ideas. Providing a classification and comparison of the existing methods is not the intent of this introduction. Instead, a selection of topics are discussed. They introduce and justify the motivations behind the different schemes developed throughout the manuscript. Their reach however goes beyond the present work as, although varied, all possible strategies are tied to the same criterion of consistency with physics.

## 2.1    "Lagrange + Remap" approach

A widespread approach for computational flow dynamics is the so-called "Lagrange + Remap" strategy [6, 50]. It essentially consists in splitting the treatment of pressure fluxes and transport.

- For the Lagrangian step, physical quantities are first computed on a moving mesh following the mixture. Cells undergoes deformations depending on the local discrete velocity field. The integration of pressure forces and dissipation must be consistent with thermodynamics. Gibbs equation (7) is then reproduced at the discrete level

$$\frac{\mathrm{d}}{\mathrm{d}t} e_c^k = -p_c^k \frac{\mathrm{d}}{\mathrm{d}t} \left( \frac{1}{\rho_c^k} \right) + T_c^k \frac{\mathrm{d}}{\mathrm{d}t} s_c^k \tag{36}$$

  where $\phi_c^k$ is the numerical approximation of $\phi^k$ in cell $c$. Equation (36) binds the energy evolution to that of the volume and the entropy. Volume is modified with respect to the
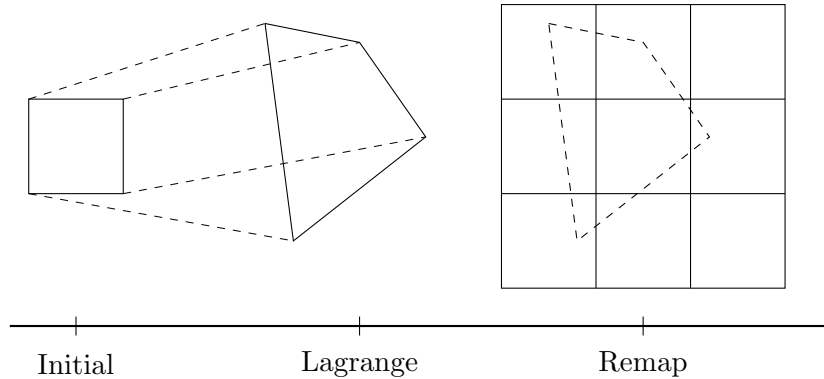
Figure 3: Schematic representation of the "Lagrange + Remap" approach. Here the remapping is performed on the initial mesh.

prescribed closure (e.g. pressure equality or the equal-strain assumption) while the entropy evolution depends on the chosen dissipation.

- For the remapping step, quantities are projected back to a reference mesh. This strategy is amenable to arbitrary mesh changes. Keeping the Lagrangian mesh amounts to bypassing the remapping step and following the fluid motion throughout the whole simulation; the method is referred to as being purely Lagrangian. Lagrangian computations usually benefits from better accuracy but mesh entanglement can occur and abruptly stop the simulation. Alternatively, if the remapping is performed at each time step on a fixed mesh, the method is then called Eulerian. Stability is improved at the cost of a more diffused solution. Generally, any intermediate choice can be considered and leads to the Arbitrary-Euler-Lagrange (ALE) formalism [50, 35]. Adequate choices ideally yield low dissipation in regions where the mesh can adapt to the fluid motion and better stability where it cannot. The issue of designing such meshes is not addressed in the present work. Only pure Lagrangian or pure Eulerian simulations will be performed.

The two steps are represented in figure 3. On a final note, the previous considerations assume there is only one Lagrangian frame; in other words, materials all share the same velocity field. This assumption is no longer valid in a multi-velocity framework where a single mesh cannot simultaneously follow the motion of every material. To circumvent this issue, the strategy can be extended to an "Averaged Lagrange + Remap" where the different quantities are first computed in the center-of-momentum frame or any other relevant averaged frame. Velocity fluctuations appear during the Lagrange step and mimicking Gibbs equation at the discrete level is more tedious. Another approach consists in a "Multi-Lagrange + Remap" splitting where each quantity is computed in its material's Lagrangian frame [21]. This choice requires additional care for volume conservation. It is the latter option which will be considered in chapter 3.

## 2.2   Numerical treatment of shocks and non-conservative products

The numerical treatment of shocks require specific care to provide both stable and accurate results. A first strategy would consist in specifying dissipation in (16) and consistently dis-

cretizing it. Convergence is expected but it would require a large number of numerical cells in the vicinity of shocks to capture their profile. If viscosity and other coefficients related to dissipation are small, shocks spread over narrow regions for which a proper meshing is reasonably out of reach. Shocks are then under-resolved as physical dissipation cannot compete with its numerical counterpart. Although the latter is not involved in the formal consistency of the scheme, shocks are regions where the Taylor approach to consistency breaks down as gradients can be arbitrarily large. A more sensible approach is to directly shape numerical dissipation so as to mimic the physics of the flow. In doing so, capturing the shock profile is discarded and the focus is rather on correctly approximating the upstream state, the downstream state and the shock speed. Generally speaking, the numerical discretization of shocks hinges on two conditions: conservation and dissipation.

- Conservation must be guaranteed at the discrete level. For (16), it concerns material masses, total momentum and total energy. If the numerical scheme fails to do so, solutions may display wrong jump relationships between the upstream and downstream states of the shock.

- As for dissipation, it is essentially equivalent to satisfying the second principle of thermodynamics at the discrete level. If the entropy production is lacking or even negative, instabilities can prevent any solution from being computed. It may also lead to entropy-destroying shocks inside rarefaction waves.

These two requirements are necessary but only sufficient for systems of conservation laws (2). For systems which cannot be cast into such form, several admissible shocks exist and their approximation is more delicate. A subtle control of dissipation is mandatory, not only in order to provide stable numerical shocks, but also to select the one of interest. Two approaches are explored in this work.

First, if shocks are specified through explicit dissipative processes, these terms can serve as a guideline for modeling numerical dissipation. This is essentially the idea behind artificial viscosity used in the seminal paper [110] but every stable scheme also contains an equivalent term, even if only implicitly. For multi-temperature multi-material applications, the main idea is to isolate the discrete total heat deposit associated with the scheme. Once identified, a discrete version of (30) can be inserted inside (36). Just as in the continuous case, different choices of coefficients $\lambda_\theta^k$ will produce different shocks. This approach stays close to the physics of the system but it is sensitive to spurious dissipation sources which can effect convergence inside shocks. The main contribution comes from the transport (or remapping), usually consisting in convex combinations and thus producing some form of discrete heat exchange [75]. Such perturbations may be reasonably small and convergence errors can be acceptable for applications.

A second approach is to specify shocks with the path theory [77] and associated jump relationships (32). Traditional Godunov-type schemes have been extended to non-conservative hyperbolic systems through path-consistent approximate Riemann solvers [1, 33, 12]. Convergence issues were shown to remain inside shocks [1] as the scheme total dissipation only partially comes from the solver. Again, spurious dissipation is added when averaging the approximate solution over the cell. In chapter 4, the method from [15] is applied to two-temperature Lagrangian

hydrodynamics. This one-dimensional numerical strategy manages to remove the excess dissipation through in-cell discontinuous reconstruction. Convergence is shown to hold for isolated shocks and is also observed for more general Riemann problems.

## 2.3   On robustness and accuracy

The different possible flow regimes induce contradictory requirements. When smooth, the flow is reversible which advocates for a strict zero entropy production. Such a feat is usually not possible and it leads to a precarious balancing act between keeping dissipation at a bare minimum while still ensuring consistency with thermodynamics. On the other hand, shocks uncompromisingly need dissipation. This almost schizophrenic behavior is addressed in two distinct manners in the literature.

- Shocks are the focal point of the Godunov scheme [42]. Dissipation is integrated into the scheme through exact Riemann solvers at the interface between cells. Approximate solvers [92, 46, 103] were shown to produce similar results while substantially decreasing computation times. The resulting schemes display robust behavior in shocks but invasive dissipation prevents isentropic flows from being properly captured. In the literature, the main solution to improve accuracy leans on higher order extensions. Upon realizing that conservative monotone linear schemes are first-order accurate at most [45], flux limiters [8, 100] and slope limiters [105] were developed. Non-linearity allows these techniques to provide second-order accuracy in smooth regions while degenerating into a robust first-order scheme in the vicinity of shocks.

- Instead of starting from intrinsically robust schemes and trying to skim off the excess dissipation, a dual approach is to first derive almost dissipation-free schemes and then add artificial dissipation to stabilize shocks. In order to stay as close as possible to a zero entropy production, strategies include conservation of kinetic energy or enstrophy [116], as well as preserving geometric (e.g. symplectic or variational) structures [10, 86, 108]. Staggered schemes are more often employed but cell-centering is also possible [91]. Designing relevant artificial dissipation and deciding where to apply it is an entire question on its own. Its specification must be driven by physics which makes it naturally suited for multi-temperature or multi-material shocks.

In the present work, the starting point of the numerical strategy is the EUCCLHYD/GLACE scheme [71, 11]. It is based on nodal Riemann solvers and thus belongs to the first category. The extension to multi-temperature multi-material flows however borrows some ideas from the second category as shaping the numerical dissipation is crucial for multi-valued shocks. This is made possible by an explicitly known discrete entropy production associated with the scheme, a feature which is seldom encountered in Godunov-type schemes where dissipation can be convoluted.

Robust shock capturing and accuracy are only two of numerous constraints applied to numerical schemes. The list includes, but is not limited to stiff radiation transport and temperature relaxation (studied in chapter 2), contrasts in equations of state [49], fundamental derivative stiffness [49] and well-balanced issues [43]. Generally speaking, compromises must be made and

are essentially conditioned by applications. In the context of this work, numerical strategies must handle strong shocks and overall stiff conditions. Robustness is then crucial and prevails over accuracy. As such, control of entropy at the discrete level will be a major concern throughout all chapters. Such an adamant stance toward entropy can affect the quality of the solution in isentropic regions of the flow. This issue will be addressed in future studies.

## 3   Outline of the thesis

The present work is made of four distinct chapters. Each chapter is meant to be standalone but their order is still meaningful. The first chapter serves as a first in-depth introduction to the multi-material equations and their numerical treatment. It introduces the core multi-material aspects, focusing on a one-temperature single-velocity model. Two closures on the volumes are discussed and compared: the equal-strain and the equal-pressure assumptions. Equal-strain corresponds to a simple transport of volume fractions, it is purely geometric and not concerned with possible thermodynamic stiffness (e.g. highly contrasted equations as in mixtures of air and water). However, it becomes physically irrelevant in some regimes where the equal-pressure assumption is then preferable. The equal-pressure assumption, as its name suggests, enforces local pressure equilibrium between materials. It is a sensible closure in the applications of interest but induces a possibly stiff thermodynamic coupling between materials. The present numerical strategy follows the "Lagrange + Remap" approach where variables first evolve following the deformation of the mixture before being projected on a arbitrary mesh. The Lagrange step, which is the main focus of the chapter, is a multi-material extension of the GLACE/EUCCLHYD scheme [71, 11]. Whichever closure (namely equal-strain or equal-pressure) is chosen, ensuring thermodynamic consistency at the discrete level is necessary in order to produce stable computations and select physically-meaningful solutions. In particular, ensuring a positive total heat deposit and tuning properly its distribution between materials is a key ingredient of the present work. It is also an essential stepping stone toward approximating more sophisticated models as it is done in the second and third chapters.

The second chapter merges the multi-material aspects developed in the previous chapter with the multi-temperature aspects of [19]. The discretization of the resulting model is challenging because of the multiplied thermodynamic potentials and the stiff phenomena coupling them all together. They include the pressure coupling from the equal-pressure assumption, radiation transport and relaxation terms between ionic, electronic and radiation energies. A thermodynamically-consistent and stable numerical approximation of all these intertwined phenomena is out of the scope of the present work. Pressure equilibrium is here left out in favor of the equal-strain assumption. Although simplified, the model remains complex and several issues still needs to be addressed. First, the discretization of the multi-material radiation transport is not trivial and is here performed with respect to Discrete Equations Method (DEM) introduced in [3]. Second, stiff radiation transport and relaxation terms require an implicit time integration which results in a highly non-linear system of equations. The iterative strategy proposed in [19] is here extended to the multi-material setting; temperatures are ensured to stay non-negative at each iteration through the use of convex combinations.

The third chapter represents a straight continuation of the first chapter where a multi-velocity

model is now considered. The multi-velocity setting brings new issues both at the continuous and discrete level. At the continuous level, consequences of the model ellipticity is discussed. As for the numerical strategy, the "Lagrange + Remap" approach of the single-velocity scheme is extended to a "Multi-Lagrange + Remap" method where each material first evolves in its own Lagrangian frame before being projected on a common mesh. A large emphasis is, again, put on thermodynamic consistency. The main ideas remain the same for the Lagrange step although total energy conservation must be given due consideration. The remapping is subject to unexpected constraints which couples all materials. The resulting semi-discrete scheme is shown to strictly comply with the second principle of thermodynamics.

The fourth and last chapter is motivated by the numerical approximation of shocks for hyperbolic equations which are not systems of conservation laws. This issue is already present in the previous chapters and addressed by the control of the total heat deposit between materials. Because of spurious (but arguably limited) additional entropy sources, the issue was only partially answered; the complexity of the models, two-dimensional nature of the schemes and tight robustness requirements on the discretization, make exactly converging to the prescribed solution a difficult task. This chapter then takes a more academic stance and consider the simplified model of single-material two-temperature Lagrangian hydrodynamics in one dimension. The path formalism introduced in [77] is chosen to describe shocks. The link between a given path and its underlying dissipation; several conditions are shown to physically constrain the path. The numerical strategy follows the ideas developed in [15] where in-cell discontinuous reconstructions are used to eliminate spurious numerical dissipation. Test cases consisting of Riemann problem for different paths and equations of state are then considered. Numerical solutions are shown to converge to the analytical solution inside shocks when a path-consistent Godunov's scheme fails to do so.

# Chapter 1

# Numerical strategy for a multi-material model with pressure equilibration[1]

## Contents

A cell-centered Lagrangian scheme is presented for a multi-material hydrodynamics model with equilibrated material pressures. The scheme is conservative in mass, momentum, and total energy while being entropic per material. This last point is critical for various engineering applications but is seldom addressed. The entropy production in each material is taken as an arbitrary part of the global entropy production hence mimicking different viscosity operators and the underlying vanishing viscosity solution. The scheme is applied to various 1 or 2-dimensional test cases where materials have highly contrasted equations of state. These challenging test cases confirm the robustness of the scheme and show that pressures are kept equal up to the scheme order or even strictly if an additional equilibration procedure is added.

# 1   Introduction

## 1.1   Motivations and existing approaches

In the context of multi-material flows, interface widths between materials are significantly smaller than observation scales for many applications and may then be considered as sharp discontinuities. Dealing accurately with these interfaces is critical and has driven most of the efforts of the community starting from the fifties. A large spectrum of models and numerical strategies has since been developed. Among all available methods, two categories have emerged in order to handle interfaces between materials [73]. The first one does not allow any mixing between materials. Materials are assigned a specific domain and the interface is defined as the border between these disjoint zones. Such methods are referred to as sharp interface methods. The second one deals with interfaces as diffuse areas in which materials may artificially mix with each other. They are referred to as diffuse interface methods.

The latter category gained popularity over the past few decades for several reasons. First, the interface is allowed to spread over a certain width, thus bypassing potential geometric difficulties which are the main drawback of sharp interface methods. Diffuse interface methods also allow the easy integration of additional physical phenomena such as capillarity, surface tension, drag forces and added mass, among others [48]. Finally, although the inherent numerical smearing of the interfaces results in a certain loss of accuracy, it still may be mitigated by anti-diffusive methods [84] and by the computational power breakthrough of the last decades. Of course, diffuse interface methods require appropriate models and numerical methods. A detailed review may be found in [96, 73].

Concerning models, several possibilities exist when dealing with multi-material flows in the framework of diffuse interface method. The sheer variety of existing models partially comes from the different possible levels of sophistication, which is traditionally indicated by the number of equations in the case of two material flows. Four-equation models consider mixture equations (i.e. equations on the average density, momentum and energy of the mixture) supplemented with a transport equation in order to take into account interface advection [2]. This transport equation may concern volume fraction, or a set of thermodynamic coefficients which completely

---

[1]This chapter was published [74] in Computers & Fluids with Rémi Chauvin, Sébastien Guisset and Antoine Llor.

characterizes the mixture equation of state. However, material thermodynamic states (i.e. material densities and internal energies) are not accessible and the accuracy of the model heavily depends on the ability to properly model the mixture state through the average pressure. On the other hand, 7-equation models [5, 21] allow for a more accurate description of the mixture, even with real equations of state, as all material variables are available (including density, momentum, energy and volume fraction). However, these models display complex wave structures and their discretization is challenging.

Five-equation models constitute a compromise between the two, providing a physically sound description of the mixture without trading off too much simplicity. Only the mixture velocity is known but individual thermodynamic states are defined, even if sometimes only implicitly. However, inside the class of 5-equation models, there is no general agreement on the equations and multiple models has been proposed [4, 81, 35]. They all converge on conservation equations (i.e. mixture momentum and energy as well as material mass equations) but may differ when it comes to material internal energies, densities, volume fractions, pressures or entropies (all of them being set as soon as two of them are known). The model under consideration in this article is a 5-equation model, obtained through a conditional averaging procedure introduced in [52] and summarized in [113, 69, 49]. The averaging procedure introduces several fluctuation terms which are then neglected. As a result, the model is naturally isentropic for each material. However, it is only a general foundation and some terms still need to be specified with physical assumptions. It encompasses most, but not all, models of the literature.

## 1.2   Generic approach on closures and on entropy

In the present article, we focus on two closures for the isentropic model: the equal strain and equal pressure assumptions. The former consists in assuming volume fractions stay constant during the Lagrangian phase; in other words, all materials are compressed or expanded with the same rate. The latter enforces equality of pressures between materials. These two closures may be interpreted as two extreme cases of the Baer-Nunziato model [5] where the volume fraction evolution depends on a dynamic compaction viscosity. As this coefficient goes to zero, the volume fraction evolution is no longer driven by thermodynamics and one recovers the equal strain assumption. As it goes to infinity, pressures are instantaneously relaxed to the same value and one recovers the equal pressure assumption.

The equal strain assumption is numerically quite simple and is relevant enough for some applications; thus, it is widely used in simulations of multi-material flows [9]. However, it leads to a strong pressure decoupling inside mixtures where materials have significantly different equations of state (e.g. mixtures of air and water). Apart from being quite unrealistic, the resulting pressure decoupling may not be compatible with chemical reactions, phase changes or other physical phenomena which depend on thresholds. It also leads to losses of robustness in highly contrasted systems with "real" equations of state (EOS) [49].

For these reasons, another closure is necessary for some applications and the equal pressure assumption is a sound one [55, 37]. Volume fractions and densities evolution is completely defined by this constraint, even if implicitly. Enforcing pressure equilibration may be done at the discrete level by solving a non-linear system of equation [27] through an iterative method.

This article follows the ideas developed in [108] by computing the evolution equation for the density and then discretizing it. As a result, the scheme is fully explicit and does not rely on any iterative solver. Moreover, it allows to properly factor in entropy contributions, which is essential to our scheme and which sets it apart from other approaches relying on the same closure [81, 27].

More generally, and for any closure, a specific attention has to be put on entropy. No dissipation process or heat exchange are taken into account so entropy variation has to be non-negative for each material as to comply with the second principle of thermodynamics. Not only entropy variation must be non-negative for each material, but ratios between materials may be freely customized. It is a key feature of multi-material flows and relates to the presence of non-conservative terms in the model. Contrary to hyperbolic conservation laws, non-conservative systems of equation do not admit a canonical solution. Solutions may then be defined with an added vanishing regularization operator or with a choice of path [77] which defines generalized Rankine-Hugoniot jump conditions. The latter choice inspired the methodology described in [15] for a path-dependent scheme based on in-cell reconstruction techniques and exact resolution of Riemann problems. Our approach, following the work made in [49], is related to vanishing regularization operators which are mimicked at the discrete level by a choice of entropy production distribution. It answers the issue of thermodynamic consistency and the multiplicity of solutions arising from the presence of non-conservative terms. It needs to be emphasized that the present methodology should be applicable to a large variety of schemes, even if it is presently illustrated on a specific scheme.

## 1.3 Present numerical scheme and tests

The scheme developed in this article is based on a "Lagrange + Remap" approach [6, 50].This procedure consists in first solving the Lagrangian equation on a mesh which moves with the flow. This formalism is naturally suitable for interface problems and prevents excessive smearing of the interface as no mass flux occurs between numerical cells. However, robustness issues may arise when facing large flow deformations which often results in mesh entanglement and code failure. The Remap phase is then introduced in order to tackle this latter problem. The solution is projected on a mesh whose regularity ensures a robust behavior of the scheme while not sacrificing most qualities of pure Lagrangian methods. The Lagrange+Remap formalism also facilitates the control of the entropy as it allows to separate thermodynamics from advection phenomena.

The Lagrangian part, which constitutes the main contribution of this article, is an extension of the Eucclhyd scheme [11, 70], written in internal energy [20, 19], for multi-material flows. It needs to be highlighted that the internal energy formulation is uncommon for cell-centered schemes but is essential here. It allows for an accurate control of each material entropy production. Practically, the semi-continuous scheme is constructed so that entropy variation is positive for each material, thus ensuring thermodynamic consistency of our approach. While being critical for various engineer applications this point is seldom addressed. The resulting Lagrangian part of the scheme is exactly conservative in mass, momentum and total energy (i.e. the sum of kinetic energy and all material internal energies).

Concerning the Remap phase, the initial Eulerian mesh is used for the projection and the remapping procedure is a standard Alternate Direction one [112, 32]. This mesh choice is not optimal and more sophisticated alternatives exist [35]. When the mesh on which the solution is projected is far from the Lagrangian one, a pressure decoupling may appear and threaten the consistency with the equal pressure assumption. As such, a pressure equilibration procedure is added, based on the work of [27] and already used in [48]. This procedure enforces pressure equilibration and is still consistent with thermodynamics in the sense that mixture volume and energy are conserved while material entropies do not decrease.

The article is organized as follows. In section 2, the two different closures (namely equal strain and equal pressure assumptions) for multi-material models are presented. The numerical scheme is then detailed in section 3, together with a note on the pressure equilibration procedure. Finally, the scheme is confronted with 1D and 2D test cases (some of which displaying highly contrasted equations of state) and results are compared between both equal strain and equal pressure closures.

## 2  Closures for a multi-material model

In this section, a model for multi-material flows is presented. This model does not provide a full description of the system and calls for an additional closure. Two closures are then introduced and discussed. The first one is the equal strain assumption and is commonly used. However, it may become particularly irrelevant in the case of materials with strongly different compressibilities. The second one aims at being relevant for a wider spectrum of applications and is based on an equal pressure assumption. An explicit formulation is derived which takes into account entropy production, hence laying the foundations for our numerical scheme.

### 2.1  Notations

A mixture of an arbitrary number of material is considered. The volume fraction of material $k$ is denoted by $\alpha^k$ and its density by $\rho^k$. Inside a given volume $V$ where a mass $m^k$ of material $k$ occupies a volume $V^k$, these quantities are defined as

$$\alpha^k = \frac{V^k}{V}, \qquad \rho^k = \frac{m^k}{V^k}. \tag{1.1}$$

The total density of the mixture is defined as

$$\rho = \frac{m}{V} = \sum_k \alpha^k \rho^k. \tag{1.2}$$

Additionally, internal energy of material $k$ is denoted $e^k$. Likewise, an energy for the mixture is defined as

$$\rho e = \sum_k \rho^k e^k. \tag{1.3}$$

Each material $k$ has its own pressure $p^k$ and entropy $\eta^k$. The quantities $\rho^k$, $e^k$ and $p^k$ are related to each other with an equation of state (EOS) $p^k(\rho^k, e^k)$. Finally, the characteristic times at

which material velocities relax to a common value are assumed to be significantly smaller than the characteristic times of observation. Only one common velocity $\mathbf{u}$ is thus considered. Equations will be written with Lagrangian time derivatives which are defined by

$$\frac{\mathrm{d}}{\mathrm{d}t}\cdot = \frac{\partial}{\partial t}\cdot + \mathbf{u}\cdot\nabla\cdot. \tag{1.4}$$

## 2.2 Isentropic model for multi-material flows

The present model is written for an arbitrary number of materials, each one of them being described by its own EOS. The EOS are arbitrary, provided they fulfill some thermodynamic constraints such as concavity of the entropy and having a real speed of sound.

$$\alpha^k\rho^k\frac{\mathrm{d}}{\mathrm{d}t}\left(\frac{1}{\alpha^k\rho^k}\right) = \nabla\cdot\mathbf{u}, \tag{1.5a}$$

$$\rho\frac{\mathrm{d}}{\mathrm{d}t}\mathbf{u} = -\nabla p, \tag{1.5b}$$

$$\alpha^k\rho^k\frac{\mathrm{d}}{\mathrm{d}t}e^k = -\alpha^k\rho^k p^k\frac{\mathrm{d}}{\mathrm{d}t}\left(\frac{1}{\rho^k}\right). \tag{1.5c}$$

Equations (1.5) are obtained through a conditional averaging procedure introduced in [52] and summarized in [113] for non-miscible materials and in [49, §B] for general mixtures. More precisely, single material Euler equations with discontinuous thermodynamic properties are initially considered. These equations undergo a material-conditional averaging procedure which allows specific material quantities to be defined. Finally, all fluctuations appearing in the averaging procedure are neglected and, as such, the model is naturally isentropic for each material. The energy equation of material $k$ thus corresponds to Gibbs identity $\mathrm{d}e^k = -p^- - k\mathrm{d}(1/\rho^k) + T^k\mathrm{d}s^k$ with $\mathrm{d}s^k = 0$. Fluctuation terms or other dissipative effects (e.g. surface tension, added mass, etc...) can be added seperately.

The total pressure $p$, not yet defined in (1.5), is actually constrained by the condition of total energy conservation and is given by the convex average

$$p = \sum_k \theta^k p^k, \qquad \theta^k = \frac{\alpha^k\rho^k\dfrac{\mathrm{d}}{\mathrm{d}t}\left(\dfrac{1}{\rho^k}\right)}{\displaystyle\sum_l \alpha^l\rho^l\dfrac{\mathrm{d}}{\mathrm{d}t}\left(\dfrac{1}{\rho^l}\right)}. \tag{1.6}$$

Indeed, in this case,

$$\sum_k \alpha^k\rho^k\frac{\mathrm{d}}{\mathrm{d}t}e^k = -\sum_k \alpha^k\rho^k p^k\frac{\mathrm{d}}{\mathrm{d}t}\left(\frac{1}{\rho^k}\right) \tag{1.7}$$

$$= -\sum_k \theta^k p^k\sum_l \alpha^l\rho^l\frac{\mathrm{d}}{\mathrm{d}t}\left(\frac{1}{\rho^l}\right) \tag{1.8}$$

$$= -p\nabla\cdot\mathbf{u}, \tag{1.9}$$

which eventually yields

$$\sum_k \left[ \alpha^k \rho^k \frac{\mathrm{d}}{\mathrm{d}t} e^k \right] + \rho \frac{\mathrm{d}}{\mathrm{d}t} \left( \frac{\|\mathbf{u}\|^2}{2} \right) = -\nabla \cdot (p\mathbf{u}). \tag{1.10}$$

A quick comparison of the number of equations and number of unknowns shows that the model is still under-determined and must be supplemented with closures or evolution equation for either volume fractions, densities, or pressures. Hence, this model is only a general framework within which numerous closures can be introduced. Two of them will now be investigated and compared, namely the equal strain and the equal pressure assumptions.

**Remark:** In [4], a model with both closures (namely the equal strain and equal pressures assumptions) is studied. However, this model does not comply with the second principle of thermodynamics as entropy may be destroyed over time (see A). Despite boasting good mathematical properties such as hyperbolicity (for a large class of equations of state), it may come at the cost of losing some consistency with physics. Ultimately, this is the reason why it will not be considered here.

## 2.3 Equal strain assumption

The first closure is the so-called equal strain assumption [6, §3.11.1] whereby all materials are assumed to experience the same volume deformation

$$\frac{1}{\rho} \frac{\mathrm{d}}{\mathrm{d}t} \rho = \frac{1}{\rho^k} \frac{\mathrm{d}}{\mathrm{d}t} \rho^k = \nabla \cdot \mathbf{u}. \tag{1.11}$$

As detailed in [35], combination of (1.11) and (1.5a) eventually yields

$$\frac{\mathrm{d}}{\mathrm{d}t} (\alpha^k) = 0. \tag{1.12}$$

Equation (1.12) is also often introduced as a transport equation in Euler formalism [4]

$$\frac{\partial}{\partial t} (\alpha^k) + \mathbf{u} \cdot \nabla \alpha^k = 0. \tag{1.13}$$

It is also called a topological equation because it exactly expresses the advection of the interface[2]. The density equation may be deduced and then reads

$$\alpha^k \rho^k \frac{\mathrm{d}}{\mathrm{d}t} \left( \frac{1}{\rho^k} \right) = \alpha^k \nabla \cdot \mathbf{u}. \tag{1.14}$$

Equation (1.6) then reduces to $p = \sum_k \alpha^k p^k$ [3]. The closed model is hyperbolic with a squared speed of sound $c^2$ of the mixture given as a convex combination of squared speeds of sound $(c^k)^2$

$$c^2 = \sum_k \frac{\alpha^k \rho^k}{\rho} (c^k)^2. \tag{1.15}$$

---

[2]More generally, this transport equation has been used with other variables such as the adiabatic coefficient $\gamma^k$ for perfect gases [56] or other parameters for more complicated EOS.

[3]For mixtures of perfect gases, it is commonly known as Dalton's law.

The resulting model is widely used for the simulation of multi-material flows, as it does not imply strong modifications of single material schemes. The numerical treatment of the set of equations is standard and for clarity we do not intend to detail it here. Instead we refer to [9, 35] in which this is clearly explained.

However convenient this model might be, it still has its shortcomings. Although if it is quite relevant for mixtures of similar materials, equation (1.11) becomes unrealistic when dealing with contrasted EOS: if a mixture of air and water is compressed, air should physically bear most of the deformation and its volume fraction should decrease accordingly instead of being constant. In the case where both air and water are compressed with the same factor, water pressure skyrockets and may exceed thresholds governing chemical reactions or phase changes, hence producing unrealistic physical behaviors. Finally, in industrial applications where some equations of state are tabulated and not known analytically, thermodynamic states where pressure is not defined might be explored. All these reasons motivate the introduction of a second closure discussed below.

## 2.4 Equal pressure assumption : from implicit to explicit formulation

In the vast majority of multi-material systems, pressure relaxation processes between materials occur on time scales much smaller compared to the characteristic hydrodynamic time scales [55]. Consequently, material pressures may be considered equal. This will be referred to as the equal pressure assumption

$$p = p^k(\rho^k, e^k), \quad \forall k \in \{1, ..., n\}, \tag{1.16}$$

which provides an implicit closure on the volume fractions and densities. Following [108, §3.5], in order to make the coupling with equations (1.16), the underlying rates of expansion $\frac{\mathrm{d}}{\mathrm{d}t}(\rho^k)$ are derived. The conservation of total mass gives a relationship between all $\frac{\mathrm{d}}{\mathrm{d}t}(\rho^k)$

$$\sum_k \left[ \rho^k \alpha^k \frac{\mathrm{d}}{\mathrm{d}t} \left( \frac{1}{\alpha^k \rho^k} \right) - \nabla \cdot \mathbf{u} \right] \alpha^k = 0,$$

$$\iff \sum_k \left[ \frac{\alpha^k}{\rho^k} \frac{\mathrm{d}}{\mathrm{d}t} \rho^k + \frac{\mathrm{d}}{\mathrm{d}t} \alpha^k \right] = -\nabla \cdot \mathbf{u},$$

$$\iff \sum_k \frac{\alpha^k}{\rho^k} \frac{\mathrm{d}}{\mathrm{d}t} \rho^k = -\nabla \cdot \mathbf{u}. \tag{1.17}$$

On the other hand, differentiating (1.16) with respect to time (both Eulerian and Lagrangian time derivatives are equivalent because materials all share the same velocity) gives

$$\frac{\mathrm{d}}{\mathrm{d}t} p = \frac{\mathrm{d}}{\mathrm{d}t} p^k. \tag{1.18}$$

Introducing the speed of sound $c^k$ and the Grüneisen coefficient $\Gamma^k$ [78] of material $k$

$$(c^k)^2 = \left. \frac{\partial p^k}{\partial \rho^k} \right|_\eta, \quad \Gamma^k = \frac{1}{\rho^k T^k} \left. \frac{\partial p}{\partial \eta} \right|_\rho, \tag{1.19}$$

pressure derivatives may be written as a function of density and entropy derivatives

$$\frac{\mathrm{d}}{\mathrm{d}t}p = (c^k)^2 \frac{\mathrm{d}}{\mathrm{d}t}\rho^k + \rho^k \Gamma^k T^k \frac{\mathrm{d}}{\mathrm{d}t}\eta^k. \tag{1.20}$$

Finding $\frac{\mathrm{d}}{\mathrm{d}t}(\rho^k)$ essentially amounts to solving the linear system (1.17)-(1.20) with unknowns $\left\{\frac{\mathrm{d}}{\mathrm{d}t}p, \frac{\mathrm{d}}{\mathrm{d}t}\rho^k\right\}$. Substituting $\frac{\mathrm{d}}{\mathrm{d}t}\rho^k$ with $\frac{1}{(c^k)^2}\left(\frac{\mathrm{d}}{\mathrm{d}t}p - \rho^k\Gamma^k T^k \frac{\mathrm{d}}{\mathrm{d}t}\eta^k\right)$ inside equation (1.17) gives

$$\frac{\mathrm{d}}{\mathrm{d}t}p = -\frac{1}{\sum_k \dfrac{\alpha^k}{\rho^k(c^k)^2}}\nabla \cdot u + \sum_k \beta^k \rho^k \Gamma^k T^k \frac{\mathrm{d}}{\mathrm{d}t}\eta^k, \tag{1.21a}$$

$$\beta^k = \frac{\dfrac{\alpha^k}{\rho^k(c^k)^2}}{\sum_l \dfrac{\alpha^l}{\rho^l(c^l)^2}}. \tag{1.21b}$$

Notice that $\sum_k \beta^k = 1$. At this point, the unknowns $\frac{\mathrm{d}}{\mathrm{d}t}(\rho^k)$ are immediately recovered as

$$\alpha^k \rho^k \frac{\mathrm{d}}{\mathrm{d}t}\left(\frac{1}{\rho^k}\right) = \beta^k \nabla \cdot u + \left(\sum_l \frac{\alpha^l}{\rho^l(c^l)^2}\right)\sum_l \beta^k \beta^l \Delta^{kl}, \tag{1.22a}$$

$$\Delta^{kl} = \rho^k \Gamma^k T^k \frac{\mathrm{d}}{\mathrm{d}t}\eta^k - \rho^l \Gamma^l T^l \frac{\mathrm{d}}{\mathrm{d}t}\eta^l. \tag{1.22b}$$

In the particular case of isentropic flows, model (1.5) is then supplemented with

$$\alpha^k \rho^k \frac{\mathrm{d}}{\mathrm{d}t}\left(\frac{1}{\rho^k}\right) = \beta^k \nabla \cdot \mathbf{u}. \tag{1.23}$$

which is equivalent to the equal strain closure (1.14) if $\beta^k$ is replaced with $\alpha^k$. This essentially means that inside a given volume containing multiple materials, the expansion of the total volume is no longer shared between materials with respect to their volume fractions $\alpha^k$. It is instead shared with respect to coefficients $\beta^k$, which take into account the thermodynamical properties of the different materials. Because of this coefficient, some stiffness may appear, especially in mixtures with highly contrasted materials (e.g. air and water). Besides, the speed of sound of the mixture $c$ is given by Wood's formula [111]

$$\frac{1}{\rho c^2} = \sum_k \frac{\alpha^k}{\rho^k(c^k)^2}. \tag{1.24}$$

It is not a convex combination of the material speed of sound and has a non-monotonic behavior. Despite the hyperbolicity of the model (see [81]), these two features (namely the stiffness and non-monotonic behavior of the speed of sound) are often invoked in order to reject it [73] in favor of others which do not have these characteristics (e.g. the model presented in section 2.3). However, the stiffness is expected in the sense that, from a physical point of view, a mixture of air and water is stiff. Hence, it should not be avoided, even though it requires additional care during the discretization process [49]. As for the non-monotonicity of the speed of sound, it has been confirmed experimentally [81, 30].

This model is not new and has already been studied and discretized in the literature. In [81], it is derived from the Baer-Nunziato model [5] in the infinitely strong relaxation limit. The authors also provide a complete study of the hyperbolicity and wave structure of the model. In [37, 108], it is derived with the least action principle. The equal pressure assumption is shown to be a direct consequence of the variation of the action with respect to the volume fraction, provided that potential energy is only internal. However, both previously mentioned sources do not take into account the entropy contribution inside the density equation (1.23), which is, as it will be seen later, essential to our numerical strategy.

**Remark:** Regarding the previous considerations on total energy conservation, one automatically recovers it from the equality of pressures. This property will need to be ensured at the discrete level with the chosen numerical strategy.

## 3 Numerical strategy

The numerical strategy for (1.5)-(1.16) is based on the continuous equations (1.22) derived in the previous section. This allows us not to rely on an iterative procedure to deal with the strongly non-linear and potentially stiff implicit initial formulation of the model (1.16). The resulting scheme is then fully explicit, conserves mass, momentum and total energy while ensuring a positive entropy production for each material.

### 3.1 Geometry and notations

The notations are similar to those introduced in [72, 19]. Each cell is assigned a unique index $c$ and is denoted $\omega_c$. Its volume is $V_c$. The cells are assumed to be polygonal so that they are defined by the set of their nodes $\mathcal{P}(c)$. The neighboring cells are collected in the set $\mathcal{N}(c)$. For a given node $p$, $\mathcal{C}(p)$ is the set of cells that contains $p$. $\mathbf{x}_p$ and $\mathbf{u}_p$ are its position and velocity. $p^+$ is the node in $\mathcal{P}(c)$ which follows $p$ in counterclockwise order and $p^-$ the previous node. Let $\mathbf{n}_{pc}^+$ be the outward normal unit vector to $\overrightarrow{pp^+}$ and consider $l_{pc}^+ = \frac{1}{2}\|\overrightarrow{pp^+}\|$. Similarly, $\mathbf{n}_{pc}^-$ and $l_{pc}^-$ are defined accordingly. Consequently, the corner outward normal unit vector $\mathbf{n}_{pc}$ is defined as follows

$$\mathbf{n}_{pc} = \frac{l_{pc}^+\mathbf{n}_{pc}^+ + l_{pc}^-\mathbf{n}_{pc}^-}{l_{pc}}, \qquad l_{pc} = \left\| l_{pc}^+\mathbf{n}_{pc}^+ + l_{pc}^-\mathbf{n}_{pc}^- \right\|_2. \qquad (1.25)$$

Finally, $V_{pc}$ denotes the volume of the area formed by $\mathbf{x}_p$, $(\mathbf{x}_p + \mathbf{x}_{p^+})/2$, $\mathbf{x}_c$ and $(\mathbf{x}_p + \mathbf{x}_{p^-})/2$. The quantity $V_p$ is the volume around $p$ defined by

$$V_p = \sum_{p \in \mathcal{P}(c)} V_{pc}. \qquad (1.26)$$

All the notations introduced are illustrated in figure 1.1. Concerning cell variables, the approach is that of a finite volume scheme. Consequently, for physical quantities $\phi \in \left\{ \frac{1}{\alpha^k \rho^k}, e^k, \frac{1}{\rho^k} \right\}$ related
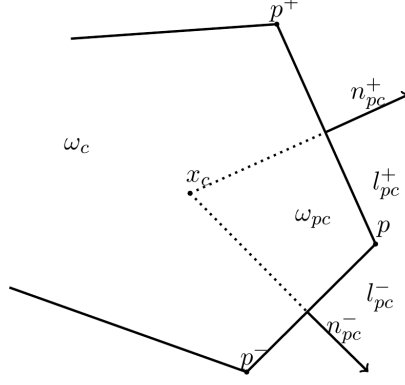
Figure 1.1: Cell notations.

to material $k$ and a cell $c$, are defined the averaged quantities over the cell by

$$m_c^k = \int_{\omega_c} \alpha^k \rho^k \mathrm{d}\mathbf{x}, \qquad \phi_c = \frac{1}{m_c^k} \int_{\omega_c} \alpha^k \rho^k \phi \mathrm{d}\mathbf{x}, \tag{1.27a}$$

$$m_c = \int_{\omega_c} \rho \mathrm{d}\mathbf{x}, \qquad \mathbf{u}_c = \frac{1}{m_c} \int_{\omega_c} \rho \mathbf{u} \mathrm{d}\mathbf{x}. \tag{1.27b}$$

**Remark:** In the following, $\rho_c^k$ denotes the inverse of $\left(1/\rho^k\right)_c$ which is technically different from the weighted average value of $\rho^k$ over the cell. Same goes for the notation $(\alpha^k \rho^k)_c$. Finally $\alpha_c^k$ is defined as the ratio of $(\alpha^k \rho^k)_c$ by $\rho^k$ so that $(\alpha^k \rho^k)_c = \alpha_c^k \rho_c^k$. With this definition, the $\alpha_c^k$ satisfy

$$\sum_k \alpha_c^k = \sum_k \frac{\left(\dfrac{1}{\rho^k}\right)_c}{\left(\dfrac{1}{\alpha^k \rho^k}\right)_c} = \sum_k \frac{\displaystyle\int_{\omega_c} \alpha^k \mathrm{d}\mathbf{x}}{\displaystyle\int_{\omega_c} 1 \mathrm{d}\mathbf{x}} = 1. \tag{1.28}$$

Defining these averaged quantities prepares for the use of Reynold's transport theorem which states that

$$\frac{\mathrm{d}}{\mathrm{d}t} \int_{\omega_c} \alpha^k \rho^k \phi \mathrm{d}\mathbf{x} = m_c^k \frac{\mathrm{d}}{\mathrm{d}t} \phi_c, \quad \phi \in \left\{ \frac{1}{\alpha^k \rho^k}, e^k, \frac{1}{\rho^k} \right\}, \tag{1.29a}$$

$$\frac{\mathrm{d}}{\mathrm{d}t} \int_{\omega_c} \rho \mathbf{u} \mathrm{d}\mathbf{x} = m_c \frac{\mathrm{d}}{\mathrm{d}t} \mathbf{u}_c. \tag{1.29b}$$

### 3.2 Total volume and momentum conservation equations

Regarding the discretization of the mass and momentum equations, no significant changes are made from the classic Eucclhyd scheme [71, 35, 70]. The mass conservation equation (1.5a), averaged over a Lagrangian cell, together with equation (1.29a) gives

$$m_c^k \frac{\mathrm{d}}{\mathrm{d}t} \left( \frac{1}{\alpha_c^k \rho_c^k} \right) = \oint_{\partial \omega_c} \mathbf{u} \cdot \mathbf{n} \mathrm{d}l = \sum_{p \in \mathcal{P}(c)} l_{pc} \mathbf{n}_{pc} \cdot \mathbf{u}_p. \tag{1.30}$$

The left hand-side may be interpreted as a sum of node fluxes. Considering that the cell remains polygonal through advection, its volume only depends on position of nodes. Then, equation

(1.30) may also be seen as the exact derivative of the Lagrangian volume, using the chain rule and the formula $\frac{\partial V_c}{\partial \mathbf{x}_p} = l_{pc}\mathbf{n}_{pc}$. More details may be found in [70]. In order to proceed with the discretization of the momentum conservation equation, sub-cell forces are defined as follows

$$\mathbf{f}_{pc} = -\int_{\partial\omega_{pc}\cap\partial\omega_c} p\mathbf{n}\mathrm{d}l. \tag{1.31}$$

For the momentum conservation, equation (1.29b) and Green's formula simply leads to

$$m_c\frac{\mathrm{d}}{\mathrm{d}t}\mathbf{u}_c = -\int_{\omega_c} \nabla p\mathrm{d}\mathbf{x} \tag{1.32a}$$

$$= -\int_{\partial\omega_c} p\mathbf{n}\mathrm{d}l \tag{1.32b}$$

$$= \sum_{p\in\mathcal{P}(c)} -\int_{\partial\omega_{pc}\cap\partial\omega_c} p\mathbf{n}\mathrm{d}l \tag{1.32c}$$

$$= \sum_{p\in\mathcal{P}(c)} \mathbf{f}_{pc}. \tag{1.32d}$$

In the spirit of [70] the closure procedure to compute $\mathbf{f}_{pc}$ is chosen to guarantee a correct material dissipation entropy as well as to ensure the momentum and total energy conservation

$$\mathbf{f}_{pc} = -l_{pc}p_c\mathbf{n}_{pc} + \mathbf{M}_{pc}\left(\mathbf{u}_p - \mathbf{u}_c\right), \tag{1.33}$$

where $\mathbf{M}_{pc}$ is a semi-positive defined matrix called in the following a dissipation matrix. Now, in order to enforce a correct discrete material entropy production, the following standard dissipation matrix definition [71] is taken

$$\mathbf{M}_{pc} = \rho_c c_c \left(l_{pc}^+\mathbf{n}_{pc}^+ \otimes \mathbf{n}_{pc}^+ + l_{pc}^-\mathbf{n}_{pc}^- \otimes \mathbf{n}_{pc}^-\right), \tag{1.34}$$

where $c$ is the speed of sound of the mixture whose expression is given by Wood's formula [111]

$$\frac{1}{\rho c^2} = \sum_k \frac{\alpha^k}{(\rho^k(c^k)^2)}. \tag{1.35}$$

### 3.3 Material internal energy and density equations

A naive discretization of energy (1.5c) and density equations (1.23) would consist in

$$m_c^k\frac{\mathrm{d}}{\mathrm{d}t}e_c^k = -p_c m_c^k\frac{\mathrm{d}}{\mathrm{d}t}\left(\frac{1}{\rho^k}\right), \tag{1.36a}$$

$$m_c^k\frac{\mathrm{d}}{\mathrm{d}t}\left(\frac{1}{\rho^k}\right) = -\beta_c^k \sum_{p\in\mathcal{P}(c)} l_{pc}\mathbf{n}_{pc} \cdot \mathbf{u}_p. \tag{1.36b}$$

However, when comparing the suggested discretization (1.36) with the standard single material scheme, one understands that some numerical dissipation needs to be added in order to stabilize the scheme. This numerical dissipation physically translates into entropy production so that the non-isentropic equations (i.e. the fundamental thermodynamic relation and equation (1.22) for

each material $k$) must be considered

$$m_c^k \frac{\mathrm{d}}{\mathrm{d}t} e_c^k = -p \, m_c^k \frac{\mathrm{d}}{\mathrm{d}t} \left( \frac{1}{\rho_c^k} \right) + \int_{\omega_c} \alpha^k \rho^k T^k \frac{\mathrm{d}}{\mathrm{d}t} \eta^k, \tag{1.37a}$$

$$m_c^k \frac{\mathrm{d}}{\mathrm{d}t} \left( \frac{1}{\rho_c^k} \right) = -\beta_c^k \sum_{p \in \mathcal{P}(c)} l_{pc} \mathbf{n}_{pc} \cdot \mathbf{u}_p + \int_{\omega_c} \frac{\alpha^k}{\rho^k (c^k)^2} \sum_l \beta^l \Delta^{kl}. \tag{1.37b}$$

The discretization of term $\alpha^k \rho^k T^k d_t(\eta^k)$ (also appearing inside the expression of $\Delta^{lk}$) needs to be specified to enforce the chosen numerical viscosity for each material. The conservation equation of the total energy $\sum_k \alpha^k \rho^k e^k$ must be discretized according to the single material scheme

$$\sum_k m_c^k \frac{\mathrm{d}}{\mathrm{d}t} e_c^k = \sum_{p \in \mathcal{P}(c)} \mathbf{f}_{pc} \cdot (\mathbf{u}_p - \mathbf{u}_c), \tag{1.38}$$

which gives

$$\sum_k \int_{\omega_c} \alpha^k \rho^k T^k \frac{\mathrm{d}}{\mathrm{d}t} \eta^k = \sum_{p \in \mathcal{P}(c)} (\mathbf{u}_p - \mathbf{u}_c)^T \mathbf{M}_{pc} (\mathbf{u}_p - \mathbf{u}_c). \tag{1.39}$$

The total entropy production now needs to be shared between materials through coefficients $\lambda^k > 0$ such that $\sum_k \lambda^k = 1$. The material discrete numerical viscosity is then written

$$\int_{\omega_c} \alpha^k \rho^k T^s \frac{\mathrm{d}}{\mathrm{d}t} \eta^k = \lambda^k \left[ \sum_{p \in \mathcal{P}(c)} (\mathbf{u}_p - \mathbf{u}_c)^T \mathbf{M}_{pc} (\mathbf{u}_p - \mathbf{u}_c) \right], \tag{1.40a}$$

$$= \sum_{p \in \mathcal{P}(c)} (\mathbf{u}_p - \mathbf{u}_c)^T \mathbf{M}_{pc}^k (\mathbf{u}_p - \mathbf{u}_c), \tag{1.40b}$$

with

$$\mathbf{M}_{pc}^k = \lambda^k \mathbf{M}_{pc}. \tag{1.41}$$

The choice of the coefficients $\lambda^k$ is no simple matter and does more than only stabilizing the scheme. Indeed, it is well-known [77, 15] that non-conservative hyperbolic systems, such as the one under study here, have no canonical solution as vanishing viscosity solutions depend on the diffusion operator; this is not the case for conservative hyperbolic systems. Hence, different choices of $\lambda^k$ may produce different numerical solutions [49] and they should be chosen according to physical considerations. For this reason, their value is left to the user's expertise. For our test cases, we chose $\lambda^k$ as the mass fraction of material $k$. Finally, our space discretization is

$$m_c^k \frac{\mathrm{d}}{\mathrm{d}t} e_c^k = -p_c \, m_c^k \frac{\mathrm{d}}{\mathrm{d}t} \left( \frac{1}{\rho_c^k} \right) + \sum_{p \in \mathcal{P}(c)} (\mathbf{u}_p - \mathbf{u}_c)^T \mathbf{M}_{pc}^k (\mathbf{u}_p - \mathbf{u}_c), \tag{1.42a}$$

$$m_c^k \frac{\mathrm{d}}{\mathrm{d}t} \left( \frac{1}{\rho_c^k} \right) = -\beta_c^k \sum_{p \in \mathcal{P}(c)} l_{pc} \mathbf{n}_{pc} \cdot \mathbf{u}_p + \frac{\alpha_c^k}{\rho_c^k (c_c^k)^2} \sum_l \beta_c^l \Delta_c^{kl}, \tag{1.42b}$$

$$\Delta_c^{kl} = \sum_{p \in \mathcal{P}(c)} (\mathbf{u}_p - \mathbf{u}_c)^T \left( \frac{\Gamma_c^k}{\alpha_c^k} \mathbf{M}_{pc}^k - \frac{\Gamma_c^l}{\alpha_c^l} \mathbf{M}_{pc}^l \right) (\mathbf{u}_p - \mathbf{u}_c). \tag{1.42c}$$

The only thing missing in the semi-discrete scheme is the expression of the node velocities $\mathbf{u}_p$. As in the single material scheme, they are computed as follows

$$\mathbf{u}_p = \left[ \sum_{c \in \mathcal{C}(p)} \mathbf{M}_{pc} \right]^{-1} \left( \sum_{c \in \mathcal{C}(p)} (p_c l_{pc} \mathbf{n}_{pc} - \mathbf{M}_{pc} \mathbf{u}_c) \right). \tag{1.43}$$

This equation is equivalent to $\sum_{c \in \mathcal{C}(p)} \mathbf{f}_{pc} = 0$, which ensures both the momentum and total energy semi-discrete conservation (see next section).

### 3.4 Time discretization

A standard Euler forward strategy is chosen for the time discretization of the equations. The scheme is then explicit, all spatial terms derived in the previous sections being taken at the initial time. Some caution may still need to be exercised on the velocity $\mathbf{u}_c$ inside the energy equation (1.42a). Indeed, taking an average value $(\mathbf{u}_c^{n+1} + \mathbf{u}_c^n)/2$ is necessary for the discrete total energy conservation as it will be discussed in the next section. The resulting scheme is still fully explicit as velocities may be computed before energies.

$$\frac{m_c^k}{\Delta t} \left( \frac{1}{(\alpha \rho)_c^{k,n+1}} - \frac{1}{(\alpha \rho)_c^{k,n}} \right) = \sum_{p \in \mathcal{P}(c)} l_{pc} \mathbf{n}_{pc} \cdot \mathbf{u}_p^n, \tag{1.44a}$$

$$m_c \frac{\mathbf{u}_c^{n+1} - \mathbf{u}_c^n}{\Delta t} = \sum_{p \in \mathcal{P}(c)} \mathbf{f}_{pc}^n, \tag{1.44b}$$

$$m_c^k \frac{e_c^{k,n+1} - e_c^{k,n}}{\Delta t} = -p_c^n \frac{m_c^k}{\Delta t} \left( \frac{1}{\rho_c^{k,n+1}} - \frac{1}{\rho_c^{k,n}} \right) + \sum_{p \in \mathcal{P}(c)} (\mathbf{u}_p^n - \mathbf{u}_c^n)^T \mathbf{M}_{pc}^{k,n} \left( \mathbf{u}_p^n - \frac{\mathbf{u}_c^n + \mathbf{u}_c^{n+1}}{2} \right), \tag{1.44c}$$

$$\frac{m_c^k}{\Delta t} \left( \frac{1}{\rho_c^{k,n+1}} - \frac{1}{\rho_c^{k,n}} \right) = -\beta_c^{k,n} \sum_{p \in \mathcal{P}(c)} l_{pc} \mathbf{n}_{pc} \cdot \mathbf{u}_p^n + \left( \sum_l \frac{\alpha_c^{l,n}}{\rho_c^{l,n}(c_c^{l,n})^2} \right) \sum_l \beta_c^{k,n} \beta_c^{l,n} \Delta_c^{kl,n}, \tag{1.44d}$$

$$\Delta_c^{kl,n} = \sum_{p \in \mathcal{P}(c)} (\mathbf{u}_p^n - \mathbf{u}_c^n)^T \left( \frac{\Gamma_c^{k,n}}{\alpha_c^{k,n}} \mathbf{M}_{pc}^{n,k} - \frac{\Gamma_c^{l,n}}{\alpha_c^{l,n}} \mathbf{M}_{pc}^{l,n} \right) \left( \mathbf{u}_p^n - \frac{\mathbf{u}_c^n + \mathbf{u}_c^{n+1}}{2} \right). \tag{1.44e}$$

As for any standard explicit Lagrangian scheme, time step $\Delta t$ is subject to two constraints. The first one is the CFL or acoustic condition which uses the mixture speed of sound (1.24). The second one prevents cell volume and volume fractions from becoming negative.

### 3.5 Numerical properties

In this section, discrete total energy conservation and semi-discrete entropy production are proven. These results are an extension of the ones given in [72] in the context of equal strain assumption. Here, they are closure-independent.

**Property 1.** *Discrete total energy conservation*

The total discrete energy is conserved

$$\sum_c m_c \left( e_c^{n+1} + \|\mathbf{u}_c^{n+1}\|^2/2 \right) = \sum_c m_c \left( e_c^n + \|\mathbf{u}_c^n\|^2/2 \right). \tag{1.45}$$

*Proof.* Multiplying equation (1.32) by $(\mathbf{u}_c^{n+1} + \mathbf{u}_c^n)/2$ one obtains

$$\frac{m_c}{2\Delta t} \left( \|\mathbf{u}_c^{n+1}\|^2 - \|\mathbf{u}_c^n\|^2 \right) = \sum_{p\in\mathcal{P}(c)} \mathbf{f}_{pc}^n \cdot \left( \frac{\mathbf{u}_c^{n+1} + \mathbf{u}_c^n}{2} \right). \tag{1.46}$$

On the other hand, adding energy equations (1.44c) over all materials leads to

$$
\begin{aligned}
m_c \frac{e_c^{n+1} - e_c^n}{\Delta t} &= \sum_k p_c m_c^k \left( \frac{1}{\rho_c^{k,n+1}} - \frac{1}{\rho_c^{k,n}} \right) + \sum_{p\in\mathcal{P}(c)} (\mathbf{u}_p - \mathbf{u}_c)^{\mathrm{T}} \mathbf{M}_{pc} \left( \mathbf{u}_p - \frac{\mathbf{u}_c^{n+1} + \mathbf{u}_c^n}{2} \right) \\
&= -p_c \sum_{p\in\mathcal{P}(c)} l_{pc}\mathbf{n}_{pc} \cdot \left( \mathbf{u}_p - \frac{\mathbf{u}_c^{n+1} + \mathbf{u}_c^n}{2} \right) + \sum_{p\in\mathcal{P}(c)} \mathbf{M}_{pc}(\mathbf{u}_p - \mathbf{u}_c) \cdot \left( \mathbf{u}_p - \frac{\mathbf{u}_c^{n+1} + \mathbf{u}_c^n}{2} \right) \\
&= \sum_{p\in\mathcal{P}(c)} \left( -p_c l_{pc}\mathbf{n}_{pc} + \mathbf{M}_{pc}(\mathbf{u}_p - \mathbf{u}_c) \right) \cdot \left( \mathbf{u}_p - \frac{\mathbf{u}_c^{n+1} + \mathbf{u}_c^n}{2} \right) \\
&= \sum_{p\in\mathcal{P}(c)} \mathbf{f}_{pc}^n \cdot \left( \mathbf{u}_p - \frac{\mathbf{u}_c^{n+1} + \mathbf{u}_c^n}{2} \right),
\end{aligned} \tag{1.47}
$$

where the total internal energy $e$ is defined by

$$me = \sum_k m^k e^k. \tag{1.48}$$

This discrete internal energy evolution equation may be combined with the kinetic energy equation (1.46) to recover the following discrete total energy equation

$$\frac{m_c}{\Delta t} \left( e_c^{n+1} - e_c^n + \frac{\|\mathbf{u}_c^{n+1}\|^2}{2} - \frac{\|\mathbf{u}_c^n\|^2}{2} \right) = \sum_{p\in\mathcal{P}(c)} \mathbf{f}_{pc}^n \cdot \mathbf{u}_p. \tag{1.49}$$

As in the single material case, node velocities $\mathbf{u}_p$ are computed to ensure both discrete momentum and total energy conservation which concludes the proof. The details of this last point can be found in [72] $\qquad\square$

**Property 2.** *Semi-discrete entropy production*

The semi-discrete entropy variation is positive in each cell and for each material:

$$m_c^k \frac{\mathrm{d}}{\mathrm{d}t} \eta_c^k \geq 0. \tag{1.50}$$

*Proof.* The semi-discrete entropy is written thanks to Gibbs' equation

$$m_c^k T_c^k \frac{\mathrm{d}}{\mathrm{d}t} \eta_c^k = m_c^k \frac{\mathrm{d}}{\mathrm{d}t} e_c^k + m_c^k p_c^k \frac{\mathrm{d}}{\mathrm{d}t} \left( \frac{1}{\rho_c^k} \right). \tag{1.51}$$

The discretization of the energy equation uses the density equation one so that

$$m_c^k \frac{\mathrm{d}}{\mathrm{d}t} e_c^k = -m_c^k p_c^k \frac{\mathrm{d}}{\mathrm{d}t}\left(\frac{1}{\rho_c^k}\right) + \sum_{p \in \mathcal{P}(c)} (\mathbf{u}_p - \mathbf{u}_c)^T \mathbf{M}_{pc}^k (\mathbf{u}_p - \mathbf{u}_c). \tag{1.52}$$

Finally

$$m_c^k T_c^k \frac{\mathrm{d}}{\mathrm{d}t} \eta_c^k = \sum_{p \in \mathcal{P}(c)} (\mathbf{u}_p - \mathbf{u}_c)^T \mathbf{M}_{pc}^k (\mathbf{u}_p - \mathbf{u}_c) \geq 0. \tag{1.53}$$

Notice that the proof does not rely on the discretization of the density equation. It only requires both density and energy equations to be consistent with each other. As a result, the semi-discrete entropy production does not depend on the closure chosen for $\frac{\mathrm{d}}{\mathrm{d}t}(\rho^k)$; in particular, it is identical for the equal strain and the equal pressure closures. $\qquad\square$

## 3.6 Pressure equilibration procedure

Here it should be highlighted that the numerical strategy presented in the previous sections only enforces the pressure equilibration between materials in a mixed cell up to the scheme time order. Consequently, as iterations accumulate, pressures may diverge from one another. This decoupling is clearly illustrated in the numerical section and decreasing the CFL number helps recover a better pressure coupling. In order to keep a large CFL number, an equilibration procedure in the spirit of the ideas introduced in [27, 48], is now presented. In practice, this correction is applied after the Lagrangian phase and remains particularly inexpensive since it is local and one already starts with a pressure decoupling of order $\mathcal{O}(\Delta t)$. Of course, this process should be carefully done in order to preserve at the discrete level all the properties proven above. The following notation is now introduced

$$[X] = X^{\text{final}} - X^{\text{initial}}, \tag{1.54}$$

where $X$ is a physical quantity and the notation $[.]$ represents the difference between a final state and an initial one. The equilibration procedure must fulfill some requirements. Firstly, the procedure must preserve the total volume of the cell as well as its total energy

$$c_1[v_1] + c_2[v_2] = 0, \tag{1.55a}$$

$$c_1[e_1] + c_2[e_2] = 0. \tag{1.55b}$$

with $c_k = \alpha_1 \rho_1 / \rho$ the mass fraction of material $k$. In addition, the process must be consistent with thermodynamics; therefore, no entropy destruction should occur on any material involved. Considering thermodynamic paths $p_1(v_1)$ and $p_2(v_2)$ (see figure 1.2), one has

$$[e_k] = -\int_{v_k^i}^{v_k^f} p_k(v) dv_k + Q_k, \quad k \in \{1, 2\}, \tag{1.56}$$

where $Q_k$ is the entropy production on material $k$. Defining the average pressure $\langle p_k \rangle$ along the path, it becomes

$$[e_k] = -\langle p_k \rangle [v_k] + Q_k, \quad k \in \{1, 2\}. \tag{1.57}$$
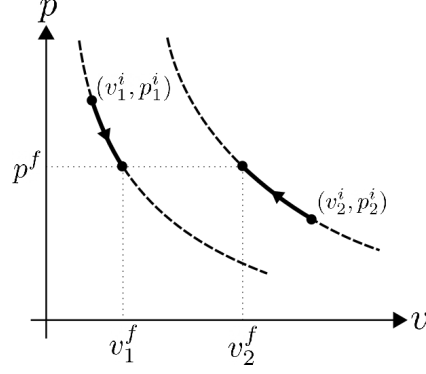
Figure 1.2: Visualization of the transformations in the $(p, v)$ plane.

Both volume and energy conservation (1.55) eventually yields

$$[e_k] = -\big(\beta_1\langle p_1\rangle + \beta_2\langle p_2\rangle\big)[v_k] \tag{1.58a}$$

$$= -p[v_k], \tag{1.58b}$$

with

$$\beta_1 = \frac{c_2 Q_2}{c_1 Q_1 + c_2 Q_2}, \quad \beta_2 = \frac{c_1 Q_1}{c_1 Q_1 + c_2 Q_2}, \quad \beta_1 + \beta_2 = 1. \tag{1.59}$$

Because $p$ does not depend on the material, taking $p = p^f$ is a sensible choice. The entropy variation sign must now be assessed.

**Property 3.** *Pressure equilibration entropy variation*
The thermodynamic path defined by $[e] = -p^f[v]$ is entropic for all equations of state

$$[\eta] > 0. \tag{1.60}$$

In particular, for the relaxation procedure, entropy variation is positive for all materials and all equations of state.

*Proof.* Taylor–Lagrange theorem is applied to the entropy $\eta(v, e)$ around the state $(v^f, e^f)$. Then, there is a convex combination $(\overline{v}, \overline{e})$ of the initial and final states for which

$$
\begin{aligned}
\eta^i = \eta^f &+ \left(\frac{\partial\eta}{\partial v}\right)^f (v^i - v^f) + \left(\frac{\partial\eta}{\partial e}\right)^f (e^i - e^f) \\
&+ \frac{1}{2}\left(\nabla^2\eta(\overline{v}, \overline{e})\right)(v^i - v^f, e^i - e^f) \\
= \eta^f &+ \frac{p^f}{T^f}(v^i - v^f) + \frac{1}{T^f}(e^i - e^f) \\
&+ \frac{1}{2}\left(\nabla^2\eta(\overline{v}, \overline{e})\right)(v^i - v^f, e^i - e^f).
\end{aligned} \tag{1.61a}
$$

Using both the equation $[e] = -p^f[v]$ and the concavity of the entropy, the entropy production positivity is then proved

$$[\eta] = -\frac{1}{2}\left(\nabla^2\eta(\overline{v}, \overline{e})\right)(v^i - v^f, e^i - e^f) > 0. \tag{1.62}$$

41

|        | $\gamma$ | $\alpha$ | $\rho$ | $p$ |
|--------|----------|----------|--------|-------|
| Gas 1  | 1.4      | $10^{-5}$ | 1     | 1.144 |
| Gas 2  | 5/3      | $1 - 10^{-5}$ | 1 | 1.144 |

Figure 1.3: Initial states inside the piston.

$\square$

**Remark:** On a unrelated note regarding the equilibration procedure, one may find that applying the Taylor-Lagrange theorem around the state $(v^i, e^i)$ shows that the formula $[e] = -p^i[v]$ leads to $[\eta] < 0$. The ideas of the proof come from [62, §III.1.5.1]. The same results have also been proved in a complete different manner in [49, §4.1].

To summarize, the following set of equations with unknowns $v_1^f$, $v_2^f$, $e_1^f$, $e_2^f$ and $p^f$ is solved with a standard Newton-Raphson method to enforce the equal pressure assumption

$$c_1[v_1] + c_2[v_2] = 0, \tag{1.63a}$$

$$p_1^f = p_2^f = p^f, \tag{1.63b}$$

$$[e_1] = -p^f[v_1], \tag{1.63c}$$

$$[e_2] = -p^f[v_2]. \tag{1.63d}$$

The methodology naturally extends to an arbitrary number of materials.

## 4   Numerical test cases

Our scheme is now confronted with 1D and 2D test cases. Apart from the last one, where mesh entanglement imposes the use of a remap and a equilibration procedure, all test cases are purely Lagrangian. The robustness and accuracy of our scheme is assessed, and the results are compared with that of a scheme based on the equal strain assumption.

### 4.1   Two-material shock tube

The system under consideration is that of a homogeneous mix of two perfect gases inside a piston, with same initial pressures, one having a very low volume fraction (see figure 1.3). The left border of the domain moves at velocity $\mathbf{u}_L$ which creates a shock. Because gas 2 is dominant, its evolution is almost not affected by gas 1 and results are expected to be the same for equal strain and equal pressure assumptions. As for gas 1, different closures may result in significantly different results.

If the two gases have different equations of state, their compression rate needs to be different in order to maintain pressure equilibrium after the shock. Numerical results (with 100 cells and at final time $t = 0.2$) on figure 1.4 confirm that the equal strain assumption leads to a decoupling of pressures while our scheme, based on the equal pressure assumption, does not, even without the equilibration procedure. Apart from the pressure decoupling, densities and internal energies
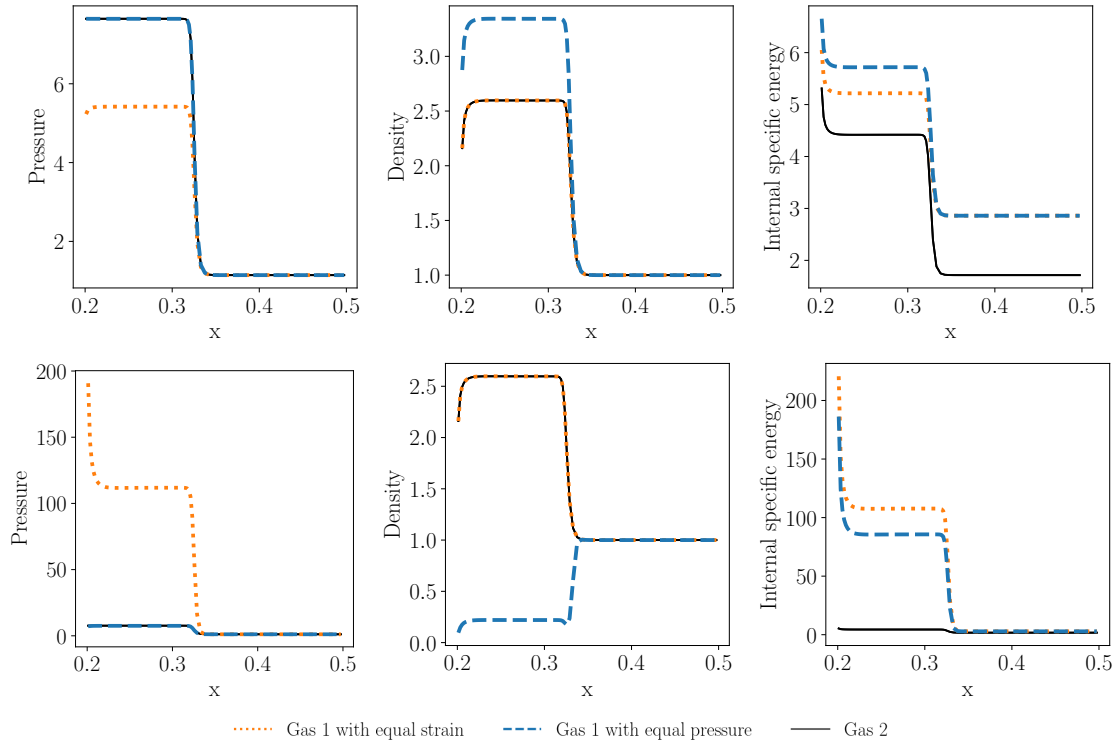
Figure 1.4: Gas 2: full black line. Gas 1: dotted orange lines for the equal strain assumption and dashed blue lines for the equal pressure one. With the equal pressure assumption, pressures are kept equal. With the equal strain assumption, densities are kept equal as the initial density and the compression rate are the same for all gases. On the first line, the entropy production is shared with respect to mass fractions while on the second line, the entropy production on gas 1 is one hundred times its mass fraction. In the second line, as gas 1 bears most of the dissipation, the resulting heating translates to an even stronger pressure decoupling for the equal strain assumption and a collapse of the density for the equal pressure one (even if the mixture is compressed, gas 1 undergoes an expansion).

are significantly different. This is of utmost importance when considering chemical reactions which may or not be triggered depending on an energy threshold. As it is physically sounder, the equal pressure assumption should provide more sensible energy and density values.

Finally, the scheme has been tested with different distribution of the entropy production. On the first line of figure 1.4, coefficient $\lambda^1$ is the mass fraction of gas 1 while on the second line it has been taken as one hundred times the same value. Qualitatively, results are substantially different for gas 1. In the second line, as it bears most of the dissipation, the resulting heating translates to an even stronger pressure decoupling for the equal strain assumption and a collapse of the density for the equal pressure one (even if the mixture is compressed, gas 1 undergoes an expansion). As surprising as it might be, the expansion is predicted from a theoretical point of view [49, §E] and is a testament to the sheer variety of admissible solutions.

## 4.2   Saurel-Abgrall shock tube

The scheme is tested on a shock tube [94] initially filled with water on the left and air on the right. The left and right states are

$$
\begin{pmatrix} \rho_L \\ u_L \\ p_L \end{pmatrix} = \begin{pmatrix} 10^3 \\ 0 \\ 10^9 \end{pmatrix} \quad \text{and} \quad \begin{pmatrix} \rho_R \\ u_R \\ p_R \end{pmatrix} = \begin{pmatrix} 50 \\ 0 \\ 10^5 \end{pmatrix}. \tag{1.64}
$$

The mesh consists of only pure cells, except at the interface where both air and water are present inside a mixed cell. Inside this cell, water volume fraction is equal to $10^{-3}$ . Water is modeled as a stiffened gas ($\gamma^w = 5/3$ and $\pi^w = 6.6 \cdot 10^8$, see [65] for more details) ; air is assumed to behave as a perfect gas with $\gamma^a = 1.4$.

Because equations of state are particularly contrasted, the equal strain assumption leads to a strong decoupling in pressures inside the mixed cell as it may be seen on figure 1.5 at time $t = 2.2 \cdot 10^{-4}$ for 100 cells and a 0.5 CFL . Water pressure skyrockets with a factor of order $10^3$. As of our scheme with equal pressure assumption, pressures stay closer to one another but not strictly equal as no pressure equilibration procedure is added. For a CFL value of 0.5, the pressure decoupling is around a hundred times smaller than with the equal strain assumption. As expected, it converges to zero as the CFL number decreases (see figure 1.6).

## 4.3   2D multi-material Taylor-Sedov blast wave

The present test is a slight adaptation of the standard 2D Sedov problem [54] to a mixture of two perfect gases ($\gamma^1 = 1.4$ and $\gamma^2 = 5/3$) with equal constant heat capacities $c_v = 1$. At the initial time, volume fractions, densities and velocities are constant across the domain. Energies are set to an almost zero value except at the center where an important energy deposit $\varepsilon_{\text{or}}$ is put. The energy deposit of gas 1 is computed so that the wave front radius is 1 at time $t = 1$. For gas 2, it is determined as to ensure equality of temperatures. All values can be found in figure 1.7.

The numerical domain used is a square $[0, 1.2]^2$ discretized with 30 cells on each direction. As the test case is a reduction of a cylindrical physical phenomenon in a 2D plane, we impose a
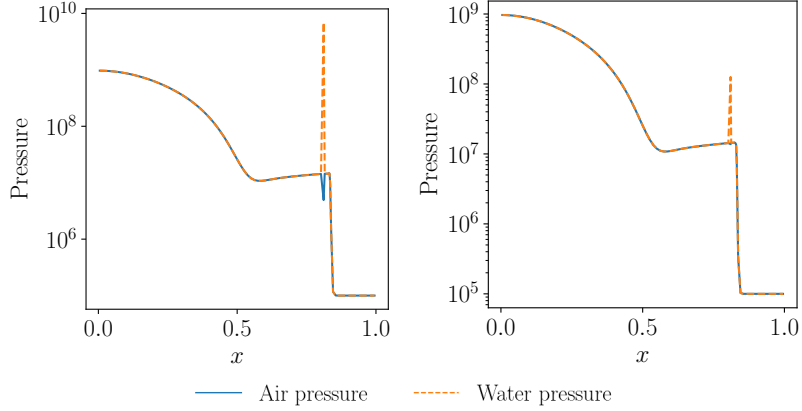
Figure 1.5: Saurel-Abgrall shock tube test results for the equal strain assumption (top) and the equal pressure one (bottom). The blue line corresponds to the air pressure while the orange dashed line corresponds to the water pressure. With the equal pressure assumption, pressures are around a hundred times closer for a large CFL value (0.5).
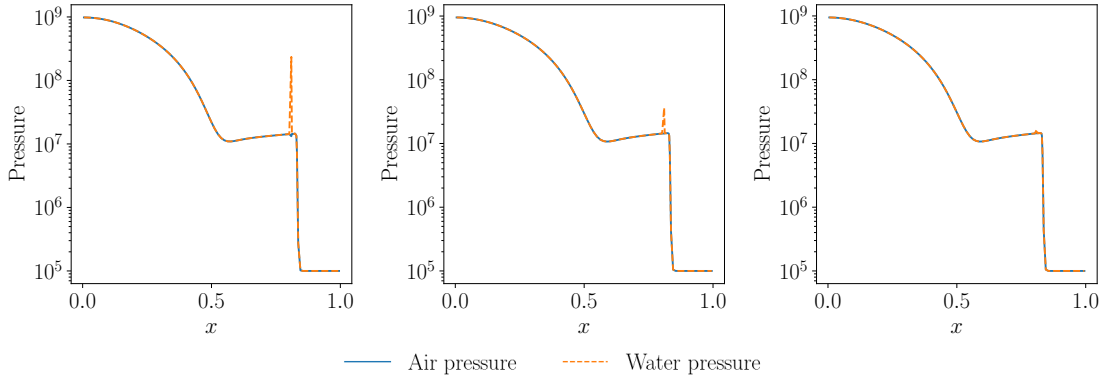


Figure 1.6: Zoom on the mixed cell for the Saurel-Abgrall shock tube test with the equal pressure assumption and different CFL. Left: CFL= 0.99; Middle: CFL= 0.1; Right: CFL= 0.01. Material pressures converge to the same value as the CFL decreases.

|        | $\gamma$ | $\alpha$      | $\rho$ | u        | $e$         | $\varepsilon_{\mathrm{or}}$ |
|--------|----------|---------------|--------|----------|-------------|------------------------------|
| Gas 1  | 1.4      | $1 - 10^{-3}$ | 1      | **0**    | $10^{-10}$  | 0.244816                     |
| Gas 2  | 5/3      | $10^{-3}$     | 1      | **0**    | $10^{-10}$  | $2.448404 \cdot 10^{-6}$     |

Figure 1.7: Initial states for the Sedov test case.

45

symmetry boundary condition on the left and on the bottom. On the right and on the top we impose a null velocity. The final time is 1.

Pressure differences are plotted on figure 1.8 for both methods and different CFL values. Aside from the central cell, the pressure decoupling is less intense for the equal pressure assumption based scheme. As for the central cell, the difference between pressures is still important, even bigger than that of the equal strain assumption scheme. This shows that if our scheme effectively deals with high contrasts of equations of state (see previous test case for example), it struggles with stiff initial conditions. This is because pressures are only kept equal up to scheme order. Hence, we believe that improving the order of the scheme would yield better results. In any case, figure 1.8 shows that decreasing the CFL makes both pressures converge to the same limit (obviously not for the equal strain assumption).

## 4.4 Shock through an air bubble

From [95, 60], a test case is considered consisting in an air bubble surrounded by water which is initially at pressure equilibrium. A shock passes through the domain. Because air and water have highly different compressibility, the bubble is expected to collapse in on itself. A pure Lagrangian approach would not work here because of mesh entanglement. As a consequence, a remap procedure is added between the Lagrangian step and the pressure equilibration procedure. The projection is performed with a Alternate Direction (AD) procedure described in [112, 32].

The air bubble coincides with the disk of center $(0.5, 0.5)$ and radius 0.4 inside the domain $[-2, 2] \times [0, 1]$. Water is modeled with a stiffened gas ($\gamma^w = 4.4$ and $\pi^w = 6.8 \cdot 10^8$, see [65] for more details); air is assumed to behave as a perfect gas with $\gamma^a = 1.4$. Air is at pressure $p^a = 10^5$ and density $\rho^a = 1$. For $x > 0.04$, water is at pressure equilibrium with air $p_R^w = p^a = 10^5$ and has density $\rho_R^w = 10^3$. In order to initiate the shock, water pressure and density are set to $p_L^w = 3.10^9$ and $\rho_L^w = 1030.9$ inside the domain $x < 0.04$. A velocity gradient is also added with $u_L = (300, 0)$ when $x < 0.04$ and $u_R = (0, 0)$ when $x > 0.04$. Numerical results with a $600 \times 300$ mesh are displayed on figure 1.9. Because of the high compressibility of air when mixed with water, the bubble shrinks until almost disappearing. Thanks to the pressure equilibration procedure, pressures are equal up to machine precision.

## 5 Conclusion

A new cell-centered Lagrangian scheme has been presented in order to deal with the equal pressure closure condition for a multi-material model. The scheme derivation is motivated by thermodynamic considerations. A particular emphasis is put on entropy production whose distribution over all material is an answer to the problem of multi-valued solutions when working with non-conservative equations. The scheme fares well when applied to test cases with high contrast of equations of state between materials. Perspectives are numerous. Improving the scheme order of accuracy could improve pressure equality without having to rely on low CFL numbers or pressure equilibration procedures. It would also reduce errors by helping capture more accurately solutions. Finally, an extension of this scheme to a multivelocity model is currently being investigated.
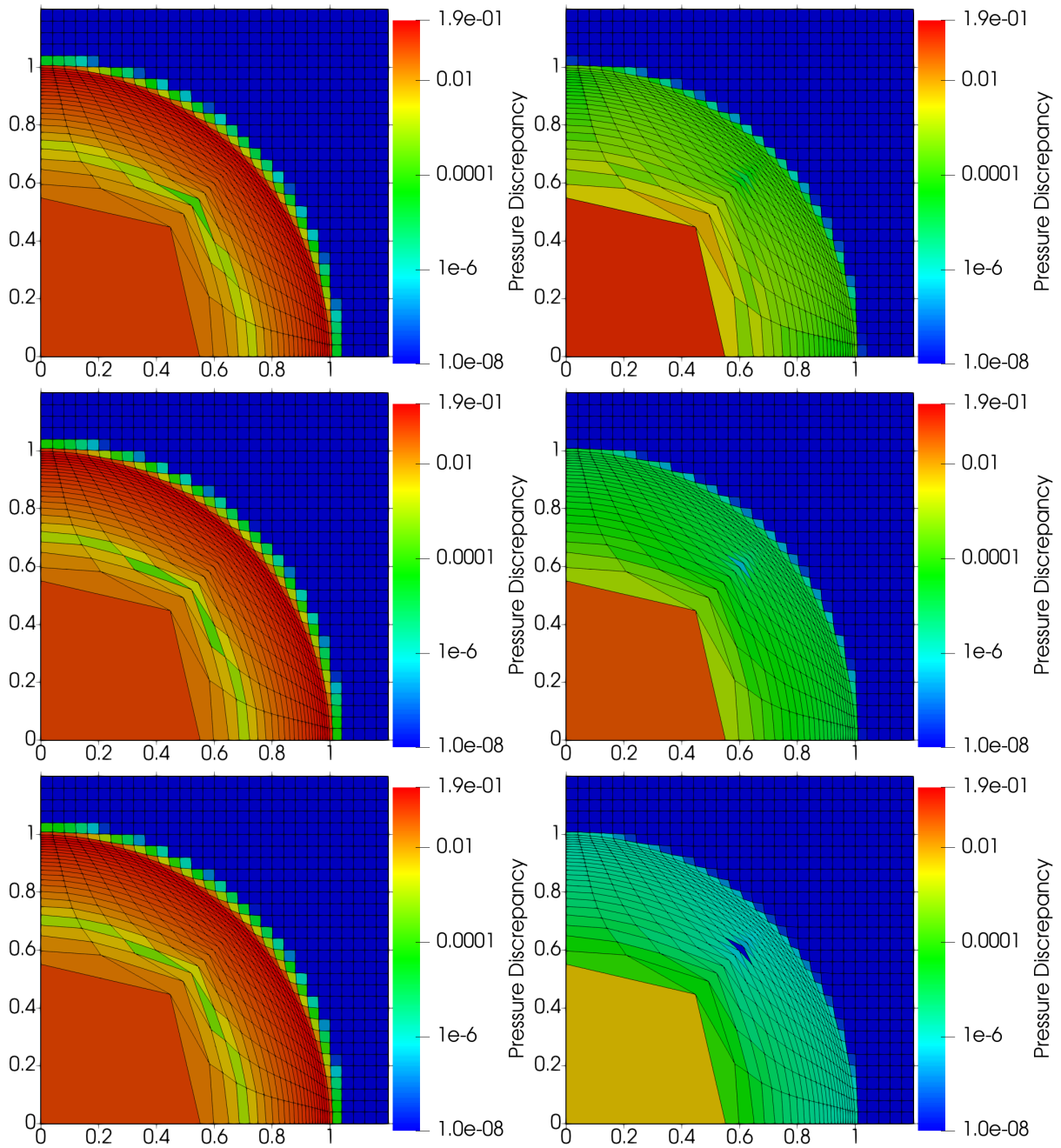
Figure 1.8: Pressure differences for different CFL values. Left: equal strain assumption ; Right: equal pressure assumption. Top: CFL = 0.4 ; Middle: CFL = 0.04 ; Bottom: CFL = 0.004. The equal pressure assumption ensures the equality of pressure between materials everywhere but inside the central cell because of the stiffness of initial conditions. Low CFL numbers help correct this problem.
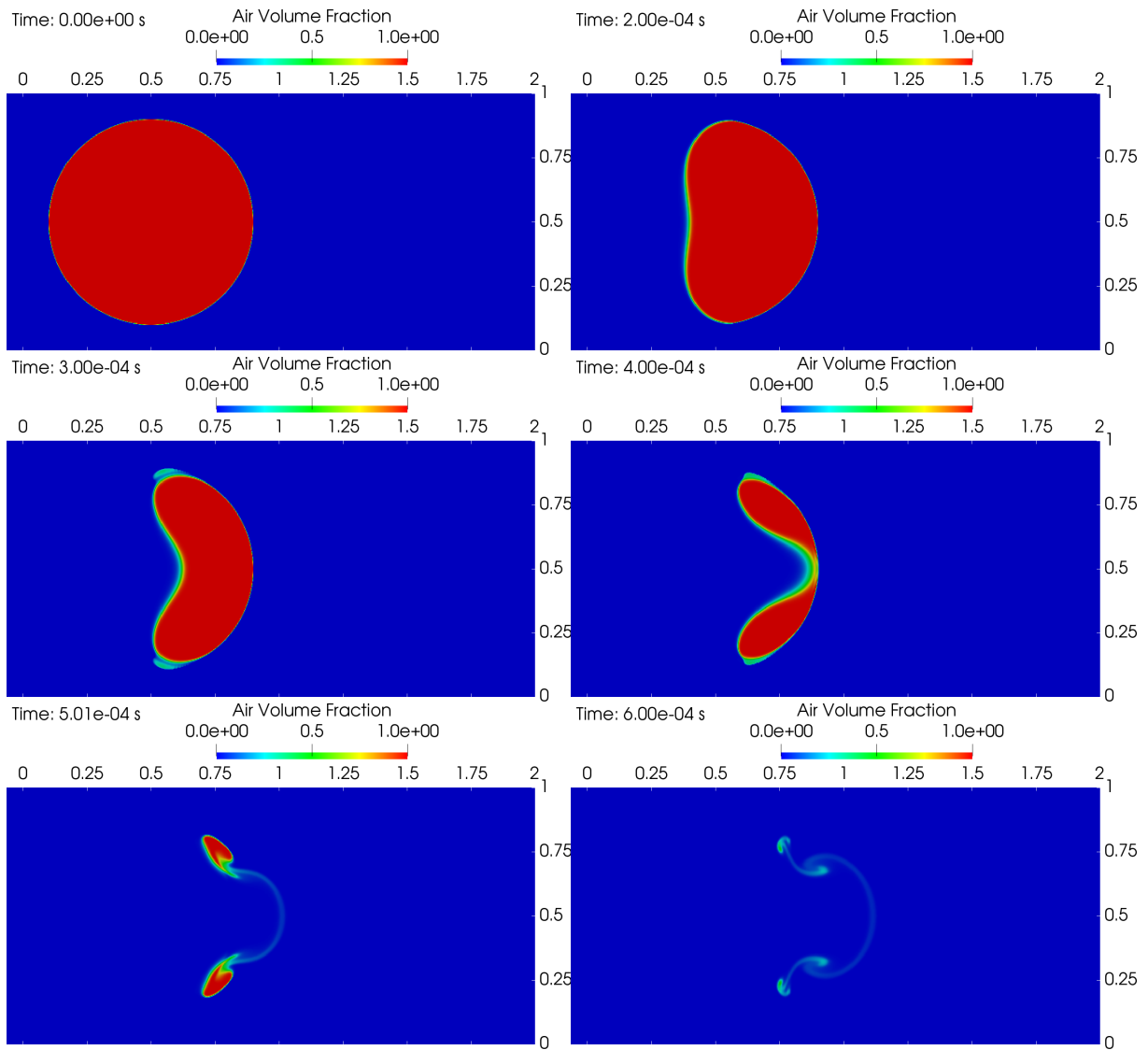
Figure 1.9: Air volume fraction for the air bubble test case at different times. The Lagrangian phase is robust with respect to the contrast between equations of state. The Remap procedure, together with the pressure equilibration, is necessary in order to deal with mesh entanglement.

# Chapter 2

# A simple diffuse interface strategy for multi-material diffusion and application to three-temperature multi-material hydrodynamics

## Contents

# 1 Introduction

## 1.1 Three temperature multi-material hydrodynamics

In applications such as inertial confinement fusion or astrophysics, ions and electrons are not at thermal equilibrium. The plasma cannot be characterized with a single constitutive law rendering necessary a separate temperature for ions and electrons [26]. In the presence of a strong radiation field, photons also need their own description which is here given by the grey diffusion approximation, relevant in the optically thick limit and assuming radiation thermalization [22]. The resulting three different temperatures are coupled through collision and opacity. These couplings can be arbitrarily stiff and the single-temperature Euler-Lagrange equations are recovered in the case of instantaneous relaxation. Besides, radiation transport accounts for the propagation of photons throughout the domain and can also display a stiff behavior. Diffusion on the ionic and electronic energies also exist but are marginal for the applications of interest.

The physical description can be supplemented with an additional multi-material layer. Multi-material aspects are essential to properly describe complex mixtures with contrasted physical characteristics (e.g. mixtures of gases and solids). The most common approach to derive multi-material equations is that of conditional averaging procedures [52, 113]. It produces averaged quantities describing the behavior of the flow, as well as additional correlation terms which encapsulate the remaining details. These correlation terms are often neglected as a first approximation as they are deemed minor, at least outside of shocks. If this approach has proven its efficiency in describing single-temperature multi-material flows, its application to radiation transport is not trivial. Indeed, averaged fluxes only express radiation transport separately within each material while the associated correlation term deals with the coupling between different materials. While radiation transport in between materials is essential for weakly opaque mixtures of materials, its expression remains unclear and heavily mixture-dependant. Alternatively, if it is neglected as a first approximation, then different materials are no longer coupled through temperatures, thus leading to questionable results.

## 1.2 Numerical strategy

### Multi-material radiation transport or diffusion

The discretization of the multi-material radiation transport consists in one of the main contribution of this chapter. As explained above, its expression at the continuous level is a difficult task. Still, its discretization is possible and different strategies exist in the literature. Interface reconstruction techniques [83, 36, 24] estimate the interface between materials inside mixed cells. Mixed cells are then separated into pure cells and the diffusion operator is discretized with any single material strategy. At their best, these techniques allow for an accurate description of the mixture. However, complex topology of the flow require *ad hoc* strategies [47] and interface reconstruction fails at describing dispersed phases. The treatment of three or more materials is usually not invariant under permutation of materials and depends on an arbitrary order [59]. Finally, the computational cost, especially in three dimensions, can be significant. Alternatively, homogenization methods [23] assume that mixture of different materials act as a

single equivalent material. Such methods are inexpensive but are usually not considered reliable [58, 23]. Apart from obvious accuracy issues on the fluxes, homogenization methods are built on the assumption that all materials share the same temperature inside a given cell. Such hypothesis is not relevant for mixtures of materials with contrasted opacity or for applications where relaxation of temperatures cannot be considered instantaneous.

Here is presented the so-called Discrete Equation Method (DEM) based on the ideas independently developed in [3, 17, 14] and latter used in numerous works including but not limited to [7, 87]. Instead of being dealt with as a local source term and approximated through interface reconstruction or instantaneous equalization, diffusion between materials takes place at each face, just like diffusion of a single material. This effectively bypasses the averaging procedure. The method remains both conceptually and computationally simple while test cases establish significant accuracy improvements over homogenization methods.

### Multi-material hydrodynamics

The numerical strategy for the hydrodynamic part is based on the single material, single temperature GLACE/EUCCLHYD scheme [11, 71]. The scheme is Lagrangian and can be integrated into an Arbitrary-Lagrange-Euler (ALE) setting [50, 35]. It will here be coupled with an Alternate Direction (AD) procedure [112, 32], chosen for both its performance and simplicity.

Generally speaking, two main difficulties arise when starting from a single temperature and single material scheme and extending it to a three-temperature multi-material one. First, an evolution equation must be added for the material volumes. Here, the equal strain assumption is made and consists in saying that volume fractions stay constant during the Lagrangian phase [9]. This closure is chosen for simplicity although it may become irrelevant for mixture of materials with contrasted equations of state [49, 74] (e.g. air and water). Second, first order models with several temperatures or several materials (and *a fortiori* with both) are not sufficient to characterize shocks. Indeed, only partial jump relationships (on individual masses, total momentum, total energy) exist and shocks are eventually small-scale dependant. The detail of the entropy production (which summarizes the contribution of the aforementioned correlation terms) is then necessary to fully describe shocks both at the continuous and at the discrete level.

### Time integration of diffusion and relaxation processes

A three-temperature model allows the description of systems which are not at thermal equilibrium. Although diffusion and relaxation processes are not instantaneous, they are usually stiff and require an implicit time integration in order to keep decent time steps. Because of the non-linearity, iterative methods are usually considered. However, enforcing positivity of temperatures both at convergence and during the different iterations is not trivial and failing to do so can abruptly stop the computation.

The method considered here is a multi-material extension of [19]. The hydrodynamics, the radiation transport and the source terms are all treated at the same time without any splitting. As pointed out in [18], doing so allows to better capture the coupling between the different terms in radiation shocks where temperatures and densities experience large variations over few numerical cells. Contrary to some approaches in the literature [18, 98], radiation transport

and source terms are here fully implicited (i.e. the implication concerns the global terms and not only the temperatures or energies). This choice arguably offers better robustness with respect to sudden changes in the constitutive laws of collision frequencies, opacities and diffusion coefficients; the effects of similar changes on the pressure were studied in [49] where they were refered to as "stiff stiffness". The system resulting from the full time implication is however all the more non-linear and harder to solve numerically. The present strategy is based on convex combinations and ensures that temperatures all stay positive during the iterative procedure.

## 2 Three-temperature multi-material equations

### 2.1 Three-temperature single-material equations

The notations are standard with $\rho$ the density, $\mathbf{u}$ the velocity, $e_i$ and $e_e$ the specific ionic and electronic internal energies, and $e_r$ the volumetric radiation energy. Additionally, ions and electrons are described with an equation of state $e_\theta(1/\rho, s_\theta)$, $\theta \in \{i, e\}$ where $s_\theta$ is the species entropy. Pressures and temperatures are then defined by Gibbs relationship

$$\mathrm{d}e_\theta = -p_\theta \mathrm{d}\left(\frac{1}{\rho}\right) + T_\theta \mathrm{d}s_\theta. \tag{2.1}$$

Positivity of temperature and density allows to express all quantities as functions of the density $\rho$ and the internal energy $e_\theta$ [78]. Likewise, photons have their own pressure, temperature and entropy, defined by

$$p_r = \frac{e_r}{3}, \tag{2.2a}$$

$$e_r = aT_r^4, \tag{2.2b}$$

$$\mathrm{d}\left(\frac{e_r}{\rho}\right) = -p_r \mathrm{d}\left(\frac{1}{\rho}\right) + T_r \mathrm{d}s_r, \tag{2.2c}$$

where $a$ is the radiation constant. The three-temperature equations [19] are here written in the Lagrangian formalism which factorizes transport into time derivatives. It lays the foundations for the "Lagrange + Remap" approach used in section 4.

$$\rho\frac{\mathrm{d}}{\mathrm{d}t}\left(\frac{1}{\rho}\right) = \nabla \cdot \mathbf{u}, \tag{2.3a}$$

$$\rho\frac{\mathrm{d}}{\mathrm{d}t}\mathbf{u} = -\nabla p, \tag{2.3b}$$

$$\rho\frac{\mathrm{d}}{\mathrm{d}t}e_i = -\rho p_i \frac{\mathrm{d}}{\mathrm{d}t}\left(\frac{1}{\rho}\right) + c\kappa\left(T_e - T_i\right), \tag{2.3c}$$

$$\rho\frac{\mathrm{d}}{\mathrm{d}t}e_e = -\rho p_e \frac{\mathrm{d}}{\mathrm{d}t}\left(\frac{1}{\rho}\right) + c\kappa\left(T_i - T_e\right) + c\sigma_P\left(aT_r^4 - aT_e^4\right), \tag{2.3d}$$

$$\rho\frac{\mathrm{d}}{\mathrm{d}t}\left(\frac{e_r}{\rho}\right) = -\rho p_r \frac{\mathrm{d}}{\mathrm{d}t}\left(\frac{1}{\rho}\right) - \nabla \cdot \mathbf{F}_r + c\sigma_P\left(aT_e^4 - aT_r^4\right). \tag{2.3e}$$

The different temperatures are coupled through relaxation terms driving the system toward local thermal equilibrium $T_e = T_i = T_r$. The coupling between ions and electrons is given by a

relaxation coefficient $\kappa$, while the coupling between electrons and photons is given by Planck's opacity $\sigma_P$. Both coefficients are functions of the different temperatures. $c$ is the speed of light. The radiation flux $\mathbf{F}_r$ couples spatially photon temperatures from one place to another, thus driving the system towards an homogenization state $\nabla T_r = 0$. It is here expressed accordingly to the Rosseland diffusion approximation [22]

$$\mathbf{F}_r = -\frac{c}{3\sigma_R}\nabla e_r \tag{2.4}$$

where the Rosseland opacity $\sigma_R$ is a function of the electronic temperature $T_e$. Physically, ionic and electronic transport should also be considered but they are usually weaker [] and here completely neglected. Thanks to these terms (namely relaxation terms and radiation transport), thermal equilibrium is not instantaneous but may still be stiff. Equations (2.3c),(2.3d), (2.3e) are deliberately written in a consistent manner with (2.1), (2.2c) so that it becomes obvious that the entropy production is given by the relaxation terms and the diffusion

$$\rho\frac{\mathrm{d}}{\mathrm{d}t}\left(s_i + s_e + s_r\right) = -\nabla\cdot\left(\frac{\mathbf{F}_r}{T_r}\right) + \frac{4acT_r}{3\sigma_R}\|\nabla T_r\|^2$$
$$+ c\kappa\frac{(T_i - T_e)^2}{T_i T_e} + ca\sigma_P\frac{(T_e - T_r)(T_e^4 - T_r^4)}{T_e T_r}. \tag{2.5}$$

Every term in the right hand side is either positive or a flux thus complying with the second principle of thermodynamics. Finally, the total pressure is $p = p_i + p_e + p_r$ and conservation of total energy is then given by

$$\rho\frac{\mathrm{d}}{\mathrm{d}t}\left(\frac{\|\mathbf{u}\|^2}{2} + e_i + e_e + \frac{e_r}{\rho}\right) = -\nabla\cdot\left(p\mathbf{u} + \mathbf{F}_r\right). \tag{2.6}$$

## 2.2 Multi-material aspects

An arbitrary number of material is now considered. The general methodology to derive multi-material equations is based on a conditional averaging procedure introduced in [52] and summarized in [113] for non-miscible materials and in [49, §B] for general mixtures. The averaging may be spatial, temporal or statistical. In all cases, averaged quantities and averaged fluxes are defined for all materials but some residuals (or correlation terms) remain unspecified and are often neglected as a first approximation. Additionally, the model can be subsequently simplified if materials are assumed to be at local velocity, pressure or temperature equilibrium. Such hypothesis depend on the characteristic times of observation. For the applications aimed at in this paper, thermal equilibrium cannot be reasonably assumed while pressure and velocity equilibrium are sensible approximations [55]. Eventually, the three-temperature single-velocity

multi-material equations read

$$\alpha^k \rho^k \frac{\mathrm{d}}{\mathrm{d}t}\left(\frac{1}{\alpha^k \rho^k}\right) = \nabla \cdot \mathbf{u}, \tag{2.7a}$$

$$\rho \frac{\mathrm{d}}{\mathrm{d}t}\mathbf{u} = -\nabla p, \tag{2.7b}$$

$$\alpha^k \rho^k \frac{\mathrm{d}}{\mathrm{d}t}e_i^k = -\alpha^k \rho^k p_i^k \frac{\mathrm{d}}{\mathrm{d}t}\left(\frac{1}{\rho^k}\right) + \alpha^k c\kappa^k \left(T_e^k - T_i^k\right), \tag{2.7c}$$

$$\alpha^k \rho^k \frac{\mathrm{d}}{\mathrm{d}t}e_e^k = -\alpha^k \rho^k p_e^k \frac{\mathrm{d}}{\mathrm{d}t}\left(\frac{1}{\rho^k}\right) + \alpha^k c\kappa^k \left(T_i^k - T_e^k\right) + \alpha^k c\sigma_P^k \left(e_r^k - a(T_e^k)^4\right), \tag{2.7d}$$

$$\alpha^k \rho^k \frac{\mathrm{d}}{\mathrm{d}t}\left(\frac{e_r^k}{\alpha^k \rho^k}\right) = -\alpha^k \rho^k p_r^k \frac{\mathrm{d}}{\mathrm{d}t}\left(\frac{1}{\rho^k}\right) - \nabla \cdot \left(\alpha^k \mathbf{F}_r^k\right) + \alpha^k c\sigma_P^k \left(a(T_e^k)^4 - E_r^k\right). \tag{2.7e}$$

The indices $k$ refer to the averaged quantities related to material $k$. $\alpha^k$ is the volume fraction of material $k$ while $\rho$ is the total density

$$\rho = \sum_k \alpha^k \rho^k. \tag{2.8}$$

Although the averaging process alleviates the treatment of interfaces, certain details of the flow are lost and, as such, model (2.7) is underdetermined. Closures need to be provided.

- The first one concerns the evolution of either densities, volume fractions or pressures and ensures that the number of equations equals the number of unknowns. In keeping with the previous considerations on pressure equilibrium, a sound closure would consists in the equality of material pressures. The numerical treatment of pressure equalization is challenging in the context of a three-temperature multi-material model with stiff source terms. It is here left out in favor of the simpler equal strain assumption

$$\alpha^k \rho^k \frac{\mathrm{d}}{\mathrm{d}t}\left(\frac{1}{\rho^k}\right) = \alpha^k \nabla \cdot \mathbf{u} \iff \frac{\mathrm{d}}{\mathrm{d}t}\alpha^k = 0. \tag{2.9}$$

This approximation is physically questionable when dealing with highly contrasted mixtures. A discussion on these two closures is performed in [74]. The total pressure then needs to be

$$p = \sum_k \alpha^k (p_i^k + p_e^k + p_r^k). \tag{2.10}$$

so as to ensure total energy conservation. The resulting first order system (without diffusion or source terms) is hyperbolic with eigenvalues $-c + u, u, c + u$ where $c$ is the speed of sound of the mixture

$$\rho c^2 = \sum_k \alpha^k \rho^k \left(\left.\frac{\partial p_i^k}{\partial \rho}\right|_{s_i^k} + \left.\frac{\partial p_e^k}{\partial \rho}\right|_{s_e^k} + \left.\frac{\partial p_s^k}{\partial \rho}\right|_{s_s^k}\right). \tag{2.11}$$

- Even with the right amount of equations, the behavior of the mixture is still not defined inside shocks. Indeed, multi-temperature multi-material shocks are small-scale dependent which means that no complete jump relationships can be written without knowing the details of what is happening inside the shock [55]. Mathematically, this failure comes from

the presence of non-conservative products which prevents any canonical weak formulation from being written [77]. In practice, entropy production on each material and on each species (i.e. ions, electrons and photons) encapsulates the details of the small-scale effects and entirely determines the a shock.

- The averaged radiation flux $\nabla \cdot (\alpha^k \mathbf{F}_r^k)$ only describes parallel diffusion for each material separately. The physically necessary coupling between materials is actually hidden in the correlation terms previously neglected. Such correlation terms could be modelled as local source terms coupling temperatures of different materials but their expression would be heavily mixture dependant. One of the main contribution of the present chapter concerns the discretization of the multi-material radiation transport and is discussed in section 3.

Concerning the entropy production of the multi-material model, an inequality similar to (2.5) can be derived. However, the expression of the radiation transport in (2.7e) will not be discretized as it is. It will be seen that the chosen approach also leads to an entropy inequality at the discrete level as well as total energy conservation.

# 3  Numerical strategies for the multi-material heat equation

In this section, the full three-temperature picture is reduced in order to focus only on the multi-material aspects of the radiation transport. The prototype is the so-called heat equation

$$\partial_t T = \nabla \cdot (\kappa \nabla T). \tag{2.12}$$

The thermal conductivity $\kappa$ is assumed to depend on the temperature $T$ and the space coordinate $x$. The space dependence reflects the multi-material aspects as $\kappa$ may experience discontinuities in the vicinity of the interfaces between different materials. In the following, two methods (namely the homogenization method and the DEM) are presented for the numerical approximation of (2.12) in the context of mixed cells, i.e. cells containing more than one material and thus as many temperatures and thermal conductivities.

## 3.1  Homogenization methods: principles and limits

In the case of the so-called homogenization methods [23], mixed cells are assumed to contain a fictive single material. It is described by only one temperature $\overline{T}_c$ and one thermal conductivity $\overline{\kappa}_c$ which is an average of the thermal conductivities of the real materials, weighted by their volume fractions.

$$\overline{\kappa}_c = \phi^{-1} \left( \sum_k \alpha_c^k \phi \left( \kappa_c^k \right) \right). \tag{2.13}$$

The mean is arithmetic for $\phi(x) = x$ and harmonic for $\phi(x) = \frac{1}{x}$. Other choices are possible as long as $\phi$ is strictly monotonic and positive, but they will not be considered in the following. The flux between cells $c$ and $d$ is then written

$$\overline{\mathbf{F}}_{cd} = \overline{\kappa}_c \frac{\overline{T}_{cd} - \overline{T}_c}{h_{cd}} S_{cd}, \tag{2.14}$$

where $\overline{T}_{cd}$ is the temperature at the interface between cells $c$ and $d$. $h_{cd}$ and $S_{cd}$ are respectively the distance between the center of $\omega_c$ and the interface, and the surface of the interface.

**Remark 1.** Continuity of the temperature at the interface implies $T_{cd} = T_{dc}$. Likewise, geometrical considerations simply leads to $S_{cd} = S_{dc}$. Finally, $h_{cd}$ obeys to no particular symmetry.

Homogenization methods may induce accuracy issues. Indeed, allowing only one temperature inside each cell is a strong approximation which does not account for mixtures with highly contrasted thermal conductivity [58] (or opacity for radiation transport). Because diffusion has a regularizing effect, temperatures are theoretically continuous across interfaces between different materials. However, steep temperature gradients may exist so that temperatures cannot be numerically considered constant inside cells close to these interfaces.

These accuracy issues have cascading effects in the context of three-temperature hydrodynamics. For a given material, electronic, ionic and photon temperatures are coupled through relaxation terms. These couplings are stiff and may occur on characteristic times smaller than those of diffusion for opaque materials. Equality of photon temperatures does not comply with this hierarchy and indirectly produces a non-physical coupling between ionic and electronic temperatures of different materials. This is critical when considering chemical or nuclear reactions depending on temperature thresholds. They may be spuriously triggered or turned off leading to physically questionable results.

## 3.2 DEM-based discretization

The present strategy follows the idea in [14, 17, 3]. Instead of discretizing the averaged equations, the single material equations are first implicitly discretized before being averaged at the discrete level. Fluxes between materials now take place at the interface between cells instead of only being dealt with as local source terms. The method is here described as implicitly resulting from an interface reconstruction where the different geometrical quantities are estimated inexpensively without sacrificing too much accuracy. An interface reconstruction implies that the averaging procedure is spatial as it is explained in [17] with the so-called stratified flow model. Probabilistic averaging can also be taken as it is done in [3]. All averaging share the same algebraic properties so that the different approaches result in *formally* equivalent schemes.

**Generic formulation**

Considering a mixed cell $c$ and assuming that the position of each material is known (with an interface reconstruction technique for example), the heat equation may be integrated on each material sub-volume $\omega_c^k$ leading to

$$\int_{\omega_c^k} \partial_t T \, dv = \int_{\partial \omega_c^k} (\kappa \nabla T) \cdot \mathbf{n} \, ds. \tag{2.15}$$

Then dividing the surface $\partial \omega_c^k$ into sub-surfaces $\partial \omega_{cd}^{kl}$ where material $k$ of cell $c$ is in contact with material $l$ of cell $d$ (it is not excluded that $c = d$), equation (2.15) becomes

$$\int_{\omega_c^k} \partial_t T \, dv = \sum_{l,d} \int_{\partial \omega_{cd}^{kl}} (\kappa \nabla T) \cdot \mathbf{n} \, ds = \sum_{l,d} \mathrm{F}_{cd}^{kl}. \tag{2.16}$$
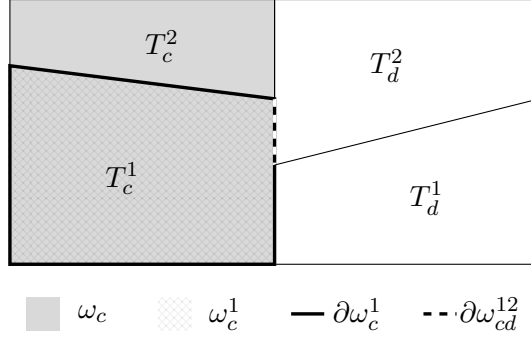
Figure 2.1: Example of two adjacent mixed cells and the corresponding notations for the geometry. The volume $\omega_c$ contains the sub-volume $\omega_c^1$. Likewise, the surface $\partial \omega_{cd}^{12}$ is includes inside the surface $\partial_c^1$.
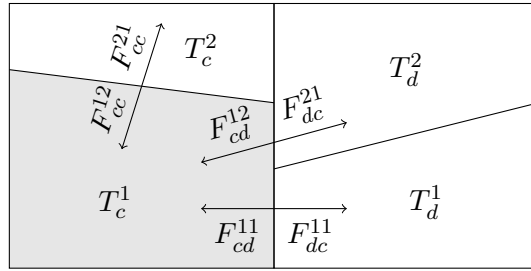


Figure 2.2: Same configuration as in figure 2.1 with the fluxes.

The sum may be taken over all materials and over all cells by arbitrarily defining $F_{cd}^{kl} = 0$ when both materials or cells are not in contact. A generic expression of these fluxes is the following

$$\mathrm{F}_{cd}^{kl} = \kappa_c^k \frac{T_{cd}^{kl} - T_c^k}{h_{cd}^{kl}} S_{cd}^{kl}, \tag{2.17}$$

where the notations are similar to that of the homogenization case, except they now depend on a pair of materials.

- $h_{cd}^{kl}$ is the distance between the center of the sub-cell $\omega_c^k$ and the interface between material $k$ of cell $c$ and material $l$ of cell $d$.

- $T_{cd}^{kl}$ is the temperature at the interface between the two materials.

- $S_{cd}^{kl}$ is the area of the interface between the two materials. It is set as a portion $\delta_{cd}^{kl}$ of the entire surface $S_{cd}$ between the two cells $S_{cd}^{kl} = \delta_{cd}^{kl} S_{cd}$.

**Remark 2.** Symmetries detailed in remark 1 are still valid (namely $T_{cd}^{kl} = T_{dc}^{lk}$ and $S_{cd}^{kl} = S_{dc}^{lk}$). They hold because both terms involve the same pair of materials. On the other hand, there is no reason for $T_{cd}^{kl}$ to be equal to $T_{cd}^{lk}$ or $T_{dc}^{kl}$ (and likewise for $S$).

Here, no information concerning the geometry of the mixed cell is assumed. In particular, the position of each material inside the cell and their surface of contact at each interfaces with neighbor cells is not known. Nevertheless, an approximation of $\mathrm{F}_{cd}^{kl}$ is still possible. Fluxes

Figure 2.3: Examples of the $\lambda_0$ (left), $\lambda_{\max}$ (center) and $\lambda_{\min}$ (right) cases for given surface fractions. On each scheme, the center line corresponds to the interface. As an example, the proportion $\delta_{cd}^{12}$ is the ratio of the surface shared by rectangles $T_c^1$ and $T_d^2$ on the total surface of the interface (i.e. $\frac{1}{6}$ for $\lambda_0$, 0 for $\lambda_{\max}$ and $\frac{1}{3}$ for $\lambda_{\min}$).
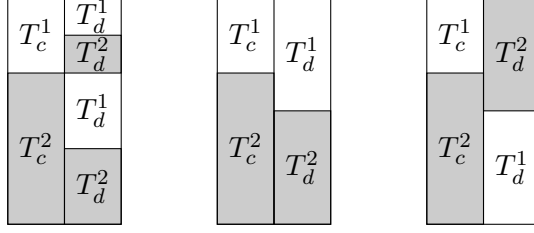
between different cells (i.e. $c \neq d$) are treated similarly to [14, 17, 3]. The method is described in the next section 3.2. Internal fluxes (i.e. $c = d$) are discussed in section 3.2.

**Computations of the geometry**

The distances $h_{cd}^{kl}$ are taken as the distance between the center of the cell $\omega_c$ and the face between cells $c$ and $d$. It does not depend on materials $k$ and $l$ and consists in a neutral standing point as, again, the location of each material inside the cell remains unknown.

Regarding proportions $\delta_{cd}^{kl}$, the strategy retained is that of [3, 17, 14]. $\delta_{cd}^k$ denotes the total surface fraction of material $k$ at the interface between cells $c$ and $d$. The surface fraction may be discontinuous so that $\delta_{cd}^k \neq \delta_{dc}^k$. Parameters $\delta_{cd}^{kl}$ are then constrained by

$$\sum_l \delta_{cd}^{kl} = \delta_{cd}^k, \quad \forall k \tag{2.18a}$$

$$\sum_k \delta_{cd}^{kl} = \delta_{dc}^l, \quad \forall l. \tag{2.18b}$$

Without any information on the location of each material inside the cell, these surface fractions can be reasonably approximated by the volume fraction of the associated cell $\delta_{cd}^k = \alpha_c^k$. For the sake of readability, the following analysis of system (2.18) is restricted to the case of two materials 1 and 2. The case of an arbitrary number of materials is discussed in B.

$$\delta_{cd}^{11} + \delta_{cd}^{12} = \alpha_c^1, \tag{2.19a}$$

$$\delta_{cd}^{21} + \delta_{cd}^{22} = \alpha_c^2, \tag{2.19b}$$

$$\delta_{cd}^{11} + \delta_{cd}^{21} = \alpha_d^1, \tag{2.19c}$$

$$\delta_{cd}^{12} + \delta_{cd}^{22} = \alpha_d^2. \tag{2.19d}$$

System (2.19) consists in four equations and four unknowns. It is not invertible as the last equation is redundant and can be deduced from the other 3. A general solution is then of the

form

$$\delta_{cd}^{11} = \alpha_c^1 \alpha_d^1 + \lambda, \tag{2.20a}$$

$$\delta_{cd}^{12} = \alpha_c^1 \alpha_d^2 - \lambda, \tag{2.20b}$$

$$\delta_{cd}^{21} = \alpha_c^2 \alpha_d^1 - \lambda, \tag{2.20c}$$

$$\delta_{cd}^{22} = \alpha_c^2 \alpha_d^2 + \lambda, \tag{2.20d}$$

where $\lambda$ is a real-valued degree of freedom. Because surface fractions need to stay in $[0, 1]$, $\lambda$ is bounded

$$-\min(\alpha_c^1 \alpha_d^1, \alpha_c^2 \alpha_d^2) \le \lambda \le \min(\alpha_c^1 \alpha_d^2, \alpha_c^2 \alpha_d^1). \tag{2.21}$$

In this continuum, three cases (displayed in figure 2.3) are retained for the rest of the chapter

- $\lambda = 0$ which adds no *a priori* with the way materials interact with each other. This choice was already explored in [14]. It will be referred to as $\lambda_0$ in the following.

- $\lambda = \min(\alpha_c^1 \alpha_d^2, \alpha_c^2 \alpha_d^1)$ for which interactions between the same material are preferred. This corresponds to the stratified flow model detailed in [17]. In [3], it is associated to separate phase flows. It will be referred to as $\lambda_{\max}$.

- $\lambda = -\min(\alpha_c^1 \alpha_d^1, \alpha_c^2 \alpha_d^2)$ which maximizes the surface between pairs of different materials. In [3], it is associated to dispersed flows. It will be referred to as $\lambda_{\min}$.

**Remark 3.** Estimations of distances $h_{cd}^{kl}$ or surface fractions $\delta_{cd}^k$ can be honed using additional information provided by estimations of volume fraction gradients as it is done for the computation of internal fluxes in C. This is the usual starting point of an interface reconstruction [83] although it is possible to extract the information of interest while bypassing the bulk of the procedure. Hence, greater accuracy could be achieved without a significant increase in computation time. As a simple example, surface fractions can be estimated with a linear reconstruction of volume fractions. The reconstruction must be limited (e.g. with a minmod limiter []).

**Internal flux**

For two materials and two dimensions, a formulation of the internal flux is suggested in C. The interface is assumed linear. Under this assumption, its surface and the length between the two centers of mass are *exactly* computed as a function of the volume fraction and its angle (i.e. the direction of the gradient of volume fractions). This serves as an illustration on how volume fractions and their derivatives can be used to estimate quantities without resorting to an explicit interface reconstruction. Still, this formulation is not relevant for dispersed phases and does not extend easily to more materials and three dimensions. These issues were already discussed earlier and were the reason why discretizing the averaged model was first excluded.

In the previous installments of the DEM ideas no internal term is considered. In [14], $\lambda_0$ is used and materials always interact at the interface (as long they all have non zero volume fractions) so the lack of internal flux is not damageable. In [17], $\lambda_{\max}$ is used for pressure forces and, loosely speaking, materials do not interact at an interface if the field of volume fractions
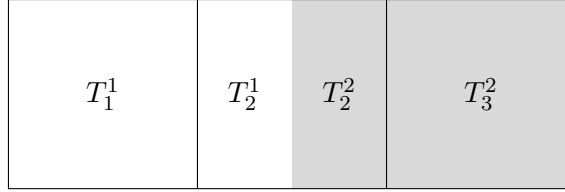
Figure 2.4: With an anti-diffusive high order technique, the estimation of the volume fraction $\delta_{23}^2$ can reach 1 so that the flux between cell 2 and cell 3 concerns material 2. Symmetrically, the volume fraction $\delta_{21}^1$ is also 1 so that the flux between cell 1 and cell 2 concerns material 1. Then, both materials do not interact at all with each other.

is constant. It is not an issue as the correlation term $p\nabla\alpha^k$ is precisely zero in this case; it is a one-pressure model, so pressure equilibrium is already reached inside each cell.

In the present case, the choice $\lambda_{\max}$ may be desirable for accurately capturing dispersed phases. However, if volume fractions are constant across the whole domain, both materials do not interact at all with each other. Contrary to [17], it seriously endangers the results as this is not a one-temperature model and materials do need to exchange heat. In a sense, the choice $\lambda_{\max}$ ends up having the same issues as a direct discretization of the averaged equation with the remaining uncertainty on the internal flux. Other choices do not suffer from the same problem and might consist in "milder" options.

**Remark 4.** Even with $\lambda_0$ or $\lambda_{\min}$, internal flux may still be needed. Indeed, if surface fractions are estimated with a strongly anti-diffusive limiter (as explained in remark 3), they can be 0 or 1 even if the cell volume fraction is not (see figure 2.4). In this case, all choices of $\lambda$ are equivalent and materials do not interact with each other. Hence, both $\lambda_{\max}$ and high order reconstruction techniques are not compatible with the omission of an internal flux.

## 3.3 Conservation and practical computations of the fluxes

Up until now, every fluxes have been expressed in terms of surface temperatures which are yet to be specified. Conservation of the scheme heavily constrains surface temperatures although some leeway exists for the DEM.

**The case of homogenization methods**

For homogenization methods, only one temperature is considered for each cell and each face. Continuity of the flux holds at the interface between two materials

$$\overline{\mathrm{F}}_{cd} = -\overline{\mathrm{F}}_{dc}. \tag{2.22}$$

(2.22) also immediately guarantees that the scheme is conservative. Solving for $\overline{T}_{cd} = \overline{T}_{dc}$ in equation (2.22) eventually yields

$$\overline{F}_{cd} = \overline{\kappa}_{cd} \frac{\overline{T}_d - \overline{T}_c}{h_{cd} + h_{dc}} S_{cd}, \tag{2.23a}$$

$$\overline{T}_{cd} = \left( \frac{\overline{\kappa}_c}{h_{cd}} \overline{T}_c + \frac{\overline{\kappa}_d}{h_{dc}} \overline{T}_d \right) \Big/ \left( \frac{\overline{\kappa}_c}{h_{cd}} + \frac{\overline{\kappa}_d}{h_{dc}} \right), \tag{2.23b}$$

$$\overline{\kappa}_{cd} = (h_{cd} + h_{dc}) \Big/ \left( \frac{h_{cd}}{\overline{\kappa}_c} + \frac{h_{dc}}{\overline{\kappa}_d} \right). \tag{2.23c}$$

**The case of the discrete equation method**

In the case of DEM, two approaches may be distinguished. First, as in [58], only one temperature is allowed on each face. Consequently, only one equation is needed to fully define the scheme. A global conservation is chosen

$$\sum_k F_{cd}^{kl} = - \sum_l F_{dc}^{lk}. \tag{2.24}$$

Alternatively, one may consider as many temperatures as there are couples of materials interacting at the face. Because of these new degrees of freedom, conservation for individual fluxes is possible

$$F_{cd}^{kl} = -F_{dc}^{lk}. \tag{2.25}$$

It is the latter choice which is retained. Indeed, having allowed more than one temperature inside the cell, it seems counterproductive to then only allow one temperature on each face. Just as for (2.23), (2.25) gives

$$F_{cd}^{kl} = \kappa_{cd}^{kl} \frac{T_d^l - T_c^k}{h_{cd}^{kl} + h_{dc}^{lk}} S_{cd}^{kl}, \tag{2.26a}$$

$$T_{cd}^{kl} = \left( \frac{\kappa_c^k}{h_{cd}^{kl}} T_c^k + \frac{\kappa_d^l}{h_{dc}^{lk}} T_d^l \right) \Big/ \left( \frac{\kappa_c^k}{h_{cd}^{kl}} + \frac{\kappa_d^l}{h_{dc}^{lk}} \right), \tag{2.26b}$$

$$\kappa_{cd}^{kl} = \left( h_{cd}^{kl} + h_{dc}^{lk} \right) \Big/ \left( \frac{h_{cd}^{kl}}{\kappa_c^k} + \frac{h_{dc}^{lk}}{\kappa_d^l} \right). \tag{2.26c}$$

**Remark 5.** Fluxes may be written in the generic form

$$F_{cd}^{kl} = A_{cd}^{kl} \left( T_d^l - T_c^k \right), \tag{2.27}$$

with $A_{cd}^{kl} = A_{dc}^{lk} \geq 0$. This factorized form will be used for the three-temperature multi-material scheme for best readability.

## 3.4 Numerical results and comparison of the two methods

The different test cases aim at comparing the performances of the different methods. The numerical error depends both on the number of cells and the relative position of the mesh with respect to the physical interfaces. Increasing the mesh size without changing its relative position from the interfaces amounts to measure the order of convergence of the different methods. The order of convergence is an important feature of numerical schemes but it is somewhat an
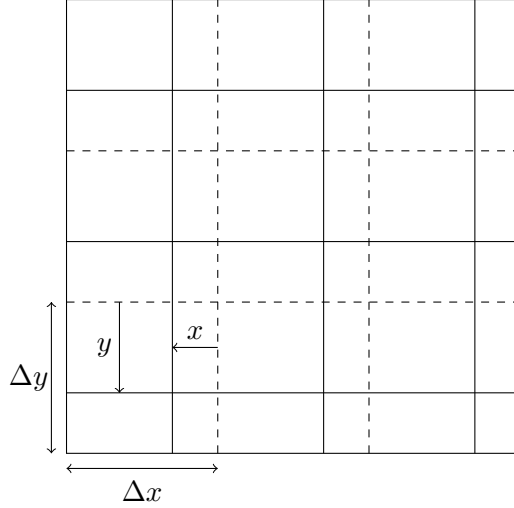
Figure 2.5: Initial mesh (dashed lines) and shifted mesh (full lines). The shift is parameterized by the lengths $x$ and $y$. The relative $x-$shift is given by $\frac{x}{\Delta x} \in [0,1]$ (and likewise for $y$).

orthogonal issue to what is investigated in this chapter. Besides, no significant difference in the order of convergence is expected; in particular, if the mesh is perfectly aligned with the interfaces, all methods are equivalent and the order will exactly be the same.

Here, performance is measured in terms of robustness with respect to changes of volume fraction. More precisely, the mesh size is fixed and the focus is put on how accuracy deteriorate when the mesh undergoes arbitrary displacements. For a cartesian mesh, the displacement is here given as a function of two parameters: the $x-$shift and the $y-$shift as depicted in figure 2.5. The $x-$shift is the relative displacement parallel to the $x-$axis. Two values of $x-$shift which are equal modulo 1 give the same mesh so only values in $[0,1]$ are considered. In particular, the values 0 and 1 induce no change on the mesh. Same goes for the $y-$shift.

In all test cases, the different methods are denoted with their own specific key. For homogenization methods, it is respectively A for the arithmetic mean and H for the harmonic mean. The discrete equation method's key is identified with the letter L and is then given in order by: the choice of $\lambda$ (0, min or max), the reconstruction of volume fractions (1 constant and 2 for linear) and the use of internal flux (F if none is used and T otherwise). For instance Lmin2F stands for the DEM with the choice $\lambda_{\min}$, linear reconstruction of volume fractions and no internal flux. Finally, time integration is implicit and not subject to any stability restriction on the time step.

**Layered wall**

The first test case consists in a wall with multiple layers of two distinct materials. The domain of the wall $[0,1] \times [0,0.1]$ is divided into 8 equal parts along the $x$-axis as shown in figure 2.6. The first material of thermal conductivity $\kappa^1 = 1$ occupies the first, third, fifth and seventh parts; the second material of thermal conductivity $\kappa^2 = 10^{-2}$ occupies the rest of the domain. Dirichlet boundary conditions are set with $T = 4$ on the left border, and $T = 0$ on the right. Fluxes are set to zero along the top and bottom borders so that the test case is essentially one-dimensional. The layout of the problem is summarized in figure 2.6.
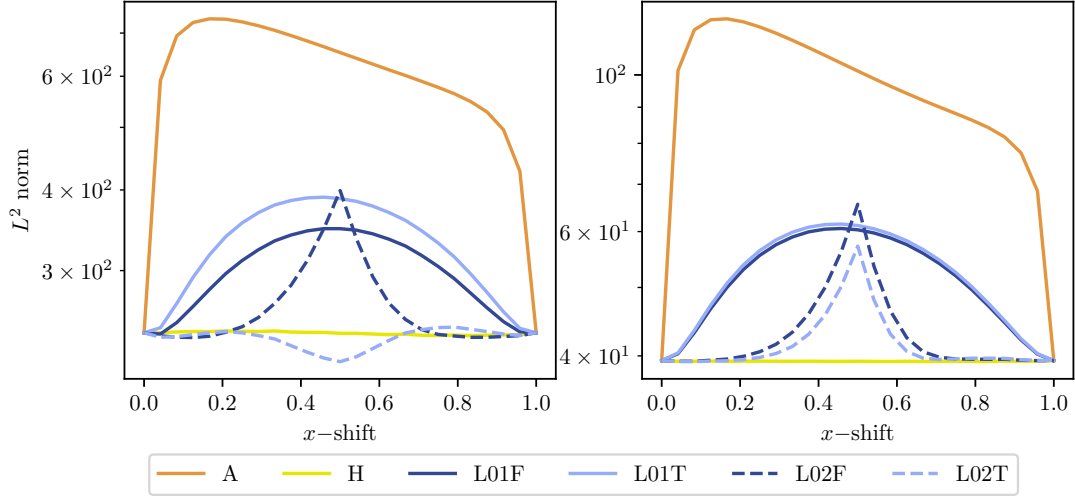
Figure 2.6: Layered wall configuration.



Figure 2.7: $L^2$ error as a function of the displacement of the mesh for the layered wall test case. Left: $32 \times 1$ mesh. Right: $160 \times 1$ mesh.

The problem is discretized on $N_x \times 1$ meshes with $N_x = 32$ a $N_x = 160$. Because in both cases $N_x \equiv 0[8]$, the unperturbed mesh only consists of pure cells. A non zero $x-$shift produces mixed cells whose effect is analysed. Results at $t = 5$ computed with times steps $\Delta t = 1$ and various values of $x$-shift are compared with a reference solution. The reference is computed on a $12\,800 \times 1$ mesh consisting of only pure cells.

Results are summarized in figure 2.7. Homogenization methods perform differently depending on the mean. Arithmetic mean gives the worst accuracy; the error skyrockets even for small displacements of the mesh. Harmonic mean fares well, even better than the DEM. It can actually be shown that, for this particular problem, it gives exact global stationary fluxes. As for the DEM, the value of $\lambda$ cannot be changed because there is no adjacent mixed cells. Only the linear reconstruction of volume fractions and the internal flux can be studied. The linear reconstruction seems to significantly improve the results, except for $x-$shifts close to 0.5. For small displacements (i.e. with an $x-$shift or volume fraction close to 0 or to 1), the linear reconstruction helps mitigate the presence of the material in minority. However, for balanced mixed cell, it seriously underestimate the flux between the two materials (as explained in remark 4). This is the reason why an additional internal flux decreases the error. However, its effect fades out for a greater number of cells. It becomes less relevant as the underlying solution is continuous and refining the mesh means that temperature inside mixed cell converge to one another.

**Sandwich problem**

While the previous test case was interested in fluxes orthogonal to the interface, the so-called sandwich problem [58] studies fluxes parallel to the interface. The domain $[0, 0.5] \times [0, 1]$ is shared between two materials as depicted in figure 2.9: the first one, with a thermal conductivity
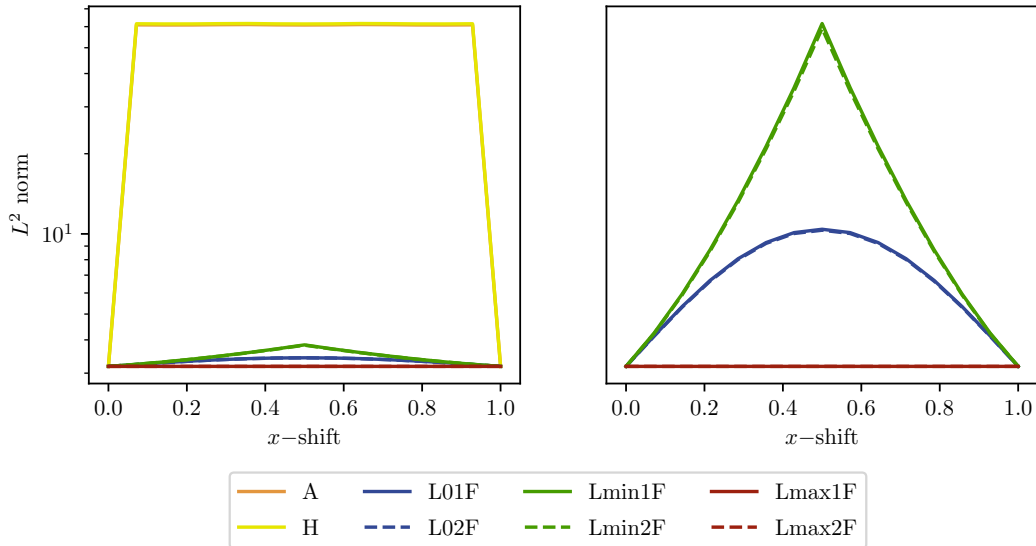
Figure 2.8: $L^2$ error as a function of the displacement of the mesh for the sandwich problem. Left: for all methods. Right: only for the DEM.

$\kappa_1 = 1$ occupies the zone $0.05 \leq x \leq 0.45$; the rest of the domain contains a material of thermal conductivity $\kappa_2 = 0$. Temperature is set to $T = 1$ at the bottom, and $T = 0$ at the top. Fluxes are set to zero along the left and right borders. Because the exterior material does not conduct heat, the solution inside the interior material is essentially one-dimensional.

The problem is discretized on a $40 \times 80$ mesh and results are compared with a reference solution computed on a $500 \times 1000$ mesh. Once again, because the number of horizontal cell is a multiple of 10, the unperturbed meshes consist only of pure cells. The final time is $t = 1$ with a time step of $\Delta t = 0.1$.

Results are given in figure 2.8. Homogenized methods give similarly poor results: small displacements of the mesh induce strong errors for both arithmetic and harmonic means. The DEM gives substantially better results. Here, no internal flux is considered as the second material does not conduct heat. Linear reconstruction of volume fractions has almost no effect as it only concerns horizontal fluxes which are supposed to be zero as the problem is one-dimensional. They are exactly zero for the choice $\lambda_{\max}$ as it exactly preserves this property of the solution. This also explains why displacements have no effect on the error with $\lambda_{\max}$. Errors are greater as $\lambda$ takes smaller values because it increases the proportion of the cell faces allocated to non-existing interactions between the two materials.

**Sand and shale**

Finally, the more sophisticated sand and shale problem [58] is considered. The domain $[0, 1] \times [0, 0.5]$ is filled with a high conductivity $\kappa_1 = 1$ medium (the sand) and small squares of a insulating $\kappa_2 = 0$ material (the shale). The squares are of dimension $0.05 \times 0.05$ and are randomly generated throughout the domain as in figure 2.9. Temperature is equal to $T = 4$ at the bottom and $T = 0$ at the top. Fluxes are set to zero along the left and right borders.

With a sufficiently fine mesh, this test case locally resembles the sandwich problem. The qualitative results are expected to be similar, preserving the previously exposed hierarchy of the
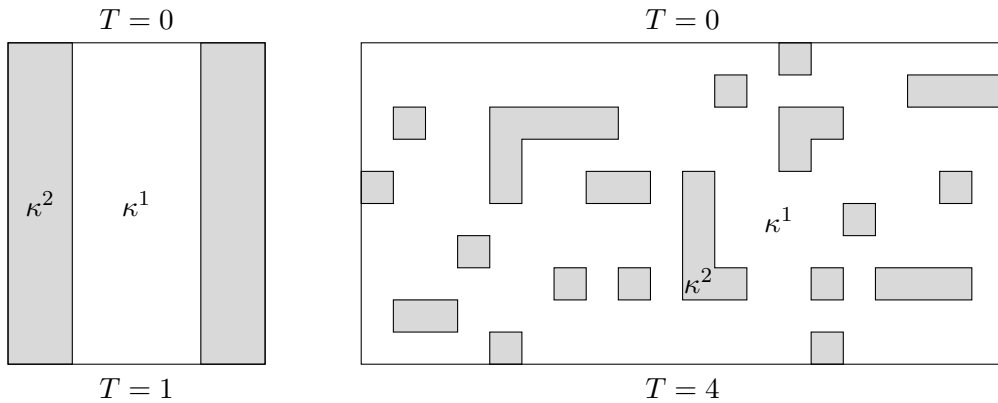
Figure 2.9: Sandwich (left) and sand and shale (right) configurations.

different methods. Such a fine mesh can however be out of reach if the structures of interest are especially small. Looking at the results for coarser meshes is then required. Here a $80 \times 40$ mesh (i.e. 4 cells along each square side) is used and the results are compared with a reference solution computed on a $1000 \times 500$ mesh. Once again, the number of cells is chosen so as to ensure that the unperturbed meshes consist only of pure cells. The final time is $t = 1$ with a time step of $\Delta t = 0.1$.

Results are given in figure 2.10 for horizontal, vertical and diagonal displacement of the mesh. Once again, homogenized method does not fare well, regardless of the chosen mean and the DEM performs better. Linear reconstruction slightly reduces the error most of the time but the more significant parameter seems to be the choice of $\lambda$. The choice $\lambda_{\min}$ is by far the worst of the three. The choices $\lambda_0$ and $\lambda_{\max}$ yield comparable results, $\lambda_0$ being more robust to horizontal displacements and $\lambda_{\max}$ to vertical ones. Strikingly, with vertical and diagonal displacements, both give a lower error than for the pure cell case (i.e. for a relative displacement of 0 or 1) which means that the presence of mixed does actually improve the results.

# 4 A cell-centered Lagrangian scheme for three-temperature multi-material hydrodynamics

## 4.1 Space discretization

### Hydrodynamics

The hydrodynamics part of the scheme consists in a multi-material extension of the GLACE/EUCCLHYD schemes [11, 70]. Global quantities (i.e. total Lagrangian volume, momentum and total energy of the system) are solved with the single-material scheme. The scheme is here written in internal energy as opposed to the usually preferred total energy. The internal energy formulation lays the necessary foundations for a thermodynamically consistent space discretization of the material

Figure 2.10: $L^2$ error for the sand and shale problem as a function of the horizontal (left), vertical (middle) or diagonal (right) displacement of the mesh. Top: for all methods. Bottom: only for the DEM.

quantities.

$$m_c^k \frac{\mathrm{d}}{\mathrm{d}t} \left( \frac{1}{(\alpha\rho)_c^k} \right) = \sum_{p \in \mathcal{P}(c)} l_{pc} \mathbf{n}_{pc} \cdot \mathbf{u}_p, \tag{2.28a}$$
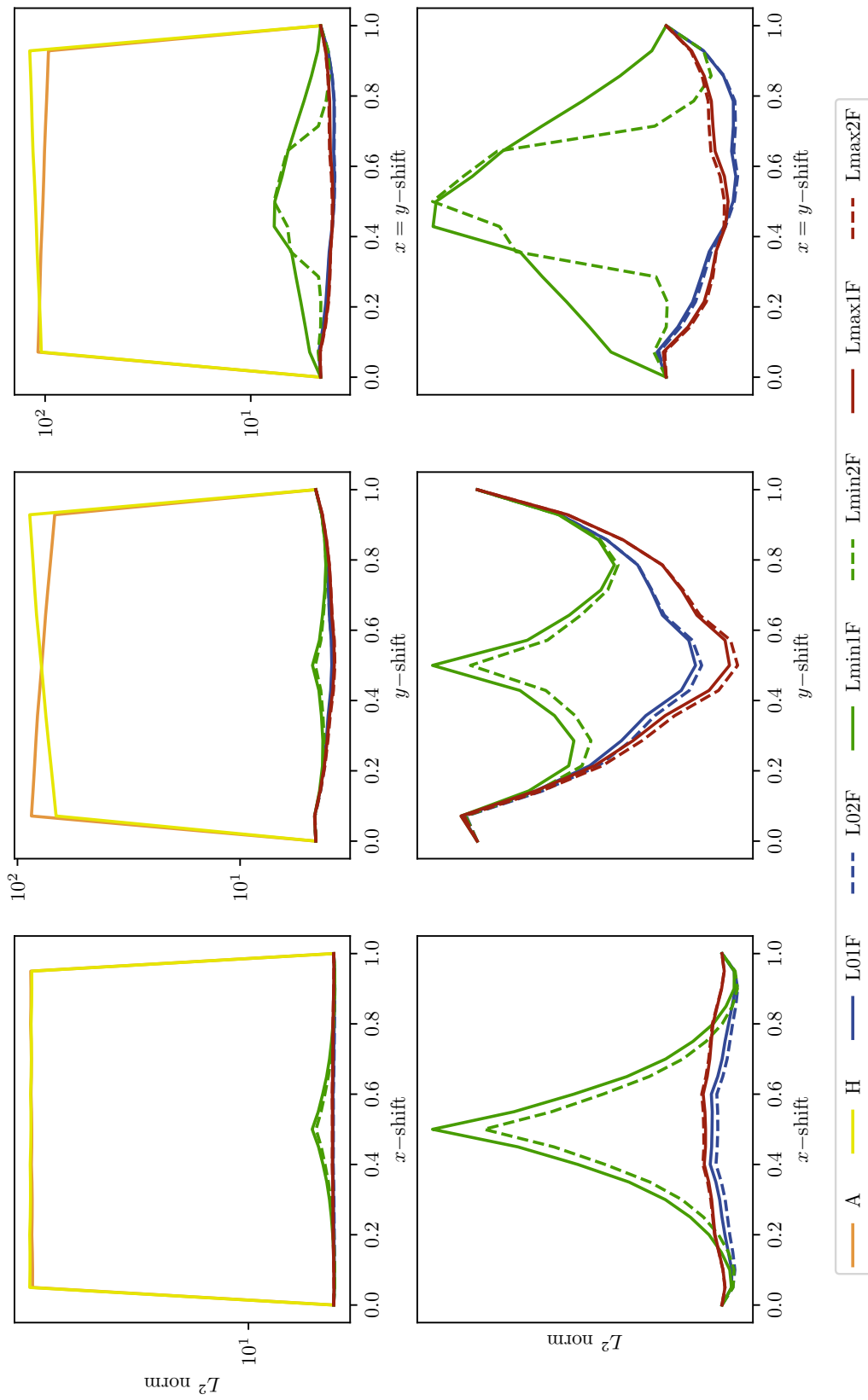
$$m_c \frac{\mathrm{d}}{\mathrm{d}t} \mathbf{u}_c = \sum_{p \in \mathcal{P}(c)} \mathbf{M}_{pc} (\mathbf{u}_p - \mathbf{u}_c), \tag{2.28b}$$

$$\sum_k m_c^k \frac{\mathrm{d}}{\mathrm{d}t} e_c^k = - p_c \sum_{p \in \mathcal{P}(c)} l_{pc} \mathbf{n}_{pc} \cdot \mathbf{u}_p + Q_c \tag{2.28c}$$

$$e_c^k = e_{i,c}^k + e_{e,c}^k + \frac{e_{r,c}^k}{\rho_c^k}, \tag{2.28d}$$

$$Q_c = \sum_{p \in \mathcal{P}(c)} (\mathbf{u}_p - \mathbf{u}_c) \cdot \mathbf{M}_{pc}(\mathbf{u}_p - \mathbf{u}_c), \tag{2.28e}$$

$$\mathbf{u}_p = \mathrm{M}_p^{-1} \sum_{c \in \mathcal{C}(p)} (\mathbf{M}_{pc} \mathbf{u}_p + p_c l_{pc} \mathbf{n}_{pc}). \tag{2.28f}$$

Equation (2.28a) governs the evolution of the total Lagrangian volume. It is often referred to as the Geometric Conservation Law [101]. Equation (2.28b) is the conservation of momentum while (2.28c) is the total internal energy equation. $Q_c$ corresponds to the total irreversible heat deposit of the scheme; the matrices $\mathbf{M}_{pc}$ are symmetric positive, thus ensuring $Q_c \geq 0$ and preventing destruction of entropy. The expressions (2.28e) and (2.28f) also enforces both consistency of the scheme and conservation of total energy. Details may be found in [28, 71]. The extension to a multi-material setting focuses on the discretization of individual densities, internal energies and entropies. For the sake of thermodynamical consistency, they are related to each other through Gibbs identity

$$\frac{\mathrm{d}}{\mathrm{d}t} e_{i,c}^k = -p_{i,c}^k \frac{\mathrm{d}}{\mathrm{d}t} \left( \frac{1}{\rho_c^k} \right) + T_{i,c}^k \frac{\mathrm{d}}{\mathrm{d}t} s_{i,c}^k, \tag{2.29a}$$

$$\frac{\mathrm{d}}{\mathrm{d}t} e_{e,c}^k = -p_{e,c}^k \frac{\mathrm{d}}{\mathrm{d}t} \left( \frac{1}{\rho_c^k} \right) + T_{e,c}^k \frac{\mathrm{d}}{\mathrm{d}t} s_{e,c}^k, \tag{2.29b}$$

$$\frac{\mathrm{d}}{\mathrm{d}t} \left( \frac{e_{r,c}^k}{\rho_c^k} \right) = -p_{r,c}^k \frac{\mathrm{d}}{\mathrm{d}t} \left( \frac{1}{\rho_c^k} \right) + T_{r,c}^k \frac{\mathrm{d}}{\mathrm{d}t} s_{r,c}^k, \tag{2.29c}$$

in such a way that is compatible with (2.28c). Densities evolve according to the equal-strain assumption (2.9)

$$m_c^k \frac{\mathrm{d}}{\mathrm{d}t} \left( \frac{1}{\rho_c^k} \right) = \alpha_c^k \sum_{p \in \mathcal{P}(c)} l_{pc} \mathbf{n}_{pc} \cdot \mathbf{u}_p. \tag{2.30}$$

It is also equivalent to $\frac{\mathrm{d}}{\mathrm{d}t} \alpha_c^k = 0$. As for the entropy, the global heat deposit $Q$ can be shared arbitrarily between materials and their temperatures with respect to coefficients $\lambda_\theta^k$, $\theta \in \{i, e, r\}$

$$m_c^k T_c^k \frac{\mathrm{d}}{\mathrm{d}t} s_{\theta,c}^k = \lambda_{\theta,c}^k Q_c, \tag{2.31a}$$

$$\sum_k \sum_{\theta \in \{e,i,r\}} \lambda_{\theta,c}^k = 1. \tag{2.31b}$$

Changing the coefficients $\lambda_\theta^k$ changes the numerical approximation of shocks, even at convergence [66, 1]. Their expression must then be motivated by physics and cannot be reasonably specified by numerical considerations alone. The coefficients $\lambda^k = \lambda_i^k + \lambda_e^k + \lambda_r^k$ depend on the mixture (separated, dispersed,...) and all the underlying small-scale phenomena (viscosity, surface tension, heat exchange,...). Once the $\lambda^k$ are known, they should be divided into $\lambda_\theta^k$. Strictly speaking, the $\lambda_\theta^k$ can be arbitrary (as long as they sum up to $\lambda^k$) but they are here defined proportionally to the mass of the different species as prescribed in [115]

$$\lambda_\theta^k = \frac{m_\theta^k}{m^k} \lambda^k. \tag{2.32}$$

Then the ions bear almost all of the dissipation and the photons none.

**Radiation transport and source terms**

Local relaxation terms are approximated with a simple quadrature rule

$$\int_{\omega_c} \alpha^k c \kappa^k \left( T_e^k - T_i^k \right) \simeq c V_c^k \kappa_c^k \left( T_{e,c}^k - T_{i,c}^k \right), \tag{2.33a}$$

$$\int_{\omega_c} \alpha^k c \sigma_P^k \left( a \left( T_r^k \right)^4 - a \left( T_e^k \right)^4 \right) \simeq c V_c^k \sigma_{P,c}^k \left( a \left( T_{r,c}^k \right)^4 - a \left( T_{e,c}^k \right)^4 \right). \tag{2.33b}$$

Each relaxation term appears twice with opposite sign and the discretization of the opposite is the opposite of the discretization. This is both natural and necessary for energy conservation. Radiation transport is discretized with one of the strategies presented in section 3. The previous thermal conductivities $\kappa$ are replaced with local approximations of opacities

$$\left[ \frac{c}{3\sigma_R^k} \right]_c = \frac{c}{3\sigma_{R,c}^k}. \tag{2.34}$$

In the following, the discrete diffusion operator for material $k$ will be written in the generic form

$$\sum_{d,l} A_{cd}^{kl} \left( e_{r,c}^k - e_{r,d}^l \right), \tag{2.35}$$

with $A_{cd}^{kl} \geq 0$ depending on the chosen strategy and the geometry of the mesh. Eventually, the semi-discrete internal energy equations read

$$m_c^k \frac{\mathrm{d}}{\mathrm{d}t} e_{i,c}^k = H_{i,c}^k + c V_c^k \kappa_c^k \left( T_{e,c}^k - T_{i,c}^k \right), \tag{2.36a}$$

$$m_c^k \frac{\mathrm{d}}{\mathrm{d}t} e_{e,c}^k = H_{e,c}^k + c V_c^k \kappa_c^k \left( T_{i,c}^k - T_{e,c}^k \right) + c V_c^k \sigma_{P,c}^k \left( a \left( T_{r,c}^k \right)^4 - a \left( T_{e,c}^k \right)^4 \right), \tag{2.36b}$$

$$m_c^k \frac{\mathrm{d}}{\mathrm{d}t} \frac{e_{r,c}^k}{\rho_c^k} = H_{r,c}^k + \sum_{d,l} A_{cd}^{kl} \left( e_{r,d}^l - e_{r,c}^k \right) + c V_c^k \sigma_{P,c}^k \left( a \left( T_{e,c}^k \right)^4 - a \left( T_{r,c}^k \right)^4 \right). \tag{2.36c}$$

with $H_{i,c}^k, H_{e,c}^k$ and $H_{r,c}^k$ the, previously detailed, discretization of the hydrodynamic part

$$H_{\theta,c}^k = -\alpha_c^k p_{\theta,c}^k \sum_{p \in \mathcal{P}(c)} l_{pc} \mathbf{n}_{pc} \cdot \mathbf{u}_{pc} + \lambda_{\theta,c}^k Q_c. \tag{2.37}$$

## 4.2 Implicit time integration: an iterative method based on convex combinations

Temperature relaxation processes and radiation transport are usually stiff phenomena. Explicit time integration of these terms is possible but would require unreasonably small time steps. An implicit integration is then preferred so that only the hydrodynamics part of the scheme constrains the time steps.

$$\frac{m_c^k}{\Delta t}\left(e_{i,c}^{k,n+1} - e_{i,c}^{k,n}\right) = H_{i,c}^{k,n} + c(V\kappa)_c^{k,n+1}\left(T_{e,c}^{k,n+1} - T_{i,c}^{k,n+1}\right), \tag{2.38a}$$

$$\frac{m_c^k}{\Delta t}\left(e_{e,c}^{k,n+1} - e_{e,c}^{k,n}\right) = H_{e,c}^{k,n} + c(V\kappa)_c^{k,n+1}\left(T_{i,c}^{k,n+1} - T_{e,c}^{k,n+1}\right)$$
$$+ c(V\sigma_P)_c^{k,n+1}\left(a\left(T_{r,c}^{k,n+1}\right)^4 - a\left(T_{e,c}^{k,n+1}\right)^4\right), \tag{2.38b}$$

$$\frac{m_c^k}{\Delta t}\left(\frac{e_{r,c}^{k,n+1}}{\rho_c^{k,n+1}} - \frac{e_{r,c}^{k,n}}{\rho_c^{k,n}}\right) = H_{r,c}^{k,n} + \sum_{d,l} A_{cd}^{kl,n+1}\left(e_{r,d}^{l,n+1} - e_{r,c}^{k,n+1}\right)$$
$$+ c(V\sigma_P)_c^{k,n+1}\left(a\left(T_{e,c}^{k,n+1}\right)^4 - a\left(T_{r,c}^{k,n+1}\right)^4\right), \tag{2.38c}$$

with the hydrodynamics part

$$H_{\theta,c}^{k,n} = -\alpha_c^{k,n}p_{\theta,c}^{k,n}\sum_{p\in\mathcal{P}(c)} l_{pc}^n \mathbf{n}_{pc}^n \cdot \mathbf{u}_{pc}^n + \lambda_{\theta,c}^{k,n}\sum_{p\in\mathcal{P}(c)}(\mathbf{u}_c^n - \mathbf{u}_p^n)\cdot\mathbf{M}_{pc}^n\left(\frac{1}{2}\left(\mathbf{u}_c^{n+1} + \mathbf{u}_c^n\right) - \mathbf{u}_p^n\right). \tag{2.39}$$

**Remark 6.** In (2.39), it is necessary to take the half-sum $\frac{1}{2}(\mathbf{u}^{n+1} + \mathbf{u}^n)$ for total energy conservation as explained in [20]. This is not an implicitation *per se* as momentum equations are solved before energy equations.

System (2.38) is non-linear as energies $e_i^k, e_e^k, e_r^k$ and coefficients $\kappa, \sigma_P, \sigma_R$ are possibly non-linear functions of temperatures. Following [19], it is then solved by an iterative strategy with which positivity of temperatures is ensured at each step (under some conditions detailed in Proposition 3). The number of the sub-iteration is indicated by the letter $m$. First, defining the new variables

$$\phi_\theta^k = aT_\theta^k, \quad \forall\theta\in\{i,e,r\}, \tag{2.40a}$$

$$\beta_{\theta,c}^{k,n+1,m} = \frac{\phi_{\theta,c}^{k,n+1,m} - \phi_{\theta,c}^{k,n}}{e_{\theta,c}^{k,n+1,m} - e_{\theta,c}^{k,n}}, \quad \forall\theta\in\{i,e\}, \tag{2.40b}$$

$$\delta_{ie,c}^{k,n+1,m} = \frac{T_{i,c}^{k,n+1,m} - T_{e,c}^{k,n}}{\phi_{i,c}^{k,n+1,m} - \phi_{e,c}^{k,n+1,m}}, \tag{2.40c}$$

the linearized equations for the $m^{\text{th}}$ iteration are

$$\frac{m_c^k}{\beta_{i,c}^{k,n+1,m}\Delta t}\left(\phi_{i,c}^{k,n+1,m+1}-\phi_{i,c}^{k,n}\right)=H_{i,c}^{k,n}+c(V\kappa\delta_{ie})_c^{k,n+1,m}\left(\phi_{e,c}^{k,n+1,m+1}-\phi_{i,c}^{k,n+1,m+1}\right), \quad (2.41a)$$

$$\frac{m_c^k}{\beta_{e,c}^{k,n+1,m}\Delta t}\left(\phi_{e,c}^{k,n+1,m+1}-\phi_{e,c}^{k,n}\right)=H_{e,c}^{k,n}+c(V\kappa\delta_{ie})_c^{k,n+1,m}\left(\phi_{i,c}^{k,n+1,m+1}-\phi_{e,c}^{k,n+1,m+1}\right)$$
$$+c(V\sigma_P)_c^{k,n+1,m}\left(\phi_{r,c}^{k,n+1,m+1}-\phi_{e,c}^{k,n+1,m+1}\right), \quad (2.41b)$$

$$\frac{m_c^k}{\Delta t}\left(\frac{\phi_{r,c}^{k,n+1,m+1}}{\rho_c^{k,n+1}}-\frac{\phi_{r,c}^{k,n}}{\rho_c^{k,n}}\right)=H_{r,c}^{k,n}+\sum_{d,l}A_{cd}^{kl,n+1,m}\left(\phi_{r,d}^{l,n+1,m+1}-\phi_{r,c}^{k,n+1,m+1}\right)$$
$$+c(V\sigma_P)_c^{k,n+1,m}\left(\phi_{e,c}^{k,n+1,m+1}-\phi_{r,c}^{k,n+1,m+1}\right) \quad (2.41c)$$

Without the diffusion, system (2.41) would only be a concatenation of $3 \times 3$ linear systems for each cell and each material. Diffusion couples all these systems both spatially and in between materials so that a global matrix inversion cannot be avoided. Instead of directly solving (2.41), the local $3 \times 3$ systems are first analytically triangularized so that the global system now only concerns the radiation temperatures. This effectively divides by 3 the size of the linear system to be inverted. The triangularization reveals the following convex combinations

$$\phi_{i,c}^{k,n+1,m+1}=h_c^{k,n+1,m}\psi_{i,c}^{k,n+1,m}+\left(1-h_c^{k,n+1,m}\right)\phi_c^{k,n+1,m}, \quad (2.42a)$$

$$\phi_{e,c}^{k,n+1,m+1}=f_c^{k,n+1,m}\left(\psi_{e,c}^{k,n+1,m}+\left(1-g_c^{k,n+1,m}\right)\psi_{i,c}^{k,n+1,m}\right)+\left(1-f_c^{k,n+1,m}\right)\phi_{r,c}^{k,n+1,m+1},$$
$$(2.42b)$$

$$\phi_{r,c}^{k,n+1,m+1}\left(\frac{m_c^k}{\rho_c^{k,n}}+\Delta tc(V\sigma_P f)_c^{k,n+1,m}+\sum_{d,l}A_{cd}^{kl,n+1,m}\right)-\sum_{d,l}A_{cd}^{kl,n+1,m}\phi_{r,d}^{l,n+1,m+1}$$
$$=m_c^k\psi_{r,c}^{k,n+1,m}+\Delta tc(V\sigma_P f)^{k,n+1,m}\left(\psi_{e,c}^{k,n+1,m}+\left(1-g_c^{k,n+1,m}\right)\psi_{i,c}^{k,n+1,m}\right). \quad (2.42c)$$

where

$$h_c^{k,n+1,m}=\frac{1}{1+c(V\kappa\delta_{ie}\beta_i)_c^{k,n+1,m}\dfrac{\Delta t}{m_c^k}}, \quad (2.43a)$$

$$g_c^{k,n+1,m}=\frac{1}{1+c(V\kappa\delta_{ie}\beta_e h)_c^{k,n+1,m}\dfrac{\Delta t}{m_c^k}}, \quad (2.43b)$$

$$f_c^{k,n+1,m}=\frac{1}{1+c(V\sigma_P\beta_e g)\dfrac{\Delta t}{m_c^k}}, \quad (2.43c)$$

and

$$\psi_{i,c}^{k,n+1,m} = \phi_{i,c}^{k,n} + \frac{\Delta t \beta_{i,c}^{k,n+1,m}}{m_c^k} H_{i,c}^{k,n}, \qquad (2.44a)$$

$$\psi_{e,c}^{k,n+1,m} = \phi_{e,c}^{k,n} + \frac{\Delta t \beta_{e,c}^{k,n+1,m}}{m_c^k} H_{e,c}^{k,n}, \qquad (2.44b)$$

$$\psi_{r,c}^{k,n+1,m} = \frac{\phi^{k,n}}{\rho^{k,n}} + \frac{\Delta t}{m_c^k} H_{r,c}^{k,n}. \qquad (2.44c)$$

The numerical time step $\Delta t$ is not restricted by the radiation transport or the source terms. It is only driven by the hydrodynamic part of the equations and its resulting CLF-like condition

$$\frac{\Delta t c_c}{V_c} P_c \leq \frac{1}{2}. \qquad (2.45)$$

where $V_c$ is the volume of the cell, $P_c$ its perimeter and $c_c$ the mixture speed of sound (2.11). This restriction is supplemented with a second restriction preventing cell inversion and thus ensuring positivity of the density.

**Remark 7.** Strictly speaking, system (2.42) consists in convex combinations if and only if coefficients $\beta_{i,c}^{k,n+1,m}$ and $\beta_{e,c}^{k,n+1,m}$ are non-negative. For a given equation of state, the heat capacity $c_v$ and the Grüneisen coefficient $\Gamma$ are defined as

$$c_v = \left. \frac{\partial e}{\partial T} \right|_\rho, \qquad (2.46a)$$

$$\Gamma = \frac{\rho}{T} \left. \frac{\partial T}{\partial \rho} \right|_s. \qquad (2.46b)$$

The following thermodynamic relation then stands

$$\mathrm{d}T = \frac{1}{c_v} \mathrm{d}e + \left( \frac{p}{c_v} - \rho \Gamma T \right) \mathrm{d}\left( \frac{1}{\rho} \right). \qquad (2.47)$$

Equation (2.47) is in particular valid for the equation of state of ions and electrons of material $k$. Because $c_{v,i}^k > 0$ and $c_{v,e}^k > 0$, coefficients $\beta_{i,c}^{k,n+1,m}$ and $\beta_{e,c}^{k,n+1,m}$ are always positive as long as the variation of volume is neglected. If not, these coefficients may become negative and convex combinations are lost. For the applications of interest, radiation phenomena occurs on time scales shorter than those of hydrodynamics so that variations of volume can reasonably be neglected.

**Remark 8.** The convergence rate of the present method is slower than a regular Newton's method. Although Newton's method may fail to ensure positivity of temperatures and may thus crash the simulation in demanding test cases [19], it usually behaves well. The present method should not be seen as the main procedure but rather as a backup to another faster-converging method.

**Properties**

**Proposition 1** (Discrete Energy conservation). The discrete total energy

$$\sum_c \left[ m_c \frac{\|\mathbf{u}_c\|^2}{2} + \sum_k m_c^k \left( e_{i,c}^{k,n} + e_{e,c}^{k,n} + \frac{e_{r,c}^{k,n}}{\rho_c^{k,n}} \right) \right], \tag{2.48}$$

is conserved.

*Proof.* When summing ionic, electronic and radiation energy, the contribution of relaxation terms disappears. Radiation transport is written in terms of fluxes which cancel when summed over all cells and all materials as explained in 3.3. Only remains the hydrodynamics part. Conservation is not obvious in (2.28) where the internal energy formulation was favored. Proof of the conservation of total energy (as well as momentum) for the GLACE/EUCCLHYD scheme can be found in [27, 71, 11, 70]. $\qquad\square$

**Proposition 2** (Semi-discrete entropy production). The following semi-discrete inequality on total entropy stands

$$\sum_{c,k} m_c^k \frac{\mathrm{d}}{\mathrm{d}t} \left( s_{i,c}^k + s_{e,c}^k + s_{r,c}^k \right) \geq 0. \tag{2.49}$$

*Proof.* The semi-discrete entropy equations read

$$m_c^k T_{i,c}^k \frac{\mathrm{d}}{\mathrm{d}t} s_{i,c}^k = \lambda_{i,c}^k Q_c + c(V\kappa)_c^k \left( T_{e,c}^k - T_{i,c}^k \right), \tag{2.50a}$$

$$m_c^k T_{e,c}^k \frac{\mathrm{d}}{\mathrm{d}t} s_{e,c}^k = \lambda_{e,c}^k Q_c + c(V\kappa)_c^k \left( T_{i,c}^k - T_{e,c}^k \right) + c(V\sigma_P)_c^k \left( a\left( T_{e,c}^k \right)^4 - a\left( T_{r,c}^k \right)^4 \right), \tag{2.50b}$$

$$m_c^k T_{r,c}^k \frac{\mathrm{d}}{\mathrm{d}t} s_{r,c}^k = \lambda_{r,c}^k Q_c + \sum_{d,l} A_{cd}^{kl} \left( e_{r,d}^l - e_{r,c}^k \right) + c(V\sigma_P)_c^k \left( a\left( T_{e,c}^k \right)^4 - a\left( T_{r,c}^k \right)^4 \right). \tag{2.50c}$$

The relaxation terms provide a local and individual (i.e. for a given cell and a given material) entropy production as it can be seen by summing all equations of (2.50). Radiation transport, however, consists in a heat exchange between cells and materials so that the associated entropy production can only be recovered by summing equations (2.50c) over all cells and all materials. Eventually

$$\sum_{c,k} m_c^k \frac{\mathrm{d}}{\mathrm{d}t} \left( s_{i,c}^k + s_{e,c}^k + s_{r,c}^k \right) = \left( \sum_k \sum_{\theta \in \{i,e,r\}} \frac{\lambda_{\theta,c}^k}{T_{\theta,c}^k} \right) Q_c + \sum_{\{c,d\},\{k,l\}} A_{cd}^{kl} \frac{\left( T_{r,c}^k - T_{r,d}^l \right) \left( \left( T_{r,c}^k \right)^4 - \left( T_{r,d}^l \right)^4 \right)}{T_{r,c}^k T_{r,d}^l}$$
$$+ \sum_{c,k} c(V\kappa)_c^k \frac{\left( T_{i,c}^k - T_{e,c}^k \right)^2}{T_{i,c}^k T_{e,c}^k} + \sum_{c,k} ca(V\sigma_P)_c^k \frac{\left( T_{e,c}^k - T_{r,c}^k \right) \left( \left( T_{e,c}^k \right)^4 - \left( T_{r,c}^k \right)^4 \right)}{T_{e,c}^k T_{r,c}^k}, \tag{2.51}$$

which is, as announced, non-negative. $\qquad\square$

**Proposition 3** (Positivity of temperatures). Under a hydrodynamics-driven CFL condition and the positivity of coefficients $\beta_{i,c}^{k,n+1,m}$ and $\beta_{e,c}^{k,n+1,m}$, temperatures stay positive at each step of the iterative procedure.

|  | Unit | Xenon | Beryllium |
|---|---|---|---|
| $\rho$ | g.cm$^{-3}$ | 0.006 | 1.85 |
| $u$ | cm.s$^{-1}$ | 0 | 0 |
| $k_B T = k_B T_r$ | eV | 100 | 1 |
| $p$ | g.cm$^{-1}$.s$^{-2}$ | $(\gamma - 1)\rho e$ | |
| $e$ | erg.g$^{-1}$ | $c_v(k_B T)$ | |
| $e_r$ | erg.cm$^{-3}$ | $a(k_B T_r)^4$ | |
| $\sigma_P = \sigma_R$ | cm$^{-1}$ | $\sigma_0 \rho^2 (k_B T)^{-7/2}$ | |
| $c_v$ | cm$^2$.s$^{-2}$.eV$^{-1}$ | $3.22 \cdot 10^{11}$ | $7.98 \cdot 10^{11}$ |
| $\gamma$ | | 5/4 | 5/3 |
| $\sigma_0$ | cm$^{-1}$ | $3.1 \cdot 10^8$ | $4.2 \cdot 10^9$ |
| $c$ | cm.s$^{-1}$ | $3.00 \cdot 10^{10}$ | |
| $k_B$ | eV.K$^{-1}$ | $8.61 \cdot 10^{-5}$ | |
| $a$ | erg.cm$^{-3}$.eV$^{-4}$ | $1.37 \cdot 10^2$ | |

Table 2.1: Initial conditions of the ablation wall problem.

*Proof.* If coefficients $\beta_{i,c}^{k,n+1,m}$ and $\beta_{e,c}^{k,n+1,m}$ are positive, coefficients $h, g$ and $f$ (2.43) belong to $[0, 1]$. On the other hand, all $\psi$ (2.44) variables are positive under a CFL-like condition which only depends on the hydrodynamics. Then, the right-hand side of equations (2.42c) is positive. The global matrix associated to the left-hand side of system (2.42c) is a $M-$matrix. Consequently, positivity of radiation temperatures is ensured. Finally, positivity of electronic and ionic temperatures follows from the convex combinations (2.42b) and (2.42a). □

### 4.3 Numerical results

### 4.4 Ablation wall problem

For this one-dimensional test case [98], a hot gas (xenon) interacts with a denser cold wall (beryllium). The radiation transport at the interface heats the beryllium and triggers an expansion wave pushing the interface towards the hot gas. Additionally, the initial pressure discontinuity generates a shock wave through the gas while the pressure difference induced by the heating of the wall causes a second shock wave to propagate inside it. The domain measures 0.16 cm and is initially divided at $x = 0.10$ cm with the wall on the right. Initial quantities are summarized in table 2.1 along with the values of the physical constants. In practice, the present three-temperature code is reduced to a two-temperature one by using infinite $\kappa$ ($10^{30}$ for both materials in our test) and taking $(c_v)_i = (c_v)_e = \frac{1}{2}c_v$.

The physics of the problem is stiff because of the high contrasted densities, pressures, temperatures and opacities. In particular, opacity experiences a sharp change at the interface ($\sigma_R/\sigma_L \approx 10^{12}$). In (2.26c), the equivalent diffusion coefficient at the interface between two materials is given by an harmonic mean. This specific averaging appears naturally because the underlying assumption is that of a stationary solution for which the flux is constant. This hypothesis however breaks down when dealing with such a highly non-stationary test case. Generally speaking, other averaging (e.g. arithmetic or geometric mean) could be used. An arithmetic mean would produce a mean diffusion coefficient close to the greatest one ($\approx 10^{10}$)

while an harmonic mean would result in a mean diffusion coefficient close to the smallest one ($\approx 10^{-2}$). This is important as the flux at the interface drives most of the physics of the system and different choices are then expected to yield different solutions.

Results at $t = 4$ns with 1024 cells, without remapping and for different means (namely arithmetic, geometric and harmonic) are displayed in figure 2.11. Without remapping, no mixed cell appears and the profiles accurately describe the state of the individual unmixed materials. All solutions, except for the harmonic mean display a similar structure which is consistent with the semi-analytical solution given in [29] and the numerical results obtained in [98, 18]. However, the previous results as well as the present ones display different wave and interface positions between each other. Several reasons can be invoked to explain this discrepancy.

- The most substantial differences come from the choice of the mean diffusion coefficient at the interface. The harmonic mean almost entirely freezes radiation transport between the two materials. In this case, the solution is then essentially driven by the hydrodynamic part of the system and consists in a leftward propagating shock wave through the lighter xenon and a rightward propagating rarefaction wave through the denser beryllium (see figure 2.11). This explains why the temperature is lower on the right side of the wall; the beryllium experiences an expansion whose resulting temperature decrease is not compensated by the heat flux from the xenon. Radiation still has an effect on the left part of the solution where the opacity is quite low. The shock is then smeared out by radiation transport while the equilibration of material and radiation temperatures lags. Alternatively, the arithmetic mean probably overestimates the interface diffusion coefficient as the interface seems to be pushed excessively to the left, so much so that performing the computation up to 5.5ns as in [98] is not possible without collision with the left border.

- Another factor may be related to convergence issues. As seen in figure 2.12, doubling the number of cell significantly shifts the interface position. Even with a decent mesh (1024 cells), the rarefaction wave is only captured with a limited number of cells and remains largely unresolved; this issue seems to be affected by the remapping procedure. Even if all numerical schemes were to converge to a common solution, the required mesh size for numerical convergence may be out of reach in practice. In this case, properly modelling the opacity at the interface is mandatory.

- Finally, because shocks propagate through two-temperature medium, their downstream and upstream states, as well as the shock speed all depend on the details of entropy production on each energies. Different numerical schemes may then produce different solutions depending on their underlying numerical diffusion. For example, in figure 2.12, the intermediate state between the left shock and the interface is different for the velocity if a remapping procedure is used because of the additional diffusion it induces. The additional diffusion translates to entropy production or heating which in turn accelerates the expansion.
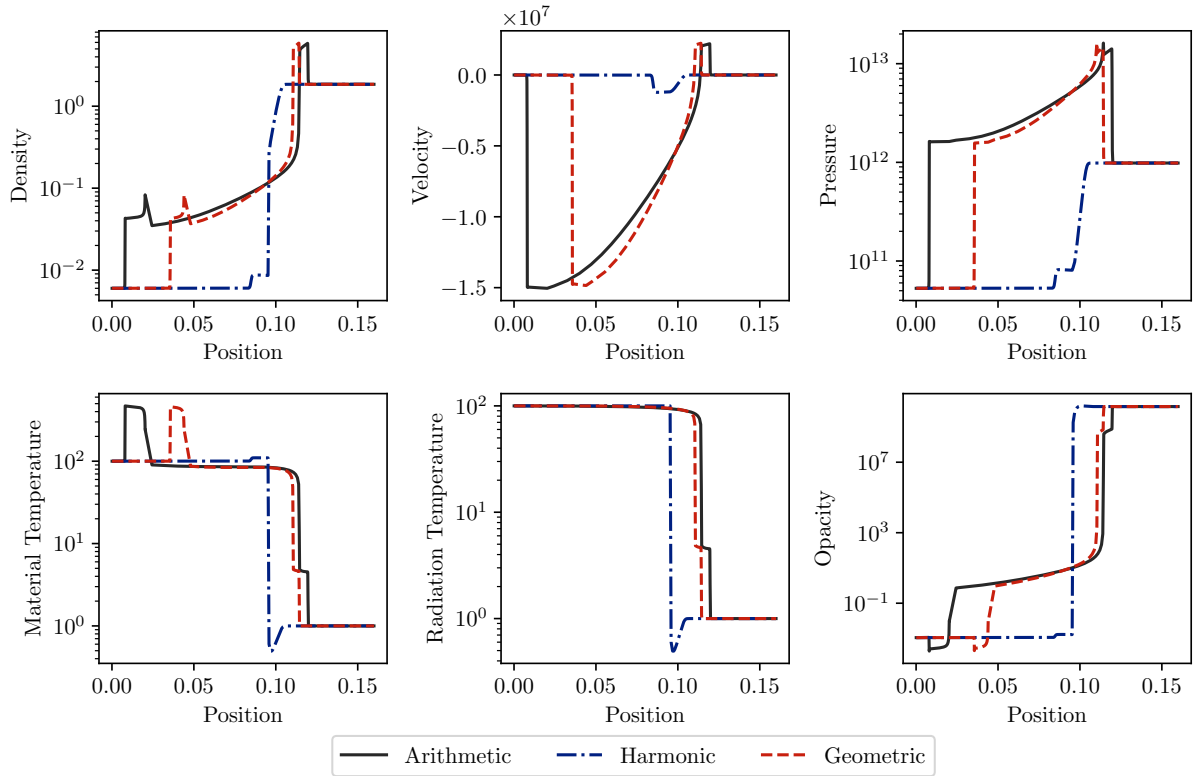
Figure 2.11: Results at 4ns of the ablation wall problem (see table 2.1) for 1024 cells and different interface average diffusion coefficient.
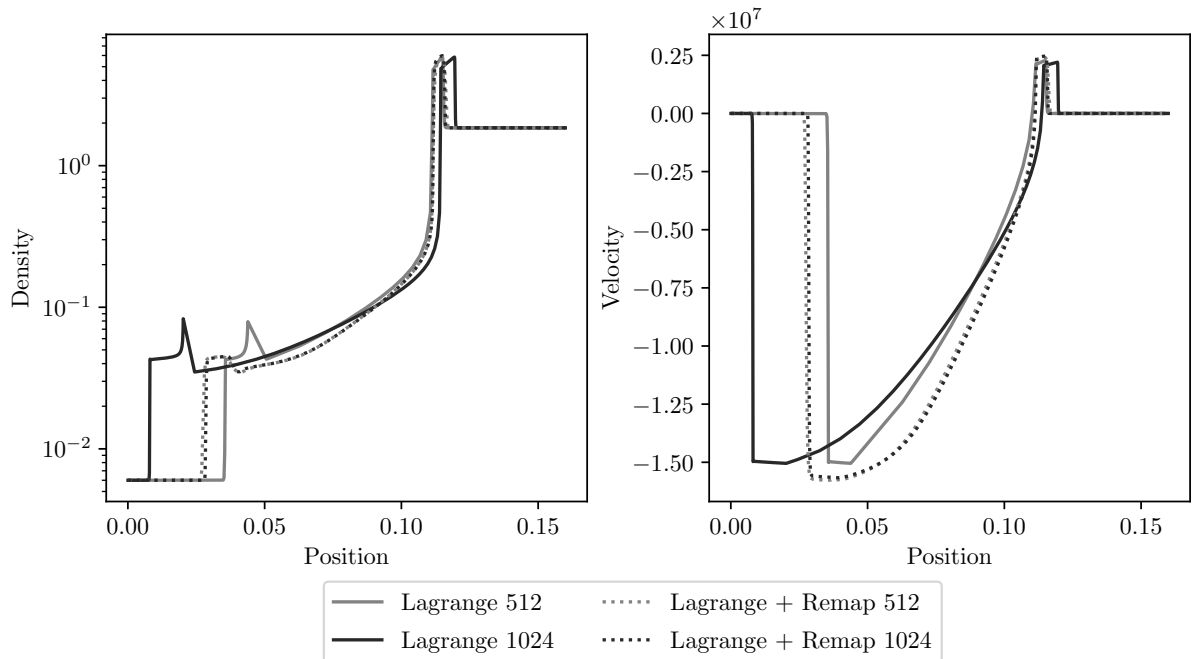


Figure 2.12: Results of the ablation wall problem with different mesh sizes (512 and 1024) and with or without an additional remapping procedure. The interface diffusion coefficient is obtained with an arithmetic mean. The remapping produces a mixture inside which multi-material equations become mandatory. They are here discretized with the choice $\lambda_0$, constant reconstruction of volume fractions and no internal flux. The plotted density is then that of the mixture.

## 4.5 Two-dimensional test case

The last test case comes from [18] and is itself inspired from the one found in [79]. Results will not be compared directly to these references as the nondimensionalization and equations of state are not specified in the former one while the latter one does not take into account hydrodynamics. In any case, this test case aims at demonstrating the proficiency of the present scheme in a two-dimensional two-temperature two-material setting; a more quantitative approach is out of the scope of this chapter. Once again, the three-temperature scheme is reduced to a two-temperature one by using infinite $\kappa$ ($10^{30}$ for both materials in our test) and taking $(c_v)_i = (c_v)_e = \frac{1}{2}c_v$.

The two materials initially occupy the domain $[0,1] \times [0,1]$ as in figure 2.13 with a radial temperature distribution

$$T(x,y) = T_r(x,y) = \left( 0.001 + 100 \exp\left( -\frac{x^2 + y^2}{0.01} \right) \right)^{\frac{1}{4}}, \tag{2.52}$$

a constant density $\rho = 1$ and a constant velocity $\mathbf{u} = \mathbf{0}$. Both the speed of light $c$ and the radiation constant $a$ are set to 1. The two materials are two identical perfect gases with $\Gamma^1 = \Gamma^2 = 0.4$. Their opacity however differ from each other. They are expressed as

$$\sigma_R = \sigma_P = \frac{z}{T^3}, \tag{2.53}$$

with $z = 0.1$ for the first material and $z = 1$ for the second. Symmetric boundary conditions are set to the left and bottom borders while zero Neumann conditions are set to the top and right borders.

Results at $t = 0.5$ for a $128 \times 128$ mesh are given in figure 2.14. The choice $\lambda_0$ with no internal flux and constant reconstruction of volume fraction is made for the radiation transport. The initial stiff temperature distribution evolves according to two phenomena. First, radiation transport propagates the centrally concentrated heat to the rest of the domain. Second, at constant density, temperature gradients induce pressure gradients which accelerate the system radially. The initial squares are eventually deformed by the acceleration. Neglecting the interaction of the heat front with the top and right borders, the solution would display a radial symmetry were it not for the difference in opacity. Indeed, the second material being more opaque, radiation does not propagate well inside. Its greater opacity also means that material and radiation temperatures are more coupled. As a result, material 2 radiation temperature is lower than its surroundings. Yet, its material temperature is actually greater than that of material 1 whose coupling between material and radiation temperature is weaker. Results with and without remapping share the same global behavior although the remapping obviously smears the solution at the interface between the two materials.

## 5   Conclusion

The present work is devoted to the discretization of three-temperature multi-material hydrodynamics. A large focus is put on the multi-material radiation transport which is here dealt with the so-called discrete equation method (DEM). When compared with homogenization methods
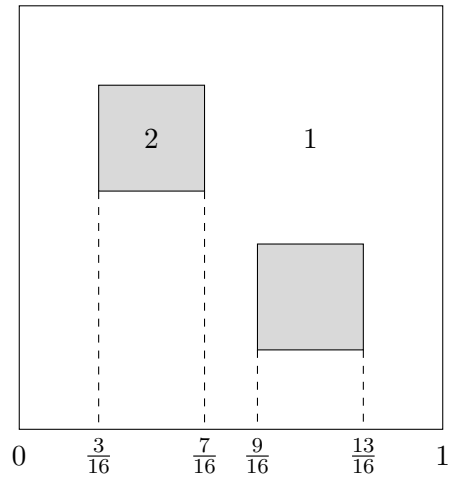
Figure 2.13: Configuration of the two-dimensional two-temperature two-material problem. The dimensions on the $y-$axis can be recovered from the symmetry with respect to the line $x = y$.
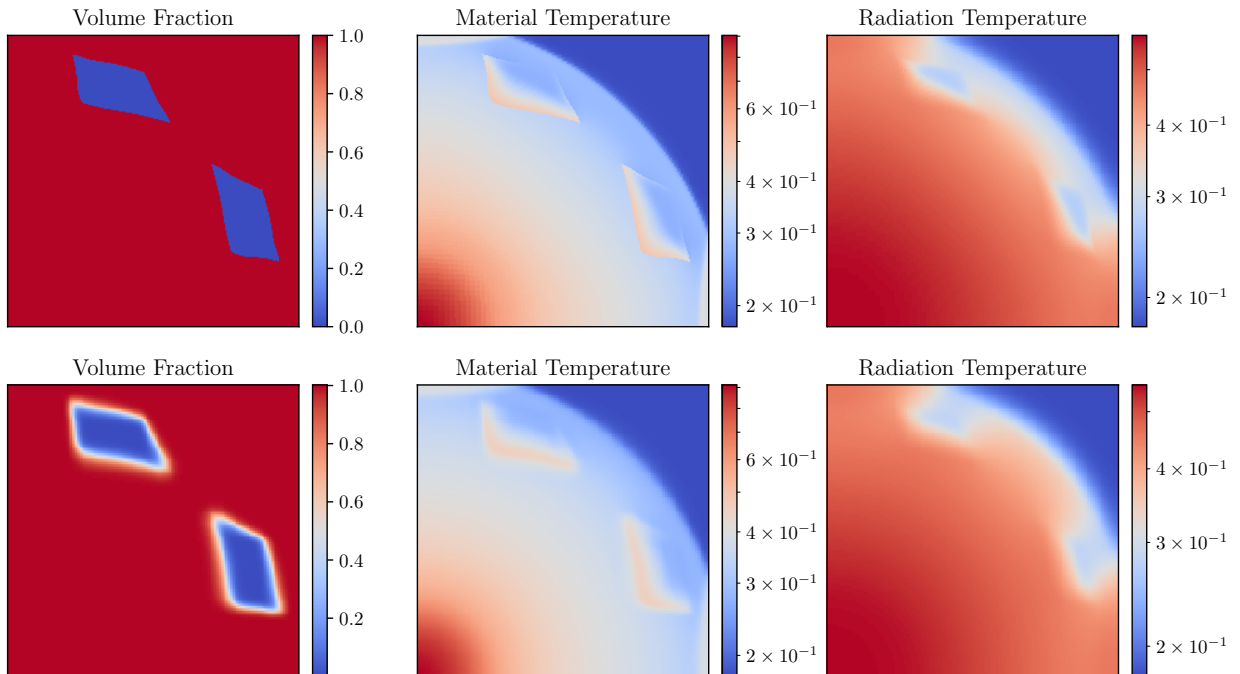


Figure 2.14: Results of the Mousseau-Knoll-Chauveheid test case at $t = 0.5$ and for a $128 \times 128$ mesh. Top: without remapping. Bottom: with remapping.

on perturbed meshes, the DEM shows significant improvement in accuracy while remaining both conceptually and computationally simple. The global numerical scheme conserves mass, momentum and total energy. Implicit time integration allows for stiff relaxation terms and radiation transport without unreasonably small time steps. The retained strategy also ensures that temperatures stay positive during the iterative time integration procedure.

Perspectives are numerous; three of them are here mentioned. First, extension to higher order is desirable for better accuracy as the present scheme is only at first order both in time and space. Anti-diffusive methods could be used to prevent over-smearing of the interface when the scheme is paired with a remapping procedure. Second, the methodology of comparison with perturbed meshes could be extended and bettered for more general meshes (with random displacements for instance). Finally, even though the scheme is written for an arbitrary number of materials, it remains to check its efficiency for more than two materials.

# Chapter 3

# Numerical strategy for a multi-material multi-velocity model with pressure equilibration

## Contents

# 1    Introduction

Multi-material hydrodynamics is of paramount importance for industrial and academic applications alike. Applications includes, among others, pharmacology, aerodynamics, combustion, astrophysics and climatology. Although all these applications differ in their physical regimes (i.e. material properties, domain and amplitude of physical quantities, dissipation, presence and strength of shocks,...), the governing equations can be derived in a unified manner. The most common method is based on a conditional averaging [52, 113] of the single-material equations. The averaging, whether performed with respect to space, time, or statistical realisations, produces a mixed zone within which several materials coexist. The description and numerical treatment of these numerically diffused interfaces is an active domain of research [73].

## 1.1    Multi-material equations

Description of multi-material hydrodynamics are numerous in the literature. The variety of equations stems from two reasons. First, different levels of description [68, 99, 73] can be used to describe the mixture. The lowest level of description considers a single equation of state for the mixture and an additional variable, namely the mass fraction, to characterize the presence of each material; for two materials, it gives 4 unknowns and the resulting equations are referred to as 4-equation models. Alternatively, each material can have its own equation of state, pressure and velocity; for two materials, it yields a 7-equation model whose most famous instance was introduced by Baer and Nunziato [5]. In between exists a large spectrum of models depending on the number of deployed physical variables. Obviously, the more are used, the more accurate the description of the mixture is, especially in the case of highly contrasted equations of state. Here, a 6-equation model is considered with multiple velocity but only one pressure. Multiple velocities allow to take into account inter-penetration and shear between materials while one common pressure is a relevant physical approximation [55]. The second reason explaining the sheer variety of models concerns short-wavelength phenomena. Multi-material flows can include several (dissipative or not) such as surface tension, drag, added mass, viscosity or heat flux. Although they are necessary for a complete description of the flow, they are heavily mixture-dependent. For a given number of variables, infinitely many models can be created depending on the chosen terms and their expression. The stance of the present work is to focus on the greatest common denominator of all these models by altogether neglecting all additional phenomena including dissipation.

Ignoring short-wave length phenomena has two major consequences. First, the neglected terms are essential to describe shocks which, contrary to the single-material case, are small-scale dependent. Part of the missing information can be recovered by looking at entropy. The evolution of the total entropy of the mixture selects physical shocks so as to comply with the second principle of thermodynamics; among all the admissible shocks, the details of the entropy production on each material then selects the one of interest. Second, the resulting system of equations features a mixed elliptic-hyperbolic behavior. Ellipticity induces instability which is the reason why the model is often left out in favor of hyperbolic equations such as in [94]. The model is still of interest as discussed in [89, 106] and should be seen as a universal starting point

rather than a comprehensive physical description; in particular, instabilities are expected to be damped as soon as dissipation is added [89]. As such, its discretization is an important and relevant issue.

## 1.2 Numerical discretization

This work is an extension of the cell-centered numerical scheme presented in [74] for multi-material single-velocity hydrodynamics. The original scheme is based on the so-called "La-grange + Remap" strategy [6, 50] where physical quantities are first computed on a moving mesh following the flow of the mixture (the Lagrange step) and are then projected on a new mesh whose choice is motivated by various user-controled criteria (the remapping step). This strategy becomes non-trivial in the context of multi-velocity flows as each material possesses its own Lagrangian trajectories. A common Lagrangian frame can be built from any average velocity of the mixture. The present work favors an alternative approach where each material evolves in its own Lagrangian frame before being projected back on a common mesh. Such a strategy will be referred to as "Multi-Lagrange + Remap" [21]. This formalism allows to exactly isolate the pressure terms in the Multi-Lagrange phase from the convection terms in the remapping phase, thus contributing to the convenient design of thermodynamically-consistent numerical schemes. In particular, compliance with the second principle of thermodynamics, namely preventing entropy destruction, is an essential requirement for multi-material schemes. Apart from providing stability and physically-sound results, distribution of entropy production between materials selects solutions inside shocks [55, 49, 74]; this issue is also explored in chapter 4 for two-temperature applications. Control of entropy production and its distribution will be the main guideline of the present work.

The Lagrange phase is based on the GLACE/EUCCLHYD method [71, 11, 70, 9]. Although the original scheme is built upon approximate Riemann solvers which fail to apply to elliptic equations, it can still be formally extended to a multi-velocity system. The present extension preserves total energy conservation while allowing for an arbitrary distribution of entropy production on the different materials. As for the remapping procedure, it prevents mesh entanglement which are usually unavoidable in pure Lagrangian computations. More generally, it allows changes of mesh during the simulation as in the Arbitrary Lagrange-Euler (ALE) setting [50, 9]. Designing such changes and measuring their relevance is not the focus of this work and solutions will only be projected on the initial mesh. In a "Multi-Lagrange + Remap" approach, the remapping must comply with to some constraints on volume conservation as well as on entropy production. As a result, it cannot be considered independent from the Lagrange step. This renders necessary a new approach to remapping which does not include usual face flux schemes.

The chapter is organized as follows. In section 2, the 6-equation model under consideration is presented. Explicit volume evolution equations are derived from the one-pressure assumption as in [108, 49]. Shocks and ellipticity are also discussed. In section 3, the numerical scheme is presented. The focus is put on the consequences and constraints of the multi-velocity aspects on the discretization. Finally, the numerical scheme is applied to various one-dimensional and two-dimensional test cases in section 4.

## 2   Multi-velocity model and thermodynamic closures

### 2.1   Core equations

The present model is written in Lagrangian formalism for an arbitrary number of materials. The notations are standard with $\alpha^k, \rho^k, \mathbf{u}^k$, and $e^k$ denoting the volume fraction, density, velocity and internal energy of material $k$. Each material is described by its own equation of state (EOS) which, in particular, defines its pressure $p^k$ as a function of $\rho^k$ and $e^k$. The EOS are arbitrary, provided they fulfill the thermodynamic constraints such as concavity of entropies $s^k$ and real speeds of sound $c^k$. Because each material possesses its own velocity, it defines its own Lagrangian derivative $\frac{\mathrm{d}^k}{\mathrm{d}t} = \frac{\partial}{\partial t} + \mathbf{u}^k \cdot \nabla$. The mass, momentum, and internal energy equations are thus

$$\alpha^k \rho^k \frac{\mathrm{d}^k}{\mathrm{d}t}\left(\frac{1}{\alpha^k \rho^k}\right) - \nabla \cdot \mathbf{u}^k = 0, \tag{3.1a}$$

$$\alpha^k \rho^k \frac{\mathrm{d}^k}{\mathrm{d}t}\mathbf{u}^k + \alpha^k \nabla p = 0, \tag{3.1b}$$

$$\alpha^k \rho^k \left[\frac{\mathrm{d}^k}{\mathrm{d}t}e^k + p^k \frac{\mathrm{d}^k}{\mathrm{d}t}\left(\frac{1}{\rho^k}\right)\right] = 0. \tag{3.1c}$$

Equations (3.1) are commonly obtained through a conditional averaging procedure introduced by numerous authors, among which [52] and summarized in [113] for non-miscible materials and in [49, app. B] for general mixtures. Single material Euler equations with discontinuous thermodynamic properties are initially considered. These equations undergo a material-conditional averaging procedure which allows specific material quantities to be defined. Finally, if fluctuations appearing in the averaging procedure are neglected the final model is naturally isentropic for each material. The internal energy equation of material $k$ thus corresponds to Gibbs identity $\mathrm{d}e^k = -p^k \mathrm{d}(1/\rho^k) + T^k \mathrm{d}s^k$ with $\mathrm{d}s^k = 0$. Correlation terms or other dissipative effects (e.g. viscosity, added mass,...) can be added separately.

Conservation of material masses and total momentum $\sum_k \alpha^k \rho^k u^k$ are naturally ensured. So is conservation of total energy as soon as the total pressure of the mixture is defined as

$$p = \sum_k \theta^k p^k, \tag{3.2a}$$

$$\theta^k = \frac{1}{\nabla \cdot \overline{\mathbf{u}}}\alpha^k \rho^k \frac{\mathrm{d}^k}{\mathrm{d}t}\left(\frac{1}{\rho^k}\right). \tag{3.2b}$$

Simple computations shows that $\sum_k \theta^k = 1$. Indeed, defining the volume averaged velocity

$$\overline{\mathbf{u}} = \sum_k \alpha^k \mathbf{u}^k, \tag{3.3}$$

it gives,

$$\sum_k \alpha^k \rho^k \frac{\mathrm{d}^k}{\mathrm{d}t} e^k = -\sum_k \alpha^k \rho^k p^k \frac{\mathrm{d}^k}{\mathrm{d}t} \left( \frac{1}{\rho^k} \right) \tag{3.4a}$$

$$= -\sum_k \theta^k p^k \nabla \cdot \overline{\mathbf{u}} \tag{3.4b}$$

$$= -p \nabla \cdot \overline{\mathbf{u}}, \tag{3.4c}$$

which eventually yields

$$\sum_k \alpha^k \rho^k \left[ \frac{\mathrm{d}^k}{\mathrm{d}t} e^k + \frac{\mathrm{d}^k}{\mathrm{d}t} \left( \frac{\|\mathbf{u}^k\|^2}{2} \right) \right] = -\nabla \cdot (p \overline{\mathbf{u}}) . \tag{3.5}$$

Although the averaging process alleviates the treatment of interfaces, some details of the flow are lost and, as such, model (3.1) is underdetermined. Thermodynamical closures then need to be provided and are of two different kinds.

- The first one concerns the evolution of either densities, volume fractions or pressures and ensures that the number of equations equals the number of unknowns. Such a closure is enough to fully describe isentropic regions of the flow. In the following, equality of material pressures will be discussed.

- The flow behavior still needs to be specified outside isentropic regions, namely inside shocks. Indeed, unlike single material shocks, multi-material ones are small-scale dependent which means that no complete jump relationships can be written without knowing the details of what is happening *inside* the shock [55]. Mathematically, this property comes from the fact that the system cannot be fully written in conservative form so that no canonical weak formulation exists [77].

## 2.2   Explicit volume closure for the equal pressure assumption

In the vast majority of multi-material systems, pressure relaxation processes between materials occur on time scales much smaller than the characteristic hydrodynamic time scales [55, 99]. Consequently, material pressures may be considered equal

$$p = p^k(\rho^k, e^k), \quad \forall k \in \{1, ..., n\}. \tag{3.6}$$

The underlying material expansion rates $\frac{\mathrm{d}^k}{\mathrm{d}t} \rho^k$ associated with the algebraic relationships (3.6) can be derived following the ideas introduced in [80] for isentropic flows and extended in [108, §3.5] for arbitrary entropy production. This new formulation allows to properly factor entropy production inside shocks which is essential to the present numerical strategy.

Through the coupling of pressures, the unknowns $\frac{\mathrm{d}^k}{\mathrm{d}t} \rho^k$ and $\frac{\partial}{\partial t} p$ all depend on each other. Consequently, a linear system, of which they are solution, is sought. The first equation is given

by total mass conservation and reads

$$\sum_k \left[ \rho^k \alpha^k \frac{\mathrm{d}^k}{\mathrm{d}t} \left( \frac{1}{\alpha^k \rho^k} \right) - \nabla \cdot \mathbf{u}^k \right] \alpha^k = 0$$

$$\Longleftrightarrow \sum_k \frac{\alpha^k}{\rho^k} \frac{\mathrm{d}^k}{\mathrm{d}t} \rho^k = -\nabla \cdot \overline{\mathbf{u}}. \tag{3.7}$$

On the other hand, differentiating (3.6) with respect to time gives

$$\frac{\partial}{\partial t} p = \frac{\mathrm{d}^k}{\mathrm{d}t} p^k - \mathbf{u}^k \cdot \nabla p. \tag{3.8}$$

Introducing the speed of sound $c^k$ and the Grüneisen coefficient $\Gamma^k$ [78] of material $k$

$$(c^k)^2 = \left. \frac{\partial p^k}{\partial \rho^k} \right|_{s^k}, \quad \Gamma^k = \frac{1}{\rho^k T^k} \left. \frac{\partial p^k}{\partial s^k} \right|_{\rho^k}, \tag{3.9}$$

pressure derivatives may be written as a function of density and entropy derivatives

$$\frac{\partial}{\partial t} p = (c^k)^2 \frac{\mathrm{d}^k}{\mathrm{d}t} \rho^k + \rho^k \Gamma^k T^k \frac{\mathrm{d}^k}{\mathrm{d}t} s^k - \mathbf{u}^k \cdot \nabla p. \tag{3.10}$$

Solving the system formed by equations (3.7) and (3.10) eventually yields

$$\alpha^k \rho^k \frac{\mathrm{d}^k}{\mathrm{d}t} \left( \frac{1}{\rho^k} \right) - \beta^k \nabla \cdot \overline{\mathbf{u}} + D^k = 0, \tag{3.11}$$

with

$$D^k = \frac{\alpha^k}{\rho^k (c^k)^2} \sum_l \beta^l \left[ (\mathbf{u}^k - \mathbf{u}^l) \cdot \nabla p + \Delta^{kl} \right], \tag{3.12a}$$

$$\beta^k = \frac{\alpha^k}{\rho^k (c^k)^2} \bigg/ \sum_l \frac{\alpha^l}{\rho^l (c^l)^2}, \tag{3.12b}$$

$$\Delta^{kl} = \rho^l \Gamma^l T^l \frac{\mathrm{d}^l}{\mathrm{d}t} s^l - \rho^k \Gamma^k T^k \frac{\mathrm{d}^k}{\mathrm{d}t} s^k. \tag{3.12c}$$

The term $\nabla \cdot \overline{\mathbf{u}}$ in equation (3.11) comes from mass conservation and, as such, is purely geometric. It corresponds, in some sense, to a global deformation rate of the mixture which is then shared between materials according to weighting coefficients $\beta^k$ ($\beta^k \geq 0$ and $\sum_k \beta^k = 1$). Because of these coefficients and their dependence on thermodynamics, some stiffness may appear, especially in mixtures with highly contrasted materials [49] (e.g. air and water when $\beta^{\mathrm{air}} >> \alpha^{\mathrm{air}}$). The second term, $D^k$, corresponds to a volume exchange rate (i.e. $\sum_k D^k = 0$) and is induced by both the velocity drift between materials and their entropy production.

## 2.3 Small-scale effect closure

Shocks are crucial phenomena in most hydrodynamic applications and demand specific care in terms of both physical modelling and numerical treatment. They correspond to zones where

quantities vary rapidly or even discontinuously in the vanishing viscosity limit. A notable feature of conservation laws (e.g. Euler equations) is that two states connected by a shock do not depend on its profile or on the underlying physical dissipation processes. This property does not extend to systems which are not fully conservative (e.g. model (3.1)) where shocks heavily depend on small-scale effects which do not always explicitly appear in the equations [55]. Both from physical and numerical points of view, it is a relevant issue to be able to characterize the range of admissible shocks.

In the case of the single fluid Euler equations, shocks are completely constrained by conservation of mass, momentum and total energy. Then, the resulting jump relationships (also known as the Rankine–Hugoniot equations in the theory of conservation laws) algebraically close the shock. The set of all right states which can be connected to a given left state through a left-moving or right-moving shock (i.e. a 1-shock or a 3-shock in mathematical terms) forms a one dimensional half-curve called the shock locus whose projection on the $p - 1/\rho$ plane is known as the Hugoniot curve []. This essentially means that once the amplitude of the shock is given, other variables are immediately recovered as a consequence of conservation, including the shock speed.

In the case of multi-material equations, this locus becomes a larger dimension object as illustrated in figure 3.1. The new dimensions offers new degrees of freedom and correspond to the total number of equations of the system minus the number of conserved quantities. For model (3.1) with $n$ materials, this number is $2(n-1)$. Hence, for a given amplitude, several shocks are admissible depending on the underlying short-wavelength phenomena. These phenomena include drag, viscosity, heat exchange, added mass, and surface tension among others. Their number is way larger than the number of degrees of freedom which shows that multiple physical regularizations can define shocks connecting the same left and right states (although the details of the shock's profile may still be different). Generally speaking, the regularized equations read

$$\alpha^k \rho^k \frac{\mathrm{d}^k}{\mathrm{d}t} \mathbf{u}^k + \alpha^k \nabla p = \varepsilon F^k, \tag{3.13a}$$

$$\alpha^k \rho^k \left[ \frac{\mathrm{d}^k}{\mathrm{d}t} e^k + p^k \frac{\mathrm{d}^k}{\mathrm{d}t} \left( \frac{1}{\rho^k} \right) \right] = \varepsilon \lambda^k Q. \tag{3.13b}$$

where

- $\varepsilon$ is an arbitrarily small parameter controlling the width and steepness of the shock. The smaller $\varepsilon$ is, the more narrow and steep the shock is.

- The term $\mathbf{F}^k$ is a global force acting on material $k$. It may include individual (i.e. only concerning material $k$) terms such as viscosity, as well as exchanges of momentum between materials such as drag. Because of total momentum conservation, the sum $\sum_k \mathbf{F}^k$ must correspond to a flux term, hence the $n-1$ first degrees of freedom.

- Because of total energy conservation, the sum of powers $-\sum_k \mathbf{u}^k \cdot \mathbf{F}^k$ is equal, up to a flux, to the total heat deposit $Q > 0$. It is then distributed among materials with respect to coefficients $\lambda^k$. According to Gibb's identity, $\varepsilon \lambda^k Q$ corresponds to the entropy variation $\alpha^k \rho^k T^k \frac{\mathrm{d}}{\mathrm{d}t} s^k$ of material $k$. If not heat exchange between materials is present (adiabatic
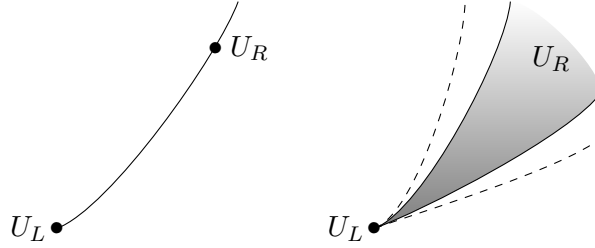
Figure 3.1: Schematic representation of the right states $U_R$ which can be connected by a shock to a given left state $U_L$. Left : the case where all equations are conservation laws. The curve is one dimensional and $U_R$ is completely determined by the shock amplitude. Right: the case where some equations cannot be written in conservative form. For a given shock amplitude, multiple states $U_R$ are admissible. The gray region corresponds to the zone inside which each material entropy increases. The larger zone encircled by the dashed lines corresponds to the addition of heat exchange which allows some material entropy to decrease as long as the global entropy still increases.

closure), coefficients $\lambda^k$ are positive and such that $\sum_k \lambda^k = 1$, hence the remaining $n-1$ degrees of freedom.

This interaction between the different terms is represented in figure 3.2. Equation (3.13b) and positivity of $Q$ and $\lambda^k$ shows that material entropies all increase with time which is a sufficient condition for the total entropy to increase, thus complying with the second principle of thermodynamics. Yet, it is not necessary as an additional heat exchange could decrease one material entropy while still inducing a total entropy production. With only incomplete EOS, temperatures are not accessible and there is no way of knowing if a given heat exchange is indeed entropic: this is why it has been excluded here. Nevertheless, it shows that heat exchange could increase the size of the locus defined by conditions (3.13a) and (3.13b) as represented by the dashed curves in figure 3.1. It is not a new degree of freedom *per se* as the dimension of the augmented locus remains the same. In this sense, (3.13) $\lambda^k \geq 0$ should spread $U_R$ over all degrees of freedom although not over their entire range.

**Remark 9.** Theories have been developed to properly define weak solutions through the addition of a path describing the profile of travelling waves [77]. If this formalism offers a solid mathematical background and has been used to extend Godunov-type schemes to non-conservative hyperbolic systems [33, 15], its physical interpretation is not always clear. As a consequence, its use for physics-driven applications is usually not straightforward. It will not be considered hereafter.

## 2.4   The elephant in the room : ellipticity of the model

Model (3.1) together with the equal pressure assumption (3.6) is known to display elliptic behavior. This feature sparked much controversy in the community as ellipticity predicts unstable behavior at vanishing small scales, effectively rendering impossible any simulation on fine meshes [21]. This chapter does not aim at extensively discussing the complex link between ellipticity and stability in the context of non-linear equations. Contributions may be found in [89, 57, 106]. The stance retained in this chapter follows [106, app. A and refs therein].

$$\mathbf{F}^1 + \quad \cdots \quad + \mathbf{F}^n \ = \text{Flux}$$

$$\mathbf{u}^1 \cdot \mathbf{F}^1 \quad \cdots \quad \mathbf{u}^n \cdot \mathbf{F}^n$$

$$\left.\begin{array}{c} \displaystyle\sum_k \mathbf{u}^k \cdot \mathbf{F}^k \\ + \\ Q \end{array}\right\} = \text{Flux}$$

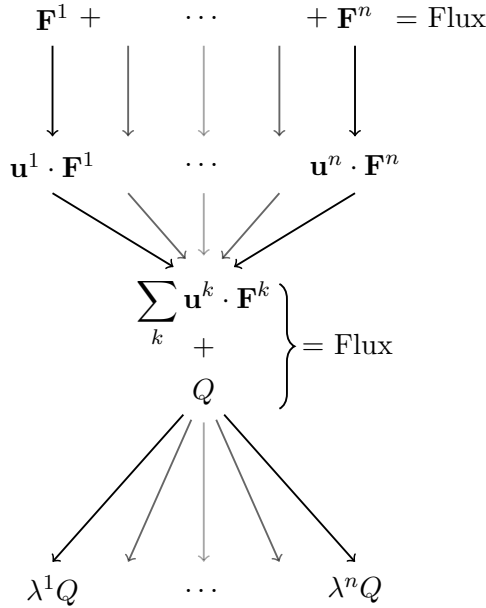$$\lambda^1 Q \quad \cdots \quad \lambda^n Q$$

Figure 3.2: Diagram displaying the physical origin of the different degrees of freedom. They all hinge around total energy conservation which allows some of the total kinetic energy to be transformed into a heat deposit. The loss of kinetic energy and increase in internal energy can both be freely shared among materials. In doing so, each of them provide $n-1$ degrees of freedom on the right state of a shock.

- Model (3.1)-(3.6) is a *universal* starting point for any description of multi-material flows. Indeed, the model relies on the strong physical basis that is the least action principle [37, 108]. It may also be derived through an averaging procedure from the Euler equations whose well-posedness is widely accepted. Hence, the model is essentially correct up to some correlation terms which have been neglected as a first approximation after the averaging.

- Small-scale effects (3.13) then need to be added to amend for the lack of these correlation terms. Apart from providing closures inside shocks (as discussed previously), they also damp short wavelength instabilities. As pointed out in [89], the model is still successful at predicting long wavelength behaviors such as Kelvin–Helmotz instabilities. Consequently, any small-scale effect that should be introduced should not be so intrusive as to seriously modify these phenomena.

With that being said, model (3.1) supplemented with (3.6) (i.e. the "universal" part of the model) will be discretized as it is. In practice, a well-controlled numerical scheme should mimick equations (3.13) at the discrete level. In this case, $\varepsilon$ is implicitly related to both the cell characteristic lengths and the order of the scheme. It is also inversely proportional to an underlying cutoff frequency beyond which instabilities are damped. Refining the mesh then allows the growth of instabilities at larger and larger frequencies, to the point where it may abruptly stop the simulation. Results can still be obtained on coarse enough meshes.
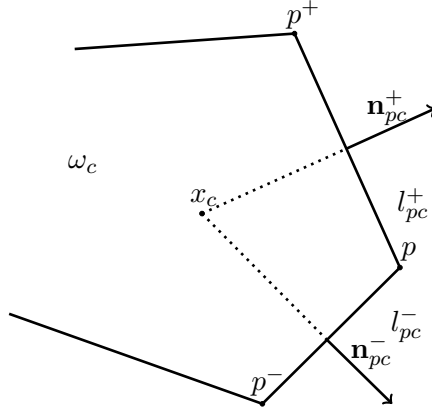
Figure 3.3: Cell notations.

# 3 Numerical strategy

## 3.1 Geometry and notations

The notations are similar to those introduced in [72, 19, 74]. Each cell is assigned a unique index $c$ and is denoted by $\omega_c$. Its volume is $V_c$. The two-dimensional cells are assumed to be polygonal so that they are defined by the set of their nodes $\mathcal{P}(c)$. For a given node $p$, $\mathbf{x}_p$ and $\mathbf{u}_p$ are its position and velocity while $\mathcal{C}(p)$ is the set of cells that contain $p$. Corner vectors [40] are given by

$$l_{pc}\mathbf{n}_{pc} = \frac{\partial V_c}{\partial \mathbf{x}_p}, \tag{3.14}$$

where $\mathbf{n}_{pc}$ is a unit vector. They can equivalently be constructed as follows : $p^+$ is the node in $\mathcal{P}(c)$ which follows $p$ in counterclockwise order and $p^-$ the previous node. Let $\mathbf{n}_{pc}^+$ be the outward normal unit vector to the edge $pp^+$ and define $l_{pc}^+ = \frac{1}{2}\|pp^+\|$ ($\mathbf{n}_{pc}^-$ and $l_{pc}^-$ are defined accordingly). Finally

$$\mathbf{n}_{pc} = \frac{l_{pc}^+\mathbf{n}_{pc}^+ + l_{pc}^-\mathbf{n}_{pc}^-}{l_{pc}}, \tag{3.15a}$$

$$l_{pc} = \left\|l_{pc}^+\mathbf{n}_{pc}^+ + l_{pc}^-\mathbf{n}_{pc}^-\right\|_2. \tag{3.15b}$$

All the notations are illustrated in figure 3.3.

## 3.2 Global strategy

The present chapter aims at extending the work introduced in [74] for a single velocity model (1.5). This previous scheme relies on a Lagrange+Remap approach, meaning that each time step consists in two main phases plus an additional pressure equilibration procedure.

- The Lagrangian phase is based on an extension of the GLACE/EUCCLHYD [11, 70] scheme to a multi-material one pressure setting. The GLACE/EUCCLHYD scheme is

Lagrangian, cell-centered and allows a semi-discrete entropy production to be written as

$$m_c T_c \frac{\mathrm{d}}{\mathrm{d}t} s_c = m_c \left[ \frac{\mathrm{d}}{\mathrm{d}t} e_c + p_c \frac{\mathrm{d}}{\mathrm{d}t} \left( \frac{1}{\rho_c} \right) \right]$$
$$= \sum_{p \in \mathcal{P}(c)} (\mathbf{u}_p - \mathbf{u}_c)^{\mathrm{T}} \mathbf{M}_{pc} (\mathbf{u}_p - \mathbf{u}_c), \qquad (3.16)$$

where $\mathbf{M}_{pc}$ are symmetric positive matrices ensuring that the entropy increases. Their exact expression is what distinguishes GLACE from EUCCLHYD. The main ingredients of the multi-material extension concern the evolution equations for the densities and the thermodynamical consistency for the internal energy equations. The density equations ensure equality of pressures up to the time order of the scheme. Once they have been specified, internal energies evolve consequently

$$\frac{\mathrm{d}}{\mathrm{d}t} e_c^k = -p_c \frac{\mathrm{d}}{\mathrm{d}t} \left( \frac{1}{\rho_c^k} \right) + T_c^k \frac{\mathrm{d}}{\mathrm{d}t} s_c^k. \qquad (3.17)$$

where $\alpha^k \rho^k T^k \frac{\mathrm{d}}{\mathrm{d}t} s^k$ is taken as an arbitrary portion of the total irreversible work of the scheme (3.16). This ensures thermodynamic consistency as each material entropy increases over time. The arbitrary distribution of the total irreversible work also allows to capture different solutions in keeping with the discussion of section 2.3.

- Once all material quantities have evolved on the Lagrangian mesh, they are remapped on the initial mesh. The remapping procedure is essentially independant of the chosen strategy for the Lagrangian step. An Alternate Direction projection [32] is chosen for its entropic character (to first order), easy extensions to second order, and overall simplicity.

- Finally, an equilibration procedure is added so as to enforce pressure equality up to machine precision. This procedure relies on an iterative method (here Newton's method) to solve the following non-linear system of equations

$$\sum_k (\alpha \rho)^{k,n+1} e^{k,n+1} = \sum_k (\alpha \rho)^{k,n+1} e^{k,\star}, \qquad (3.18a)$$

$$e^{k,n+1} - e^{k,\star} = -p \left( \frac{1}{\rho^{k,n+1}} - \frac{1}{\rho^{k,\star}} \right), \qquad (3.18b)$$

$$p = p^k (\rho^{k,n+1}, e^{k,n+1}). \qquad (3.18c)$$

where the exponent $\star$ is used for the quantities before correction and $n+1$ for the corrected variables. This system, by virtue of its implicit pressure work [62, 49], prevents entropy destruction while conserving total volume and total energy of the system.

Extending this approach to a multi-velocity model is no simple task. The main challenge comes from the very definition of the Lagrangian phase as there exists as many Lagrangian frames as there are materials. The choice retained for this work consists in a "Multi-Lagrange + Remap" approach where all quantities associated with a given material are first computed on its own Lagrangian frame as in [21]. Quantities then evolve on different frames before being projected on a common mesh, which is here taken as the initial one (see figure 3.4). Finally, the
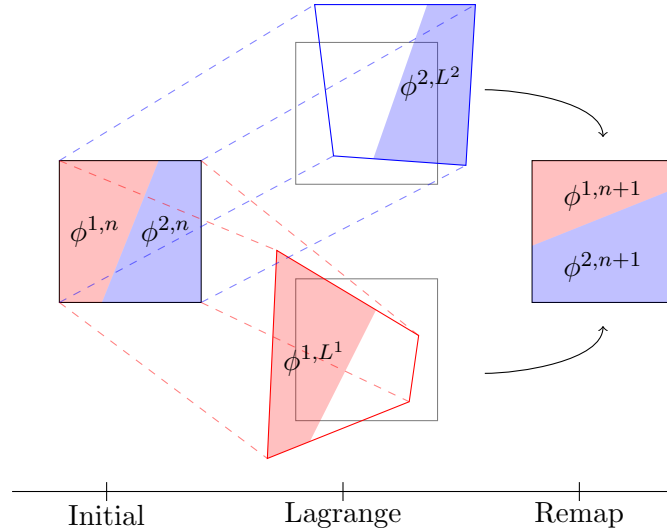
Figure 3.4: Schematic representation of the "Multi-Lagrange + Remap" approach with two materials. The notation $L^k$ is used for quantities computed on the Lagrangian frame of material $k$.

pressure relaxation procedure is not concerned with the multi-velocity aspects and is thus left unchanged.

The multi-Lagrange and the remapping steps will be presented in sections 3.4 and 3.5 respectively. Both discussions will be carried out in the light of the general common theme that is entropy. In the Lagrangian phase, entropy production is mainly given by what may be interpreted as numerical viscosity and which is shown to be constrained by the GLACE/EUCCLHYD setting. As for the remapping procedure, entropy considerations heavily constrain it and, contrary to the single velocity scheme, total volume conservation binds it to the Lagrange phase. Before delving into these issues, a global overview of entropy production of the scheme is given in section 3.3. It serves as a foundation for the following discussions and justifies the adamant requirements on entropy.

## 3.3 Considerations on entropy

Control of entropy production is a key ingredient for all multi-material compressible schemes. It serves two main purposes, namely stabilizing and selecting solutions of interest. Stabilization ensures that numerical simulations do not explode over time, especially around shocks where a strict entropy inequality is required [110, 64]. More generally, it ensures that solutions are physically admissible as destroying entropy could create spurious shocks inside what should be rarefaction waves. Secondly, as explained in section 2.3, ensuring an entropy inequality is not sufficient to fully define solutions; the details of entropy production are then crucial to properly select solutions inside shocks and consist in the second $n - 1$ degrees of freedom identified in section 2.3.

A comprehensive list of entropy sources in the present numerical scheme is now given.

- The main source of entropy is introduced during the Lagrange phase where some kind of numerical viscosity is added to the pressure work in the internal energy equations. If

the total irreversible work $Q$ is known explicitly, then it may be shared *arbitrarily* among materials

$$\alpha^k \rho^k \left[ \frac{\mathrm{d}^k}{\mathrm{d}t} e^k + p \frac{\mathrm{d}^k}{\mathrm{d}t} \left( \frac{1}{\rho^k} \right) \right] = \lambda^k Q, \tag{3.19}$$

where $\lambda^k$ are arbitrary coefficients between 0 and 1 whose sum over all materials is 1. Changing the coefficients will change the numerical solution inside shocks, even at convergence [49, 74]. Their specification must then be driven by physics and cannot reasonably be determined by numerical considerations alone.

- The second main source of entropy (and more generally of numerical diffusion) is the remapping step. A sensible remapping procedure should consist in some sort of averaging. Convex inequalities then ensure that no entropy is destroyed over time. If it provides strong robustness, the remapping procedure may induce accuracy issues as its underlying numerical diffusion pollutes the numerical viscosity terms. Their sum acts as an *effective* viscosity which remains partially uncontroled, thus inducing some potential convergence issues [66, 49] for systems whose shock are small-scale dependent. These can still be mitigated by a higher order remapping procedure and, more generally, consist in a compromise between accuracy and robustness. This discussion also applies to the following items of the list for which entropy distribution is also not controlled, although their effect is not as substantial as for the remapping procedure.

- Pressure equilibration also creates an entropy residue. Its sign is always positive thanks to the implicit pressure formulation [62, 49, 74]. Because pressures are already equal up to the scheme order, this residue may be deemed minor compared to the other entropy contributions.

- Time integration of pressure work produces an additional entropy residue whose sign depends on the time at which pressure is taken. Implicit pressure will always result in a positive entropy production while explicit pressure will always destroy entropy [49]. Once again, this entropy contribution is minor compared to the other entropy contribution but still needs to be taken into account for demanding test cases [49].

- Finally, the conservation law

$$\frac{\partial}{\partial t} \sum_k \alpha^k = 0 \tag{3.20}$$

must also be satisfied at the discrete level. If the spatial discretization fails to preserve the sum of volume fractions, one might be tempted to add, what would seem at first, a mere normalization step. However, because masses must be conserved, products $\alpha^k \rho^k$ cannot be modified. Changes in volume fractions $\alpha^k$ then carry out as changes in densities $\rho^k$ which, in turn, alter entropy. More precisely, if the sum $\sum_k \alpha^k$ is greater than 1 at the end of a time iteration, then normalization will reduce volume fractions and increase densities $\rho^k$, thus destroying entropy for all materials (for positive pressures). This issue will be further discussed in section 3.5.

### 3.4  Multi-Lagrange phase

**Conservation of total momentum and total energy**

Momentum and internal energy equations must be discretized in a consistent manner with (3.13) so as to produce stable results, particularly in the vicinity of shocks. In the single fluid GLACE/EUCCLHYD scheme, (3.16) serves this very purpose and may be interpreted as a form of numerical viscosity. However, the exact expression of the numerical viscosity comes from approximate Riemann solvers at the nodes. Consequently, fluxes act as black boxes where both pressure and viscous terms are intertwined. They cannot be separated in the sense that it is not possible to find an estimation of the gradient $[\nabla p]_c$ such that

$$p_c[\nabla \cdot \mathbf{u}]_c + \mathbf{u}_c \cdot [\nabla p]_c \tag{3.21}$$

is a flux. Details may be found in appendix D. This failure has two major consequences : (1) numerical viscosity cannot be removed from the scheme in regions where it is not needed (e.g. rarefaction waves); (2) its discretization must take into account that of the pressure terms. The latter consequence heavily constrains the discretization of total momentum and total energy so as to ensure conservation of both. A possibility is to take

$$m_c^k \frac{\mathrm{d}^k}{\mathrm{d}t} \mathbf{u}_c^k = \alpha_c^k \sum_{p \in \mathcal{P}(c)} \mathbf{M}_{pc}(\overline{\mathbf{u}}_p - \overline{\mathbf{u}}_c), \tag{3.22a}$$

$$\sum_k m_c^k \frac{\mathrm{d}^k}{\mathrm{d}t} e_c^k = -p_c \sum_{p \in \mathcal{P}(c)} l_{pc} \mathbf{n}_{pc} \cdot \overline{\mathbf{u}}_p + \sum_{p \in \mathcal{P}(c)} (\overline{\mathbf{u}}_p - \overline{\mathbf{u}}_c)^{\mathrm{T}} \mathbf{M}_{pc}(\overline{\mathbf{u}}_p - \overline{\mathbf{u}}_c). \tag{3.22b}$$

**Proposition 4.** Equations (3.22) ensure conservation of both total momentum and total energy provided that

$$\overline{\mathbf{u}}_p = \mathbf{M}_p^{-1} \sum_{c \in \mathcal{C}(p)} [\mathbf{M}_{pc}\overline{\mathbf{u}}_c + p_c l_{pc} \mathbf{n}_{pc}] \tag{3.23}$$

with $\mathbf{M}_p = \sum_{c \in \mathcal{C}(p)} \mathbf{M}_{pc}$.

*Proof.* The proof follows the approach introduced in [71]. Node forces are defined by

$$\mathbf{F}_{pc} = -p_c l_{pc} \mathbf{n}_{pc} + \mathbf{M}_{pc}(\overline{\mathbf{u}}_p - \overline{\mathbf{u}}_c). \tag{3.24}$$

Summing equation (3.22a) over all materials gives the total momentum evolution

$$\sum_k m_c^k \frac{\mathrm{d}^k}{\mathrm{d}t} \mathbf{u}_c^k = \sum_{p \in \mathcal{P}(c)} \mathbf{M}_{pc}(\overline{\mathbf{u}}_p - \overline{\mathbf{u}}_c) \tag{3.25a}$$

$$= \sum_{p \in \mathcal{P}(c)} [-p_c l_{pc} \mathbf{n}_{pc} + \mathbf{M}_{pc}(\overline{\mathbf{u}}_p - \overline{\mathbf{u}}_c)] \tag{3.25b}$$

$$= \sum_{p \in \mathcal{P}(c)} \mathbf{F}_{pc}. \tag{3.25c}$$

Pressure terms have been artificially added although they do not contribute to the sum (because $\sum_{p \in \mathcal{P}(c)} l_{pc} \mathbf{n}_{pc} = 0$). On the other hand, lengthy algebraic computations show that the total

energy is given by

$$\sum_k m_c^k \left[ \frac{\mathrm{d}^k}{\mathrm{d}t} \frac{|\mathbf{u}_c^k|^2}{2} + \frac{\mathrm{d}^k}{\mathrm{d}t} e_c^k \right] = \sum_{p \in \mathcal{P}(c)} \mathbf{F}_{pc} \cdot \overline{\mathbf{u}}_c. \tag{3.26a}$$

A local (nodal) conservation property is sought and reads

$$\sum_{c \in \mathcal{C}(p)} \mathbf{F}_{pc} = 0, \tag{3.27a}$$

$$\sum_{c \in \mathcal{C}(p)} \mathbf{F}_{pc} \cdot \overline{\mathbf{u}}_c = 0. \tag{3.27b}$$

Factorizing $\overline{\mathbf{u}}_c$ in (3.27b) shows that the latter equation is a direct consequence of the former, which is itself satisfied as soon as $\overline{\mathbf{u}}_p$ is defined by (3.23). $\qquad\square$

**Remark 10.** It is not immediately clear that the right-hand side of (3.22a) is consistent with a pressure gradient. Injecting expression (3.23) in (3.22a) makes it more apparent. Details may be found in [28] and appendix D.

**Remark 11.** The original derivation of the single material scheme [11] is based on nodal solvers which define node pressures fluxes from linearized jump relationships. Thanks to total momentum conservation, such an approach can be naturally extended and gives the following discretization

$$m_c^k \frac{\mathrm{d}^k}{\mathrm{d}t} \mathbf{u}_c^k = \alpha_c^k \sum_{p \in \mathcal{P}(c)} \mathbf{M}_{pc}(\hat{\mathbf{u}}_p - \hat{\mathbf{u}}_c), \tag{3.28a}$$

$$\hat{\mathbf{u}}_p = \mathbf{M}_p^{-1} \sum_{c \in \mathcal{C}(p)} \left[ \mathbf{M}_{pc}\hat{\mathbf{u}}_c + p_c l_{pc}\mathbf{n}_{pc} \right]. \tag{3.28b}$$

with $\hat{\mathbf{u}}_c = \sum_k c^k \mathbf{u}_c^k$. Total energy conservation then gives

$$\sum_k m_c^k \frac{\mathrm{d}^k}{\mathrm{d}t} e_c^k = -p_c \sum_{p \in \mathcal{P}(c)} l_{pc}\mathbf{n}_{pc}\overline{\mathbf{u}}_p + \sum_{p \in \mathcal{P}(c)} (\hat{\mathbf{u}}_p - \hat{\mathbf{u}}_c)^{\mathrm{T}}\mathbf{M}_{pc}(\overline{\mathbf{u}}_p - \overline{\mathbf{u}}_c). \tag{3.29}$$

Although this alternate scheme is quite appealing as it leans on the well-established ideas of Godunov's type scheme and approximate Riemann solvers, it is no longer consistent with thermodynamics. Indeed, the term $\sum_{p \in \mathcal{P}(c)} (\hat{\mathbf{u}}_p - \hat{\mathbf{u}}_c)^{\mathrm{T}}\mathbf{M}_{pc}(\overline{\mathbf{u}}_p - \overline{\mathbf{u}}_c)$ cannot be interpreted as a squared norm and may become negative. As explained in the next section 3.4, it may result in entropy destruction which is ultimately why this scheme has been excluded.

### Density, internal energy and entropy equations through thermodynamical consistency

The discussion conducted in the previous section 3.4 are deeply tied to the GLACE/EUCCLHYD formalism. Although total momentum and total energy conservation should be a universal concern, the provided answer to this issue is specific to the present approach. The following discussion has however a larger scope. It is rooted in thermodynamical consistency and should apply

to a wide range of multi-material schemes (as in [108] for instance). Internal energy, density, and entropy discretizations are related to each other through Gibbs identity. It is the first step to warrant thermodynamic consistency of the scheme.

$$\frac{\mathrm{d}^k}{\mathrm{d}t}e_c^k = -p_c\frac{\mathrm{d}^k}{\mathrm{d}t}\left(\frac{1}{\rho_c^k}\right) + T_c^k\frac{\mathrm{d}^k}{\mathrm{d}t}s_c^k. \tag{3.30}$$

Both density and entropy evolution rates are chosen to guarantee that (3.30) is compatible with (3.22b). The geometric term $\nabla\cdot\overline{\mathbf{u}}$ is identified as $\sum_{p\in\mathcal{P}(c)}l_{pc}\mathbf{n}_{pc}\overline{\mathbf{u}}_p$ in equation (3.22b). It is then shared between materials with respect to coefficients $\beta_c^k$. A consistent discretization $D_c^k$ of the exchanges (3.12a) is added to complete the density evolution

$$m_c^k\frac{\mathrm{d}^k}{\mathrm{d}t}\left(\frac{1}{\rho_c^k}\right) = \beta_c^k\sum_{p\in\mathcal{P}(c)}l_{pc}\mathbf{n}_{pc}\overline{\mathbf{u}}_p + D_c^k, \tag{3.31a}$$

$$D_c^k = \frac{\alpha_c^k}{\rho_c^k(c_c^k)^2}\sum_l\beta_c^l\left[(\mathbf{u}_c^k - \mathbf{u}_c^l)\cdot\sum_{p\in\mathcal{P}(c)}\mathbf{M}_{pc}(\overline{\mathbf{u}}_p - \overline{\mathbf{u}}_c) + \Delta_c^{kl}\right], \tag{3.31b}$$

$$\Delta_c^{kl} = \frac{\Gamma_c^l}{\alpha_c^l}m_c^lT_c^l\frac{\mathrm{d}^l}{\mathrm{d}t}s_c^l - \frac{\Gamma_c^k}{\alpha_c^k}m_c^kT_c^k\frac{\mathrm{d}^k}{\mathrm{d}t}s_c^k. \tag{3.31c}$$

Finally, the total heat deposit is identified in (3.22b) to be $\sum_{p\in\mathcal{P}(c)}(\overline{\mathbf{u}}_p - \overline{\mathbf{u}}_c)^{\mathrm{T}}\mathbf{M}_{pc}(\overline{\mathbf{u}}_p - \overline{\mathbf{u}}_c)$. As in (3.19), it is shared arbitrarily between materials with respect to coefficients $\lambda_c^k$

$$m_c^kT_c^k\frac{\mathrm{d}^k}{\mathrm{d}t}s_c^k = \lambda_c^k\sum_{p\in\mathcal{P}(c)}(\overline{\mathbf{u}}_p - \overline{\mathbf{u}}_c)^{\mathrm{T}}\mathbf{M}_{pc}(\overline{\mathbf{u}}_p - \overline{\mathbf{u}}_c). \tag{3.32}$$

If both the total heat deposit and coefficients $\lambda_c^k$ are positive, the next proposition immediately follows.

**Proposition 5.** The semi-discrete Lagrangian procedure increases entropy inside each cell and for each material

$$\frac{\mathrm{d}^k}{\mathrm{d}t}s_c^k \geq 0. \tag{3.33}$$

To conclude this section on thermodynamic consistency, the expression of the matrices $\mathbf{M}_{pc}$ is now discussed. The matrices are symmetric in order to ensure a positive total heat deposit. As in [71, 70], they are chosen to be proportional to

$$\mathbf{M}_{pc} \propto \left(l_{pc}^+\mathbf{n}_{pc}^+\otimes\mathbf{n}_{pc}^+ + l_{pc}^-\mathbf{n}_{pc}^-\otimes\mathbf{n}_{pc}^-\right). \tag{3.34}$$

The amplitude must ensure sufficient dissipation so as to produce a stable scheme. It is usually given by $\rho c$ where $\rho$ is the density of the mixture and $c$ is its the speed of sound. For multi-velocity hydrodynamics, the latter is bounded by its value at zero drag [76]

$$c_c^2 = \sum_k\beta_c^k(c_c^k)^2. \tag{3.35}$$

In practice, this choice did not produce stable computations; it was replaced with

$$c_c^2 = \sum_k \frac{(\alpha\rho)_c^k}{\rho_c}(c_c^k)^2. \tag{3.36}$$

In the case of a mixture of air and water, the latter choice is a rough overestimation which should produce excessive dissipation. Properly tuning it would require further studies.

**Lagrangian volume and node velocities**

The derivation of Lagrangian volume equations are quite straightforward. The only essential modification from the single material scheme is the fact that as many equations as there are materials are now needed.

$$m_c^k \frac{\mathrm{d}^k}{\mathrm{d}t}\left(\frac{1}{(\alpha\rho)_c^k}\right) = \sum_{p\in\mathcal{P}(c)} l_{pc}\mathbf{n}_{pc}\cdot\mathbf{u}_p^k. \tag{3.37}$$

The term $l_{pc}\mathbf{n}_{pc}\cdot\mathbf{u}_p^k$ is a node flux ensuring conservation of total volume. The conservation is local as the sum of fluxes over all cells of a given node is zero (as in the proof of proposition 4). Equation (3.37) may be seen as a consistent discretization of equation (3.1a). It also corresponds to the derivative of the Lagrangian volume, using the chain rule and the formula $\frac{\partial V_c}{\partial \mathbf{x}_p} = l_{pc}\mathbf{n}_{pc}$. This double interpretation is why equation (3.37) is often referred to as the Geometric Conservation Law [101].

The remaining difficulty lies in the definition of material node velocities $\mathbf{u}_p^k$. Up until now, only the average node velocity $\overline{\mathbf{u}}_p$ is known (3.23). It is then natural to enforce equality

$$\overline{\mathbf{u}}_p = \sum_k \alpha_p^k \mathbf{u}_p^k, \tag{3.38}$$

where node estimates of volume fractions $\alpha_p^k$ still need to be specified. Equation (3.38) will be shown to have profound consequences on the remapping procedure and $\alpha_p^k$ will only then be defined. From (3.38), material node velocities are taken as

$$\mathbf{u}_p^k = \mathbf{M}_p^{-1}\sum_{c\in\mathcal{C}(p)}\left[\mathbf{M}_{pc}\mathbf{u}_c^k + p_c l_{pc}\mathbf{n}_{pc}\right] + C_p, \tag{3.39a}$$

$$C_p = \sum_k \mathbf{M}_p^{-1}\left[\sum_{c\in\mathcal{C}(p)}\mathbf{M}_{pc}\alpha_c^k\mathbf{u}_c^k - \alpha_p^k\sum_{c\in\mathcal{C}(p)}\mathbf{M}_{pc}\mathbf{u}_c^k\right]. \tag{3.39b}$$

$C_p$ is a covariance term that may also be written $\sum_k \mathbb{E}_p[\alpha^k\mathbf{u}^k] - \mathbb{E}_p[\alpha^k]\mathbb{E}_p[\mathbf{u}^k]$ where $\mathbb{E}_p[X]$ is some node estimation of $X$. It is necessary for (3.38) but might be negligible in practice.

**Time integration**

A standard Euler forward strategy is chosen for the time discretization. The scheme is then explicit, all spatial terms derived in the previous sections being taken at the initial time. In keeping with [20], some caution still needs to be exercised on the velocity $\overline{\mathbf{u}}_c$ for discrete total

energy conservation.

$$m_c^k \frac{e_c^{k,L^k} - e_c^{k,n}}{\Delta t} = -p_c^n \frac{m_c^k}{\Delta t} \left( \frac{1}{\rho_c^{k,L^k}} - \frac{1}{\rho_c^{k,n}} \right) + \lambda_c^k \sum_{p \in \mathcal{P}(c)} (\overline{\mathbf{u}}_p^n - \overline{\mathbf{u}}_c^n)^{\mathrm{T}} \mathbf{M}_{pc}^n \left( \overline{\mathbf{u}}_p^n - \frac{\overline{\mathbf{u}}_c^n + \overline{\mathbf{u}}_c^L}{2} \right). \quad (3.40)$$

The exponent $L^k$ is used for the quantities computed in the Lagrangian frame of material $k$ and

$$\overline{\mathbf{u}}_c^L = \sum_k \alpha_c^{k,n} \mathbf{u}_c^{k,L^k}. \quad (3.41)$$

The resulting scheme is still fully explicit as velocities are computed before internal energies. As stated earlier, although the semi-discrete scheme is strictly entropic for each material, time integration may destroy small amounts of entropy. It does so through the explicit time integration of pressure work [49] and the discrete energy deposit in (3.40) where the half sum $(\overline{\mathbf{u}}_c^n + \overline{\mathbf{u}}_c^L)/2$ prevents it from being a perfect squared norm.

The time step $\Delta t$ is subject to two constraints. First, a CFL-like condition accounts for the propagation of acoustic waves. It reads

$$\Delta t = \mathrm{CFL} \times \min_{k,c} \left( \frac{V_c}{P_c(c_c + \|\mathbf{u}_c^k\|)} \right), \quad (3.42)$$

where $V_c$ is the volume of the cell, $P_c$ its perimeter and $c_c$ the speed of sound of the mixture (3.36). CFL is a parameter, of the order of 1, which must be tuned. Additionally, $\Delta t$ is chosen so as to prevent cell volumes and volume fractions from becoming negative.

## 3.5 Remap phase : Lagrange/Remap consistency and volume conservation

The following discussion is restricted to the one dimensional scheme where cells are ordered from left to right by indexes $i \in \mathbb{Z}$ while nodes are denoted by half-integers $i + \frac{1}{2}$. The one dimensional setting is sufficient to illustrate the necessity of some form of consistency between the Lagrange an the remapping, as well as how the issue was tackled in the present work. The general multi-dimensional remapping procedure may be found in appendix E.

### From volume conservation to a common diffusion

In the context of a Multi-Lagrange+Remap approach, enforcing the volume filling condition (3.20) at the discrete level is no simple matter. Because each $\alpha^k$ is first computed on its own Lagrangian frame, the sum may not be conserved during the Lagrange step, nor may it be maintained during the remapping step. It is then crucial to ensure that both steps compensate each other as best as possible. Failing to do so would make the normalization step all the more intrusive which, as explained in 3.3, may jeopardize the scheme stability and its consistency with thermodynamics.

In practice, the divergence term $\nabla \cdot \overline{\mathbf{u}}$ appearing in the Lagrange step (3.7) must cancel with the sum of the remapping fluxes for the volume fractions $\sum_k \nabla \cdot (\alpha^k \mathbf{u}^k)$. It should not come as a surprise considering the computations performed in (3.7) and the geometric nature of the

term $\nabla \cdot \overline{\mathbf{u}}$. In one dimension, the sum over all materials of equation (3.11) yields

$$\sum_k \left(V_i^{k,L^k} - V_i^{k,n}\right) = \Delta t \left(\overline{u}_{i+\frac{1}{2}} - \overline{u}_{i-\frac{1}{2}}\right),$$ (3.43)

while a generic remapping procedure should be written

$$\sum_k \left(V_i^{k,n+1} - V_i^{k,L^k}\right) = -\Delta t \sum_k \left((\alpha u)_{i+\frac{1}{2}}^k - (\alpha u)_{i-\frac{1}{2}}^k\right),$$ (3.44)

where $(\alpha u)_{i+\frac{1}{2}}^k$ are node flux estimations. Total volume conservation means that fluxes from equations (3.43) and (3.44) should cancel out. It yields the following equation which is to be compared with (3.38)

$$\overline{u}_{i+\frac{1}{2}} = \sum_k (\alpha u)_{i+\frac{1}{2}}^k.$$ (3.45)

Remap procedures often consist in upwinding physical quantities as it provides stability while still remaining quite simple. In a multi-velocity setting, two major choices exist.

- Physical quantities are upwinded with respect to their respective material velocities. Then

$$(\alpha u)_{i+\frac{1}{2}}^k = \alpha_{i+\frac{1}{2},\mathrm{up}^k}^k u_{i+\frac{1}{2}}^k,$$ (3.46)

with $\alpha_{i+\frac{1}{2},\mathrm{up}^k}^k = \alpha_i^k$ if $u_{i+\frac{1}{2}}^k \geq 0$ and $\alpha_{i+\frac{1}{2},\mathrm{up}^k}^k = \alpha_{i+1}^k$ if not. This is a robust choice as it generates convex combinations []. However, because volume fractions are upwinded with respect to different velocities, their value may come from different cells. As such, their sum needs not be one at a given node. Apart from inducing potentially dubious geometrical interpretations, it prevents the Lagrange volume evolution rate $\nabla \cdot \overline{\mathbf{u}}$ from being translation invariant as

$$\sum_k \alpha_{i+\frac{1}{2},\mathrm{up}^k}^k (u_{i+\frac{1}{2}}^k - u_0) = \sum_k \alpha_{i+\frac{1}{2},\mathrm{up}^k}^k u_{i+\frac{1}{2}}^k - u_0 \sum_k \alpha_{i+\frac{1}{2},\mathrm{up}^k}^k,$$ (3.47)

may differ from $\overline{u}_{i+\frac{1}{2}} - u_0$.

- Physical quantities are upwinded with respect to a common velocity $U$. Node volume fractions now come from the same cell so that translation symmetry is recovered. However convex combinations are lost for material whose velocities are opposite to $U$, leading to possible stability issues.

In order to correct these shortcomings, upwind fluxes (3.46) are written in the alternate form

$$\alpha_{i+\frac{1}{2}}^{k,\mathrm{up}^k} u_{i+\frac{1}{2}}^k = u_{i+\frac{1}{2}}^k \frac{\alpha_i^k + \alpha_{i+1}^k}{2} + \left|u_{i+\frac{1}{2}}^k\right| \frac{\alpha_i^k - \alpha_{i+1}^k}{2},$$ (3.48)

which can be interpreted as the sum of a centered flux (for which the sum of volume fractions adds up to one) and a diffusion flux, necessary for stability. When summing these fluxes over all materials, the effective nodal volume fractions are not centered because diffusion fluxes do not cancel out. It shows that the diffusion level must be the same for all materials. Consequently,

fluxes are replaced with

$$(\alpha u)^k_{i+\frac{1}{2}} = u^k_{i+\frac{1}{2}} \frac{\alpha^k_i + \alpha^k_{i+1}}{2} + W_{i+\frac{1}{2}} \frac{\alpha^k_i - \alpha^k_{i+1}}{2}, \tag{3.49}$$

where $W_{i+\frac{1}{2}}$ no longer depends on material $k$. Then constraint (3.45) becomes consistent with translation symmetry. Stability is discussed in the next section 3.5; it is shown to hold for a specific value of $W_{i+\frac{1}{2}}$.

**Remark 12.** Equation (3.49) implies that node volume fractions used in (3.39) are

$$\alpha^k_{i+\frac{1}{2}} = \frac{\alpha^k_i + \alpha^k_{i+1}}{2}. \tag{3.50}$$

Although probably negligible, the correlation term (3.39b) is non zero. Enforcing $C_p = 0$ is possible (at least in one dimension) but at the cost of introducing thermodynamics inside the remapping procedure. It has been excluded so as to keep the projection purely geometrical.

**Remark 13.** Consistency between the volume-filling constraint and the upwinding is recurring issue in multi-material schemes [21, 108] whatever their approach (Eulerian, Lagrangian, with remap,...). It appears to be generally solved with decomposition "tricks" similar to (3.49).

**From a common diffusion to stability**

All Eulerian quantities $\phi \in \{1, \alpha, \alpha\rho, \alpha\rho u, \alpha\rho e\}$ are treated in the same manner

$$V^{n+1}_i \phi^{k,n+1}_i - V^{L^k}_i \phi^{k,L^k}_i = -\Delta t \left( F^k_{i+\frac{1}{2}}(\phi) - F^k_{i-\frac{1}{2}}(\phi) \right), \tag{3.51}$$

with

$$F^k_{i+\frac{1}{2}}(\phi) = u^k_{i+\frac{1}{2}} \frac{\phi^k_i + \phi^k_{i+1}}{2} + W_{i+\frac{1}{2}} \frac{\phi^k_i - \phi^k_{i+1}}{2}. \tag{3.52}$$

The following proposition shows that the "over-upwinding"

$$W_{i+\frac{1}{2}} = \max_l \left| u^l_{i+\frac{1}{2}} \right| \tag{3.53}$$

is sufficient to ensure stability in the sense detailed in the next proposition.

**Proposition 6.** The remapping procedure (3.51)-(3.53) consists in convex combinations under a CFL-like condition on the time step. They ensure positivity of the densities and volume fractions as well as positive entropy production for each material in the sense that

$$\sum_{i\in\mathbb{Z}} \left( m^{k,n+1} s^{k,n+1}_i - m^{k,n} s^{k,L^k}_i \right) \geq 0. \tag{3.54}$$

*Proof.* Equation (3.51), together with (3.52), yields

$$V^{n+1}_i \phi^{k,n+1}_i = \omega^n_{i,i} \phi^{k,L^k}_i + \omega^n_{i,i-1} \phi^{k,L^k}_{i-1} + \omega^n_{i,i+1} \phi^{k,L^k}_{i+1}, \tag{3.55a}$$

$$\omega^n_{i,i} = V^{L^k}_i - \omega^n_{i,i-1} - \omega^n_{i,i+1}, \tag{3.55b}$$

$$\omega^n_{i,i\pm1} = \frac{\Delta t}{2} \left( \max_l \left| u^l_{i\pm\frac{1}{2}} \right| - u^k_{i\pm\frac{1}{2}} \right). \tag{3.55c}$$

All coefficients $\omega_{i,j}^n$ are positive under a CFL-like condition which is essentially (but not exactly) the same global restriction which would have resulted from an upwind remapping procedure on each material. Dividing (3.55a) by the very same equation for $\phi = 1$ gives convex combinations on the Eulerian variables $\phi$. It ensures positivity of the volume fraction. Alternatively, dividing (3.55a) by the very same equation for $\phi = \alpha\rho$ gives convex combinations on the Lagrangian variables $\phi/(\alpha\rho)$ which ensures positivity of the density. In particular, for $\phi = \alpha$ and $\phi = \alpha\rho e$, it reads

$$\frac{1}{\rho_i^{k,n+1}} = \kappa_{i,i}^n \frac{1}{\rho_i^{k,L^k}} + \kappa_{i,i-1}^n \frac{1}{\rho_{i-1}^{k,L^k}} + \kappa_{i,i+1}^n \frac{1}{\rho_{i+1}^{k,L^k}}, \tag{3.56a}$$

$$e_i^{k,n+1} = \kappa_{i,i}^n e_i^{k,L^k} + \kappa_{i,i-1}^n e_{i-1}^{k,L^k} + \kappa_{i,i+1}^n e_{i+1}^{k,L^k}, \tag{3.56b}$$

with $\kappa_{i,j}^n = \omega_{i,j}^n / m_i^{k,n+1}$. By concavity of the function $s^k(1/rho^k, e^k)$

$$s_i^{k,n+1} \geq \kappa_{i,i}^n s_i^{k,L^k} + \kappa_{i,i-1}^n s_{i-1}^{k,L^k} + \kappa_{i,i+1}^n s_{i+1}^{k,L^k}. \tag{3.57}$$

Unwinding all the previous computations eventually gives

$$m^{k,n+1} s_i^{k,n+1} - m^{k,L^k} s_i^{k,L^k} \geq -\Delta t \left( F_{i+\frac{1}{2}}^k(\alpha\rho s) - F_{i-\frac{1}{2}}^k(\alpha\rho s) \right), \tag{3.58}$$

which is consistent with the continuous inequality $\partial_t(\alpha^k \rho^k s^k) + \partial_x(\alpha^k \rho^k s^k u^k) \geq 0$. Summing over all cells, it implies the weaker global result (3.54). $\square$

Going beyond the previous result, some nuances are brought to the discussion in the following remarks. They also hold for the multi-dimensional extension presented in appendix E.

**Remark 14.** The remapping fluxes depend on the Lagrangian values. Enforcing equation (3.45) would require a global implicitation of the volume fraction during the Lagrange step. It has been excluded for the sake of simplicity and computation time. Consequently, equation (3.45) is verified only up to a $O(\Delta t)$ residue. Then, a normalization step may still be needed but should be significantly less intrusive. Just as for the Lagrange step, the semi-discrete remapping step is strictly entropic for each material but integration in time may induce small entropy destructions after normalization.

**Remark 15.** While some entropy destruction cannot be completely excluded, the remapping procedure should actually be quite diffusive as all material quantities are now diffused with respect to the maximum velocity and no longer with their own. It may cause singular asymptotic behavior when a high-velocity phase disappears (i.e. $u^k$ large and $\alpha^k \to 0$), effectively driving the dissipation of the whole mixture. A possible answer is to replace the diffusion coefficient $\max_l |u_{i+\frac{1}{2}}^l|$ in (3.52) with some weighted average

$$\sum_l \theta^l \left| u_{i+\frac{1}{2}}^l \right|, \tag{3.59}$$

where $\theta^l \to 0$ as $\alpha^l \to 0$. Then the proof of proposition 6 is no longer valid and entropy might be destroyed over time for the fastest materials. However, convex combinations are sufficient for the

proof but perhaps not necessary. Besides, the second principle of thermodynamics only requires an increase in total entropy so that an entropy destruction for a fast disappearing material might not be such a concern. The general issue of phase disappearance is a painful recurring hassle in several situations. It is usually taken care of by a brute force clipping below some threshold [85, §1].

**Remark 16.** Conservation of total energy is not given *a priori*. The issue comes from the difference between projected kinetic energy and kinetic energy computed from the projected velocities [25]. A solution is to look at the gap between the two and dump it into the internal energy. Convexity of the square function ensures that the correction does not destroy entropy.

# 4   Numerical results

The various test cases presented in this section are concerned with stiffened gas and perfect gas equations of state (EOS). The stiffened gas EOS (of which the perfect gas EOS is simply a specific case) is presented in appendix F.

## 4.1   Sod test case

The first test case extends the classical Sod shock tube problem to a multi-velocity context. A domain $[0, 1]$ is filled with a mixture of two perfect gases. The properties of the mixture initially displays a discontinuity at $x = 0.5$. The left and right states are found in table 3.1. An additional drag force can be considered in order to couple the fluid velocities. The modified equations read

$$\alpha^1 \rho^1 \frac{\mathrm{d}}{\mathrm{d}t} \mathbf{u}^1 = -\alpha^1 \nabla p + \nu \rho \left( \mathbf{u}^2 - \mathbf{u}^1 \right), \tag{3.60a}$$

$$\alpha^2 \rho^2 \frac{\mathrm{d}}{\mathrm{d}t} \mathbf{u}^2 = -\alpha^2 \nabla p + \nu \rho \left( \mathbf{u}^1 - \mathbf{u}^2 \right). \tag{3.60b}$$

Numerically, the time integration of the drag force is implicit, resulting in a local $2 \times 2$ linear system which can easily be inverted by hand. In figures 3.5 and 3.6 are displayed the results at $t = 0.2$ obtained with the present multi-velocity scheme as well as with the single-velocity scheme found in [74]. Because of the discontinuity in volume fraction, the densities and velocities of the materials are different in the mixing zone. The velocity difference between the two materials mainly depends on two parameters. First, the stronger the drag force is, the smaller the difference gets (see figure 3.5). With an infinite drag force, the single-velocity scheme is eventually recovered. Second, adding more cells reduces the width of the diffused interface and thus the width over which a relative drift is observed (see figure 3.6). As the mixing zone gets thinner, the amplitude of the velocity difference also decreases.

## 4.2   Triple point test case

The second test case consists in the so-called triple point problem [9]. Just as the Sod shock tube, it is a standard numerical test in computational fluid dynamics and it is here adapted to a multi-velocity setting. The geometry of the problem and its initial conditions can be found in

|        | $\gamma$ | $\rho_L$ | $u_L$ | $p_L$ | $\alpha_L$ | $\rho_R$ | $u_R$ | $p_R$ | $\alpha_R$ |
|--------|----------|----------|-------|-------|------------|----------|-------|-------|------------|
| Gas 1  |          |          |       |       | 0.9        |          |       |       | 0.1        |
|        | 1.4      | 1        | 0     | 1     |            | 0.125    | 0     | 0.1   |            |
| Gas 2  |          |          |       |       | 0.1        |          |       |       | 0.9        |

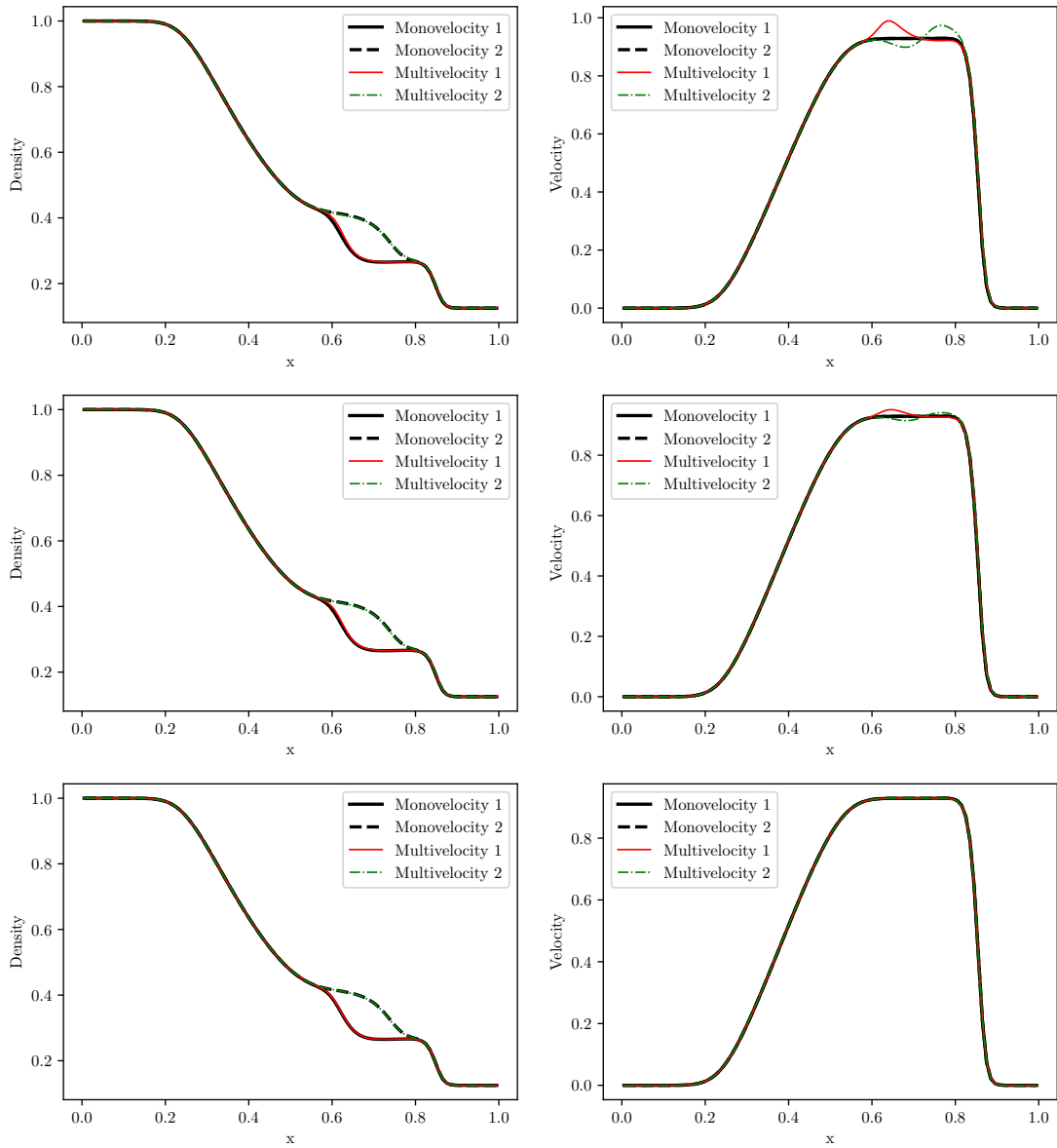Table 3.1: Initial conditions for the Sod test case.



Figure 3.5: Density (left) and velocity (right) profiles obtained using 100 cells for $\nu = 0$ (top), $\nu = 1$ (middle), $\nu = 10$ (bottom).
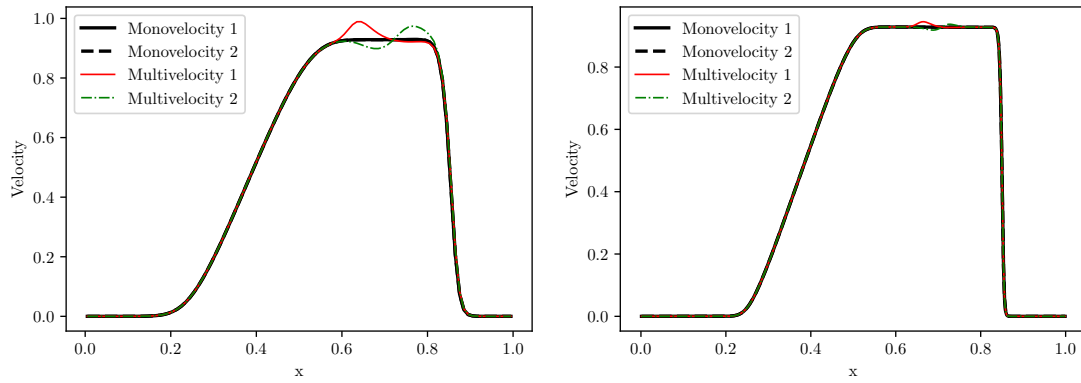
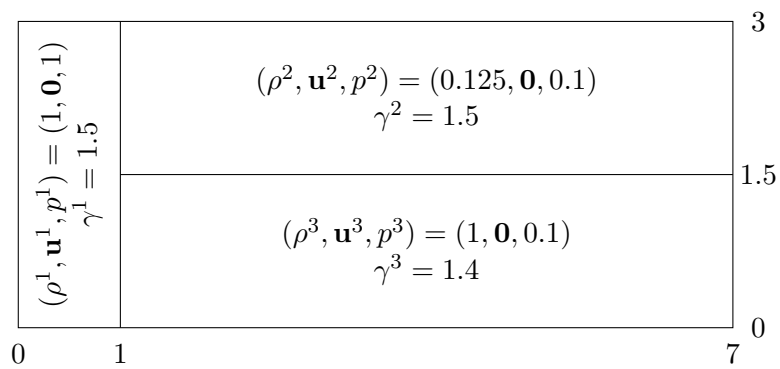Figure 3.6: Velocity profiles obtained for $\nu = 0$, using 100 (left) and 400 (right) cells.



Figure 3.7: Triple point layout and initial conditions.

| | $\rho$ | $u$ | $p$ | $\alpha$ |
|---|---|---|---|---|
| Air | 1 | 0 | $10^5$ | 0.2 |
| Water | 1000 | 10 | | 0.8 |

Table 3.2: Initial conditions inside the domain for the Ransom faucet problem.

figure 3.7. Wall boundary conditions are set on each side. The three materials are separated at first but the remapping procedure eventually creates mixing zones in which material velocities can drift away from each other. Results for different drag coefficients $\nu$ are shown in figure 3.8. With no drag force, the scheme displays a robust behavior although further interpretation of the results is not easy. With a large drag coefficient $\nu = 10^5$, the solution is similar to what can usually be observed with a single-velocity scheme. The curl appearing at the interface between the three materials is quite diffused; a better resolution would require extending the scheme to higher order.

## 4.3 Ransom water faucet problem

The Ransom water faucet problem is a standard benchmark in multi-velocity two-phase numerical simulations [90, 107, 106]. A 12m long vertical pipe is filled with an initially homogeneous mixture of air and water whose properties are detailed in table 3.2. Air and water are respectively described by a perfect gas ($\gamma = 1.4$) and a stiffened gas ($\Gamma = 3.4$ and $\pi = 10^9$) equations of state. At the top of the tube, water is injected at 10 m.s$^{-1}$ with a volume fraction of 0.8, density of 1000 Kg.m$^{-3}$ and pressure $p = 10^5$ Pa. The bottom of the tube is left opened at atmospheric pressure $p = 10^5$ Pa. Additionally, a downward gravity force $g = 10$ m.s$^{-2}$ is applied to the mixture.

Because of the highly contrasted equations of state, water behaves in an almost incompressible manner while its dynamics is essentially insensitive to that of air. The dynamics of water can then be approximated with a free fall. Because its upstream velocity is constant, the newly injected water lags behind the continuously accelerated stream. As a result, the water stream narrows while the space left unoccupied fills with air. Details of the semi-analytical solution are recalled in appendix G.

Figure 3.9 displays the numerical results for the air volume fraction and the water velocity. Good agreement with the semi-analytical solution is observed. For finer meshes, an undershoot appears upstream of the contact wave. This instability is not numerical but rather comes from the elliptic nature of the model itself. This well-known issue echoes the discussion in section 2.4 and is also largely examined in [106] and references therein.

## 4.4 Sedimentation problem

This numerical test case from [99] studies the evolution of a mixture of water and air in a vertical column $[0, 7]$. Equations of state are the same as in the Ransom faucet problem. At first, the mixture is homogeneous and at rest; its characteristics are detailed in table 3.3. Wall conditions are set on each side. The mixture is set into motion by gravity and density contrast: the denser
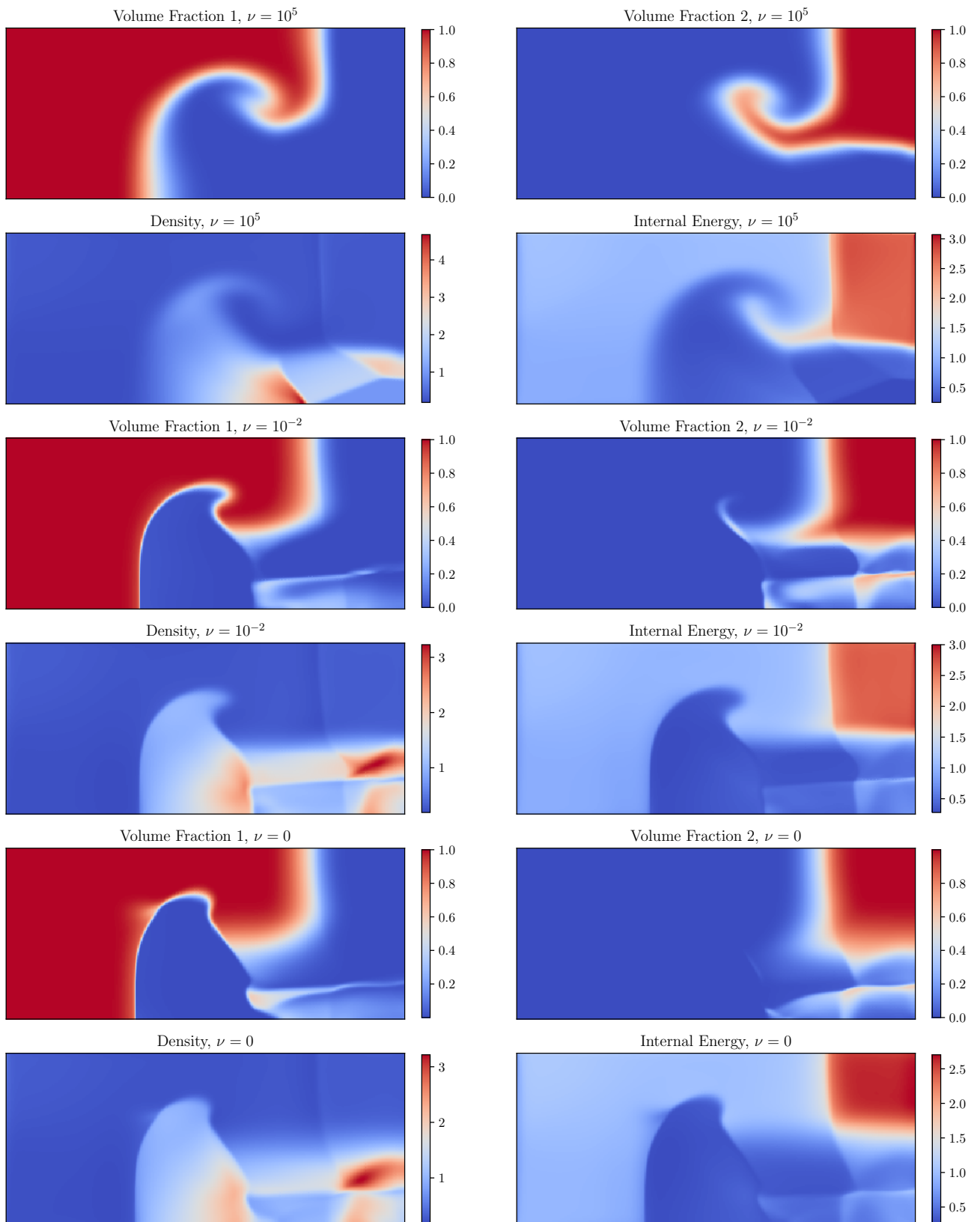
Figure 3.8: Results of the triple point problem at $t = 5$ with a $350 \times 150$ mesh and different values of the drag coefficient.
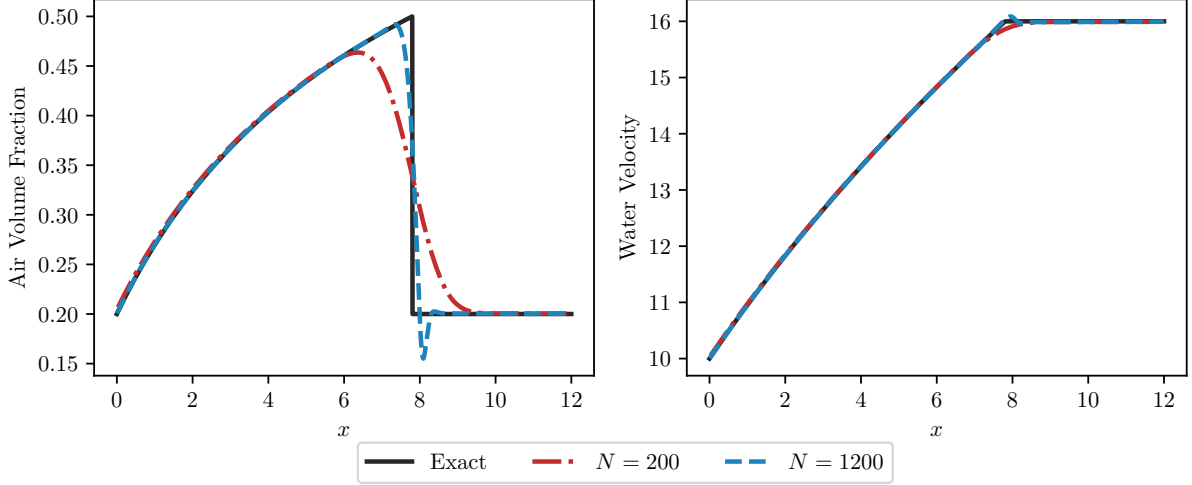
Figure 3.9: Air volume fraction (left) and water velocity (right) profiles displayed at time $t = 0.6$. With 1200 cells, an undershoot appears on the upstream state of the volume fraction wave.

|        | $\rho$ | $u$ | $p$      | $\alpha$ |
|--------|--------|-----|----------|----------|
| Air    | 1      | 0   | $10^5$   | 0.5      |
| Water  | 1000   | 0   |          | 0.5      |

Table 3.3: Initial conditions inside the domain for the sedimentation problem.

water moves downwards while air goes upwards. As a consequence, a volume fraction wave forms on each side and both eventually merge into an interface between the then fully separated air and water. Figure 3.10 shows the air volume fraction profile at different times obtained with 200 cells. These numerical results are in good agreement with those obtained in [53].

## 4.5  Crossing particles

From [107] is considered a test case consisting in the crossing of water droplet clouds ($\rho = 1000$) at supersonic speeds in air ($\rho = 1$). The equations of state are the same as in the two previous test cases. The volume fraction profile of each cloud is Gaussian

$$\alpha(\mathbf{x}, 0) = 0.12 \exp\left(\frac{(\mathbf{x}_0 - \mathbf{x})^2}{0.08}\right). \tag{3.61}$$

The initial position $\mathbf{x}_0$ and velocity of the clouds can be found in figure 3.11. The pressure is homogeneous throughout the domain with $P = 10^5$. Numerical results at different times are displayed on figure 3.12.

Just as for the Ransom faucet problem, the effect of the air medium on the particles can reasonably be neglected because of the high contrast in densities and compressibilities. The particles then move steadily until crossing each other in the center at $t = 10^{-3}$. There, their movement remains unperturbed as air inhibits all pressure perturbations. Although such behavior may seem counter-intuitive, one has to remember that the model has been stripped of all dissipative terms so as to focus on the universal features of dissipation-free multi-material
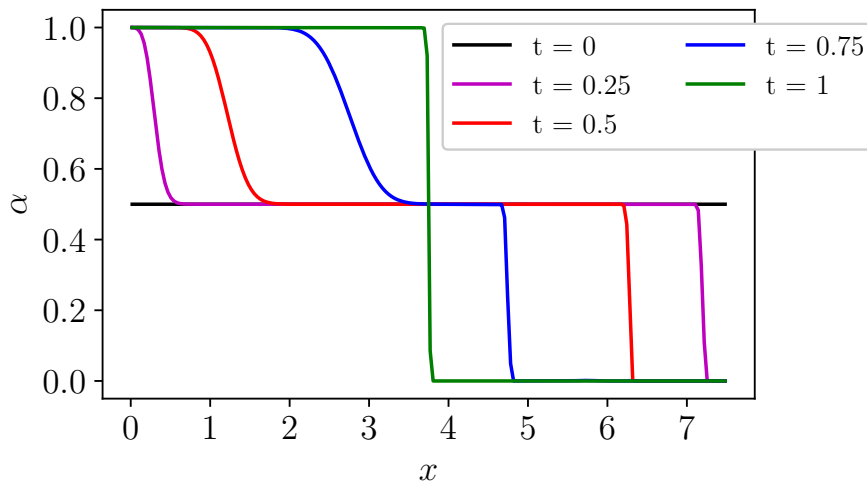
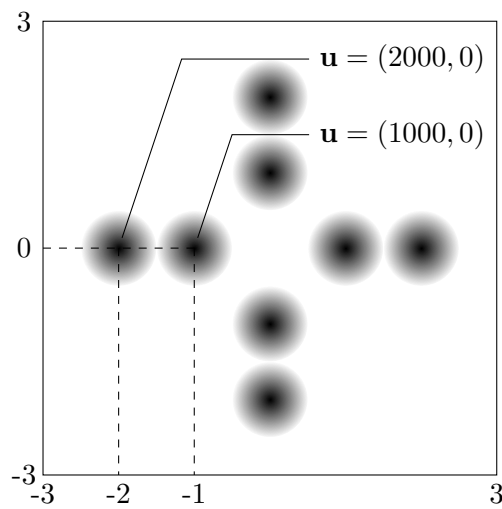Figure 3.10: Air volume fraction profile at time t=0.5 with 200 cells.



Figure 3.11: Geometry and initial velocities for the crossing particle test. Only the information for two out of six particles is given; the rest can be deduced from symmetry considerations (namely invariance with respect to repeated 90° rotations and reflections trough the $x-$axis).

flows. A complete physical description would include exchanges of momentum such as drag which would slow the clouds down upon crossing each other, the form and amplitude of such exchanges being heavily system-dependant. Eventually, at $t = 2 \cdot 10^{-3}$, the clouds reach the other side, modified only by the numerical diffusion induced by the remapping step. It is worth noticing that the resulting smearing seems isotropic (i.e. their circular shape is preserved). With usual remapping procedures, diffusion is only observed in the direction of the propagation. Here, it is common to all materials, including those moving horizontally and those moving vertically. As a result, all materials are equally subject to both horizontal and vertical diffusion.

Overall, the numerical scheme shows good robustness with respect to the supersonic velocities of the droplets, to the highly contrasted equations of state, as well as to the small values reached by the air volume fraction when the particles are all superimposed at $t = 10^{-3}$.

# 5   Conclusion

A numerical scheme was presented for a multi-material multi-velocity one-pressure model. A Lagrangian phase is first performed in parallel on each material before being followed by a remapping procedure. A large emphasis is put on thermodynamic consistency and in particular on entropy as a mean of stabilizing the scheme and selecting the solutions of interest inside shocks. Space integration of both the Lagrange phase and the remapping is shown to be strictly entropic while the main source of entropy (namely the Lagrangian numerical viscosity) can be arbitrarily shared between materials. The numerical scheme is confronted to several test cases assessing its robustness to shocks and contrasted equations of state.

The present work paves the way for further studies. Without trying to produce a comprehensive list, perspectives include going to higher order (both in time and space), extending the present method to an Arbitrary Lagrangian-Eulerian setting, bettering time step restrictions and dissipation tuning, and evaluating the performances on more demanding test cases [49].

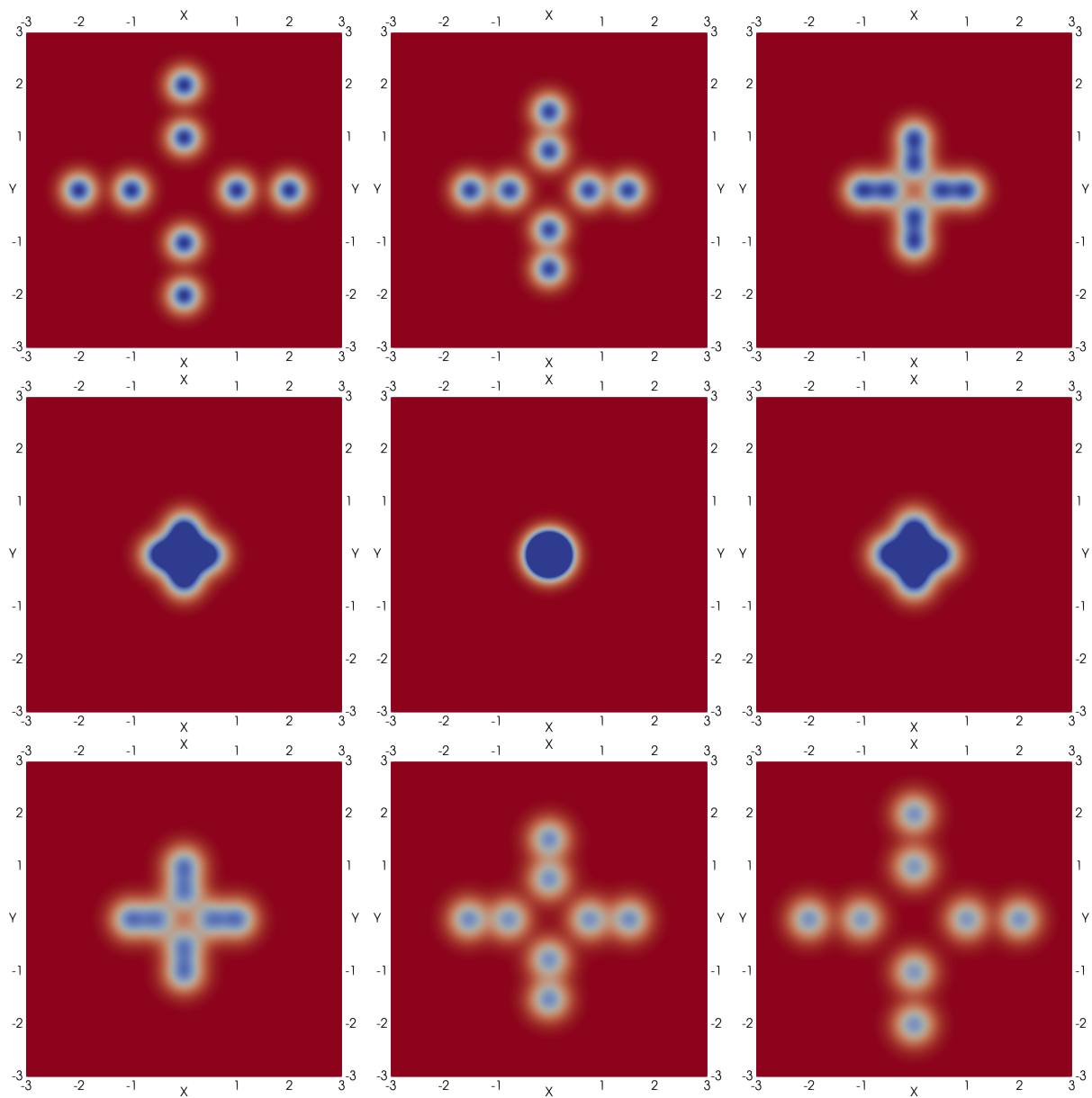Figure 3.12: Medium volume fraction profile with $1200 \times 1200$ cells at $t = 0$ (top left), $t = 2.5 \cdot 10^{-4}$ (top center), $t = 5 \cdot 10^{-4}$ (top right), $t = 7.5 \cdot 10^{-4}$ (middle left), $t = 1 \cdot 10^{-3}$ (middle center), $t = 1.25 \cdot 10^{-3}$ (middle right), $t = 1.5 \cdot 10^{-3}$ (bottom left), $t = 1.75 \cdot 10^{-3}$ (bottom center), $t = 2 \cdot 10^{-3}$ (bottom right).

# Chapter 4

# Two-temperature Lagrangian hydrodynamics: path-consistent solutions and their numerical approximation through in-cell discontinuous reconstruction[1]

## Contents

The present work is devoted to the numerical approximation of two temperature Lagrangian hydrodynamics with the ideas introduced in [15] and based on in-cell shock reconstruction techniques. The model under consideration is not fully conservative which raises several issues in terms of defining solutions and then numerically approximating them. The path formalism offers a solid mathematical background on which the present scheme heavily relies. However, the physical interpretation of paths is not a trivial question and some constraints and asymptotic behavior are here discussed. The path dependant scheme is applied to several Riemann problems, equations of state and paths. In all cases, the numerical solution is shown to correctly approximate the exact solution in the vicinity of shock, a feature which is not achieved by Godunov's type scheme.

# 1 Introduction

The theoretical background behind hyperbolic conservation laws has been extensively studied over the last two centuries. A large numerical arsenal for solving them now exists and enables for accurate simulations of the Euler equations or the Shallow water equations among others. Conservation is a crucial property not only for the theory, as it allows to define weak solutions and jump conditions inside shocks [64], but also for the numerical strategies as it is critical for ensuring convergence of the schemes to the correct solution.

Unfortunately, numerous physical systems are not conservative. For instance, when dealing with multiphasic flows, the mixture evolution must comply with conservation laws but individual phases are described with non conservative equations. Likewise, properly modelling non-equilibrium plasma calls for two temperatures : one for the electrons and one for the ions. The resulting equations are, again, non conservative. These examples and many others all illustrate how critical the study and development of adequate numerical schemes are.

The classic theory of conservation laws fails to extend to non conservative ones. No canonical weak formulation exists and, as such, solutions are ill-defined inside discontinuities. Dal Maso, LeFloch and Murat overcame these shortcomings by suggesting to define shocks with the additional help of a path [77]. Although it solves the issues of the definition, existence and uniqueness of solutions, the question of translating this formalism within the scope of numerical schemes is still a burgeoning one.

## 1.1 Defining solutions for non conservative hyperbolic systems

From a physical point of view, hyperbolic equations correspond to a limit of parabolic equations, the textbook example of such limit being the Euler equations asymptotically coming from Navier and Stokes equations when viscosity and heat exchanges are neglected. The parabolic regularization should be taken into account so as to define solutions. When the corresponding dissipative terms tend to zero, they leave an evanescent effect on solutions even though they are no longer explicitly present inside the hyperbolic equations. In particular, vanishing viscosity solutions satisfy an entropy inequality as first shown by Lax [77] which explains why entropic

---

[1]This chapter was submitted with Christophe Chalons to Communications in Mathematical Sciences.

solutions are the usual solutions of interest.

In the case of conservation laws, specifying the exact dissipative effects is not mandatory and a simple entropy inequality is sufficient. Indeed, variables being conserved over time constrains the behavior of shocks through Rankine-Hugoniot relationships

$$\sigma(U_R - U_L) = F(U_R) - F(U_L) \tag{4.1}$$

which relates the speed of the shock $\sigma$ with its left and right states $U_L$ and $U_R$, and this, regardless of the expression of dissipative terms. The entropy inequality then selects the shocks actually coming from a viscous limit.

In the case of non conservative systems, equation (4.1) no longer holds true. Dal Maso, LeFloch and Murat [77] showed that taking into account the underlying dissipative effects amounts to specifying a path $\phi(U_L, U_R, s)$ as a function of the left and right states $U_L$ and $U_R$ as well as of a parameter $s \in [0,1]$. This path allows to define jump conditions

$$\sigma(U_R - U_L) = \int_0^1 A(\phi(U_L, U_R, s)) \frac{\partial \phi}{\partial s} ds. \tag{4.2}$$

They consist in generalized Rankine-Hugoniot relationships as they reduce to (4.1) when $A$ is the jacobian of a flux $F$. Once a choice of a path has been made, the classic theory of hyperbolic conservation laws formally extends to non conservative systems [77].

## 1.2 Approximating solutions to non conservative hyperbolic systems

Numerical diffusion is the key ingredient in order to capture and stabilize shocks in numerical schemes. The upwind scheme for the advection equation is the most typical finite volume scheme and is written

$$\frac{u_i^{n+1} - u_i^n}{\Delta t} + a \frac{u_{i+1}^n - u_{i-1}^n}{2\Delta x} = |a| \frac{u_{i+1}^n - 2u_i^n + u_{i-1}^n}{2\Delta x} \tag{4.3}$$

which displays a second hand term that may be interpreted as the dominant (but not sole) source of numerical diffusion. This additional term corrects the otherwise unstable centered scheme and shows that mimicking a parabolic regularization at the discrete level is crucial for capturing shocks.

Loosely speaking, for conservative equations, vanishing viscosity solutions do not depend on the viscosity form which explains the large spectrum of existing numerical methods [42, 92, 46, 103, 41, 102] (the list of references being far from comprehensive), albeit their widely different intrinsic numerical diffusion. However, as stated before, for non conservative systems, the solution depends on a path and its underlying parabolic regularization. In order to design a scheme approximating this solution, one needs to control, not only the sign and order of the numerical diffusion, but also its form. Hence, when directly applying a classic scheme to such equations, the numerical diffusion is large enough to robustly produce a result but it may not converge to the wanted solution [51, 1].

Several endeavors has been conducted in order to assess, quantify and minimize this issue. Two main strategies may be identified. The first approach is geometrical or mimetic and consists in preserving geometrical or algebraic structures at the discrete level in the hope of minimizing

numerical diffusion. Consequently, schemes are rendered almost isentropic which makes them unstable inside shocks. Artificial numerical diffusion is then added and can be customized to mimic physical dissipation. These ideas have been applied to several physical systems such as the Euler equations [109] or multiphase flows [108]. Although these methods are heavily system-dependant and still have convergence issues (spurious numerical diffusion is minimized but not completely eliminated) they provide very satisfactory results for industrial purposes where the remaining convergence errors are to be compared with the inherent inaccuracies related to the physical model. This first approach benefits from the so-called equivalent equation which provides the form of the numerical diffusion up to a chosen order [66].

A second approach, inside which this article falls into, aims at extending Godunov's scheme to arbitrary non conservative hyperbolic systems. Different path-dependant solvers have then been developed [12, 16, 33]. When used in conjunction with Godunov's method, numerical results are shown not to converge to the exact solution even though the mismatch is deemed small enough for shocks of small amplitude [12, 66]. This failure may be explained by the dissipation introduced in the averaging step. While the resolution of Riemann problems at interfaces naturally produces dissipation which is relevant (in a sense that it can be made consistent with a given path), the averaging step's dissipation is not related to any path whatsoever and is the one preventing the scheme from converging to the correct solution.

Other works have been dedicated to finding schemes converging to the exact solution by negating the dissipation introduced during the averaging process. In [39], the averaging is replaced with a random selection of one of the values resulting from the Riemann problem. This comes at the cost of having only a weaker, probabilistic, form of consistency. With this method, isolated shock do not spread over any cell but their position is only correct on average. In [15, 88], the averaging procedure is left unchanged but a shock reconstruction is performed at the beginning of every time step and aims at unraveling the averaging. Consequently, isolated shock are allowed to spread over one cell at most. This in-cell reconstruction technique was first introduced as an anti-diffusive strategy in the context of scalar conservation laws in order to accurately capture shocks [63]. It is the second strategy [15] which is considered in this article and applied to two-temperature Lagrangian hydrodynamics.

## 1.3 Two-temperature Lagrangian hydrodynamics

In this article, the ideas of [15] are applied to the so-called two-temperature system, written in Lagrangian coordinate and in one dimension

$$\partial_t \tau - \partial_x u = 0, \tag{4.4a}$$

$$\partial_t u + \partial_x p = 0, \tag{4.4b}$$

$$\partial_t e^1 + p^1 \partial_x u = 0, \tag{4.4c}$$

$$\partial_t e^2 + p^2 \partial_x u = 0. \tag{4.4d}$$

The notations are standard with $\tau$ denoting the specific volume, $u$ the velocity, $e^i$ the internal energy of component $i$ and $p^i$ its pressure which is given as a function of $\tau$ and $e^i$. The total pressure $p$ corresponds to the sum of all individual pressures $p^i$. Such equations arise when

dealing with totally ionized plasma far from temperature equilibrium. Electrons and ions have not yet relaxed to the same temperature and are then described with their own equation of state. A source term needs to be added in order to take into account the ongoing temperature relaxation process. It will not be considered here as the article focuses on the study and discretization of the hyperbolic part. This omission is acceptable as, numerically, the hyperbolic part and the source terms are often split and treated separately [97, 34].

The system is truly non conservative in the sense that no equivalent *physical* conservative version of the equations exists. Surely, the energy equations may be replaced with the conservation of (physical) entropy $\partial_t s^i = 0$ with $i \in \{1, 2\}$ but this formulation is not physical as it would imply that entropies are conserved inside shocks but not the total energy $E = e^1 + e^2 + u^2/2$ which satisfies the additional conservation law

$$\partial_t E + \partial_x(pu) = 0. \tag{4.5}$$

An arbitrary path supplementing system (4.4) does not necessarily ensures the conservation of total energy and even with this constraint, no canonical path exists. This non uniqueness echoes the fact that, physically, multiple solutions are admissible depending on the entropy deposit on ions and electrons [115]. Indeed, a physically relevant parabolic regularization is given by the additional viscosity

$$\partial_t \tau - \partial_x u = 0, \tag{4.6a}$$
$$\partial_t u + \partial_x p = (\epsilon^1 + \epsilon^2)\partial_{xx}u, \tag{4.6b}$$
$$\partial_t e^1 + p^1 \partial_x u = \epsilon^1 (\partial_x u)^2, \tag{4.6c}$$
$$\partial_t e^2 + p^2 \partial_x u = \epsilon^2 (\partial_x u)^2. \tag{4.6d}$$

The vanishing viscosity solution is expected to only depend on the ratio $\epsilon^1/\epsilon^2$. The explicit link between the parabolic regularization and the corresponding path is a relevant but difficult question. It will only be partially addressed in this paper in the case where one compound bears all the entropy production (i.e. $\epsilon^1 = 0$ or $\epsilon^2 = 0$). This asymptotic case is physically meaningful in the case of a completely ionized gas as the ions are expected to carry almost all of the dissipation [115].

The present work, from the analysis of the equations to the numerical strategy, can be easily extended to the N temperature system (i.e. model (4.4) with N energy equations). In particular, the three temperature system could model the ion, electron and photon energy of a strongly radiative completely ionized plasma.

The article is organized as follows. In section 2, the solution of the Riemann problem for the two-temperature system is presented. The solution inside shocks depends on a arbitrary path on the variable $\Delta p$, the path on the other variables having been defined so as to ensure total energy conservation. Different restrictions on the path on $\Delta p$ are derived and exhibit two asymptotic cases whose underlying parabolic regularization is known. In section 3, the numerical strategy is presented. It consists in the methods introduced in [15] and uses an approximate Roe solver [92, 104] adapted to the two-temperature model and stiffened gas equations of state. Finally,

in section 4, several test cases based on Riemann problems are considered. The approximate solution obtained with the previously presented scheme is compared with the exact solution obtained with the exact solver, thus assessing convergence.

# 2 Riemann problem for two-temperature Lagrangian hydrodynamics

## 2.1 Hyperbolicity and fields

In order to study its wave structure, the two-temperature system (4.4) is usually written in entropy variables $s^1$ and $s^2$ as the equations are simpler and the speed of sound $\rho c = \sqrt{-\partial_\tau p|_{s^1,s^2}}$ naturally comes up.

$$\partial_t \tau - \partial_x u = 0 \tag{4.7a}$$

$$\partial_t u + \partial_x p = 0 \tag{4.7b}$$

$$\partial_t s^1 = 0 \tag{4.7c}$$

$$\partial_t s^2 = 0. \tag{4.7d}$$

System (4.7) may be written in quasi-linear form

$$\partial_t U + A(U)\partial_x U = 0 \tag{4.8}$$

with $U = (\tau, u, s^1, s^2)$ and

$$A(U) = \begin{pmatrix} 0 & -1 & 0 & 0 \\ \partial_\tau p & 0 & \partial_{s^1} p & \partial_{s^2} p \\ 0 & 0 & 0 & 0 \\ 0 & 0 & 0 & 0 \end{pmatrix}. \tag{4.9}$$

The matrix $A(U)$ is diagonalizable. Defining $\rho c = \sqrt{-\partial_\tau p|_{s^1,s^2}}$, its eigenvalues and eigenvectors are

$$\lambda_1 = -\rho c, \quad r_1 = (1, \rho c, 0, 0), \tag{4.10a}$$

$$\lambda_2 = 0, \quad r_{21} = \left(\partial_{s^1} p, 0, (\rho c)^2, 0\right), \tag{4.10b}$$

$$r_{22} = \left(\partial_{s^2} p, 0, 0, (\rho c)^2\right), \tag{4.10c}$$

$$\lambda_3 = +\rho c, \quad r_3 = (1, -\rho c, 0, 0). \tag{4.10d}$$

Assuming that $\partial_\tau \rho c|_{s^1,s^2}$ (which is proportional to the fundamental derivative $\mathcal{G}$ of the system) is of constant sign, the first and third characteristic fields are genuinely nonlinear while the second (of dimension 2) is linearly degenerate. The derivative $\partial_\tau \rho c|_{s^1,s^2}$ is here assumed positive so that the entropy condition is $p_L < p_R$ for $1-$shocks and $p_L > p_R$ for $3-$shocks.
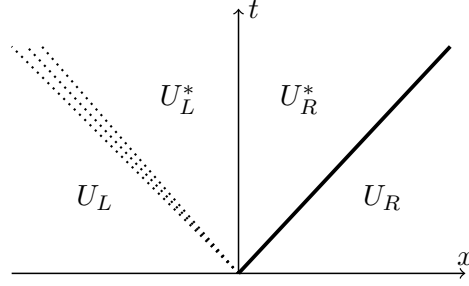
Figure 4.1: Typical solution of the Riemann problem consisting in a 1-rarefaction wave and a 3-shock.

## 2.2 Global strategy

Hence the typical solution of a Riemann problem consists in a left and right waves which are either shocks or rarefaction waves and separated by two superimposed contact discontinuities. The key feature to the strategy for finding the intermediate states of the solution is to notice that both $u$ and $p$ are constant trough the contact discontinuity. Indeed, contact discontinuities connect states that belong to a certain integral curve of a vector field which is a linear combination of $r_{21}$ and $r_{22}$ but

$$\langle \nabla u, r_{21} \rangle = 0 \tag{4.11a}$$

$$\langle \nabla p, r_{21} \rangle = \partial_\tau p \, \partial_{s^1} p + (\rho c)^2 \partial_{s^1} p = 0 \tag{4.11b}$$

and likewise for $r_{22}$. Hence, in order to compute the solution of the Riemann problem, one needs to be able to compute all left states $U_L^*$ (respectively all right states $U_R^*$) that can be connected to $U_L$ from the right by a 1-wave (respectively to $U_R$ from the left by a 3-wave) as functions of $p^*$. These functions are of the form

$$U_L^*(p^*) = \begin{cases} U_L^{\text{shock}}(p^*) & \text{if } \tau^* > \tau_L, \\ U_L^{\text{wave}}(p^*) & \text{else,} \end{cases} \tag{4.12a}$$

$$U_R^*(p^*) = \begin{cases} U_R^{\text{shock}}(p^*) & \text{if } \tau^* > \tau_R, \\ U_R^{\text{wave}}(p^*) & \text{else.} \end{cases} \tag{4.12b}$$

Then, it only remains to find $p^*$ such that $u_L^* = u_R^*$.

**Remark 17.** A general analytical solution is difficult to obtain, even for two perfect gas equations of state, and this, for several reasons. First computing $U_{L/R}^{\text{wave}}$ requires solving an ordinary differential equation which does not necessarily admit an analytical solution. Same goes for $U_{L/R}^{\text{shock}}$ which requires to solve a non-linear equation. Finally, the equation $u_L^* = u_R^*$ is also highly non-linear. For all these reasons, the exact solution of a general Riemann problem will be solved numerically with, for example, Newton's method.

## 2.3 Rarefaction waves

Rarefaction waves are smooth solutions of equation (4.4). As a consequence, they are independent of the chosen path. Just as this is the case for conservative systems, states that can

be joined by a rarefaction wave belong to the same integral curve of the vector field $r_k$ with $k \in \{1, 3\}$. If these curves are parameterized with the total pressure $p$ as in (4.12), then, for 1-waves

$$\frac{\mathrm{d}}{\mathrm{d}p} U_L^{wave} \propto \ r_1 \tag{4.13a}$$

$$\Longleftrightarrow \frac{\mathrm{d}}{\mathrm{d}p} U_L^{wave} \perp \ (\rho c, -1, 0, 0), \ (0, 0, 0, 1), \ (0, 0, 1, 0) \tag{4.13b}$$

which gives the following system of ordinary differential equations

$$\frac{\mathrm{d}}{\mathrm{d}p} u = \rho c \frac{d}{dp} \tau, \tag{4.14a}$$

$$\frac{\mathrm{d}}{\mathrm{d}p} s^1 = 0, \tag{4.14b}$$

$$\frac{\mathrm{d}}{\mathrm{d}p} s^2 = 0. \tag{4.14c}$$

Using the definition of the speed of sound, it then may be written

$$\frac{\mathrm{d}}{\mathrm{d}p} \tau = -\frac{1}{(\rho c)^2}, \tag{4.15a}$$

$$\frac{\mathrm{d}}{\mathrm{d}p} u = -\frac{1}{\rho c}, \tag{4.15b}$$

$$\frac{\mathrm{d}}{\mathrm{d}p} \Delta p = \frac{(\rho c^1)^2 - (\rho c^2)^2}{(\rho c)^2}. \tag{4.15c}$$

with $\Delta p = p^1 - p^2$. For a 3-wave, the equations are the same, except for the velocity equation which reads $du/dp = +1/(\rho c)$. In order to find $U_L^{wave}(p^*)$ (respectively $U_R^{wave}(p^*)$), one only needs to integrate the previous equation from $p_L$ with initial state $U_L$ (respectively $p_R$ with initial state $U_R$) to $p^*$.

**Remark 18.** When equations are written in the form $df/dp = 0$, $f$ is called a Riemann invariant and using it directly allows to bypass an otherwise necessary numerical integration. Here, $s^1$ and $s^2$ are Riemann invariant for 1 and 3−waves. However, the expression of the entropy is not always known for an arbitrary EOS. Besides, one last Riemann invariant is needed and is expected to highly depend on the EOS. In the case of the single temperature equations and with a perfect gas EOS, it is well-known that a last Riemann invariant can be taken as $u + 2c/(\gamma - 1)$ for 1−waves and $u - 2c/(\gamma - 1)$ for 3−waves. For the two-temperature model and perfect gas EOS, it consists in the less practical formula

$$u \pm \int_{\tau_0}^{\tau} \sqrt{\gamma^1 e^{s^1} \tau^{-(\gamma^1 + 1)} + \gamma^2 e^{s^2} \tau^{-(\gamma^2 + 1)}} d\tau. \tag{4.16}$$

For all these reasons, a general and EOS independent approach is preferred although it relies on numerical approximations.

**Remark 19.** The previous ODE only provides the set of states that can be joined from a given state by an expansion wave. It does not provide the profile of the wave $U^{wave}(\xi)$ (where $\xi$ denotes the auto-similar variable $x/t$), needed to compute analytical solutions. In order to obtain the

profile, one needs to add the following characteristic speed condition

$$\xi = \lambda_k, \quad \text{or} \quad \frac{d\lambda_k}{d\xi} = 1, \quad k \in \{1, 3\}. \tag{4.17}$$

Once again, through the EOS (see F for stiffened gases), it gives the evolution of density with respect to the variable $\xi$ and, consequently, the rarefaction wave profile. The equations are then

$$\frac{\mathrm{d}}{\mathrm{d}\xi}\tau = \mp \left.\frac{\partial \rho c}{\partial \tau}\right|_{s^1,s^2}^{-1}, \tag{4.18a}$$

$$\frac{\mathrm{d}}{\mathrm{d}\xi}u = \pm \rho c \frac{\mathrm{d}}{\mathrm{d}\xi}\tau, \tag{4.18b}$$

$$\frac{\mathrm{d}}{\mathrm{d}\xi}p^i = -(\rho c^i)^2 \frac{\mathrm{d}}{\mathrm{d}\xi}\tau, \tag{4.18c}$$

### 2.4 Shocks

Contrary to rarefaction waves, shocks will depend on a choice of path $\phi$. Generally speaking, jump relationships are

$$\sigma(U_R - U_L) = \int_0^1 A(\phi(U_L, U_R, s))\frac{\partial}{\partial s}\phi(s)ds. \tag{4.19}$$

The volume and velocity equations are conservative so that their jump relationship simply reads

$$\sigma(\tau_R - \tau_L) = u_R - u_L, \tag{4.20a}$$

$$\sigma(u_R - u_L) = p_R - p_L \tag{4.20b}$$

regardless of the chosen path. Assuming the path in $u$ is monotonic, it may be parameterized as

$$u(s) = u_L + s(u_R - u_L). \tag{4.21}$$

Then both energy equations in (4.19) become

$$\sigma(e_R^1 - e_L^1) = \frac{1}{2}\left(\int_0^1 p(s)ds + \int_0^1 \Delta p(s)ds\right)(u_R - u_L), \tag{4.22a}$$

$$\sigma(e_R^2 - e_L^2) = \frac{1}{2}\left(\int_0^1 p(s)ds - \int_0^1 \Delta p(s)ds\right)(u_R - u_L). \tag{4.22b}$$

Energy jump conditions only depend on the average value of the path in $p$ and $\Delta p$ and does not depend at all on the path on $\tau$. Algebraic manipulations show that the conservation of total energy

$$\sigma(E_R - E_L) = (p_R u_R - p_L u_L), \tag{4.23}$$

is equivalent to

$$\int_0^1 p(s)ds = \frac{p_R + p_L}{2}. \tag{4.24}$$

117

As such, an admissible path on $p$ is $p(s) = p_L + s(p_R - p_L)$ but any path with the same average value would also work. For an arbitrary path on the pressure difference $\Delta p = p^1 - p^2$, jump relationships read

$$\sigma(\tau_R - \tau_L) = u_L - u_R \tag{4.25a}$$

$$\sigma(u_R - u_L) = p_R - p_L \tag{4.25b}$$

$$(e_R^1 - e_L^1) = \frac{1}{2}\left(\frac{p_R + p_L}{2} + \int_0^1 \Delta p(s)ds\right)(\tau_L - \tau_R) \tag{4.25c}$$

$$(e_R^2 - e_L^2) = \frac{1}{2}\left(\frac{p_R + p_L}{2} - \int_0^1 \Delta p(s)ds\right)(\tau_L - \tau_R) \tag{4.25d}$$

Coming back to the Riemann problem, for a given left state $U_L$, $U_L^{shock}(p^*)$ consists in the solution $(\tau_R, u_R, e_R^1, e_R^2)$ of (4.25) with $p_R = p^*$ and negative shock speed $\sigma$. Similarly, for a given right state $U_R$, $U_R^{shock}(p^*)$ consists in the solution $(\tau_L, u_L, e_L^1, e_L^2)$ of (4.25) with $p_L = p^*$ and positive shock speed $\sigma$.

**Remark 20.** Equations (4.25) only depend on the average value of the pressure difference $\Delta p$. This unique degree of freedom echoes the discussion on system (4.6) for which the vanishing viscosity solution is expected to only depend on the, again, unique parameter $\epsilon^1/\epsilon^2$.

The choice of the path on the pressure difference $\Delta p$ is not completely arbitrary as it needs to fulfill some conditions to be physically sound.

1. First, physical invariance with respect to reflection through the shock position implies that if

$$(\tau_L, u_L, p_L, \Delta p_L, \tau_R, u_R, p_R, \Delta p_R, \sigma) \tag{4.26}$$

is a solution of (4.25) then

$$(\tau_R, -u_R, p_R, \Delta p_R, \tau_L, -u_L, p_L, \Delta p_L, -\sigma) \tag{4.27}$$

is also a solution of the same system. As a consequence, $\int_0^1 \Delta p(s)ds$ must be invariant with respect to the aforementioned change of variable. A simple way of satisfying this invariance is to take it as a function $f(\Delta p_L, \Delta p_R)$ such that $f(\Delta p_L, \Delta p_R) = f(\Delta p_R, \Delta p_L)$. A natural choice is then

$$\int_0^1 \Delta p(s)ds = \frac{\Delta p_R + \Delta p_L}{2}. \tag{4.28}$$

2. A second necessary condition is that the path does not go through impossible thermodynamical states. For stiffened gases (see F), thermodynamical consistency (namely the positivity of the speed of sound) implies

$$p^1(s) + \pi^1 > 0, \tag{4.29a}$$

$$p^2(s) + \pi^2 > 0, \tag{4.29b}$$

or, equivalently,

$$-p(s) - 2\pi^1 < \Delta p(s) < p(s) + 2\pi^2. \tag{4.30}$$

Integrating these inequalities provides a lower and upper bound for the average value of $\Delta p$ along a path

$$-\frac{p_R + p_L}{2} - 2\pi^1 < \int_0^1 \Delta p(s) ds < \frac{p_R + p_L}{2} + 2\pi^2. \tag{4.31}$$

It may be checked that the choice (4.28) naturally satisfies this condition.

3. The choice of path should not only ensure that all intermediate states are compatible with the EOS but also that their evolution complies with the second principle of thermodynamics : the system entropy $s^1 + s^2$ must increase inside shocks. A sufficient condition to enforce such inequality is to require that $s^1$ and $s^2$ both increase. Consequently, assuming a linear path on $\tau$

$$\tau(s) = \tau_L + s(\tau_R - \tau_L), \tag{4.32}$$

and integrating the pressure $p^i$ ($i \in \{1, 2\}$) along the isentropic curve in the $p^i - \tau$ plane provides a lower bound (for a positive Grüneisen coefficient) for the average pressure $p^i$

$$\int_0^1 p^i(s) ds = \frac{1}{\tau_R - \tau_L} \int_{\tau_L}^{\tau_R} p^i(\tau, e^i(\tau)) d\tau \tag{4.33a}$$

$$\geq \frac{1}{\tau_R - \tau_L} \int_{\tau_L}^{\tau_R} p^{1,\text{iso}}(\tau) d\tau. \tag{4.33b}$$

or, equivalently,

$$\int_0^1 \Delta p(s) ds \geq -\frac{p_R + p_L}{2} - \frac{2}{\tau_R - \tau_L} \int_{\tau_L}^{\tau_R} p^{1,\text{iso}}(\tau) d\tau \tag{4.34a}$$

$$\int_0^1 \Delta p(s) ds \leq \frac{p_R + p_L}{2} + \frac{2}{\tau_R - \tau_L} \int_{\tau_L}^{\tau_R} p^{2,\text{iso}}(\tau) d\tau. \tag{4.34b}$$

In F, these inequalities are derived in closed form for the stiffened gas and condition (4.34) is shown to be more restrictive than (4.31). The limit where (4.34a) becomes an equality is expected to correspond to the limit $\epsilon^1/\epsilon^2 \to 0$ in (4.6) while the limit where (4.34b) becomes an equality is expected to correspond to the limit $\epsilon^1/\epsilon^2 \to +\infty$.

As stated earlier, this condition is sufficient but not necessary in the sense that one of the entropy could decrease as long as it is compensated by the second entropy so that their sum still increases. Physically, this amounts to adding heat exchange between the two compounds. However, with only incomplete equations of state, temperatures are not accessible and there is no way of knowing if the heat exchange is indeed entropic.

Once again, (4.28) naturally satisfies (4.34) as it reduces to the physical Rankine-Hugoniot relationship for each compound which is known to produce an increase of entropy in compression.

**Remark 21.** While the two first constraints concern arbitrary pairs of left and right states and will have consequences on approximate solvers, the third constraint should be understood differently. Indeed, entropy is a function of state, meaning that it only depends on the left and right states themselves and not on the path connecting them. When claiming that the

path should comply with the second principle of thermodynamics, it should be understood as only concerning pairs of state which are actual solutions of system (4.25) and which is itself path-dependant.

# 3 Numerical strategy

## 3.1 Approximate solvers for two-temperature Lagrangian hydrodynamics

The numerical strategy relies on a solver which is able to compute intermediate states of Riemann problems. One could use the exact solver derived earlier. However, it is computationally expensive and would make simulations on large meshes unreachable. Approximate solvers are then necessary. Even if the intermediate states they provide are allowed to slightly differ from the exact solution, approximate solvers need to coincide with the exact solver in the case of an isolated shock (i.e. both intermediate states and shock speed must be exact). Roe approximate solvers naturally satisfy this property.

**Path-consistent Roe approximate solver**

**Definition 1.** Generalized Roe solvers [104] are adapted to non-conservative hyperbolic system of equations of the form

$$\partial_t U + A(U)\nabla U = 0. \tag{4.35}$$

They consist on finding the solution of the following linearized system of equation

$$\partial_t U + A(U_L, U_R)\nabla U = 0. \tag{4.36}$$

The matrix $A(U_L, U_R)$ must fulfill the three following conditions:

(i) $A(U_L, U_R)$ must be consistent in the sense that if $U_L = U_R = U$, then $A(U, U) = A(U)$.

(ii) $A(U_L, U_R)$ is diagonalizable with real eigenvalues.

(iii) $A(U_L, U_R)$ must also be consistent with a given choice of path

$$A(U_L, U_R)(U_R - U_L) = \int_0^1 A(\phi(s, U_L, U_R))\partial_s\phi(s, U_L, U_R)ds. \tag{4.37}$$

**Remark 22.** When the equations are conservative ($A$ is the jacobian matrix of a flux $F$), then condition (iii) becomes

$$A(U_L, U_R)(U_R - U_L) = F(U_R) - F(U_L), \tag{4.38}$$

and ensures that the scheme is conservative.

**Remark 23.** In order to automatically comply with the two first conditions, $A(U_L, U_R)$ is often taken as $A(\overline{U})$ with $\overline{U}(U_L, U_R)$ which still has to be specified in order to check condition (iii).

According to condition (iii) matrix $A(U_L, U_R)$ is diagonalizable, its eigenvalues are written $\lambda_1 \leq \lambda_2 \leq \cdots \leq \lambda_n$ and the corresponding left and right eigenvectors $l_k$ and $r_k$. The eigenvectors are normalized so as to ensure

$$\langle l_i, r_j \rangle = \delta^{ij} \tag{4.39}$$

where $\delta^{ij}$ is the Kronecker symbol. In this case, the exact solution to the Riemann problem of equation (4.36) is given by

$$U(x,t) = \sum_{k=0}^{m} \langle l_k, U_R \rangle r_k + \sum_{k=m+1}^{n} \langle l_k, U_L \rangle r_k \tag{4.40}$$

with $m$ the unique integer such that $\lambda_m < x/t < \lambda_{m+1}$ (with the convention $\lambda_0 = -\infty$ and $\lambda_{n+1} = +\infty$).

**Application to two-temperature hydrodynamics**

An average state $\overline{U}(U_L, U_R) = (\overline{\tau}, \overline{u}, \overline{e}^1, \overline{e}^2)$ is now computed so that the matrix $A(\overline{U})$ is a Roe matrix for the two-temperature system (4.4) with a linear path on specific volume, velocity and total pressure. Condition (iii) reads

$$\begin{pmatrix} 0 & -1 & 0 & 0 \\ \partial_{\overline{\tau}}\overline{p} & 0 & \partial_{\overline{e^1}}\overline{p^1} & \partial_{\overline{e^2}}\overline{p^2} \\ 0 & \overline{p}^1 & 0 & 0 \\ 0 & \overline{p}^2 & 0 & 0 \end{pmatrix} \begin{pmatrix} \tau_R - \tau_L \\ u_R - u_L \\ e_R^1 - e_L^1 \\ e_R^2 - e_L^2 \end{pmatrix} = \begin{pmatrix} u_L - u_R \\ p_R - p_L \\ \frac{1}{4}\left(p_R + p_L + 2\int_0^1 \Delta p(s)ds\right)(u_R - u_L) \\ \frac{1}{4}\left(p_R + p_L - 2\int_0^1 \Delta p(s)ds\right)(u_R - u_L) \end{pmatrix}. \tag{4.41}$$

The stiffened gas closure (see F for details) gives

$$\partial_{\overline{\tau}}\overline{p} = -\frac{\overline{p} + \sum_i (\Gamma^i + 1)\pi^i}{\overline{\tau}}, \quad \partial_{\overline{e^i}}\overline{p}^i = \frac{\Gamma^i}{\overline{\tau}}. \tag{4.42}$$

Hence

$$-\frac{\overline{p} + \sum_i (\Gamma^i + 1)\pi^i}{\overline{\tau}} + \sum_i \frac{\Gamma^i}{\overline{\tau}} \frac{e_R^i - e_L^i}{\tau_R - \tau_L} = \frac{p_R - p_L}{\tau_R - \tau_L}, \tag{4.43a}$$

$$\overline{p}^1 = \frac{1}{4}\left(p_R + p_L + \int_0^1 \Delta p(s)ds\right), \tag{4.43b}$$

$$\overline{p}^2 = \frac{1}{4}\left(p_R + p_L - \int_0^1 \Delta p(s)ds\right). \tag{4.43c}$$

Average pressures are immediately recovered from (4.43b) and (4.43c). Once injected inside equation (4.43a), the average specific volume is obtained after some basic algebraic manipulations. The average velocity remains arbitrary and is here taken as an arithmetic mean.

Eventually

$$\overline{\tau} = \frac{\tau_L + \tau_R}{2}, \quad \overline{u} = \frac{u_L + u_R}{2}, \tag{4.44a}$$

$$\overline{p} = \frac{p_L + p_R}{2}, \quad \overline{\Delta p} = \int_0^1 \Delta p(s)ds. \tag{4.44b}$$

A set of left $l_k$ and right $r_k$ eigenvectors are given by (overlines are omitted for clarity)

$$\begin{aligned}
\lambda_1 = -(\rho c) \quad &\tilde{r}_1 = (\tau, c, -\tau p^1, -\tau p^2) \\
&\tilde{l}_1 = (\partial_\tau p, -\rho c, \partial_{e^1} p^1, \partial_{e^2} p^2) \\
\lambda_2 = 0 \quad &\tilde{r}_{21} = (\partial_{e^1} p^1, 0, -\partial_\tau p, 0) \\
&\tilde{l}_{21} = (\partial_{e^1} p^1, 0, \partial_\tau p, 0) \\
&\tilde{r}_{22} = (\partial_{e^2} p^2, 0, 0, -\partial_\tau p) \\
&\tilde{l}_{22} = (\partial_{e^2} p^2, 0, 0, \partial_\tau p) \\
\lambda_3 = +(\rho c) \quad &\tilde{r}_3 = (\tau, -c, -\tau p^1, -\tau p^2) \\
&\tilde{l}_3 = (\partial_\tau p, \rho c, \partial_{e^1} p^1, \partial_{e^2} p^2).
\end{aligned}$$

(4.45a)

(4.45b)

(4.45c)

Eventually, Roe intermediate states are given by

$$U_L^* = \langle l_1, U_R \rangle r_1 + \sum_{k=2}^{4} \langle l_k, U_L \rangle r_k = U_L + \langle l_1, U_R - U_L \rangle r_1 \tag{4.46}$$

$$U_R^* = \sum_{k=1}^{3} \langle l_k, U_R \rangle r_k + \langle l_4, U_L \rangle r_4 = U_R + \langle l_4, U_L - U_R \rangle r_4 \tag{4.47}$$

with

$$r_k = \tilde{r}_k, \quad l_k = \frac{\tilde{l}_k}{\langle \tilde{l}_k, \tilde{r}_k \rangle}, \quad k \in \{1, 3\}. \tag{4.48}$$

**Remark 24.** One of the shortcomings of this solver is that it does not work for a general equation of state. For an arbitrary equation of state, equation (4.43a) would be replaced with a possibly highly non-linear equation on $\overline{\tau}$.

**Remark 25.** Regarding the different constraints detailed in 2.4,

1. All symmetries on the path are carried out as symmetries on the Roe solver.

2. If the path does not go through any impossible thermodynamical state, then the average state of the Roe solver is also consistent with thermodynamics (i.e. $\overline{p}^i + \pi^i > 0$).

3. However, Roe solvers are known not to necessarily be entropic. As such, the approximate solution may not comply with the second principle of thermodynamics even if the underlying path does.

## 3.2 In-cell discontinuous reconstruction scheme

The numerical strategy is the one introduced in [15]. It consists in 1) detecting and reconstructing cells containing a shock, 2) updating the cells in question and their neighbor by exactly

advecting the corresponding shock and 3) applying a classic finite volume scheme around the remaining cells. The method relies on a Riemann solver at each aforementioned step as it defines 1) where shocks may appear, 2) what are the states and speed of the shock and 3) is at the basis of Godunov-type scheme. In order for the scheme to be able to capture isolated shocks, the solver itself must be exact in such cases. Two solvers satisfying this property will then be considered: the exact solver and the approximate Roe solver derived in the previous section.

**Notations**

The following notations are standard in the finite volume literature. The one dimensional mesh consists in cells $c_i$ defined by their left and right node positions $x_{i-1/2}$ and $x_{i+1/2}$ and center point $x_i = \frac{1}{2}(x_{i+1/2} + x_{i-1/2})$. The cell width $\Delta x_i = x_{i+1/2} - x_{i-1/2}$ is assumed constant and will simply be written $\Delta x$. Variables are averaged over each cell $c_i$ at each time step $t^n$ and are then written $\phi_i^n$ with $\phi \in \{\tau, u, e^1, e^2\}$

$$\phi_i^n = \frac{1}{\Delta x} \int_{x_{i-1/2}}^{x_{i+1/2}} \phi(x, t^n) dx. \tag{4.49}$$

For cells where no shock reconstruction is performed, the cell value are updated with respect to Riemann problems at the nodes. Consequently, the left and right halves of a single cell will evolve independently which motivates the following definition

$$\phi_{i,L}^n = \frac{2}{\Delta x} \int_{x_{i-1/2}}^{x_i} \phi(x, t^n) dx, \tag{4.50a}$$

$$\phi_{i,R}^n = \frac{2}{\Delta x} \int_{x_i}^{x_{i+1/2}} \phi(x, t^n) dx. \tag{4.50b}$$

Finally, the equations of state allow the definition of cell pressures $(p^k)_i^n = p(\tau_i^n, (e^k)_i^n)$, $k \in \{1, 2\}$.

**Shock detection and reconstruction**

The first step is to detect and reconstruct shocks inside cells. From the exact solution of the Riemann problem, a shock is expected to appear inside cell $c_i$ if

$$u_{i-1}^n > u_{i+1}^n. \tag{4.51}$$

Once a shocks has been deemed possible, it is reconstructed inside the cell. It means that instead of considering that the value of any variable $\phi \in \{\tau, u, e^1, e^2\}$ is constant inside the cell, they are described by a discontinuity. The discontinuity is defined by a left state $\phi_{i,l}^n$, a right state $\phi_{i,r}^n$, a speed of propagation $\sigma_i^n$ and a position $x_i^{n,\phi}$ which may *a priori* depend on the variable $\phi$.

- The nature of the shock is determined by the pressure difference : it is a 1-shock if $\tau_{i+1}^n < \tau_{i-1}^n$ and a 3-shock if $\tau_{i+1}^n > \tau_{i-1}^n$. Its speed $\sigma_i^n$ is then taken as the corresponding shock speed of the solver under consideration.

- The chosen solver also provides the reconstructed states depending on the nature of the
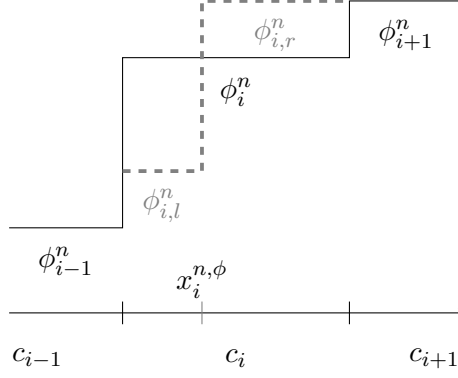
Figure 4.2: Example of a reconstructed 3-shock (dashed lines) inside cell $c_i$ for variable $\phi$.

shock

$$\phi_{i,l}^n = \phi_{i-1}^n, \quad \phi_{i,r}^n = \phi_L^*(U_{i-1}^n, U_{i+1}^n) \quad \text{if } \sigma_i^n < 0, \tag{4.52a}$$

$$\phi_{i,l}^n = \phi_R^*(U_{i-1}^n, U_{i+1}^n), \quad \phi_{i,r}^n = \phi_{i+1}^n \quad \text{if } \sigma_i^n > 0. \tag{4.52b}$$

- The shock position $x_i^{n,\phi}$ is chosen so as to ensure that the reconstruction procedure is conservative. Expressing the position as

$$x_i^{n,\phi} = x_{i-1/2} + d_i^{n,\phi}\Delta x, \tag{4.53}$$

the conservation

$$d_i^{n,\phi}\phi_{i,l}^n + (1 - d_i^{n,\phi})\phi_{i,r}^n = \phi_i^n \tag{4.54}$$

eventually yields

$$d_i^{n,\phi} = \frac{\phi_{j,r}^n - \phi_j^n}{\phi_{j,r}^n - \phi_{j,l}^n}. \tag{4.55}$$

Some shock reconstructions are ultimately not considered. In order not to deal with shock interactions, an admissible shock in cell $c_i$ is not considered if a 3-shock is admissible in cell $c_{i-1}$ or if a 1-shock is admissible in cell $c_{i+1}$. Besides, its position needs to be inside its corresponding cell, or equivalently, one must have $d_i^{n,\phi} \in [0, 1]$ for all variables $\phi \in \{\tau, u, e^1, e^2\}$.

**Remark 26.** The failure of Godunov type schemes lies in the averaging process which creates superficial physical entropy (or, equivalently, destroys mathematical entropy). This production of entropy is not physical in the sense that it does not result from thermodynamics but rather may be interpreted, in the lights of statistical entropy, as a loss of information and creation of disorder. The shock reconstruction procedure undoes what the averaging step did in the previous time step. As a consequence, the shock reconstruction *destroys* entropy as the cell is injected with an *a priori* information that a shock exists inside. This justifies the necessity of robust shock detection and reconstruction techniques as insufficient ones would needlessly destroy entropy and jeopardize the scheme stability. This issue has been discussed in [63] for scalar conservation laws.
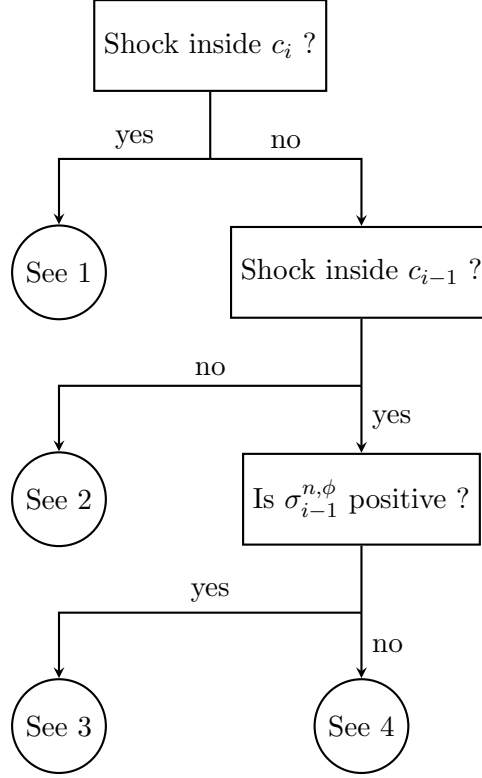
Figure 4.3: Decision tree for computing $\phi_{i,L}^{n+1}$.

**Cell values update**

Cell values are updated depending on whether or not a shock has been reconstructed. The general idea is to exactly advect the reconstructed shocks while applying the classic Godunov's scheme elsewhere. The different cases, described for the computation of the half integral $\phi_{i,L}^{n+1}$ in figure 4.3, are discussed one by one. The other half integral $\phi_{i,R}^{n+1}$ is treated symmetrically. Finally

$$\phi_i^{n+1} = \frac{1}{2}(\phi_{i,L}^{n+1} + \phi_{i,R}^{n+1}). \tag{4.56}$$

**Case 1.** In this case, the whole cell value $\phi_i^{n+1}$ is updated at once

$$\phi_i^{n+1} = \phi_i^n - \frac{\sigma_i^n(\phi_{i,r}^n - \phi_{i,l}^n)}{\Delta x} \min(\Delta t, \Delta t_i^\phi), \tag{4.57}$$

where $\Delta t_i^\phi$ corresponds to the time it takes for the discontinuity to leave the cell, namely

$$\Delta t^\phi = \frac{1 - d_i^{n,\phi}}{\sigma_i^{n,\phi}}\Delta x \quad \text{if } \sigma_i^{n,\phi} > 0, \tag{4.58a}$$

$$\Delta t^\phi = -\frac{d_i^{n,\phi}}{\sigma_i^{n,\phi}}\Delta x \quad \text{if } \sigma_i^{n,\phi} < 0. \tag{4.58b}$$

**Case 2.** No shock is considered around the node $x_{i-1/2}$ so $\phi_{i,L}^{n+1}$ (and for the very same reason $\phi_{i-1,R}^{n+1}$) is updated with Godunov's method together with the chosen solver : the (approximated or exact) solution at time $\Delta t$ of the Riemann problem between $U_{i-1}$ and $U_i$ is exactly computed

and then averaged over each half cells.

**Case 3.** A shock is reconstructed inside cell $c_{i-1}$ and travels towards cell $c_i$ through which it may then propagate. Consequently,

$$\phi_{i,L}^{n+1} = \phi_i^n - \frac{2\sigma_{i-1}^n(\phi_i^n - \phi_{i-1,l}^n)}{\Delta x} \min(0, \Delta t - \Delta t_{i-1}^\phi). \tag{4.59}$$

Where $\Delta t_{i-1}^\phi)$ is given by (4.58) adapted to $c_{i-1}$. In particular, if $\Delta t_{i-1}^\phi < \Delta t$ (i.e. the shock has not reach the node $x_{i-1/2}$), then the value is unchanged.

**Case 4.** A shock is reconstructed inside cell $c_{i-1}$ and travels towards the opposite direction of cell $c_i$. Then, $\phi_{i,L}^{n+1}$ is set to

$$\phi_{i,L}^{n+1} = \phi_i^n + \frac{2\sigma_{i-1}^n(\phi_i^n - \phi_{i-1,r}^n)}{\Delta x}\Delta t. \tag{4.60}$$

**Remark 27.** The resulting scheme is exact for isolated shocks if the Riemann solver is also exact in such a case. This means that the shock is spread over one cell at most. In particular, the numerical solution converges to the exact solution. A proof of this result can be found in [15].

## 4  Numerical results

Different Riemann problems are considered in order to assess the scheme's convergence and robustness. The initial states of each Riemann problem are gathered in tabular 4.1. The CFL is set at 0.9. Unless specified otherwise, the path on the pressure difference is the linear path

$$\Delta p(s) = \Delta p_L + s(\Delta p_R - \Delta p_L), \tag{4.61}$$

which gives back expression (4.28). Both the shock reconstruction and Godunov's schemes are used together with the Roe solver for numerical simulations and their results are compared with analytical solutions provided by the exact solver. It is shown that Godunov's scheme fails to converge to the analytical solution for Riemann problem displaying at least one shock, while the shock reconstruction scheme concurs with the analytical solution and is even exact in the case of an isolated shock (i.e. the shock is spread over one cell at most).

### 4.1  Single temperature double shock

The first test case comes from [15]. Both energies are initialized with half the prescribed value and their respective EOS are identical. Consequently, the two-temperature model degenerates to the single temperature Euler equations while the Roe solver derived in section 3.1 degenerates to the Roe solver found in [15]. As such, the results are expected to be exactly the same. They are displayed in figure 4.4 and indeed corresponds to the previously published ones. Godunov's scheme provides a solution with a false right intermediate state (the error is especially

| n° | $t_{\text{final}}$ | Left State | | | | Right State | | | | EOS |
|----|------|---------|----------|----------|------------|----------|-------|-------|------------|-----|
| | | $\tau_L$ | $u_L$ | $p_L$ | $\Delta p_L$ | $\tau_R$ | $u_R$ | $p_R$ | $\Delta p_R$ | |
| 1 | 0.5 | 5.0 | 3,323014 | 0,481481 | 0.0 | 8.0 | 0.0 | 0.1 | 0.0 | $\gamma^1 = 1.4$ <br> $\gamma^2 = 1.4$ |
| 2 | 0.5 | 2.773790 | 2.168776 | 1.0 | -0.476715 | 8.0 | 0.0 | 0.1 | 0.0 | $\gamma^1 = 1.4$ <br> $\gamma^2 = 1.8$ |
| 3 | 0.4 | 5.050679 | 0.475348 | 2.0 | 0.855799 | 8.0 | 0.0 | 0.1 | 0.0 | $\gamma^1 = 1.4$ <br> $\gamma^2 = 1.8$ |
| 4 | 0.1 | 3.241852 | 11.92764 | 30.0 | -24.56237 | 8.0 | 0.0 | 0.1 | 0.0 | $\Gamma^1 = 0.4, \quad \pi^1 = 1.0$ <br> $\Gamma^2 = 0.8, \quad \pi^1 = 4.0$ |

Table 4.1: Final time, initial conditions and equations of state for each test case.

pronounced on the specific volume) while the shock reconstruction scheme gives an accurate solution in the sense that intermediate states are correctly captured and that the solution is almost not diffused around the shocks.

## 4.2   Isolated shock

For the first genuine two-temperature test case, the solution of the Riemann problem consists in a single isolated wave. Godunov's scheme generates a spurious contact wave and, again, does not converge to the right solution. As for the shock reconstruction scheme, the shock is well maintained and spread only over one cell.

## 4.3   Rarefaction wave

The exact solution for this test case consists in a left rarefaction wave, a contact wave, and a right shock wave. For the shock wave, the results are similar to that of previous test cases, meaning that Godunov's scheme create a wrong intermediate state while the shock reconstruction scheme captures correctly the shock. For the rarefaction wave, both scheme provide similar results. This is not surprising as the shock reconstruction scheme reduces to Godunov's scheme in such a case.

## 4.4   Isentropic path and stiffened gas

The last test case aims at illustrating how the shock reconstruction scheme together with the Roe solver perform with stiffened gases and an alternative choice of path. The paths under consideration are designed so as to transform (4.33b) into an equality for one $i \in \{1, 2\}$, meaning that compound $i$ undergoes no entropy increase inside shocks. Equation (4.33b) is only defined when states $(\tau_L, p_L^i)$ and $(\tau_R, p_R^i)$ belong to the same isentropic curve ; in order to fully define a path (or, sufficiently, its average value), it must be extended to an arbitrary couple of states. A possibility is given by

$$\int_0^1 p^i(s)ds = \frac{1}{\tau_R - \tau_L} \int_{\tau_L}^{\tau_R} p^i(\tau, \min(s_L^i, s_R^i))d\tau, \tag{4.62}$$

where the pressure is integrated along the isentropic curve going through the state of minimal entropy (i.e. the curve $s^i = s_L^i$ if $s_L^i < s_R^i$ and $s^i = s_R^i$ otherwise, see figure 4.7 for a visual
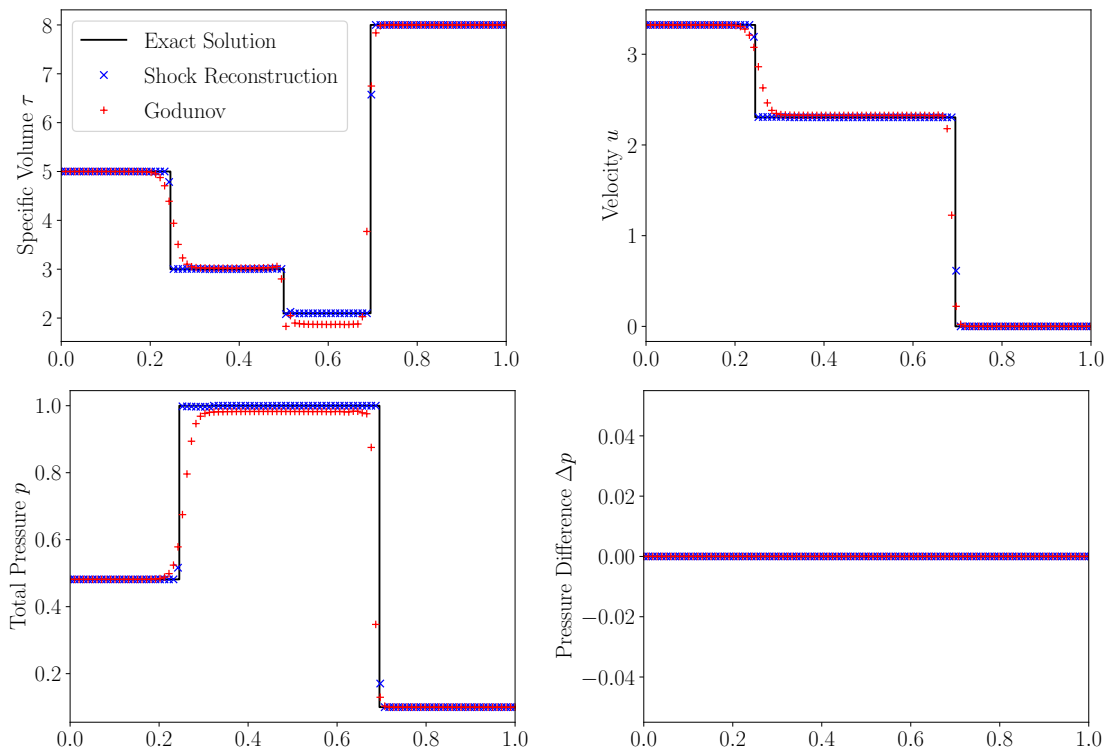
Figure 4.4: The single temperature double shock test case with 100 cells and a 0.9 CFL. Godunov's scheme provides a solution with a false right intermediate state (the error is especially pronounced on the specific volume). The shock reconstruction scheme gives an accurate solution in the sense that intermediate states are correctly captured and that the solution is almost not diffused around the shocks.
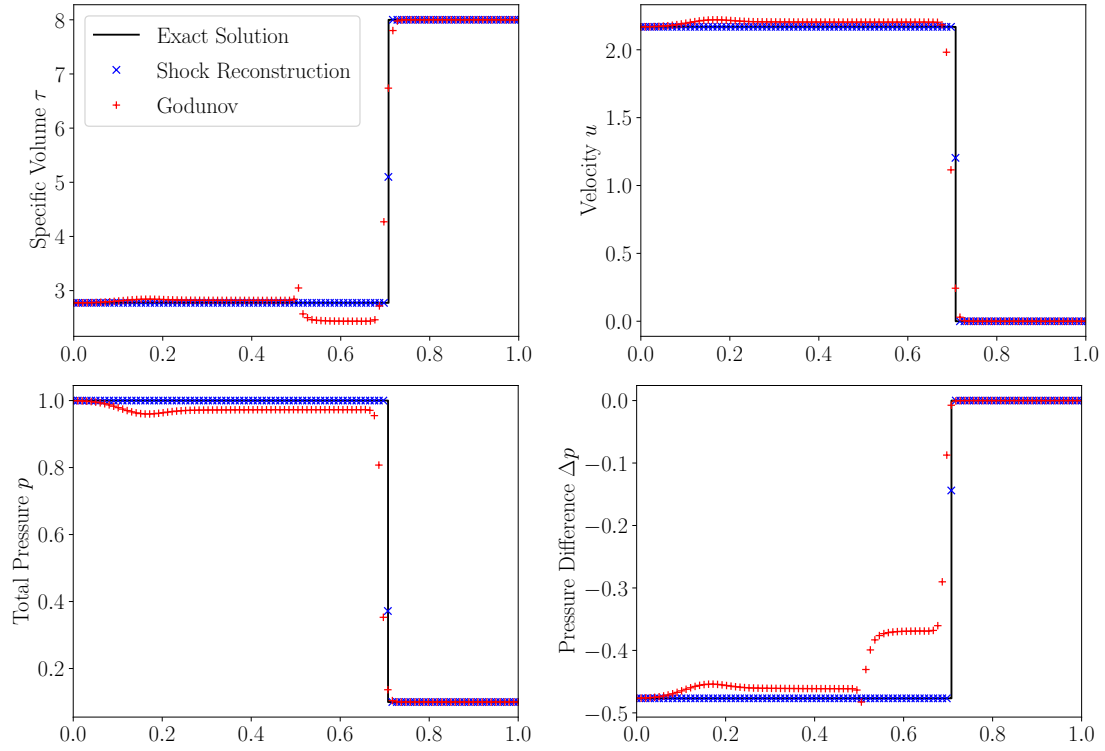
Figure 4.5: The two-temperature isolated shock test case with 100 cells and a 0.9 CFL. Godunov's scheme provides a solution with an additional contact wave which is not present in the analytical solution. The shock reconstruction scheme exactly captures the shock.
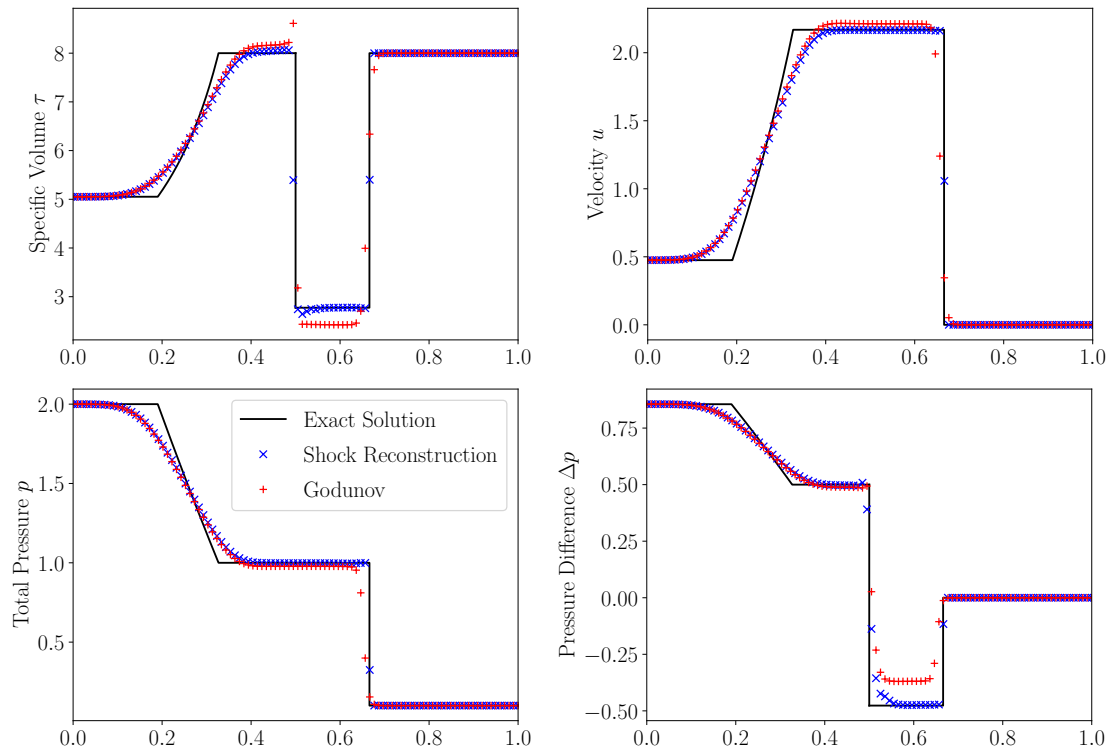


Figure 4.6: Two-temperature test case with a left rarefaction wave with 100 cells and a 0.9 CFL. The results around it are similar for Godunov's scheme and the shock reconstruction on which is normal as the latter reduces to the former in such a case.
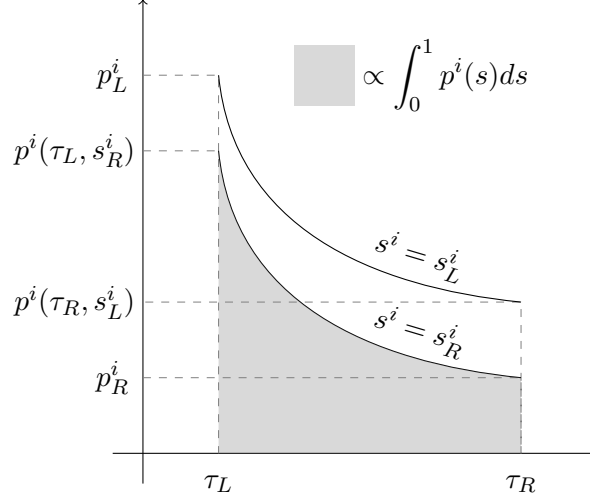
Figure 4.7: Visualization of the path on $p^i$ and the corresponding integral. Because isentropic curves are convex, the integral is smaller than the area under the line connecting the states $(\tau_L, p_L^i)$ and $(\tau_R, p_R^i)$.

illustration). The exact expression of the integral is computed in appendix for a stiffened gas (F.7). In regards with the different constraints identified in 2.4,

1. The extension does not break the symmetry,

2. It does not infringe upon thermodynamical feasibility. Indeed, if isentropic curves are convex in the $\tau - p^i$ plane (i.e. if the fundamental derivative $\mathcal{G}^i$ is positive), (4.62) implies

$$\int_0^1 p^i(s)ds < \frac{p_L^i + p_R^i}{2}, \tag{4.63}$$

which gives, together with (4.24),

$$\int_0^1 p^j(s)ds = \int_0^1 p(s)ds - \int_0^1 p^i(s)ds, \tag{4.64a}$$

$$> \frac{p_L + p_R}{2} - \frac{p_L^i + p_R^i}{2}, \tag{4.64b}$$

$$> \frac{p_L^j + p_R^j}{2}, \tag{4.64c}$$

$$> -\pi^j. \tag{4.64d}$$

In particular, if states $(\tau_L, p_L^i, p_L^j)$ and $(\tau_R, p_R^i, p_R^j)$ both comply with thermodynamical constraints, so does the average state (4.44) given by the Roe solver.

3. Entropy considerations are only relevant for couples of states which may actually be connected by a shock and are thus not concerned with the extension of the path to arbitrary states.

The test case consists in an strong isolated shock for an isentropic path on compound 1. It may be seen in figure 4.8 that the entropy $s^1$ stays constant across the shock while the entropy $s^2$ increases hence ensuring consistency with the second principle of thermodynamics. On the

same figure are found the results of a simulation with the same initial condition but with an isentropic path on compound 2. The exact solution no longer consists in an isolated shock and displays instead a right shock together with a contact wave and a left rarefaction wave. The entropy $s^2$ is kept constant across the shock wave while the entropy $s^1$ increases, as expected. In both cases, the numerical results obtained with the shock reconstruction scheme coincide with exact solution.

**Remark 28.** This choice of path is relevant in the case of a completely ionized plasma. Ions are significantly heavier than electrons and are expected to assume almost all of the entropy production, leaving the electrons with an almost isentropic evolution [115].

# 5 Conclusion

In this article, a scheme, based on in-cell shock reconstruction [15] is applied to two-temperature Lagrangian hydrodynamics. The system is genuinely non-conservative, a fact which has several consequences, both mathematically and physically. From a mathematical perspective, no canonical weak formulation exists inside discontinuities. The method for solving Riemann problems is presented and relies on the path formalism first introduced in [77]. Physically, solutions inside shocks heavily depend on dissipative effects (e.g. viscosity and heat transfer) occurring in the vicinity of the shock. The article tries to bridge the gap between the two points of view by investigating how physical considerations on entropy constrain the path used to define jump relationships. Numerically, the scheme is shown to converge to the exact solution for different choices of path, including the asymptotic case where one compound bears all the dissipation, leaving the other one with an isentropic behavior.

Perspectives are numerous. First, the link between the choice of path and physical considerations could be tighten, in the full spectrum between the two asymptotic cases identified in this article, as well as beyond these limits if an additional heat transfer is taken into account. As for the scheme based on in-cell shock reconstruction, extensions to higher order (see [88] for second order), higher dimensions or more sophisticated equations of state could be investigated.
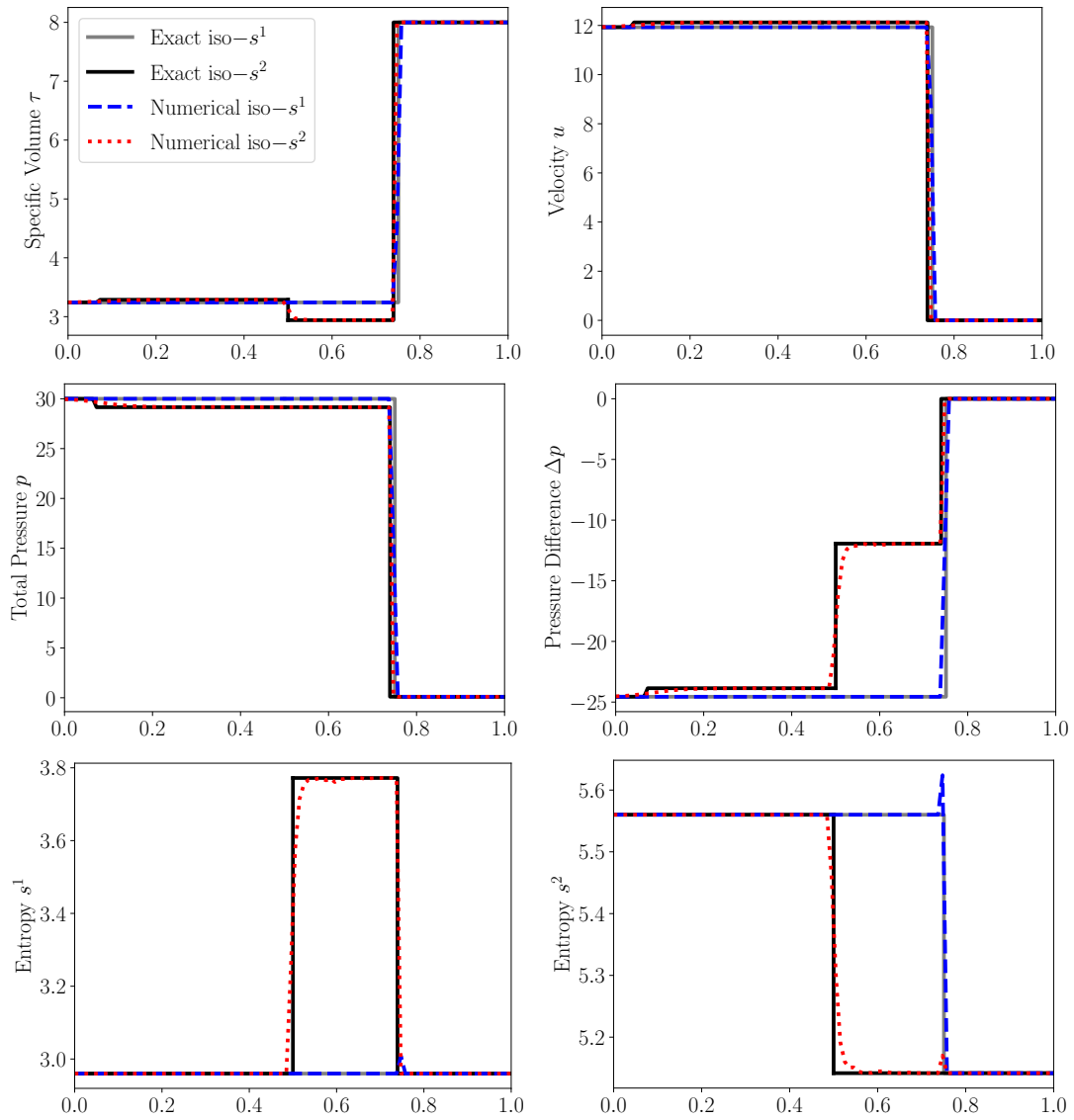
Figure 4.8: Fourth test case with 100 cells,a 0.9 CFL and two different paths ensuring either that compound 1 or compound 2 is isentropic. Both numerical solutions provided by the shock reconstruction scheme match the exact solution. In particular, the isentropic behavior is recovered in both cases.

# Conclusion

## Contents

Results of the different studies are already summarized at the end of each chapter. Here are mentioned general concluding remarks and perspectives.

## 1 Toward three-temperature multi-velocity multi-material hydrodynamics with pressure equilibration

A relevant challenge, subsequent to the present work, is to merge the strategies of chapters 2 and 3 in order to obtain a complete discretization of three-temperature multi-velocity multi-material hydrodynamics with pressure equilibration (i.e. equations (16) with drag, temperature relaxations and radiation transport). The inclusion of drag or any additional force can be written in a generic fashion

$$m_c^k \frac{\mathrm{d}^k}{\mathrm{d}t} \mathbf{u}_c^k = \alpha_c^k \sum_{p \in \mathcal{P}(c)} \mathbf{M}_{pc}(\overline{\mathbf{u}}_p - \overline{\mathbf{u}}_c) + \mathbf{F}_c^k. \tag{5.1}$$

Forces are subject to the conditions $\sum_k \mathbf{F}_c^k = 0$ (conservation of momentum) and $\sum_k \mathbf{F}_c^k \cdot \mathbf{u}_c^k > 0$ (second principle of thermodynamics). Once again, a discrete Gibbs equation is written for each potential

$$\frac{\mathrm{d}^k}{\mathrm{d}t} e_{i,c}^k = -p_{i,c}^k \frac{\mathrm{d}^k}{\mathrm{d}t}\left(\frac{1}{\rho_c^k}\right) + T_{i,c}^k \frac{\mathrm{d}^k}{\mathrm{d}t} s_{i,c}^k, \tag{5.2a}$$

$$\frac{\mathrm{d}^k}{\mathrm{d}t} e_{e,c}^k = -p_{e,c}^k \frac{\mathrm{d}^k}{\mathrm{d}t}\left(\frac{1}{\rho_c^k}\right) + T_{e,c}^k \frac{\mathrm{d}^k}{\mathrm{d}t} s_{e,c}^k, \tag{5.2b}$$

$$\frac{\mathrm{d}^k}{\mathrm{d}t}\left(\frac{e_{r,c}^k}{\rho^k}\right) = -p_{r,c}^k \frac{\mathrm{d}^k}{\mathrm{d}t}\left(\frac{1}{\rho_c^k}\right) + T_{r,c}^k \frac{\mathrm{d}^k}{\mathrm{d}t} s_{r,c}^k. \tag{5.2c}$$

Volume evolution is given by the equal pressure assumption. The discretization of chapter 3 is amenable to three-temperature flows and gives

$$m_c^k \frac{\mathrm{d}^k}{\mathrm{d}t}\left(\frac{1}{\rho_c^k}\right) = \beta_c^k \sum_{p\in\mathcal{P}(c)} l_{pc}\mathbf{n}_{pc}\overline{\mathbf{u}}_p + D_c^k, \tag{5.3a}$$

$$D_c^k = \frac{\alpha_c^k}{\rho_c^k\left(c_c^k\right)^2} \sum_l \beta_c^l \left[(\mathbf{u}_c^k - \mathbf{u}_c^l)\cdot \sum_{p\in\mathcal{P}(c)} \mathbf{M}_{pc}(\overline{\mathbf{u}}_p - \overline{\mathbf{u}}_c) + \Delta_c^{kl}\right], \tag{5.3b}$$

$$\Delta_c^{kl} = \sum_{\theta\in\{i,e,r\}} \left[\frac{\Gamma_{\theta,c}^l}{\alpha_c^l}m_c^l T_{\theta,c}^l \frac{\mathrm{d}^l}{\mathrm{d}t}s_{\theta,c}^l - \frac{\Gamma_{\theta,c}^k}{\alpha_c^k}m_c^k T_{\theta,c}^k \frac{\mathrm{d}^k}{\mathrm{d}t}s_{\theta,c}^k\right]. \tag{5.3c}$$

where $(c^k)^2 = \sum_{\theta\{i,e,r\}}(c_\theta^k)^2$ and the definition of coefficients $\beta^k$ remains unchanged. Finally, the entropy evolution is given by the total heat deposit distribution (which takes it account the work of forces $\mathbf{F}_c^k$) and the additional term $Q_{\theta,c}^k$ which encapsulates temperature relaxation and radiation transport.

$$m_c^k T_{\theta,c}^k \frac{\mathrm{d}^k}{\mathrm{d}t}s_{\theta,c}^k = \lambda_{\theta,c}^k\left[\sum_k \mathbf{F}_c^k\cdot\mathbf{u}_c^k + \sum_{p\in\mathcal{P}(c)}(\overline{\mathbf{u}}_p - \overline{\mathbf{u}}_c)^{\mathrm{T}}\mathbf{M}_{pc}(\overline{\mathbf{u}}_p - \overline{\mathbf{u}}_c)\right] + Q_{\theta,c}^k. \tag{5.4}$$

If space discretization is an essentially straightforward continuation of the ideas developed in the manuscript, time integration remains a challenging issue. While an implicit time integration of forces $\mathbf{F}_c^k$ is essentially independent on pressure equality or on the number of temperatures, the implicit treatment of temperature relaxations and radiation transport is not trivial. The strategy presented in chapter 2 cannot be directly adapted as $Q_{\theta,c}^k$ generates an entropy production which, in turn, affects the pressure equilibrium and volume evolution in (5.3c). Solving the resulting convoluted coupling between numerous stiff phenomena would require specific and robust numerical methods.

## 2   Toward better accuracy

Accuracy issues are twofold and generally stems from over-dissipation. In isentropic regions of the flow, dissipation is not required and can lead to nonphysical heating or smearing; dissipation should ideally be completely removed. In the vicinity of shocks, unrequested dissipation pollutes the specification of the total heat deposit distribution, thus leading to convergence issues; a distinction must then be made between the necessary physically-driven dissipation and its spurious counterpart.

During the Lagrange phase, the scheme entropy production is almost entirely physical. It must be kept for stabilizing shocks but could be removed where it is not needed. Removal can be tedious and endanger total energy conservation if the numerical viscosity is entangled with the work of pressure forces as discussed in appendix D. It is worth mentioning that the pressure terms preventing conservation can be removed from the GLACE/EUCCLHYD discrete divergence of the velocity (D.2). In this case, a corresponding discrete pressure gradient exists

and they read

$$[\nabla \cdot \mathbf{u}]_c = \sum_{p \in \mathcal{P}(c)} \sum_{d \in \mathcal{C}(p)} l_{pc} \mathbf{n}_{pc}^{\mathrm{T}} \mathbf{M}_p^{-1} \mathbf{M}_{pd} \mathbf{u}_d, \tag{5.5a}$$

$$[\nabla \mathbf{p}]_c = \sum_{p \in \mathcal{P}(c)} \sum_{d \in \mathcal{C}(p)} p_d l_{pd} \mathbf{M}_{pc} \mathbf{M}_p^{-1} \mathbf{n}_{pd}. \tag{5.5b}$$

Because pressure and viscosity can now be separated from one another, isentropic flows could be captured. The resulting scheme however drifts away from the GLACE/EUCCLHYD scheme for two main reasons.

- Because of the GCL, node velocities needs to be changed and now read

$$\mathbf{u}_p = \mathbf{M}_p^{-1} \sum_{c \in \mathcal{C}(p)} \mathbf{M}_{pc} \mathbf{u}_c. \tag{5.6}$$

- Numerical viscosity still needs to be added in the vicinity of shocks to guarantee stability. The GLACE/EUCCLHYD innate one is not a possibility as it can no longer count on the pressure terms to compensate its lack of conservation.

Even if pressure forces are properly separated from dissipation, removing the latter can produce oscillations resulting from an odd-even decoupling. Odd-even decoupling is a common issue on cell-centered configurations when viscosity is neglected. Asymmetric space derivatives seem to alleviate this issue [91] but further studies would be needed to properly tailor their expression.

The remapping also introduces its share of dissipation. Transport is a reversible process but its approximation is usually not. Upwind fluxes are commonly used and guarantee monotony, a condition which is critical in strong regimes where volume fraction or density are prone to becoming negative. Upwinding however induces a discrete entropy production. It appears that monotony and reversibility are mutually exclusive [86]. If a stricly isentropic transport approximation is not reasonnable, the design of high order limiters for transport remains a relevant direction toward better accuracy [61, 85]; the present work could substantially benefit from them. Caution still needs to be exercised as mindless high-order strategies can destroy thermodynamic consistency [75].

## 3   Toward a general framework for multi-material discretization

Although the number of possible numerical approaches is virtually infinite, the physics remains universal. Some principles can hardly be ignored without jeopardizing the credibility of numerical approximations. Pinpointing the generalities that can be extracted from the present work is a worthy effort. This list could serve as a guideline from which comparisons could be drawn with previous work on multi-material flows including [94, 17, 108]. Common features could be identified while discrepancies and their impact on solutions could be evaluated.

Masses, total momentum and total energy conservation are necessary correct jumps inside shocks. In finite volume schemes, conservation is obtained by writing integral equations and fluxes between cells [41]. Other techniques focus on the algebraic requirements underpinning conservation [38, 13, 108]. The three first chapters extend the finite volume EUCCLHYD/GLACE

scheme to multi-material flow. Conservation is obtained through node fluxes. The discussion in the previous section however shows that a proper discrete integration by part could help designing an essentially diffusion-free scheme.

Another critical point of fluid applications is consistency with thermodynamics. This point is a major concern across all chapters and is addressed by writing a discrete form of Gibbs equation (3.30). Entropy evolution can then be directly discretized and inserted into the internal energy evolution. A general formalism to deal with dissipative systems is the GENERIC framework [44]. The state variable $X$ evolves consistently with

$$\frac{\mathrm{d}}{\mathrm{d}t}X = A(X)\nabla E(X) + B(X)\nabla S(X), \tag{5.7}$$

where $E$ is the total energy, $S$ the entropy, and $A$ and $B$ are matrices. The GENERIC framework consists in a minimum set of algebraic conditions on $A$ and $B$ that are necessary for total energy conservation and an increase of entropy. It is applied to hydrodynamics in [82] and its use for multi-material flows could be investigated.

Finally, multi-temperature multi-material shocks depend on small-scale phenomena. Numerically, the multiplicity of admissible shocks must translate into some form of degrees of freedom at the discrete level. If not, the scheme will only be able to capture specific shocks thus implicitly binding it to specific applications.

- In chapter 1, 2 and 3, shocks are defined through coefficients $\lambda_\theta^k$ (1.41) (2.31) (3.32). They can arbitrarily be chosen inside a limited range whose boundary is dictated by thermodynamics. This strategy is already employed in previous works [108, 19].

- In chapter 4, shocks are defined by paths [77] and, again, must answer to several physical constraints. Path-consistency numerical approximations have been extensively studied [33, 12]. Shocks are highly non-linear phenomena and, as such, dissipation cannot commute with any form of averaging. The main issue with general path-consistent schemes comes from specifying the dissipation in the approximate solver *before* the averaging. This issue can only be circumvented if the averaging is bypassed as in [15, 88] and chapter 4, or is somehow made path-consistent as in [114].

- Finally, in [3, 87], shocks are understood as arising from the geometry of the mixture. The numerical approximations of pressure fluxes is formally equivalent to that of the radiation transport in chapter 2. According to [87], maximizing same-material interactions corresponds to separated phases while minimizing them corresponds to dispersed phases.

Beyond any abstract considerations, relating whichever description is chosen to genuine physical systems is a question that cannot be avoided.

# Appendix A

# Single-velocity model with both equal-strain and equal-pressure assumptions

In this section, it is shown that using both equal strain and equal pressure assumption is possible, at the expense of loosing the consistency with the second principle of thermodynamics. In [4], such a model is studied. The system of equation then reads

$$\alpha^k \rho^k \frac{\mathrm{d}}{\mathrm{d}t} \left( \frac{1}{\alpha^k \rho^k} \right) = \nabla \cdot \mathbf{u}, \tag{A.1a}$$

$$\rho \frac{\mathrm{d}}{\mathrm{d}t} \mathbf{u} = -\nabla p, \tag{A.1b}$$

$$\rho \frac{\mathrm{d}}{\mathrm{d}t} e = -p \nabla u, \tag{A.1c}$$

$$\frac{\mathrm{d}}{\mathrm{d}t} \alpha^k = 0, \tag{A.1d}$$

$$p = p^k(\rho^k, e^k). \tag{A.1e}$$

As shown in the two previous sections, equal strain and equal pressure assumptions both provide full closure of system (1.5); hence they are not compatible unless completely equivalent, which is not the case as soon as equation of states are different. The reason why both assumptions may here be considered jointly is because material isentropy of model (1.5) is given up. Indeed, it may be shown that (A.1c) and (1.20) imply

$$\alpha^k \rho^k T^k \frac{\mathrm{d}}{\mathrm{d}t} \eta^k = \left( \sum_l \frac{\alpha^l \rho^l (c^l)^2}{\Gamma^l} \right) \left( \xi^k - \zeta^k \right) \nabla \cdot \mathbf{u}, \tag{A.2}$$

with

$$\xi^k = \frac{\dfrac{\alpha^k \rho^k (c^k)^2}{\Gamma^k}}{\displaystyle\sum_l \frac{\alpha^l \rho^l (c^l)^2}{\Gamma^l}}, \qquad \zeta^k = \frac{\dfrac{\alpha^k}{\Gamma^k}}{\displaystyle\sum_l \frac{\alpha^l}{\Gamma^l}}, \tag{A.3}$$

and such that

$$\sum_k \alpha^k \rho^k \frac{\mathrm{d}}{\mathrm{d}t} \eta^k = \left( \sum_l \frac{\alpha^l \rho^l (c^l)^2}{\Gamma^l} \right) \left( \sum_k \frac{\xi^k - \zeta^k}{T^k} \right) \nabla \cdot \mathbf{u}, \tag{A.4}$$

which may become negative for some temperatures. As such, this model does not necessarily respect the second principle of thermodynamics and accounts for an heat exchange between materials which has yet to be justified physically. The advantage of model (1.5) is that it provides a framework where the isentropic behavior is dealt with independently of dissipative terms which may be added depending on the physical context. In [81], the authors also pointed out the fact that the mixture sound of speed of model (A.1) may not be properly defined for real equations of state.

# Appendix B

# Interface area proportions: extension to more than two materials

This section extends the analysis exposed in section 3.2 for system (2.18) (rewritten below) when dealing with an arbitrary number $N$ of materials.

$$\sum_l \delta_{cd}^{kl} = \delta_{cd}^k, \quad \forall k \tag{B.1a}$$

$$\sum_k \delta_{cd}^{kl} = \delta_{dc}^l, \quad \forall l. \tag{B.1b}$$

The set of unknowns may be gathered on the $N \times N$ array where the $(k,l) - th$ entry is $\delta_{cd}^{kl}$. Then, equations (B.1a) constrain the sum of rows and (B.1b) the sum of columns. in Figure B.1 is displayed the matrix for $N = 3$. The array form of the equations substantially eases the analysis. It may be seen that a necessary and sufficient condition for (B.1) to have a solution is

$$\sum_k \delta_{cd}^k = \sum_l \delta_{dc}^l, \tag{B.2}$$

which is trivially satisfied because both sides of the equation are equal to one. In terms of linear algebra, it means that the Image of the linear mapping related to (B.1) is the hyperplane defined by (B.2). The rank (i.e. the dimension of the Image) is then $2N - 1$. By the rank-nullity theorem, the Kernel is then of dimension $N^2 - (2N - 1) = (N - 1)^2$ which corresponds to the number of degrees of freedom on the solution. It is not surprising as setting the value of a $(N-1) \times (N-1)$ sub-array of the variable array is enough to fill up the rest with the conditions

$$
\begin{array}{ccc|c}
\delta_{cd}^{11} & \delta_{cd}^{12} & \delta_{cd}^{13} & \delta_{cd}^1 \\[6pt]
\delta_{cd}^{21} & \delta_{cd}^{22} & \delta_{cd}^{23} & \delta_{cd}^2 \\[6pt]
\delta_{cd}^{31} & \delta_{cd}^{32} & \delta_{cd}^{33} & \delta_{cd}^3 \\[6pt]
\hline
\delta_{dc}^1 & \delta_{dc}^2 & \delta_{dc}^3 &
\end{array}
$$

Figure B.1: Matrix of variables for $N = 3$.

on the sum of the lines and columns. In the case $N = 2$, there is only $(N-1)^2 = 1$ degree of freedom which corresponds to $\lambda$ in (2.20). The three cases $\lambda_0, \lambda_{max}$ and $\lambda_{min}$ do not all extend well to an arbitrary number of materials.

- An natural equivalent of $\lambda_0$ is given by

$$\delta_{cd}^{kl} = \delta_{cd}^k \delta_{dc}^l. \tag{B.3}$$

- The case $\lambda_{\max}$ consists in maximizing diagonals element in the variable matrix. A possible extension is

$$\delta_{cd}^{kk} = \min(\delta_{cd}^k, \delta_{dc}^k), \tag{B.4a}$$

$$\delta_{cd}^{kl} = \frac{(\delta_{cd}^k - \delta_{cd}^{kk})(\delta_{dc}^l - \delta_{cd}^{ll})}{\sum_k (\delta_{cd}^k - \delta_{cd}^{kk})}, \tag{B.4b}$$

where (B.4a) corresponds to the maximum value diagonal elements can take. The rest of surface proportions are arbitrarily given by (B.4b), although other choices are still possible because of the great number of degrees of freedom.

- The case $\lambda_{\min}$ has no natural extension. Applying $\lambda_{\min}$ to every couple of materials is possible but heavily depends on the order with which couples are taken.

# Appendix C

# Computation of the internal flux for two materials

In this section, all the detail required to compute the internal flux are presented. The internal flux between two materials of a given cell is

$$F^{12} = \kappa^{12}\frac{T^2 - T^1}{L}S.$$ (C.1)

where $S$ is the surface of the interface between the two materials and $L$ denotes the length between the center of gravity of their respective domain. In the following, in the case of a cell containing two materials separated by a straight interface, the surface and length are computed exactly as functions of the volume fraction $\alpha$ of one of the material and the angle $\theta$ between the interface and the horizontal axis. The angle is given by a consistent discretization of the volume fraction gradient

$$\theta = \tan^{-1}\left(-\frac{\partial \alpha}{\partial x}\middle/\frac{\partial \alpha}{\partial y}\right).$$ (C.2)

## 1 Computation of the internal surface

Consider a rectangular cell of dimensions $\Delta x \times \Delta y$ which contains two materials, such as in Figure C.1. In the case where the interface between the two materials is linear, we want to compute its length $S$ as a function of $\alpha$ (the volume fraction of the first material), $\theta$ (the angle
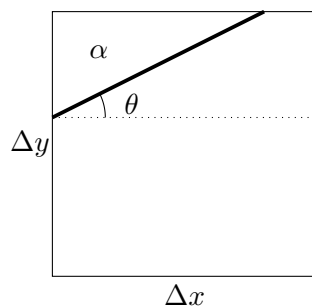


Figure C.1: Vizualisation of the internal surface.

between the interface and the horizontal axis) and the lengths $\Delta x$ and $\Delta y$. The following functional equations must hold

$$S(1 - \alpha, \theta, \Delta x, \Delta y) = S(\alpha, \theta, \Delta x, \Delta y), \tag{C.3a}$$

$$S(\alpha, -\theta, \Delta x, \Delta y) = S(\alpha, \theta, \Delta x, \Delta y), \tag{C.3b}$$

$$S(\alpha, \pi - \theta, \Delta x, \Delta y) = S(\alpha, \theta, \Delta x, \Delta y), \tag{C.3c}$$

$$S(\alpha, \pi/2 - \theta, \Delta x, \Delta y) = S(\alpha, \theta, \Delta y, \Delta x), \tag{C.3d}$$

and correspond respectively to invariance with respect to material subsitution, reflection through the x-axis, reflection through the y-axis and reflection through the first diagonal. These equations allow us to restrict our attention to the domain $(\alpha, \theta) \in [0, \frac{1}{2}] \times [0, \frac{\pi}{2}]$. For a given $\theta$, there exists some $\alpha_{\lim}(\theta)$ such that for all $\alpha \in [\alpha_{\lim}(\theta), \frac{1}{2}]$, the surface is constant, as seen in Figure C.2. The limit volume fraction is reached when one of the end of the interface is at a corner of the cell. The corner first reached is determined by the ratio $\frac{\Delta x}{\Delta y}\tan(\theta)$: it is the upper right corner if the ratio is lower than one and the lower left one if it is greater than 1. If $\frac{\Delta x}{\Delta y}\tan(\theta) < 1$ then trigonometric identities eventually yield

$$S\left(\alpha_{\lim}(\theta) \le \alpha \le \frac{1}{2}\right) = \frac{\Delta x}{\cos(\theta)}, \tag{C.4a}$$

$$\alpha_{\lim}(\theta) = \frac{1}{2}\frac{\Delta x}{\Delta y}\tan(\theta). \tag{C.4b}$$

The other case is directly recovered from the last functional equality of (C.3). Indeed, if $\frac{\Delta x}{\Delta y}\tan(\theta) > 1$ then $\frac{\Delta y}{\Delta x}\tan\left(\frac{\pi}{2} - \theta\right) < 1$ and we get from equation (C.4)

$$S\left(\alpha_{\lim}(\theta) \le \alpha \le \frac{1}{2}\right) = \frac{\Delta y}{\sin(\theta)}, \tag{C.5a}$$

$$\alpha_{\lim}(\theta) = \frac{1}{2}\frac{\Delta y}{\Delta x}\text{cotan}(\theta), \tag{C.5b}$$

As for the case $0 \le \alpha \le \alpha_{\lim}(\theta)$, it can be shown that

$$S = \sqrt{\frac{2\alpha\Delta x\Delta y}{\cos(\theta)\sin(\theta)}}. \tag{C.6}$$

A plot of the function $S(\cdot, \theta)$ for different values of theta may be visualized in Figure C.4.

## 2 Computation of the internal length

We now consider the same cell as before and are interested in computing the distance $L = \|\overrightarrow{G_1G_2}\|$ between the center of gravity of the two materials. The previous functional equations
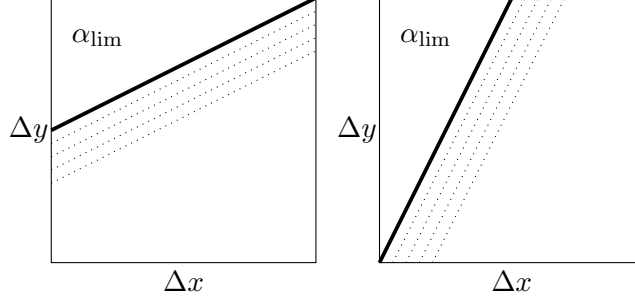
Figure C.2: Both possible cases when $\alpha_{\lim}(\theta) \leq \alpha \leq 1/2$: ratio $\frac{\Delta x}{\Delta y}\tan(\theta)$ lower than 1 (left) and ratio greater than 1 (right).

must still hold:

$$L(1 - \alpha, \theta, \Delta x, \Delta y) = L(\alpha, \theta, \Delta x, \Delta y), \tag{C.7a}$$

$$L(\alpha, -\theta, \Delta x, \Delta y) = L(\alpha, \theta, \Delta x, \Delta y), \tag{C.7b}$$

$$L(\alpha, \pi - \theta, \Delta x, \Delta y) = L(\alpha, \theta, \Delta x, \Delta y), \tag{C.7c}$$

$$L(\alpha, \pi/2 - \theta, \Delta x, \Delta y) = L(\alpha, \theta, \Delta y, \Delta x), \tag{C.7d}$$

Without loss of generality, we assume $\frac{\Delta x}{\Delta y}\tan(\theta) < 1$ so that the interface first reaches the top right corner (if $\frac{\Delta x}{\Delta y}\tan(\theta) > 1$ then $\frac{\Delta y}{\Delta x}\tan\left(\frac{\pi}{2} - \theta\right) < 1$ and the last functional equality may be applied). Similarly to the computation of the surface, two cases are studied separately, both represented in Figure C.3. We first consider the case $0 < \alpha < \alpha_{\lim}$ where the volume occupied by the first material is a triangle. In this case

$$\overrightarrow{G^1G^2} = \frac{1}{V^2}\int_{\omega^2}\overrightarrow{OM}dv - \frac{1}{V^1}\int_{\omega^1}\overrightarrow{OM}dv, \tag{C.8a}$$

$$= \frac{1}{V^2}\int_{\omega}\overrightarrow{OM}dv - \left(\frac{1}{V^1} + \frac{1}{V^2}\right)\int_{\omega^1}\overrightarrow{OM}dv. \tag{C.8b}$$

At this point, we only need to compute the center of gravity of a rectangle and a triangle which is merely the barycenter of their vertices. Finally

$$\overrightarrow{G^1G^2} = \frac{1}{2}\frac{1}{1 - \alpha}\begin{pmatrix}\Delta x \\ \Delta y\end{pmatrix} - \frac{1}{3}\frac{1}{1 - \alpha}\begin{pmatrix}\sqrt{2\alpha\Delta x\Delta y\,\cot an(\theta)} \\ \sqrt{2\alpha\Delta x\Delta y\tan(\theta)}\end{pmatrix}. \tag{C.9}$$

Then, when $\alpha_{\lim} < \alpha < \frac{1}{2}$, the volume $\omega^1$ may be decomposed into a triangle and a parallelogram

$$\overrightarrow{G^1G^2} = \frac{1}{V^2}\int_{\omega^2}\overrightarrow{OM}dv - \frac{1}{V_t^1 + V_p^1}\int_{\omega_t^1\cup\omega_p^1}\overrightarrow{OM}dv, \tag{C.10a}$$

$$= \frac{1}{V^2}\int_{\omega}\overrightarrow{OM}dv - \left(\frac{1}{V_t^1 + V_p^1} + \frac{1}{V^2}\right)\int_{\omega_t^1\cup\omega_p^1}\overrightarrow{OM}dv. \tag{C.10b}$$
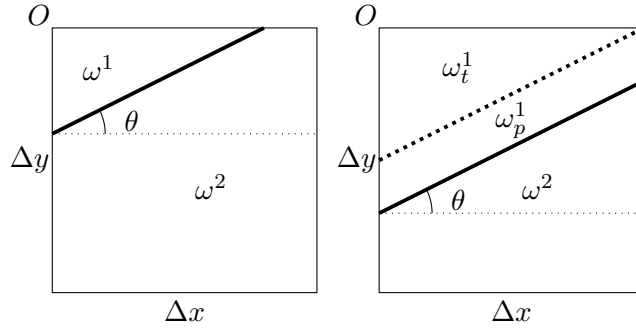
Figure C.3: Both cases. Left: first material's volume is a triangle ($\alpha < \alpha_{\mathrm{lim}}$). Right: first material's volume is the union of a triangle and a parallelogram.
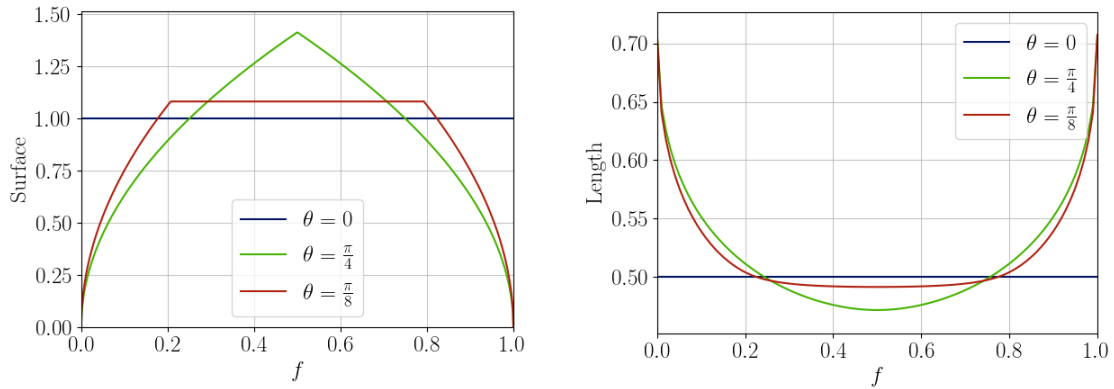


Figure C.4: Interface surface (top) and length between gravity centers (bottom) as functions of volume fractions $\alpha$ for different angles $\theta$.

Once again, finding $\overrightarrow{G_1 G_2}$ amounts to computing centers of gravity of simple shapes which eventually yields

$$\overrightarrow{G^1 G^2} = \frac{1}{2}\frac{1}{1-\alpha}\begin{pmatrix}\Delta x\\\Delta y\end{pmatrix} - \frac{1}{1-\alpha}\frac{\Delta x}{2f\Delta y}\tan(\theta)\frac{1}{3}\begin{pmatrix}\Delta x\\\Delta x\tan(\theta)\end{pmatrix}$$

$$+ \frac{1}{1-\alpha}\left(1 - \frac{\Delta x}{2\alpha\Delta y}\tan(\theta)\right)\frac{1}{2}\begin{pmatrix}\Delta x\\\alpha\Delta y + \frac{1}{2}\Delta x\tan(\theta)\end{pmatrix} \quad \text{(C.11)}$$

A plot of the function $L(\cdot, \theta)$ for different values of theta may be visualized in Figure C.4.

# Appendix D

# GLACE/EUCCLHYD and discrete integration by part failure

The single-fluid GLACE/EUCCLHYD scheme, written in internal energy, reads

$$m_c \frac{\mathrm{d}}{\mathrm{d}t}\left(\frac{1}{\rho_c}\right) = \sum_{p\in\mathcal{P}(c)} l_{pc}\mathbf{n}_{pc}\cdot\mathbf{u}_p, \tag{D.1a}$$

$$m_c \frac{\mathrm{d}}{\mathrm{d}t}\mathbf{u}_c = \sum_{p\in\mathcal{P}(c)} \mathbf{M}_{pc}(\mathbf{u}_p - \mathbf{u}_c), \tag{D.1b}$$

$$m_c \frac{\mathrm{d}}{\mathrm{d}t}e_c = -p_c \sum_{p\in\mathcal{P}(c)} l_{pc}\mathbf{n}_{pc}\cdot\mathbf{u}_p$$

$$+ \sum_{p\in\mathcal{P}(c)} (\mathbf{u}_p - \mathbf{u}_c)^{\mathrm{T}}\mathbf{M}_{pc}(\mathbf{u}_p - \mathbf{u}_c), \tag{D.1c}$$

$$\mathbf{u}_p = \mathbf{M}_p^{-1} \sum_{c\in\mathcal{C}(p)} \left[\mathbf{M}_{pc}\mathbf{u}_c + p_c l_{pc}\mathbf{n}_{pc}\right], \tag{D.1d}$$

$$\mathbf{M}_p = \sum_{c\in\mathcal{C}(p)} \mathbf{M}_{pc}. \tag{D.1e}$$

The discrete divergence of the velocity $[\nabla\cdot\mathbf{u}]_c$ directly comes from the Geometric Conservation Law (GCL) in equation (D.1a).

$$[\nabla\cdot\mathbf{u}]_c = \sum_{p\in\mathcal{P}(c)} l_{pc}\mathbf{n}_{pc}\cdot\mathbf{u}_p. \tag{D.2}$$

It must be the same in the energy equation (D.1c) to properly mimic Gibbs identity and ensure consistency with thermodynamics. Excluding viscous terms (i.e. the entropy production) in (D.1c), total energy conservation advocates for the existence of a discrete pressure gradient $[\nabla p]_c$ such that

$$m_c \frac{\mathrm{d}}{\mathrm{d}t}|\mathbf{u}_c|^2 + m_c \frac{\mathrm{d}}{\mathrm{d}t}e_c = \mathbf{u}_c\cdot[\nabla p]_c + p_c[\nabla\cdot\mathbf{u}]_c \tag{D.3}$$

can be written in terms of fluxes. Injecting (D.1d) in (D.2) gives

$$[\nabla\cdot\mathbf{u}]_c = \sum_{p\in\mathcal{P}(c)}\sum_{d\in\mathcal{C}(p)} l_{pc}\mathbf{n}_{pc}^{\mathrm{T}}\mathbf{M}_p^{-1}\mathbf{M}_{pd}\mathbf{u}_d + \sum_{p\in\mathcal{P}(c)}\sum_{d\in\mathcal{C}(p)} p_d l_{pc}l_{pd}\mathbf{n}_{pc}^{\mathrm{T}}\mathbf{M}_p^{-1}\mathbf{n}_{pd}. \tag{D.4}$$

The first part only depends on the velocity and is consistent with $\nabla\cdot\mathbf{u}$ [28]. The second part only depends on the pressure and comes from approximate Riemann solvers at the nodes. It is the second part which does not allow the discrete integration by part (D.3). Neglecting boundary conditions, for (D.3) to imply conservation, it would require that

$$\sum_c \left(\mathbf{u}_c \cdot [\nabla p]_c + p_c[\nabla \cdot \mathbf{u}]_c\right) = 0. \tag{D.5}$$

Using the fact that

$$\sum_c \sum_{p\in\mathcal{P}(c)} \sum_{d\in\mathcal{C}(p)} = \sum_p \sum_{c,d\in\mathcal{C}(p)} \tag{D.6}$$

and the symmetry of matrices $\mathbf{M}_{pc}$ when switching between indexes $c$ and $d$, it eventually leads to

$$\sum_c \mathbf{u}_c \cdot \left[[\nabla p]_c + \sum_{p\in\mathcal{P}(c)} \sum_{d\in\mathcal{C}(p)} p_d l_{pd}\mathbf{M}_{pc}\mathbf{M}_p^{-1}\mathbf{n}_{pd}\right] + \sum_p \sum_{c,d\in\mathcal{C}(p)} p_c p_d l_{pc} l_{pd}\mathbf{n}_{pc}^{\mathrm{T}}\mathbf{M}_p^{-1}\mathbf{n}_{pd} = 0. \tag{D.7}$$

As stated earlier, no pressure gradient can compensate for the pressure terms in the second part of the equation. In the GLACE/EUCCLHYD scheme, conservation of total energy is obtained through subtle compensations between the work of pressure forces and the numerical viscosity. In other words, both terms do not individually generate a flux; they only generate a global flux together.

# Appendix E

# Multi-dimensional remapping procedure

In order to extend the one-dimensional remapping procedure of section 3.5, the following generic scheme is written

$$V_c^{n+1}\phi_c^{k,n+1} = V_c^{L^k}\phi_c^{k,L^k} - \Delta t \sum_{p\in\mathcal{P}(c)} F_{pc}^k(\phi), \tag{E.1}$$

with $\phi \in \{1, \alpha, \alpha\rho, \alpha\rho\mathbf{u}, \alpha\rho e\}$. Node fluxes are chosen instead of face fluxes because consistency with the Lagrange step is needed. It will be seen that a remapping procedure with face fluxes is actually not compatible with volume conservation. As in the one-dimensional case, fluxes are written as the sum of a centered and a diffusion contribution

$$F_{pc}^k(\phi) = \phi_p^{k,L^k} l_{pc}\mathbf{n}_{pc}\cdot\mathbf{u}_p^k + \sum_{d\in\mathcal{C}(p)} A_{dpc}\left(\phi_c^{k,L^k} - \phi_d^{k,L^k}\right). \tag{E.2}$$

Node estimations $\phi_p^{k,L^k}$ are given as convex combinations over the neighboring cells

$$\phi_p^{k,L^k} = \sum_{d\in\mathcal{C}(p)} \theta_{dp}\phi_d^{k,L^k} \tag{E.3}$$

with positive coefficients $\theta_{dp}$ summing up to one. They are assumed to only depend on the geometry of the initial mesh, hence being the same for all materials. This is essential to ensure that the sum of node volume fractions ($\phi = \alpha$) over all materials equals one. As for the diffusion coefficients $A_{dpc}$, necessary for stability, they are also assumed not to depend on the material so as to ensure their sum over all materials is zero for $\phi = \alpha$. Both parameters answer to different constraints:

(i) Consistency needs to be ensured.

(ii) $F_{pc}^k(\phi)$ must be fluxes. A local conservation property is sought

$$\sum_{c\in\mathcal{C}(p)} F_{pc}^k(\phi) = 0. \tag{E.4}$$

(iii) Lagrangian quantities $\psi_c^{n+1} = \phi_c^{n+1}/(\alpha\rho)_c^{n+1} \in \{1/\alpha\rho, 1/\rho, 1, \mathbf{u}, e\}$ are convex combina-

tions of the initial values (under a CFL-like condition). In this case, the proof of 6 extends naturally to the multi-dimensional case.

In the following, the exponent $L^k$ will be omitted for readability purposes. Condition (i) is automatically recovered as long as $A_{dpc}$ are $\mathcal{O}(h)$ with $h$ a characteristic length of the cells. Condition (ii) reads

$$\sum_{c \in \mathcal{C}(p)} \left( l_{pc} \mathbf{n}_{pc} \cdot \mathbf{u}_p^k \phi_p^k + \sum_{d \in \mathcal{C}(d)} A_{dpc}(\phi_c^k - \phi_d^k) \right) = 0, \tag{E.5a}$$

$$\mathbf{u}_p^k \phi_p^k \cdot \sum_{c \in \mathcal{C}(p)} l_{pc} \mathbf{n}_{pc} + \sum_{c,d \in \mathcal{C}(p)} A_{dpc}(\phi_c^k - \phi_d^k) = 0, \tag{E.5b}$$

$$\sum_{\{c,d\}} (A_{dpc} - A_{cpd})(\phi_c^k - \phi_d^k) = 0. \tag{E.5c}$$

It is then natural to enforce symmetry of the coefficients $A_{dpc} = A_{cpd}$. In regards to condition (iii), equation (E.1) may be written

$$V_c^{n+1} \phi_c^{k,n+1} = \left( V_c - \Delta t \sum_{p \in \mathcal{P}(c)} \left( \theta_{cp} l_{pc} \mathbf{n}_{pc} \cdot \mathbf{u}_p^k + A_{dpc} \right) \right) \phi_c^k$$

$$+ \Delta t \sum_{d \neq c} \left( \sum_{p \in \mathcal{P}(c) \cap \mathcal{P}(d)} \left( A_{dpc} - \theta_{dp} l_{pc} \mathbf{n}_{pc} \cdot \mathbf{u}_p^k \right) \right) \phi_d^k. \tag{E.6}$$

Dividing (E.6) for an arbitrary $\phi$ by the same equation for $\phi = 1$ then gives a convex combination provided that

$$V_c - \Delta t \sum_{p \in \mathcal{P}(c)} \left( \theta_{cp} l_{pc} \mathbf{n}_{pc} \cdot \mathbf{u}_p^k + \sum_{d \in \mathcal{C}(p)} A_{dpc} \right) \geq 0, \tag{E.7a}$$

$$\sum_{p \in \mathcal{P}(c) \cap \mathcal{P}(d)} \left( A_{dpc} - \theta_{dp} l_{pc} \mathbf{n}_{pc} \cdot \mathbf{u}_p^k \right) \geq 0. \tag{E.7b}$$

Equation (E.7a) is essentially a CFL-like restriction on the time step. Equation (E.7b) gives a lower-bound for the diffusion coefficient. In the present work, only regular cartesian meshes are considered. In all test cases, node estimations were given by

$$\theta_{cp} = 1/4. \tag{E.8}$$

As for the diffusion coefficients $A_{dc}$, constraint (E.7b) is saturated so that

$$\sum_{p \in \mathcal{P}(c) \cap \mathcal{P}(d)} A_{dpc} = \frac{1}{4} \max_k \max_{e \in \{c,d\}]} \left( \sum_{p \in \mathcal{P}(c) \cap \mathcal{P}(d)} l_{pe} \mathbf{n}_{pe} \cdot \mathbf{u}_{pe}^k \right). \tag{E.9}$$

The sum contains one or two terms depending on if the cells $c$ and $d$ share a face or only a single node.

**Remark 29.** With a usual remapping procedure based on face fluxes, no flux exists between two cells only sharing one node (and no face). Here, it is worth noticing that for all materials not satisfying the maximum $\max_k$ in (E.9), the flux between two such cells is non zero. This is necessary to comply with the constraints on total volume conservation.

# Appendix F

# Stiffened gas equation of state

A stiffened gas is described by two constant coefficients $\Gamma$ and $\pi$

$$p = \Gamma \frac{e}{\tau} - (\Gamma + 1)\pi. \tag{F.1}$$

The parameter $\Gamma$ coincides with the Grüneisen coefficient $\Gamma = \tau/T \partial_s p|_\tau$ while the parameter $\pi$, homogeneous to a pressure, allows to take into account attraction between molecules. Here are now detailed some computations whose results are used in the article. For any EOS, the following relationships stand

$$dp = -(\rho c)^2 d\tau + \rho \Gamma T ds, \tag{F.2a}$$

$$= -(\rho c)^2 d\tau + \rho \Gamma (de + p d\tau), \tag{F.2b}$$

$$= \left(\rho \Gamma p - (\rho c)^2\right) d\tau + \rho \Gamma de. \tag{F.2c}$$

On the other hand, equation (F.1) yields

$$dp = -\Gamma \rho^2 e d\tau + \rho \Gamma de. \tag{F.3}$$

Identifying equations (F.2c) and (F.3) confirms the fact that the parameter $\Gamma$ in (F.1) is the Grüneisen coefficient. It also gives the expression of the speed of sound

$$(\rho c)^2 = \partial_\tau p\big|_s = (\Gamma + 1)\frac{p + \pi}{\tau}. \tag{F.4}$$

Because the speed of sound is real, equation (F.4) implies the thermodynamical consistency condition

$$p + \pi > 0. \tag{F.5}$$

Integrating the equation $dp = -(\rho c)^2 d\tau$ shows that the product

$$(p + \pi)\tau^{\Gamma+1} \tag{F.6}$$

is a constant $C > 0$ along isentropic curves. Considering two specific volumes $\tau_R$ and $\tau_L$, the average pressure along the isentropic curve between these two states is

$$\frac{1}{\tau_R - \tau_L} \int_{\tau_L}^{\tau_R} p^{iso}(\tau) d\tau = \frac{C}{\Gamma} \frac{\tau_L^{-\Gamma} - \tau_R^{\Gamma}}{\tau_R - \tau_L} - \pi > -\pi. \tag{F.7}$$

Equation (F.3) also provides the following partial derivatives necessary in order to compute the Roe solver

$$\partial_\tau p\big|_e = -\frac{p + (\Gamma + 1)\pi}{\tau}, \quad \partial_e p\big|_\tau = \frac{\Gamma}{\tau}. \tag{F.8}$$

Finally, in order to be able to compute the profile of rarefaction waves, the partial derivative $\partial_\tau \rho c\big|_s$ is needed. Differentiating equation (F.4) gives

$$d(\rho c)^2 = (\Gamma + 1) \left( \rho dp - \rho^2 (p + \pi) d\tau \right). \tag{F.9}$$

Using equation (F.2a) and performing simple algebraic manipulations, the expression of the partial derivative is eventually recovered

$$\partial_\tau \rho c\big|_s = \frac{1}{2(\rho c)} \partial_\tau (\rho c)^2 \big|_s = -(\Gamma + 2) \frac{\rho c}{2\tau}. \tag{F.10}$$

**Remark 30.** When $\pi = 0$, the stiffened gas EOS reduces to the perfect gas EOS. The perfect gas EOS is generally written with the adiabatic exponent $\gamma$ which, in this case, is equal to $\Gamma + 1$

$$p = (\gamma - 1) \frac{e}{\tau} \tag{F.11}$$

# Appendix G

# Ransom faucet semi-analytical solution

In this section is recalled the computation of the semi-analytical solution for the Ransom faucet. Water density and pressure are assumed constant. Following a given water parcel, its momentum balance reads

$$\frac{\mathrm{d}}{\mathrm{d}t}u = g. \tag{G.1}$$

Integration with respect to time yields

$$u(t) = g(t - t_0) + u_0, \tag{G.2a}$$

$$x(t) = \frac{g}{2}(t - t_0)^2 + u_0(t - t_0), \tag{G.2b}$$

where $t_0$ is the time at which the fluid parcel enters the domain of computation and $u_0$ is its entering velocity ($u_0 = 10$ in the test case). Solving for $(t - t_0)$ in (G.2b) and substituting the result in (G.2a) gives

$$u(x(t), t) = \sqrt{u_0^2 + 2gx(t)}. \tag{G.3}$$

Finally, conservation of mass implies the following differential equation for $\alpha(x(t), t)$

$$\alpha\rho\frac{\mathrm{d}}{\mathrm{d}t}\left(\frac{1}{\alpha\rho}\right) = \partial_x u, \tag{G.4a}$$

$$\Longleftrightarrow \frac{\mathrm{d}}{\mathrm{d}t}\alpha = -\alpha\partial_x u, \tag{G.4b}$$

which eventually yields

$$\alpha(x(t), t) = \frac{\alpha_0 u_0}{\sqrt{u_0^2 + 2gx(t)}}, \tag{G.5}$$

where $\alpha_0$ is the entering water volume fraction ($\alpha_0 = 0.8$ in the test case). This gives the profile of the volume fraction up to the contact wave beyond which it is trivially constant. The position of the interface is given by $x(t)$ with $t_0 = 0$.

# Bibliography

[1] Remi Abgrall and Smadar Karni. A comment on the computation of non-conservative products. *Journal of Computational Physics*, 229(8):2759–2763, 2010.

[2] Rémi Abgrall. How to prevent pressure oscillations in multicomponent flow calculations: A quasi conservative approach. *Journal of Computational Physics*, 125(1):150–160, 1996.

[3] Rémi Abgrall and Richard Saurel. Discrete equations for physical and numerical compressible multiphase mixtures. *Journal of Computational Physics*, 186(2):361–396, 2003.

[4] Grégoire Allaire, Sébastien Clerc, and Samuel Kokh. A five-equation model for the simulation of interfaces between compressible fluids. *Journal of Computational Physics*, 181(2):577–616, 2002.

[5] M.R. Baer and J.W. Nunziato. A two-phase mixture theory for the deflagration-to-detonation transition (DDT) in reactive granular materials. *International Journal of Multiphase Flow*, 12(6):861–889, 1986.

[6] David J. Benson. Computational methods in Lagrangian and Eulerian hydrocodes. *Computer Methods in Applied Mechanics and Engineering*, 99(2):235–394, 1992.

[7] Ray A. Berry, Richard Saurel, and Olivier LeMetayer. The discrete equation method (dem) for fully compressible, two-phase flows in ducts of spatially varying cross-section. *Nuclear Engineering and Design*, 240(11):3797–3818, 2010.

[8] Jay P Boris and David L Book. Flux-corrected transport. I. SHASTA, a fluid transport algorithm that works. *Journal of Computational Physics*, 11(1):38–69, 1973.

[9] Jérôme Breil. *Numerical methods for Lagrangian and Arbitrary-Lagrangian-Eulerian Hydrodynamic Contribution to the simulation of High-Energy-Density-Physics Problems*. Habilitation à diriger des recherches, Université de Bordeaux, 2016.

[10] Thomas J. Bridges and Sebastian Reich. Multi-symplectic integrators: numerical schemes for hamiltonian pdes that conserve symplecticity. *Physics Letters A*, 284(4):184–193, 2001.

[11] G. Carré, S. Del Pino, B. Després, and E. Labourasse. A cell-centered Lagrangian hydrodynamics scheme on general unstructured meshes in arbitrary dimension. *Journal of Computational Physics*, 228(14):5160–5183, 2009.

[12] Castro Díaz, Manuel Jesús, Kurganov, Alexander, and Morales de Luna, Tomás. Path-conservative central-upwind schemes for nonconservative hyperbolic systems. *ESAIM: M2AN*, 53(3):959–985, 2019.

[13] Elena Celledoni, Håkon Marthinsen, and Brynjulf Owren. An introduction to Lie group integrators–basics, new developments and applications. *Journal of Computational Physics*, 257:1040–1061, 2014.

[14] C. Chaigneau. Rapport CEA.

[15] C. Chalons. Path-conservative in-cell discontinuous reconstruction schemes for non conservative hyperbolic systems. *Commun. Math. Sci. 18 (2020) 1-30*, 2019.

[16] Praveen Chandrashekar, Boniface Nkonga, Asha Kumari Meena, and Ashish Bhole. A path conservative finite volume method for a shear shallow water model. *Journal of Computational Physics*, 413:109457, 2020.

[17] Chih-Hao Chang and Meng Liou. A new approach to the simulation of compressible multifluid flows with ausm+up scheme. *AIAA J*, 227, 06 2003.

[18] Daniel Chauveheid. *Ecoulements multi-matériaux et multi-physiques : solveur volumes finis eulérien co-localisé avec capture d'interfaces, analyse et simulations*. PhD thesis, Mathématiques Cachan, Ecole normale supérieure 2012, 2012. Thèse de doctorat dirigée par Ghidaglia, Jean-Michel.

[19] R. Chauvin, S. Guisset, B. Manach-Pérennou, and L. Martaud. A colocalized scheme for three-temperature grey diffusion radiation hydrodynamics. *Commun. Comput. Phys. 31(1), 293-330*, 2021.

[20] Juan Cheng, Chi-Wang Shu, and Qinghong Zeng. A Conservative Lagrangian Scheme for Solving Compressible Fluid Flows with Multiple Internal Energy Equations. *Communications in Computational Physics*, 12:1307–1328, 2012.

[21] Paul-Henry Cournède. *Un schéma bilagrange plus projection pour la simulation bifluide des instabilités de mélange*. PhD thesis, Mathématiques appliquées Châtenay-Malabry, École centrale de Paris, 2001. Thèse de doctorat dirigée par Saguez, Christian.

[22] B. Mihalas D. Mihalas. *Foundations of radiation hydrodynamics*. Oxford University Press Oxford, 1964.

[23] A. S. Dawes. Solving the diffusion equation on a non-aligned mesh. *Computers & Fluids*, 83:77–89, 2013.

[24] A.S. Dawes. Three-dimensional multi-material polyhedral method for diffusion. *Computers & Fluids*, 156:485–495, 2017. Ninth International Conference on Computational Fluid Dynamics (ICCFD9).

[25] R. B. DeBar. Fundamentals of the KRAKEN code. *Lawrence Livermore National Lab.*, 3 1974.

[26] A. Decoster, P.A. Markowich, B. Perthame, and P.A. Raviart. *Modelling of Collisions.* Series in Applied Mathematics. Editions Scientifiques et Medicales Elsevier, 1998.

[27] B. Després and F. Lagoutière. Numerical resolution of a two-component compressible fluid model with interfaces. *Progress in Computational Fluid Dynamics*, 2007.

[28] Bruno Després. Weak consistency of the cell-centered Lagrangian GLACE scheme on general meshes in any dimension. *Computer Methods in Applied Mechanics and Engineering*, 199(41):2669–2679, 2010.

[29] R. P. Drake, E. S. Myra, M. J. Grosskopf, E. Rutter, and B. Torralva. Behavior of irradiated low-Z walls and adjacent plasma. In *APS Division of Plasma Physics Meeting Abstracts*, volume 52 of *APS Meeting Abstracts*, page NP9.053, 2010.

[30] D.A. Drew and S.L. Passman. *Theory of Multicomponent Fluids.* Springer, 2014.

[31] Donald A Drew. Mathematical modeling of two-phase flow. *Annual review of fluid mechanics*, 15(1):261–291, 1983.

[32] Frédéric Duboc, Cédric Enaux, Stéphane Jaouen, Hervé Jourdren, and Marc Wolff. High-order dimensionally split Lagrange-remap schemes for compressible hydrodynamics. *Comptes Rendus Mathematique*, 348(1):105–110, 2010.

[33] Michael Dumbser and Dinshaw S. Balsara. A new efficient formulation of the HLLEM Riemann solver for general conservative and non-conservative hyperbolic systems. *Journal of Computational Physics*, 304:275–319, 2016.

[34] Cedric Enaux, Sebastien Guisset, C. Lasuen, and Quentin Ragueneau. Numerical resolution of a three temperature plasma model. *Journal of Scientific Computing*, 82, 02 2020.

[35] Stéphane Galera, Pierre-Henri Maire, and Jérôme Breil. A two-dimensional unstructured cell-centered multi-material ALE scheme using VOF interface reconstruction. *J. Comput. Phys.*, 229(16):5755–5787, aug 2010.

[36] Rao V Garimella, Vadim Dyadechko, Blair K Swartz, and Mikhail J Shashkov. Interface reconstruction in multi-fluid, multi-phase flow simulations. In *Proceedings of the 14th international meshing roundtable*, pages 19–32. Springer, 2005.

[37] Sergey Gavrilyuk. Multiphase flow modeling via Hamilton's principle. *CISM International Centre for Mechanical Sciences*, 535, 2011.

[38] Marc Gerritsma. An introduction to a compatible spectral discretization method. *Mechanics of Advanced Materials and Structures*, 19(1-3):48–67, 2012.

[39] James Glimm. Solutions in the large for nonlinear hyperbolic systems of equations. *Communications on Pure and Applied Mathematics*, 18:697–715, 1965.

[40] Walter B Goad. *WAT: a numerical method for two-dimensional unsteady fluid flow*, volume 2365. Los Alamos Scientific Laboratory of the University of California, 1960.

[41] E. Godlewski and P.A. Raviart. *Numerical Approximation of Hyperbolic Systems of Conservation Laws.* Applied Mathematical Sciences. Springer New York, 1996.

[42] Sergei K. Godunov and I. Bohachevsky. Finite difference method for numerical computation of discontinuous solutions of the equations of fluid dynamics. *Matematičeskij sbornik*, 47(89)(3):271–306, 1959.

[43] J. M. Greenberg and A. Y. Leroux. A well-balanced scheme for the numerical processing of source terms in hyperbolic equations. *SIAM Journal on Numerical Analysis*, 33(1):1–16, 1996.

[44] Miroslav Gremla and Hans Christian Öttinger. Dynamics and thermodynamics of complex fluids. I. Development of a general formalism. *Physical Review E*, 56(6):6620, 1997.

[45] A. Harten, J. M. Hyman, P. D. Lax, and B. Keyfitz. On finite-difference approximations and entropy conditions for shocks. *Communications on Pure and Applied Mathematics*, 29(3):297–322, 1976.

[46] Amiram Harten, Peter D. Lax, and Bram van Leer. On upstream differencing and godunov-type schemes for hyperbolic conservation laws. *SIAM Review*, 25(1):35–61, 1983.

[47] Philippe Hergibo, Timothy N. Phillips, and Zhihua Xie. A moment-of-fluid method for resolving filamentary structures using a symmetric multi-material approach. *Journal of Computational Physics*, page 112401, 2023.

[48] Eric Heulhard de Montigny. *Thermo-hydro-dynamic consistency and stiffness in general compressible multiphase flows.* PhD thesis, Mathématiques aux interfaces université Paris-Saclay, 2021. Thèse de doctorat dirigée par Llor, Antoine.

[49] Éric Heulhard de Montigny and Antoine Llor. Taming the "stiff stiffness" of pressure work and equilibration in numerical schemes for compressible multi-fluid flows. *International Journal of Multiphase Flow*, 153:104078, 2022.

[50] C.W Hirt, A.A Amsden, and J.L Cook. An arbitrary Lagrangian-Eulerian computing method for all flow speeds. *J. Comput. Phys.*, 14(3):227–253, 1974.

[51] Thomas Y. Hou and Philippe G. Le Floch. Why nonconservative schemes converge to wrong solutions: Error analysis. *Mathematics of Computation*, 62(206):497–530, 1994.

[52] M. Ishii. *Thermo-fluid dynamic theory of two-phase flow.* Collection de la Direction des études et recherches d'Electricité de France. Eyrolles, 1975.

[53] J. Fochesato. Personal communication.

[54] R. Kamm and F.X. Timmes. On efficient generation of numerically robust Sedov solutions. *LANL Report LA-UR-07-2849*, 2007.

[55] Ashwani Kapila, R. Menikoff, J. Bdzil, Steven Son, and D. Stewart. Two-phase modeling of deflagration-to-detonation transition in granular materials: Reduced equations. *Phys. Fluids*, 13:3002–3024, 10 2001.

[56] Smadar Karni. Multicomponent flow calculations by a consistent primitive algorithm. *Journal of Computational Physics*, 112(1):31–43, 1994.

[57] Barbara Lee Keyfitz. Mathematical properties of nonhyperbolic models for incompressible two-phase flow. In *Proc. Fourth Int. Conf. Multiphase Flow*. EE Michaelides, ICMF, 2001.

[58] Evgeny Kikinzon, Yuri Kuznetsov, Konstatin Lipnikov, and Mikhail Shashkov. Approximate static condensation algorithm for solving multi-material diffusion problems on meshes non-aligned with material interfaces. *Journal of Computational Physics*, 347:416–436, 2017.

[59] Evgeny Kikinzon, Mikhail Shashkov, and Rao Garimella. Establishing mesh topology in multi-material cells: Enabling technology for robust and accurate multi-material simulations. *Computers & Fluids*, 172:251–263, 2018.

[60] Samuel Kokh and Frédéric Lagoutière. An anti-diffusive numerical scheme for the simulation of interfaces between compressible fluids by means of a five-equation model. *J. Comput. Phys.*, 229:2773–2809, 2010.

[61] Dmitri Kuzmin, Rainald Löhner, and Stefan Turek. *Flux-corrected transport: principles, algorithms and applications*. Springer, 2012.

[62] Frédéric Lagoutière. *Modélisation mathématique et résolution numérique de problèmes de fluides à plusieurs constituants*. Thèses, Université Pierre et Marie Curie - Paris VI, 2000.

[63] Frédéric Lagoutière. A non-dissipative entropic scheme for convex scalar equations via discontinuous cell-reconstruction. *Comptes Rendus Mathematique*, 338(7):549–554, 2004.

[64] Peter D. Lax. *Hyperbolic Systems of Conservation Laws and the Mathematical Theory of Shock Waves*. Society for Industrial and Applied Mathematics, 1973.

[65] Olivier Le Métayer and Richard Saurel. The Noble-Abel stiffened-gas equation of state. *Physics of Fluids*, 28(4):046102, 2016.

[66] Philippe G. LeFloch and Siddhartha Mishra. Numerical methods with controlled dissipation for small-scale dependent shocks. *Acta Numerica*, 23:743–816, 2014.

[67] Daniel Lhuillier, Chih-Hao Chang, and Theo G. Theofanous. On the quest for a hyperbolic effective-field model of disperse flows. *Journal of Fluid Mechanics*, 731:184–194, 2013.

[68] Gaute Linga and Tore Flåtten. A hierarchy of non-equilibrium two-phase flow models. *ESAIM: Proceedings and Surveys*, 66:109–143, 2019.

[69] Antoine Llor. Modèles hydrodynamiques statistiques pour les écoulements d'instabilités de mélange en régime développé: critères théoriques d'évaluation 0D et comparaison des approches mono et bifluides. *CEA DAM DIF*, 2001.

[70] Raphaël Loubère, Pierre-Henri Maire, and Bernard Rebourcet. Staggered and colocated finite volume schemes for lagrangian hydrodynamics. *Handbook of Numerical Methods for Hyperbolic Problems: Basic and Fundamental issues*, 17:319–352, 2016.

[71] P.H. Maire, R. Abgrall, J. Breil, and J. Ovadia. A cell-centered lagrangian scheme for two-dimensional compressible flow problems. *SIAM J.on Scientific Computing, Vol.29, No.4, p.1781-1824*, 2007.

[72] Pierre-Henri Maire. Contribution to the numerical modeling of inertial confinement fusion. *Habilitation à Diriger des Recherches*, 2011.

[73] V. Maltsev, M. Skote, and P. Tsoutsanis. High-order methods for diffuse-interface models in compressible multi-medium flows: A review. *Physics of Fluids*, 34(2):021301, 2022.

[74] B. Manach-Pérennou, R. Chauvin, S. Guisset, and A. Llor. Cell-centered lagrangian scheme for multi-material flows with pressure equilibration. *Computers & Fluids*, 250:105705, 2023.

[75] A. Marboeuf. *Schémas ALE multi-matériaux totalement conservatifs pour l'hydrodynamique*. PhD thesis, École Ploytechnique, 2018.

[76] Pedro José Martínez Ferrer, Tore Flåtten, and Svend Tollak Munkejord. On the effect of temperature and velocity relaxation in two-phase flow models. *ESAIM: Mathematical Modelling and Numerical Analysis*, 46(2):411–442, 2012.

[77] Gianni Dal Maso, Patrick Le Floch, and François Murat. Definition and weak stability of nonconservative products. *Journal de Mathématiques Pures et Appliquées*, 74:483–548, 1995.

[78] Ralph Menikoff and Bradley J. Plohr. The Riemann problem for fluid flow of real materials. *Rev. Mod. Phys.*, 61:75–130, Jan 1989.

[79] Vincent A Mousseau and Dana A Knoll. Temporal accuracy of the nonequilibrium radiation diffusion equations applied to two-dimensional multimaterial simulations. *Nuclear Science and Engineering*, 154(2):174–189, 2006.

[80] Svend Tollak Munkejord, Steinar Evje, and Tore FlÅtten. A MUSTA Scheme for a Nonconservative Two-Fluid Model. *SIAM Journal on Scientific Computing*, 31(4):2587–2622, 2009.

[81] Angelo Murrone and Hervé Guillard. A five equation reduced model for compressible two phase flow problems. *Journal of Computational Physics*, 202(2):664–698, 2005.

[82] Hans Christian Öttinger and Miroslav Gremla. Dynamics and thermodynamics of complex fluids. II. Illustration of a general formalism. *Physical Review E*, 56(6):6633, 1997.

[83] B.J. Parker and D.L. Youngs. Two and three dimensional Eulerian simulations of fluid flow with material interfaces. *Technical Report 01/92*, 1992.

[84] Christina Paulin. *Improved numerical schemes for monotonic conservative scalar advection : tackling mesh imprinting and numerical wetting*. PhD thesis, Mathématiques appliquées université Paris-Saclay, 2021. Thèse de doctorat dirigée par Llor, Antoine.

[85] Christina Paulin, Antoine Llor, Thibaud Vazquez-Gonzalez, Jean-Philippe Perlat, and Éric Heulhard de Montigny. Doubly monotonic constraint on interpolators: bridging second-order to singularity preservation to cancel "numerical wetting" in transport schemes. *SIAM Journal on Scientific Computing*, 44(3):A1227–A1253, 2022.

[86] D. Pavlov, P. Mullen, Y. Tong, E. Kanso, J.E. Marsden, and M. Desbrun. Structure-preserving discretization of incompressible fluids. *Physica D: Nonlinear Phenomena*, 240(6):443–458, 2011.

[87] M. Petrella, R. Abgrall, and S. Mishra. On the discrete equation model for compressible multiphase fluid flows. *Journal of Computational Physics*, 478:111974, 2023.

[88] Ernesto Pimentel-García, Manuel J. Castro, Christophe Chalons, Tomás Morales de Luna, and Carlos Parés. In-cell discontinuous reconstruction path-conservative methods for non conservative hyperbolic systems - second-order extension. *Journal of Computational Physics*, 459:111152, jun 2022.

[89] John D. Ramshaw and John A. Trapp. Characteristics, Stability, and Short-Wavelength Phenomena in Two-Phase Flow Equation Systems. *Nuclear Science and Engineering*, 66(1):93–102, 1978.

[90] VH Ransom. Numerical benchmark test No 2.1: Faucet flow. *Multiphase science and technology*, 3(1-4), 1987.

[91] Julius Reiss. A family of energy stable, skew-symmetric finite difference schemes on collocated grids: a simple way to avoid odd–even decoupling. *Journal of Scientific Computing*, 65:821–838, 2015.

[92] P.L Roe. Approximate riemann solvers, parameter vectors, and difference schemes. *Journal of Computational Physics*, 43(2):357–372, 1981.

[93] Manuel D Salas. The curious events leading to the theory of shock waves. *Shock waves*, 16(6):477–487, 2007.

[94] R. Saurel and R. Abgrall. A Multiphase Godunov Method for Compressible Multifluid and Multiphase Flows. *Journal of Computational Physics*, 1999.

[95] Richard Saurel and Rémi Abgrall. A simple method for compressible multifluid flows. *SIAM J. Sci. Comput.*, 21:1115–1145, 1999.

[96] Richard Saurel and Carlos Pantano. Diffuse-interface capturing methods for compressible two-phase flows. *Annual Review of Fluid Mechanics*, 50(1):105 – 130, 2018.

[97] C.D. Sijoy and S. Chaturvedi. Combining node-centered parallel radiation transport and higher-order multi-material cell-centered hydrodynamics methods in three-temperature radiation hydrodynamics code TRHD. *Computer Physics Communications*, 203:94–109, 2016.

[98] Dave Peter Starinshak. *Level set methods for multimaterial radiative shock hydrodynamics*. PhD thesis, 2012. PhD Thesis.

[99] Städtke, H. *Two-Fluid Model of Two-Phase Flow*, chapter 3, pages 35–43. John Wiley & Sons, Ltd, 2006.

[100] P. K. Sweby. High resolution schemes using flux limiters for hyperbolic conservation laws. *SIAM Journal on Numerical Analysis*, 21(5):995–1011, 1984.

[101] P. D. Thomas and C. K. Lombard. Geometric Conservation Law and Its Application to Flow Computations on Moving Grids. *AIAA Journal*, 17(10):1030–1037, 1979.

[102] E.F. Toro. *Riemann Solvers and Numerical Methods for Fluid Dynamics: A Practical Introduction*. Springer, 1997.

[103] Eleuterio F. Toro, M. Spruce, and William Speares. Restoration of the contact surface in the hll-riemann solver. *Shock Waves*, 4:25–34, 1994.

[104] I Toumi. A weak formulation of Roe's approximate Riemann solver. *Journal of Computational Physics*, 102(2):360–373, 1992.

[105] Bram van Leer. Towards the ultimate conservative difference scheme. *Journal of Computational Physics*, 135(2):229–248, 1997.

[106] T. Vazquez-Gonzalez, A. Llor, and Christophe Fochesato. Ransom test results from various two-fluid schemes: Is enforcing hyperbolicity a thermodynamically consistent option? *International Journal of Multiphase Flow*, 81:104–112, 2016.

[107] Thibaud Vazquez Gonzalez. *Schémas numériques mimétiques et conservatifs pour la simulation d'écoulements multiphasiques compressibles*. PhD thesis, Mathématiques appliquées Université Paris-Saclay, 2016. Thèse de doctorat dirigée par Llor, Antoine.

[108] Thibaud Vazquez-Gonzalez, Antoine Llor, and Christophe Fochesato. A mimetic numerical scheme for multi-fluid flows with thermodynamic and geometric compatibility on an arbitrarily moving grid. *International Journal of Multiphase Flow*, 132:103324, 2020.

[109] Arthur E. P. Veldman. Supraconservative finite-volume methods for the euler equations of subsonic compressible flow. *SIAM Review*, 63(4):756–779, 2021.

[110] J. Von Neumann and R. D. Richtmyer. A Method for the Numerical Calculation of Hydrodynamic Shocks. *Journal of Applied Physics*, 21(3):232–237, March 1950.

[111] A.B. Wood. *A Textbook of Sound*. Macmillan, 1930.

[112] Paul Woodward and Phillip Colella. The numerical simulation of two-dimensional fluid flow with strong shocks. *Journal of Computational Physics*, 54(1):115–173, 1984.

[113] Martin Wörner. *A compact introduction to the numerical modeling of multiphase flows*, volume 6932. FZKA, 2003.

[114] Ke Xu, Zhenxun Gao, Zhansen Qian, Chongwen Jiang, and Chun-Hian Lee. Numerical path-preserving Godunov schemes for hyperbolic systems. *Journal of Computational Physics*, page 112297, 2023.

[115] B. Zeldovich and P. Raizer. *The mechanics and thermodynamics of continua. Physics of shock waves and high-temperature hydrodynamic phenomena*. Academic Press, 1966.

[116] Yi Zhang, Artur Palha, Marc Gerritsma, and Leo G. Rebholz. A mass-, kinetic energy- and helicity-conserving mimetic dual-field discretization for three-dimensional incompressible Navier-Stokes equations, part I: Periodic domains. *Journal of Computational Physics*, 451:110868, 2022.